Towards a clinical implementation of mixed electron-photon radiation therapy.

Veng Jean Heng

Department of Physics
McGill University, Montreal

Montreal, Quebec

2024

A thesis submitted to McGill University in partial fulfillment of the requirements of the degree of Doctor of Philosophy

ACKNOWLEDGEMENTS

First and foremost, I must thank my supervisor Dr. Jan Seuntjens for his wise guidance and unwavering support throughout the years. As uncertain and chaotic any research project of this magnitude may be, you always found the way to keep me on the right track. Whenever I was faced with a puzzling challenge, all it took was an hour(s!) of discussion with you to nudge me in the correct direction. Your encouragements and continued trust in me were the motivations that kept me pushing through the hard times and helped me build my own self-confidence. You've always kept my best interest in mind by providing me with opportunities that were and will be invaluable to me beyond graduate school.

Equally instrumental to my completion of this work is Dr. Marc-André Renaud. I owe all of my programming knowledge to you and the codebase that you've left me. I cannot express how grateful I am for the time and insight you've selflessly provided me. Whether in research or in life, you've been the mentor that I never knew I so much needed. I will be forever indebted to you.

I would like to also thank Dr. Monica Serban for providing me with invaluable clinical insight. I have learned so much from you of what it means to be a clinical medical physicist. Your kind compliments and encouragements pushed me to be where I am today.

I am grateful for having had the opportunity to collaborate with Dr. Carolyn Freeman, who showed me how my research could actually improve clinical care and patient outcomes. Her insight into clinical practice and vast experience in the treatment of sarcomas were monumental to the retrospective sarcoma planning study.

I was also fortunate to have had the chance to collaborate with and befriend Yee Man Tai. I still cherish the many evenings we spent doing measurements and racking our brain over our confusing results.

Over the years I've received the help of many medical physicists and staff members from the Medical Physics Unit at the McGill University Health Centre. A big "Thank you!" to

Margery Knewstubb and Tatjana Nisic for facilitating my numerous administrative requests and questions. I must acknowledge the tremendous machining help I received from Joe Larkin and Bhavan Siva. I have greatly benefited from the teachings and assistance of Russel Ruo, Michael Evans, Ackeem Joseph and Dr. Tanner Connell with regards to dosimeter and linac operations, and patient data collection.

"Maybe the real treasure was the friends we made along the way." I have truly been blessed to have had the chance to work alongside such bright, fun, and caring colleagues in the MPU. Thank you Julien, Santiago, Chris, Morgan, Joel, Judy, Federico, Liam, Felix, Haley, Kayla, Logan, Gabriel, Saad, Tony and every student of the MPU! You have made my PhD years ones that I will fondly remember.

Finally, I owe my greatest gratitude to my parents Kheng Heng and Sophea and sister Emily who have been with me at each step of this journey and always given me their unconditional love and support.

ABSTRACT

External megavoltage electron beams have well-established dosimetric properties that are clinically beneficial for the treatment of superficial tumors. Their high entrance dose and rapid dose falloffs allow for better sparing of healthy tissue beyond the tumor depth. Mixed electron-photon beam radiation therapy (MBRT) is an emerging technique which aims to combine the use of external electron and photon beams, both delivered using multi-leaf collimators (MLC). MBRT treatment plans can leverage the dosimetric benefits of either particle type while benefiting from the flexibility in treatment deliveries found in state-of-the-art photon treatments.

To ensure that the MBRT dose calculated by our treatment planning system (TPS) is representative of the dose delivered to patients, quality assurance (QA) of MBRT plans must be performed. This QA is often based on a measurement with a detector or detector array in a phantom, representing the patient. To account for differences in beam quality between reference conditions and patient-specific QA of MBRT plans, we introduce a formalism that corrects the measurement reading with a ratio of stopping power ratios of water to air. An MBRT plan was delivered on a polymethyl methacrylate (PMMA) cylindrical phantom and dose measurements were taken with an ion chamber and film. Ion chamber measurements agreed with Monte Carlo calculations with 2.1% and a gamma passing rate of 97.3% was obtained for film with a gamma criterion of 3%/2 mm.

For more routine patient-specific QA, we commissioned the MapCHECK® (Sun Nuclear, Inc), a diode array detector, and a log file-based dose reconstruction approach for MBRT dose verification. An *ab initio* model of the MapCHECK® was created using the manufacturer's blueprint data to precisely model detector's geometry. Five MBRT plans were delivered onto the MapCHECK® and measurements were compared to Monte Carlo calculation through a gamma analysis with a gamma criterion of 3%/2 mm. All five plans had a gamma passing rate of above 97%. For one representative plan, the trajectory log files were

collected, and the machine parameters were used to recalculate the patient's Monte Carlo dose. No clinically relevant differences in dose to any relevant structures were found between the log file-recalculated dose and the theoretical planned dose.

To demonstrate the dosimetric benefit of MBRT compared to the standard of care, a retrospective treatment planning study was performed on a cohort of 22 soft tissue sarcoma of the lower extremity. Robust MBRT plans were re-optimized for each patient and dosimetrically compared to their standard of care Volumetric Modulated Arc Therapy (VMAT) treatment plans. Although VMAT plans required the use of bolus in 10 of the 22 patients, no MBRT plans required bolus to reach an equivalent coverage of the clinical target volume by the prescription dose. Doses to organs-at-risk were significantly lower in MBRT plans with $V_{20\mathrm{Gy}}$ to normal tissue decreasing by $14.9 \pm 3.2\%$ ($p < 10^{-}6$) and $V_{50\mathrm{Gy}}$ to bone decreasing by $8.2 \pm 4.0\%$ ($p < 10^{-}3$).

In this study, the impact of range uncertainties on MBRT plans due to errors in the mass density assignment are investigated. Range scenarios are introduced by calculating beamlets in 2 additional scenarios. Patient CT numbers are either upscaled or downscaled by a constant factor conservatively chosen to be 3.5%. The most susceptible regions to dose discrepancies due to range errors were found to be located along electron beams' path, immediately downstream from the target.

The work included in this thesis provides the necessary framework and motivation for an efficient clinical implementation of MBRT. While further improvements can be made on the technical front, any clinical implementation requires the endorsement of radiation oncologists. Unequivocal clinical benefits of MBRT must be demonstrated for clearly identified cancer types. Although lower extremity soft tissue sarcomas were shown to benefit from MBRT treatments, other treatment sites with superficial tumors remain to be investigated at a larger scale.

ABRÉGÉ

Les faisceaux d'électrons de haute énergie ont des propriétés dosimétriques bien établies qui sont cliniquement bénéfiques pour le traitement des tumeurs superficielles. Leur haute dose d'entrée et leur chute rapide de dose permettent une meilleure préservation des tissus sains au-delà de la profondeur de la tumeur.

La radiothérapie par faisceaux mixtes d'électrons et de photons (MBRT) est une technique émergente qui vise à combiner l'utilisation de faisceaux externes d'électrons et de photons, tous deux délivrés à l'aide de collimateurs multilames (MLC). Les plans de traitement MBRT peuvent exploiter les avantages dosimétriques de chaque type de particule tout en bénéficiant de la flexibilité dans les administrations de traitement trouvées dans les traitements photoniques de pointe.

Pour garantir que la dose MBRT calculée par notre système de planification de traitement (TPS) est représentative de la dose délivrée aux patients, une assurance qualité (QA) des plans MBRT doit être effectuée. Pour tenir compte des différences de qualité du faisceau entre les conditions de référence et la QA spécifique au patient des plans MBRT, nous introduisons un formalisme qui corrige la lecture de mesure avec un quotient de pouvoir d'arrêt eau/air. Un plan MBRT a été délivré sur un fantôme cylindrique en polyméthacrylate de méthyle (PMMA) et des mesures de dose ont été prises avec une chambre d'ionisation et un film. Les mesures de chambre d'ionisation étaient en accord avec les calculs Monte Carlo avec 2.1% et un taux de passage gamma de 97.3% a été obtenu pour le film avec un critère gamma de 3%/2 mm.

Pour une QA spécifique au patient plus routinière, nous avons commissionné le MapCHECK® un détecteur de réseau de diodes, et une approche de reconstruction de dose basée sur les fichiers journaux pour la vérification de dose MBRT. Un modèle *ab initio* du MapCHECK® a été créé en utilisant les données de plan du fabricant pour modéliser précisément la géométrie du détecteur. Cinq plans MBRT ont été délivrés sur le MapCHECK® et les

mesures ont été comparées au calcul Monte Carlo par une analyse gamma avec un critère gamma de 3%/2 mm. Les cinq plans ont eu un taux de passage gamma de plus de 97%. Pour un plan représentatif, les fichiers journaux de trajectoire ont été collectés, et les paramètres de la machine ont été utilisés pour recalculer la dose Monte Carlo du patient. Aucune différence cliniquement significative de dose à aucune structure pertinente n'a été trouvée entre la dose recalculée à partir des fichiers journaux et la dose théoriquement planifiée.

Pour démontrer l'avantage dosimétrique de la technique MBRT par rapport à la norme de soins, une étude rétrospective de planification du traitement a été réalisée sur une cohorte de 22 sarcomes des tissus mous des membres inférieurs. Des plans MBRT robustes ont été réoptimisés pour chaque patient et comparés dosimétriquement à leurs plans de traitement standard d'arcthérapie volumétrique modulée (VMAT). Bien que les plans VMAT aient nécessité l'utilisation de bolus chez 10 des 22 patients, aucun plan MBRT n'a nécessité de bolus pour atteindre une couverture équivalente du volume cible clinique par la dose prescrite. Les doses aux organes à risque étaient significativement plus faibles dans les plans MBRT avec $V_{20\mathrm{Gy}}$ pour les tissus normaux diminuant de $14.9 \pm 3.2\%$ ($p < 10^{-6}$) et $V_{50\mathrm{Gy}}$ pour l'os diminuant de $8.2 \pm 4.0\%$ ($p < 10^{-3}$).

Dans cette étude, l'impact des incertitudes de portée sur les plans MBRT dues à des erreurs dans l'attribution de la masse volumique est étudié. Des scénarios de portée sont introduits en calculant des faisceaux de rayons dans 2 scénarios supplémentaires. Les nombres CT des patients sont soit augmentés soit diminués par un facteur constant choisi de manière conservatrice à 3.5%. Les régions les plus susceptibles de présenter des divergences de dose en raison d'erreurs de portée ont été trouvées le long du trajet des faisceaux d'électrons, immédiatement en aval de la cible.

Le travail inclus dans cette thèse fournit le cadre nécessaire et la motivation pour une mise en œuvre clinique efficace du MBRT. Bien que des améliorations supplémentaires puissent être apportées sur le plan technique, toute mise en œuvre clinique nécessite l'approbation de radio-oncologues. Les avantages cliniques indiscutables de la technique MBRT doivent être

démontrés pour des types de cancer clairement identifiés. Bien que les sarcomes des tissus mous des membres inférieurs semblent bénéficier des traitements MBRT, d'autres sites de traitement avec des tumeurs superficielles restent à être étudiés à plus grande échelle.

TABLE OF CONTENTS

LIST OF FIGURES

LIST OF TABLES

LIST OF ABBREVIATIONS

BEV Beams Eye View.

CPU Central Processing Unit.

CT Computed Tomography.

CTV Clinical Target Volume.

EBRT External Beam Radiation Therapy.

FLEC Few-Leaf Electron Collimator.

GPU Graphics Processing Unit.

GTV Gross Tumor Volume.

IMRT Intensity Modulated Radiation Therapy.

MBRT Mixed Electron-Photon Beam Radiation Therapy.

MERT Modulated Electron Radiation Therapy.

NTCP Normal Tissue Complication Probability.

OD Optical Density.

PMC Pre-calculated Monte Carlo.

PTV Planning Target Volume.

RAM Random-access memory.

RMP Restricted Master Problem.

SAD Source-to-Axis Distance.

SSD Source-to-Surface Distance.

TCP Tumor Control Probability.

TPS Treatment Planning System.

VMAT Volumetric Modulated Arc Therapy.

CONTRIBUTION TO ORIGINAL KNOWLEDGE

The thesis contains 3 published manuscripts and 1 in preparation. The first manuscript presents a method for QA of MBRT plans with both ion chamber and film measurements. In particular, the framework to correct the chamber's response to the beam quality of MBRT fields is novel. The second manuscript describes the commissioning of MapCHECK for measuremnts of MBRT field and its validation as PSQA method of MBRT plans in conjunction with log file data. This offers a more streamlined PSQA option of MBRT plans that had not been investigated in the past. In the third manuscript, the dosimetric benefits of MBRT compared to standard of care VMAT are showcased for 22 retrospective cases of soft tissue sarcoma of the lower extremity. This is the first MBRT planning study of this scale for sarcomas and provides a clinical motivation for a potential clinical trial. Finally, in the last manuscript, the effect of range uncertainties is considered on MBRT dose distribution. This is the first MBRT study to incorporate range scenarios by scaling CT numbers prior to phantom generation.

CONTRIBUTION OF AUTHORS

Chapters 1-4 are introductory chapters, establishing the basic theory behind dose delivery, calculation, and measurement in external beam radiotherapy. A literature review of MBRT is given in Chapter 4 and the conclusions of this thesis is summarized in Chapter 10. I wrote all these chapters and they were proofread by Jan Seuntjens. Chapter 5 provides a description of the MBRT treatment planning workflow on `brems` and describes the implementation of a pre-calculated Monte Carlo (PMC) method for electron beamlet dose calculation. This chapter was also written by myself and proofread by Jan Seuntjens, respectively. The work presented in this chapter is a continuation of the Radify TPS and builds upon the PMC algorithm both developed by Marc-André Renaud. I implemented a photon transport within PMC and performed the validation and benchmark of electron beamlet calculations against EGSnrc.

Chapters 6-9 are manuscripts, for which the contribution of each co-author is as follows:

1. Veng Jean Heng, Monica Serban, Jan Seuntjens, Marc-André Renaud. "*Ion chamber and film-based quality assurance of mixed electron-photon radiation therapy.*" Med Phys. 2021; 48: 5382–5395. (Chapter 6)

   I generated the MBRT treatment plan and performed dose calculations on the solid water and cylindrical phantoms. I performed all measurements and analysis. I tuned our beam model and made improvements to the column generation optimizer to reach better agreements with measurements. I participated in writing the manuscript. Monica Serban assisted in the design, scanning and contouring of the phantoms, in designing the phantom setup methodology and in performing some measurements. Jan Seuntjens and Marc-André Renaud oversaw and designed the study, while providing interpretation of ion chamber and film measurements. They both assisted in performing some measurements. Marc-André Renaud was responsible for the coding of the SPRXYZnrc user code, allowing for calculations of stopping power ratios in voxelized geometries.

Marc-André Renaud also participated in the writing of the manuscript. Each co-author reviewed the manuscript.

2. Yee Man Tai, Veng Jean Heng, Marc-André Renaud, Monica Serban, Jan Seuntjens. "*Quality assurance for mixed electron–photon beam radiation therapy using treatment log files and MapCHECK.*" Med Phys. 2023; 50: 7996–8008. (Chapter 7)

   Yee Man Tai created the Monte Carlo model of the MapCHECK, performed and analyzed all measurements and log file recalculations of the MBRT plans. She also wrote the manuscript. I provided assistance in the design of the MapCHECK model. I implemented the pipeline for log file dose recalculations, performed all measurements and provided interpretation of the results. I generated the MBRT plans that were delivered in this study. I participated in the writing of the manuscript. Marc-André Renaud is credited for the design of the `brems` treatment planning system used for MBRT planning. Monica Serban provided the CT scan of the MapCHECK and assisted with MapCHECK measurements. Jan Seuntjens designed and oversaw the direction of the study and provided interpretation of the results. Each co-author reviewed the manuscript.

3. Veng Jean Heng, Monica Serban, Marc-André Renaud, Carolyn Freeman, Jan Seuntjens. "*Robust mixed electron-photon radiation therapy planning for soft tissue sarcoma.*" Med Phys. 2023; 50: 6502–6513. (Chapter 8)

   I was responsible for the design of the study, made improvements to `brems`' contour manipulation features and optimizer, performed treatment planning of all patients and analysis of the results. Finally, I wrote the manuscript. Monica Serban provided expert planning guidelines and feedback on the quality of MBRT treatment plans, as well as insights on clinical practice and interpretation of the results. Marc-André Renaud is credited for the design of `brems` and the MBRT planning pipeline. Carolyn Freeman provided guidelines on the cohort exclusion/inclusion criteria, feedback on overall plan quality, insight on clinical practice and goals, and interpretation of the results. Jan

Seuntjens was responsible for the design of the study and provided interpretation of the results. Each co-author reviewed the manuscript.

4. Veng Jean Heng, Marc-André Renaud, Monica Serban, Jan Seuntjens. "*Technical Note: Impact of range uncertainties for MBRT.*" Manuscript in preparation. (Chapter 9)

   I designed the study, implemented the calculations of range scenarios on `brems`, investigated their impact on electron and photon doses, and analyzed the range robustness of MBRT plans on 2 clinical cases. I also wrote the manuscript. Marc-André Renaud is responsible for the design of the setup-robust optimizer upon which the range scenarios were introduced. Monica Serban provided feedback regarding the planning of the clinical cases. Jan Seuntjens assisted in the design of the study and helped with the interpretation of the result. Each co-author reviewed the manuscript.

CHAPTER 1
Introduction

1.1 Radiation Therapy

1.1.1 Radiation therapy as a cancer treatment

Cancer is the leading cause of death in Canada [1] with 22% of Canadians expected to die from cancer. Projections estimate that 45% of Canadians will be diagnosed with some form of cancer over their lifetime [1]. Although cancer primarily affects adults over the age of 50, the incidence of early-onset cancer has been on the rise in the recent decades [2]. The main treatment methods for cancer in oncology have traditionally been: surgery, chemotherapy, hormone therapy and radiation therapy. In the case of solid tumors, surgery directly removes the physical tumor. Chemotherapy provides a systemic treatment through the use of drugs to kill or stop the growth of cancer over the entire body. Hormone therapy consists of inhibiting hormones needed by specific cancers for their growth. Radiation therapy uses ionizing radiation to kill cancer cells through DNA damage. Cancer patients will receive one or more often a combination of these treatments that is best suited to their cancer type, stage and their overall health. It is estimated that around half of cancer patients would stand to benefit from the use of radiation therapy over the course of their treatment [3].

Radiation therapy is based on the premise that ionizing radiation can cause genomic damage through its energy deposition in matter. The damage can either occur through a direct action whereby the radiation directly breaks base pair bonds or indirectly through the release of free radicals from water molecules within the cell, which in turn cause DNA strand breaks. Damage to the DNA structure can either lead to cellular death through apoptosis or an inhibition of the cell's ability to replicate. [4] Ionizing radiation are also separated into 2 categories: directly and indirectly ionizing. Directly ionizing radiation are charged particles

such as electrons and protons that will cause ionization in matter through their Coulomb interaction. Indirectly ionizing radiation are other particles, such as photons and neutrons, that are capable of releasing charged particles through their own interaction with matter. At a macroscopic level, the local energy deposition in matter by these ionizing radiation is described by the concept of absorbed dose D:

$$D = \frac{\mathrm{d}\epsilon}{\mathrm{d}m}, \tag{1.1}$$

where $\mathrm{d}\epsilon$ is the differential amount of energy deposited to an infinitesimal mass $\mathrm{d}m$ of a material. As such the absorbed dose (or simply dose) D has dimensions of energy per unit mass. Its SI unit is the gray (Gy) and 1 Gy is equivalent to 1 J/kg.

Ionizing radiation is thus used in radiation therapy to kill cancerous cells. *A priori*, healthy tissue are also susceptible to DNA damage from ionizing radiation. The mission of radiation therapy is to minimize the dose delivered to such healthy organs-at-risk (OAR) while giving a sufficiently high dose to the targeted tumor. The optimization of a radiation therapy treatment to best meet this mission for each individual patient is part of the treatment planning process. Increasing the dose delivered to a tumor increases the chance of achieving a control of the tumor. This is described by the Tumor Control Probability (TCP). Similarly, the Normal Tissue Complication Probability (NTCP) describes the probability of causing damage to OAR as a function of dose. These 2 functions are generally accepted to be sigmoid in shape as shown in Fig. 1–1 [5]. The NTCP curve is depicted to start at higher dose point than the TCP curve as healthy cells are typically more apt at repairing DNA damage than cancerous cells. Radiation therapy treatments are also spread out over multiple sessions, called fractions, to allow for healthy cells to repair.

Radiation therapy can be broadly classified under 2 large umbrellas: brachytherapy and External Beam Radiation Therapy (EBRT). Brachytherapy consists of the use of radioisotopes to deliver high doses of radiation in close proximity to the tumor. This procedure is

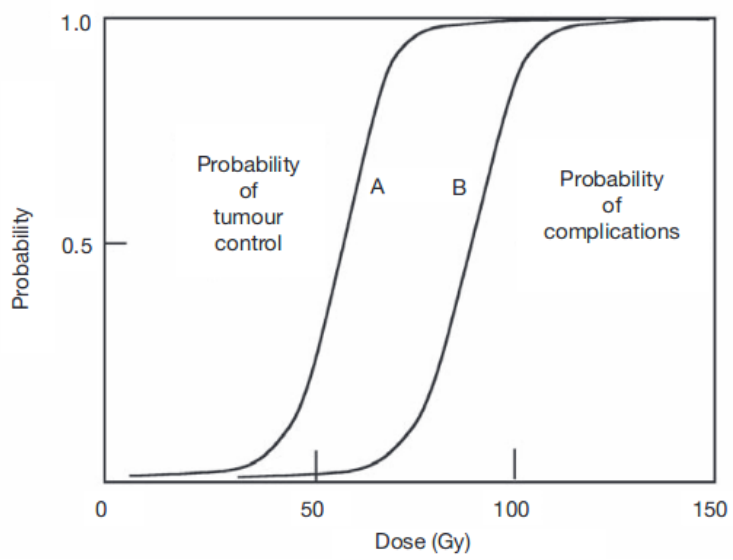

Figure 1–1: Ideal shape of the TCP and NTCP curves.

invasive as the source must be positioned inside the patient body using catheters, needles or applicators. Conversely, with EBRT, the radiation source is produced outside of the patient's body and subsequently directly towards the tumor from the outside.

1.1.2 External beam radiation therapy

To be able to optimize the patient dose delivery, an EBRT treatment plan must be individualized to each patient geometry. The precise location and dimension of the tumor and the OARs, the density and thickness of beam attenuating tissue surrounding them must be mapped. This is done via the use of Computed Tomography (CT) images. A CT simulation scan of the patient is carried out in the same patient positioning setup as anticipated during treatment. Through information on the attenuation of kV X-rays, the CT scan provides a 3D representation of the patient density with millimeter-scale resolution. This information is used to optimize EBRT treatment plans and calculate its dose on Treatment Planning System (TPS). Important structures such as the target and the relevant OARs must be delineated on the CT images to be spatially identified. The extent of each structure is thus drawn on a TPS to form a "contour". With regards to the tumor, there are 3 contours that are commonly drawn. The Gross Tumor Volume (GTV) represents the extent of the

discernible solid tumor. However, it is of therapeutic interest to irradiate a larger volume that also encapsulates the microscopic spread of the disease. This region is the Clinical Target Volume (CTV). When setting up the patient for treatments, there can be a mismatch with their position in the CT images from which the treatment plan was planned with. A large patient setup error could lead to the CTV being positioned outside of the radiation field. Similarly, patient or internal organ motion during the treatment can also lead to underdosage of the CTV. To account for these possible sources of errors, the dose is instead planned to be delivered to a Planning Target Volume (PTV) which is often represented by implementing a geometrical expansion of the CTV by a few millimeters.

Clinical linear accelerators

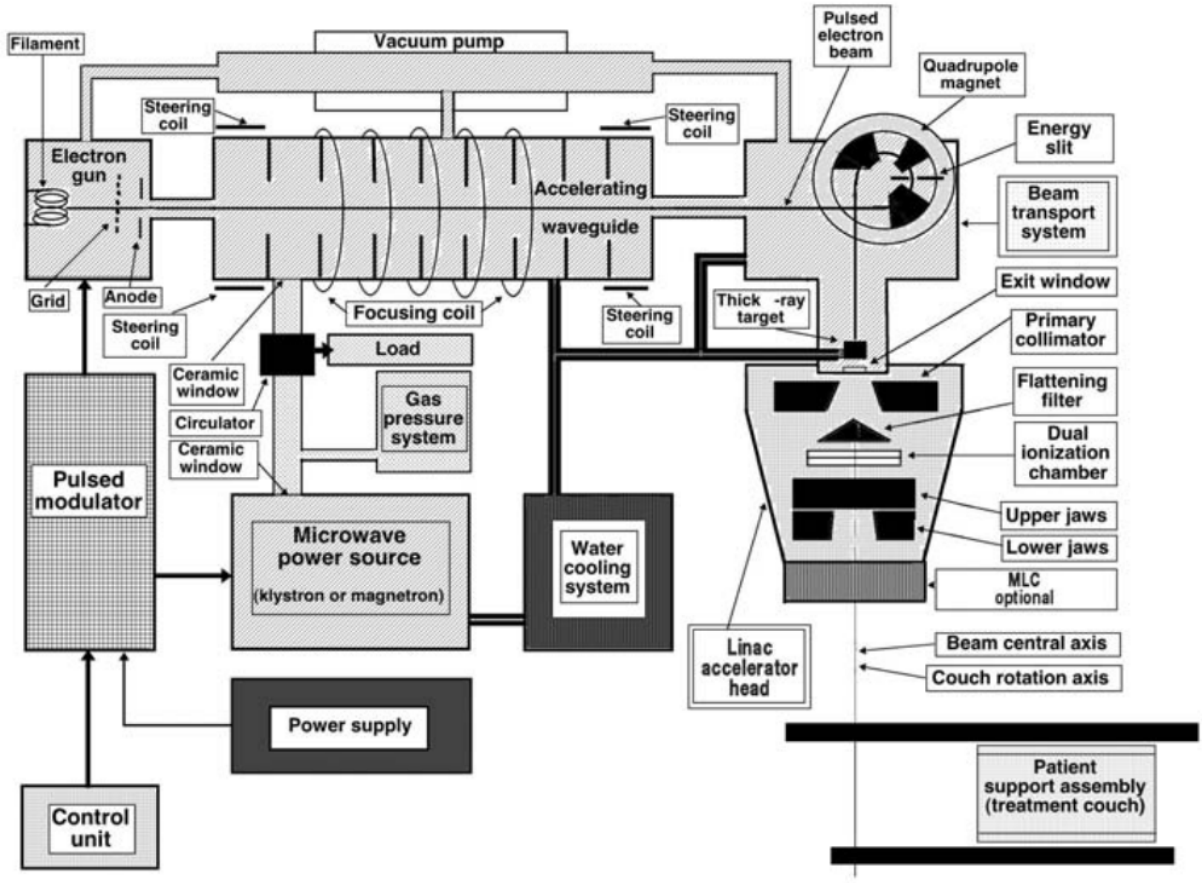

Figure 1–2: Diagram illustrating the different components of a linear accelerator. Reproduced from [6].

Both photon and electron-based EBRT rely on the external generation of either particle type to be then directed towards the patient. Although historically, Cobalt-60 radioisotopes had been widely used as sources of megavoltage gamma rays until these were replaced by medical Linacs. Linacs can produce both megavoltage photon and electron beams using the same fundamental principle. Electrons are generated through thermionic emission by simply heating up a filament cathode in the electron gun (see Fig. 1–2). The anode is located at the entrance of an accelerating waveguide, thus directing the liberated electrons towards the latter. An oscillating electric field injected by a microwave power source accelerates the electrons through the waveguide to their peak desired energies. This provides an almost mono-energetic focused beam of megavoltage electrons which can be then be used for the production of either photon or electron external beams.

To produce photon beams, a target slab, usually made out of a high-Z material like tungsten, is placed in the trajectory of the beam. As electrons travel through the target, they are deflected by the Coulomb field of atomic nucleii and thus produce bremsstrahlung photons as they decelerate. Photons generated in this manner form a continuous spectrum with a maximum energy equal to the peak electron energy. This is the energy that is used to commonly describe the photon beam. A 6 MV photon beam therefore corresponds to one that was generated from first accelerating electrons up to 6 MeV. The mean photon energy of this spectrum is around one third of the peak electron energy. At megavoltage energies, bremsstrahlung photons are preferentially emitted in the forward direction. This creates an inhomogeneous beam with significantly higher intensity in the center of the field. However, this is often impractical in radiotherapy settings. A flattening filter, shaped like a cone, can thus be placed to preferentially attenuate the photon fluence closer to the central axis.

For electron beams, the electrons must be scattered over a larger field to produce a wide enough beam to be practical. This is done by placing a thin high-Z scattering foil instead of

the flattening filter. Both the electron scattering foil and the flattening filter are positioned on a carousel that can be rotated to accommodate the beam type desired.

Three types of collimators, usually made of tungsten, are used to shape the radiation field. The primary collimators are fixed and located immediately below the target. They provide an initial collimation, blocking any particles that would be scattered in the target beyond the extent of the largest practical field allowed by the linac. The secondary collimators are a set of 2 pairs of blocks called jaws. The blocks are movable, with each pair moving along a perpendicular direction to the other. These 2 pairs are thus named the X-jaws and the Y-jaws, defined by the plane along which they can be shifted. The jaws are made sufficiently thick to stop most particles from crossing them. Together, they therefore shape the beam into a rectangular field of dimension (X, Y) dictated by the open gap between each jaw pair. For photon beams, a final collimation system can be used to have a much finer control on the shape of the beam. This is achieved with the Multileaf collimators (MLC) similar to the one in Fig. 1–3. Opposing pairs of cross-sectionally thin leaves are individually controlled by a motor to precisely create an aperture of potentially irregular shape.

An ion chamber, called the monitor chamber, measures the output of radiation being delivered by the linac. It is positioned upstream from the jaws. The monitor chamber readings are normalized to a quantity called the Monitor Unit (MU). For each beam energy deliverable by the linac, 1 MU of linac output is calibrated to deliver a well-known absorbed dose to water in well-defined conditions (e.g. 1 cGy in water at a specific depth, distance and jaws position).

Photon and electron radiation therapy

At the time of writing, all EBRT treatments in Canada are currently delivered using either photons or electrons. Due to the different way they interact with matter, these 2 particle types have distinct dose deposition characteristics that dictate their therapeutic use

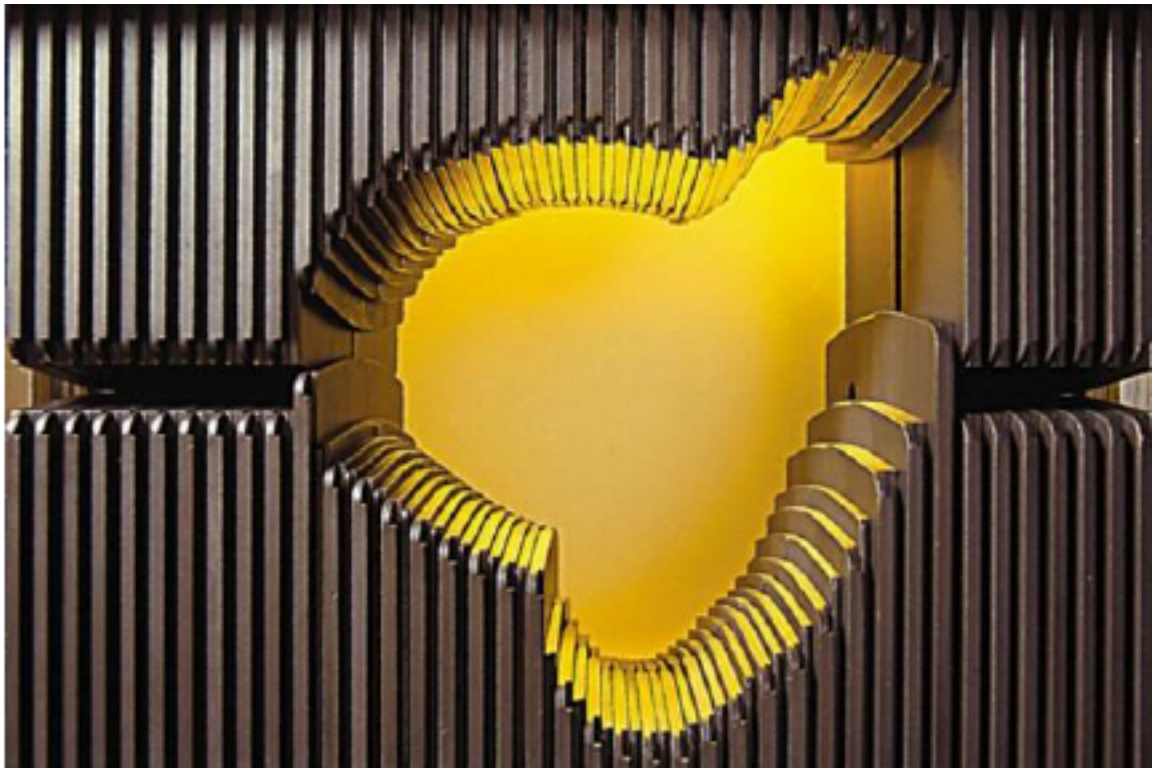

Figure 1–3: Image of the Varian's Millennium MLC, made of 120 leaves. From Varian Medical Systems.

case. Photon-based EBRT is by far the most common form of radiation therapy. Because of the modest attenuation of megavoltage photon beams with depth in matter (i.e., typically 3% per cm), they are able to reach deep-seated tumors. Photon beams can be delivered from various angles such that they intersect within the targeted tumor. This way, the dose to the tumor at the beam's intersection is at its maximum as it receives a contribution from every beam. Conversely, the dose to other regions in the patient can be reduced to only the dose due to 1 beam. State-of-the-art photon treatment plans such as Intensity Modulated Radiation Therapy (IMRT) and Volumetric Modulated Arc Therapy (VMAT) will commonly use MLCs to form aperture shapes that block radiation from being undesirably transmitted to healthy organs. As they are indirectly ionizing radiation, the photon energy deposition is achieved through the release of secondary electrons as they interact with matter and impart energy. Most of the secondary electrons have sufficiently high energy to spread out their dose deposition over several millimeters. This has an important consequence on the superficial

patient dose. Due to the low density of air, very few secondary electrons are released as photons travel from the linac head to the patient. At the patient's surface, the locally released electrons will travel further downstream to deposit their energy but there is a lack of upstream electron fluence. There is thus substantially less dose being deposited at the surface than a few centimeters downstream. This region is called the "build-up" region and is useful when treating deep-seated tumors as it allows for sparing of healthy skin tissue. However, this makes photons ill-suited for superficial tumors like skin cancers. Megavoltage electrons being directly ionizing, have much higher surface dose than photons. However, they also have a finite range in matter with the entirety of the primary electron beam being stopped after a few centimeters into the patient. This limits their use cases to relatively superficial tumors. Electrons interactions are also several orders of magnitude more common than photons. This makes them more susceptible to scatter in air, resulting in a widening of the field's lateral shape. This is highly undesirable as a sharp field fall-off is needed to minimize the dose to healthy tissue immediately adjacent to the PTV. For this reason, MLCs are not used in current standard of care electron treatments. Instead, an additional collimator, called "applicator", is attached below the linac head to shape the electron beam down to as close to the patient's surface as possible. At the bottom of the applicator, an aperture cutout made out of cerrobend and molded to the shape of the target can be placed to provide a customizable aperture shape. The preparation of cutout constitutes a significant logistical burden for radiotherapy clinics and presents a risk of inhaling toxic vapor during its manipulation due to the presence of lead and cadmium in cerrobend. Furthermore, the presence of the applicator severely limits the beam arrangement to mostly a setups with a single field delivered from a single angle.

1.2 Mixed Beam Radiation Therapy

Despite their dosimetric benefit, electron therapy usage in EBRT remains limited. The logistical overhead involved with the preparation of Cerrobend cutouts and the constrained delivery setups makes it a cumbersome treatment modality. Studies have been made to

assess the feasibility of using photon MLCs to collimate electron fields. In Modulated Electron Radiation Therapy (MERT) deliveries, the patient is positioned much closer to the gantry head to minimize the in-air scatter of electrons. With the possibility of delivering MLC-collimated electron fields, the idea of using both electron and photon beams in EBRT treatment plans has emerged. Mixed Electron-Photon Beam Radiation Therapy (MBRT) leverages the high surface dose and limited penetration depth of electron beams to provide better sparing to underlying normal tissue, while maintaining a homogeneous coverage of the target by using photon beams' sharp lateral dose fall-off. Compared to photon-only plans, MBRT has been shown to offer superior sparing of healthy tissue without sacrificing target coverage [7]–[11]. Renaud *et al.* [9] applied the column generation approach to perform simultaneous optimization of electron and photon fields. They also described a framework for robust optimization of MBRT plans, explicitly accounting for setup errors [12]. Due to the sensitivity of electron dose to changes in depth, they demonstrated the necessity of performing optimization of MBRT plans robustly. However, the increased complexity of robust optimization significantly inflated its calculation time, lengthening the total treatment planning time to over a week. The treatment planning process in the clinical workflow is expected to be completed within 1-2 days [13], making the time scale of MBRT treatment planning impractical. Although the method to perform optimization of MBRT treatment plans had been established, limited work had been performed to validate the dose delivery of MBRT plans.

1.3 Thesis objectives

The overarching goal of this thesis is to bring MBRT closer to a realistic clinical implementation. MBRT must be shown to be a clinically-beneficial technique that can fit within the clinical workflow in a practical manner, and whose safe and accurate delivery can be verified. To do so, we must address the following distinct, yet interconnected, objectives:

1. *Decreasing treatment planning time of robust MBRT plans through more efficient electron beamlet dose calculation.* Due to the lack of analytical approximation technique

for electron dose calculations, Monte Carlo calculation of robust electron beamlets required for the optimization of MBRT plans is a major bottleneck. This Monte Carlo calculation time can be substantially reduced by using a precalculated track approach.

2. *Validating MBRT deliveries through absolute dose measurements.* The best treatment technique is only worthwhile if it can be accurately delivered. We must establish a method to verify that the MBRT dose calculated by our TPS coincides with the dose delivered by the linac. Dose measurements in phantom setups will be made with ion chamber and film while accounting for corrections to their response in MBRT fields.
3. *Establishing a streamlined and practical patient-specific quality assurance procedure for MBRT plans.* As any new technique, each patient plan must be individually verified to be accurately deliverable. A more streamlined method to perform quality assurance of these plans must be available to not overburden the clinical workflow. We explore the possibility of using a MapCHECK device and machine log files data to fulfill this role.
4. *Demonstrating the dosimetric benefits of MBRT compared to current standard of care for a well-defined subset of cases belonging to a treatment site.* No patient treatment can occur unless clinically-motivated to be beneficial. To pave the way towards a clinical trial, we must clearly identify a subset of patients for whom MBRT presents a distinct dosimetric advantage over the currant standard of care. This will be done through a retrospective treatment planning study of soft tissue sarcoma of the lower extremity.
5. *Investigating the necessity for accounting range uncertainties when performing robust optimization of MBRT plans.* As robust optimization to setup errors has been established to be necessary for MBRT plans, this leads to the question of robustness of MBRT dose to uncertainties in electron range. Errors in assignment of CT number can be as large as 3.7% [14] in lung tissue. This CT number is then used to assign the mass density required for MBRT patient dose calculations. We investigate the impact

of the uncertainty in CT number assignment on the range of MBRT beams and on the necessity to perform range-robust MBRT optimization.

1.4 Thesis outline

A brief description of how dose calculation can be performed through Monte Carlo simulation of particle interactions is given in Chapter 2. Various methods for dose measurements and quality assurance relevant to radiotherapy are presented in Chapter 3. In Chapter 4, we provide a review of the literature on MERT and how it has led to recent studies of MBRT.

In Chapter 5, we present the workflow to perform the treatment planning of MBRT plans on an in-house TPS. The implementation of a precalculated Monte Carlo method for electron beamlet calculation is also described. Chapter 6 consists of a manuscript published in *Medical Physics* on the validation of MBRT deliveries with ion chamber and film measurements. Further methods for quality assurance of MBRT plans are investigated with the MapCHECK® device and log file dose reconstruction in the manuscript of Chapter 7, published in *Medical Physics*. In the manuscript of Chapter 8, published in *Medical Physics*, we present a retrospective treatment planning study comparing MBRT to standard of care VMAT for 22 sarcoma patients. Chapter 9 is a manuscript in preparation investigating the impact of range uncertainties on MBRT dose distributions.

We conclude this thesis in Chapter 10 by summarizing the work presented thus far and exploring possible future research avenues for MBRT.

REFERENCES

[1] Candian Cancer Statistics Advisory Committee. "Canadian cancer statistics 2023." (2023), [Online]. Available: https://cancerstats.ca/ (visited on 2023).

[2] T. Ugai, N. Sasamoto, H.-Y. Lee, *et al.*, "Is early-onset cancer an emerging global epidemic? current evidence and future implications," en, *Nat. Rev. Clin. Oncol.*, vol. 19, no. 10, pp. 656–673, Oct. 2022.

[3] G. P. Delaney and M. B. Barton, "Evidence-based estimates of the demand for radiotherapy," en, *Clin. Oncol. (R Coll. Radiol.)*, vol. 27, no. 2, pp. 70–76, Feb. 2015.

[4] E. J. Hall and (. Giaccia Amato J., *Radiobiology for the radiologist*, English, Seventh edition. Philadelphia, PA : Wolters Kluwer Health/Lippincott Williams & Wilkins, 2012.

[5] T. R. Munro and C. W. Gilbert, "The Relation Between Tumour Lethal Doses and the Radiosensitivity of Tumour Cells," *British Journal of Radiology*, vol. 34, no. 400, pp. 246–251, Dec. 1960. DOI: 10.1259/0007-1285-34-400-246.

[6] E. Podgorsak, *Radiation Oncology Physics: A Handbook for Teachers and Students*. Vienna: International Atomic Energy Agency, 2005, p. 696. DOI: 10.1038/sj.bjc.6604224.

[7] A. Alexander, E. Soisson, M.-A. Renaud, and J. Seuntjens, "Direct aperture optimization for FLEC-based MERT and its application in mixed beam radiotherapy.," *Medical physics*, vol. 39, no. 8, pp. 4820–31, Aug. 2012. DOI: 10.1118/1.4736423.

[8] B. A. Palma, A. U. Sánchez, F. J. Salguero, *et al.*, "Combined modulated electron and photon beams planned by a Monte-Carlo-based optimization procedure for accelerated partial breast irradiation," *Physics in Medicine and Biology*, vol. 57, no. 5, pp. 1191–1202, 2012. DOI: 10.1088/0031-9155/57/5/1191.

[9] M.-A. Renaud, M. Serban, and J. Seuntjens, "On mixed electron-photon radiation therapy optimization using the column generation approach," *Medical Physics*, vol. 44, no. 8, pp. 4287–4298, 2017. DOI: 10.1002/mp.12338.

[10] S. Mueller, M. K. Fix, A. Joosten, *et al.*, "Simultaneous optimization of photons and electrons for mixed beam radiotherapy," *Physics in Medicine and Biology*, vol. 62, no. 14, pp. 5840–5860, 2017. DOI: 10.1088/1361-6560/aa70c5.

[11] S. Mueller, P. Manser, W. Volken, *et al.*, "Part 2: Dynamic mixed beam radiotherapy (dymber): Photon dynamic trajectories combined with modulated electron beams," *Medical Physics*, vol. 45, no. 9, pp. 4213–4226, 2018. DOI: https://doi.org/10.1002/mp.13085.

[12] M.-A. Renaud, M. Serban, and J. Seuntjens, "Robust mixed electron-photon radiation therapy optimisation," *Medical Physics*, vol. 0, no. ja, 2019. DOI: 10.1002/mp.13381.

[13] N. Yu, D. LaHurd, A. Mastroianni, *et al.*, "Using standardized workflows and quantitative data-driven management to reduce time interval from simulation to treatment initiation," en, *J. Appl. Clin. Med. Phys.*, Jan. 2024.

[14] M. Yang, X. R. Zhu, P. C. Park, *et al.*, "Comprehensive analysis of proton range uncertainties related to patient stopping-power-ratio estimation using the stoichiometric calibration," en, *Phys. Med. Biol.*, vol. 57, no. 13, pp. 4095–4115, Jul. 2012.

CHAPTER 2
Dose calculation

Accurate characterization of the dose deposition of a radiation beam in matter is at the core of radiation therapy. Any dose calculation method must in some form take into account the type of interactions undergone by ionizing radiation that will eventually lead to their dose deposition. We therefore start with a description of the relevant interactions of electrons and photons with matter.

2.1 Particle interaction

2.1.1 Electron interaction

As electrons are charged particles, they interact with matter through Coulomb interactions with either the negatively-charged orbital electrons or the positively-charged nuclei. The type of possible interactions that an electron will undergo with an atom can be understood from a classical view of collision theory. Let us consider the trajectory of an electron with respect to an atom of atomic radius r_a at rest (see Fig.2–1). In this scenario, the impact parameter b is the perpendicular distance between the initial trajectory of the incoming electron and the center of mass of the atom and is a parameter that characterizes the interaction.

For b larger or on the same order as r_a, the incoming electron will interact with the atomic electrons through inelastic collisions. If b is much larger than r_a, the incident electron transfers a small part of its kinetic energy to the atomic electron cloud as a whole. This can either cause excitation to higher shells or ionization of a valence electron. This is the most common type of electron interactions in matter, accounting for around half of its energy deposition in matter. In cases where $b \approx r_a$, the incoming electron can be understood to collide with one single atomic electron to which it imparts most of its kinetic energy. The atomic electron is then ejected from the atom and is known as a "delta ray" or a "knock-on

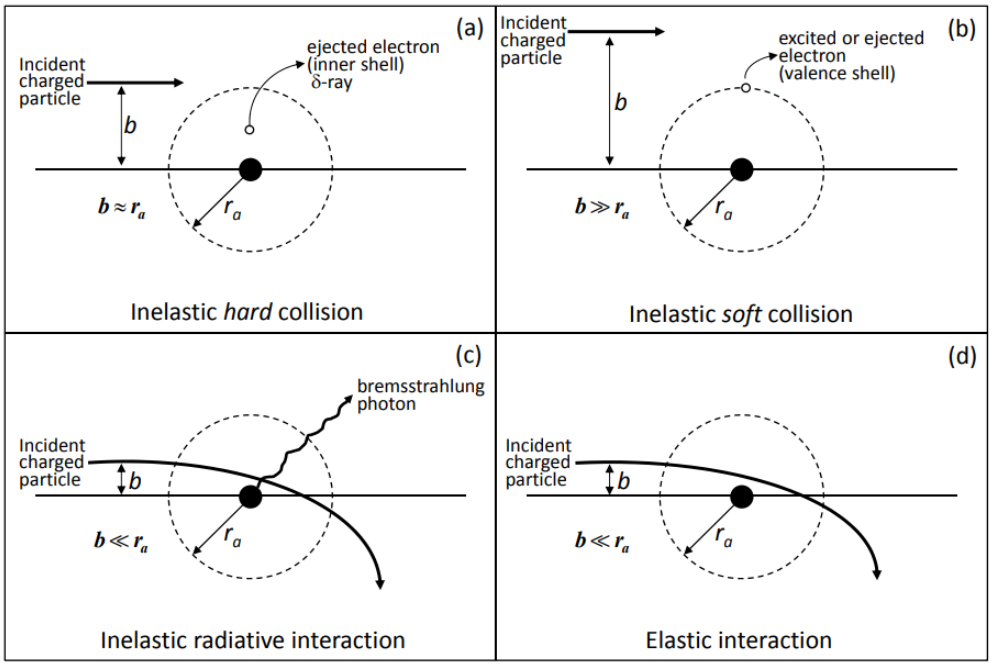

Figure 2–1: Types of electron interaction with an atom depending on the impact parameter b. Reproduced from [1].

electron". They will often have sufficiently large kinetic energy to cause further ionization in matter through subsequent Coulomb interactions away from the original track.

When b is much smaller than r_a, most of the Coulomb interaction can be attributed to the nucleus. The incident electron path is deflected through a collision with the nucleus. As the nucleus is much heavier than the electron, there is almost no energy transfer to the atom. However, the deceleration of the incident electron during this deflection causes the electron to lose its energy in the form of emission of bremsstrahlung photons. In classical electromagnetism, the power P emitted as photons is dictated by the Larmor formula:

$$P = \frac{q^2 a^2}{6\pi\epsilon_0 c^3}, \tag{2.1}$$

where q is the charge of the charged particle and a its acceleration. The magnitude of the acceleration of an electron subjected to the nucleus' electric field is proportional to the nucleus charge Ze and inversely proportional to its own electron mass m_e. Therefore $P \propto Z^2/m_e^2$,

making bremsstrahlung a particularly important interaction for electrons due to their relatively low mass.

We define the stopping power S as a macroscopic quantity that describes the loss of kinetic energy E_k by a charged particle like electrons through its interaction with matter per unit path length x:

$$S = \frac{dE_k}{dx}. \tag{2.2}$$

The stopping power is itself a function of the charged particle's energy E_k and is proportional to the mass density ρ of a material. It is therefore more commonly recorded as the mass stopping power S/ρ.

Electron interactions with orbital electrons and with the nucleus lead to distinct implication for the energy absorbed by the matter. In the former, the energy loss by the electron is transferred to excitation or ionization of the atom and can be described by the mass collision stopping power $(S/\rho)_{\text{col}}$. In the latter, the electron loses its energy to bremsstrahlung photons that are not directly depositing energy locally and can be described by the mass radiative stopping power $(S/\rho)_{\text{rad}}$. We thus have:

$$S/\rho = (S/\rho)_{\text{col}} + (S/\rho)_{\text{rad}}. \tag{2.3}$$

$(S/\rho)_{\text{col}}$ is particularly useful in radiotherapy as it can be related to the local dose deposition D in matter:

$$D = \phi(S/\rho)_{\text{col}}, \tag{2.4}$$

where ϕ is the fluence of the incident electron beam.

2.1.2 Photon interaction

At energies relevant to megavoltage EBRT, there are 3 types of photon interactions that are of interest: photoelectric effect, Compton scattering and pair-production. All 3 of these interactions lead to the scattering of a secondary electron that is capable of producing

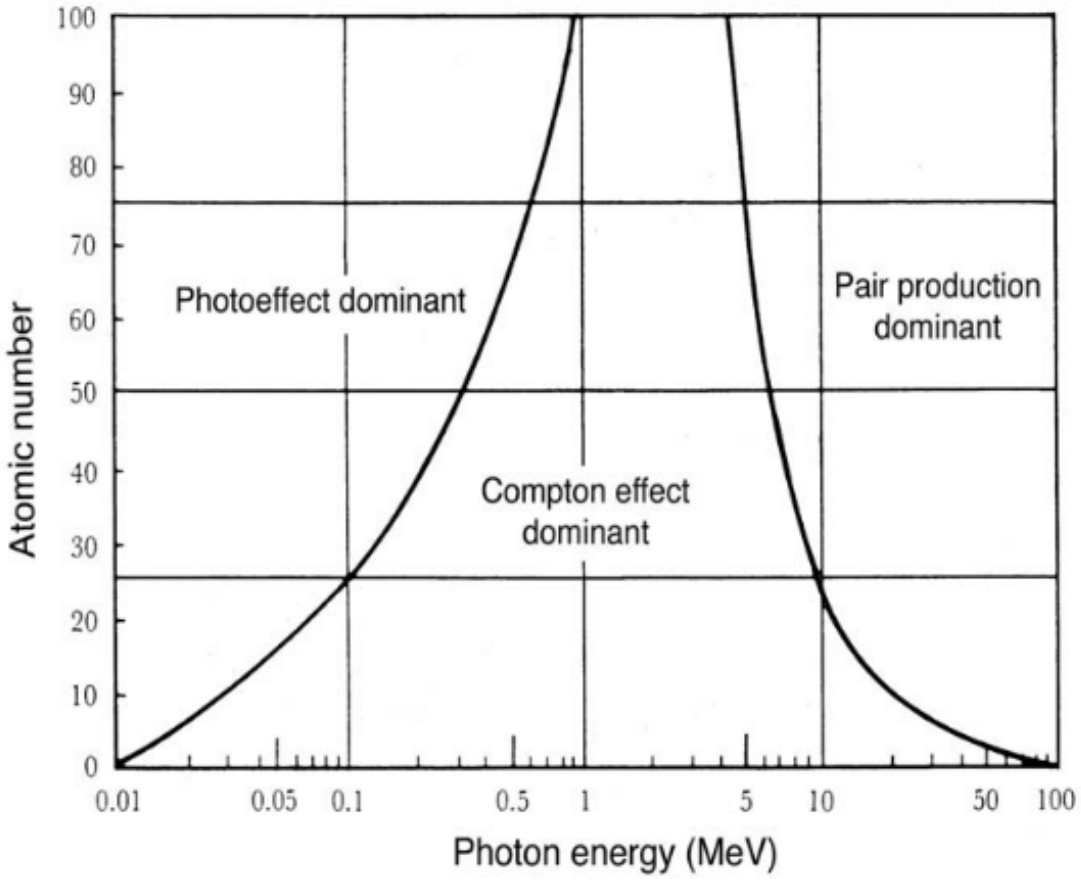

Figure 2–2: Energy and atomic number regions where each photon interaction is dominant in. Reproduced from [2].

ionization in matter. The cross-section of each interaction type depends on the energy of the incident photon and the atomic number of the material; in water and at the radiotherapy energy range, Compton is the most dominant interaction (see Fig. 2–2). In the work presented in this thesis, we ignore the effects of Rayleigh and photonuclear interactions. Rayleigh scattering results in a scattered photon of the same energy and at low scattering angle. Its cross-section is inversely proportional to the square of the photon energy and therefore plays little role in dose deposition in the EBRT energy range. Photonuclear reactions can only occur at photon energies above a threshold energy on the order of 10 MeV. For ^{16}O, the energy threshold of photoneutron reactions is 15.66 MeV [1] and its cross-section remains relatively small compared to other interactions.

The total photon cross-section σ_{tot} represents the sum of the cross-sections σ_i for each possible photon interaction i with matter. It can be understood as a measure of the probability of a photon, at a microscopic level, interacting with an atom. At a macroscopic level, it is more useful to know the probability of the photon to interact with a unit mass of a given medium. We can thus multiply by the number of atoms per unit mass $N_a = N_A/A$, where N_A is the Avogadro constant and A is the atomic mass number:

$$\mu/\rho = \sigma_{\text{tot}} N_A/A, \tag{2.5}$$

where μ/ρ is called the mass attenuation coefficient. If we consider a monoenergetic beam of initial intensity I_0 travelling through a medium, its intensity would attenuate for increasing depth x travelled in the medium due to occurrence of any photon interactions with matter. This attenuation is governed by the photon's linear attenuation coefficient μ such that:

$$I(x) = I_0 e^{-\mu x}. \tag{2.6}$$

With the photoelectric effect, the incident photon of energy $h\nu$ interacts with a tightly bound electron of binding energy E_B. For $h\nu \geq E_B$, the photon can be totally absorbed by the atomic electron, imparting it a kinetic energy $E_k = h\nu - E_B$ and ejecting it out of the atom.

Compton scattering involves the scattering of the incident photon off an orbital electron for which, the photon energy is much larger than the electron's binding energy. In this case, the photon only transfers a part of its energy, ejecting the electron from the atom. As $h\nu >> E_B$, we can approximate the scattering process by only considering the kinematics of the photon-electron interaction while ignoring the rest of the atom that the electron is bound to (see Fig.2–3. Let $E_k = h\nu - h\nu'$ be the kinetic energy of the scattered electron and $h\nu'$ the scattered photon energy. Then by applying conservation of energy and momentum

we can derive:

$$h\nu' = h\nu \frac{1}{1 + \frac{h\nu}{m_e c^2}(1 - \cos\theta)} \tag{2.7}$$

$$E_k = h\nu \frac{\frac{h\nu}{m_e c^2}(1 - \cos\theta)}{1 + \frac{h\nu}{m_e c^2}(1 - \cos\theta)}, \tag{2.8}$$

where $m_e c^2$ is the electron rest mass energy and θ is the scattering angle of the scattered photon. Let $\epsilon \equiv h\nu'/h\nu$ be the ratio of energies of the scattered photon to the incident photon. Then its minimum and maximum value can be evaluated from Eq. 2.7 by setting $\cos\theta = -1$ and 1, respectively giving $\epsilon_{\min} = \frac{1}{1+2\frac{h\nu}{m_e c^2}}$ and $\epsilon_{\max} = 1$. The differential Compton cross-section in this approximation is given by the famous Klein-Nishina formula:

$$\frac{d\sigma_C}{d\Omega} = \frac{r_e^2 \epsilon^2}{2}(\epsilon + \frac{1}{\epsilon} - \sin^2\theta), \tag{2.9}$$

where r_e is the classical electron radius. Integrating this differential cross-section over 4π would give the cross-section for the Compton interaction of a photon with a free electron σ_C. Multiplying by the number of electrons in the atom Z and the number of atoms per unit mass, we obtain the Compton contribution to the mass attenuation coefficient $\mu_C/\rho = ZN_A/A\sigma_C$. As $\frac{d\sigma_C}{d\Omega}$ and therefore σ_C are independent of Z, μ_C/ρ is directly proportional to ZN_A/A. However, for most materials, we can approximate Z/A to be constant and therefore approximate μ_C/ρ to also be Z independent. We note that $\mu_C \propto \rho Z N_A/A$ which corresponds to the electron density of the material.

For a photon of energy $h\nu > 2m_e c^2$ subjected to a Coulomb field, there is also the possibility of it annihilating and creating a pair of electron and positron. The resulting electron and positrons have a combined kinetic energy $E_{\text{tot}} = h\nu - 2m_e c^2$. This most commonly happens in the nucleus' Coulomb field, in which case the interaction is called pair production. It can also occur in the orbital electron field, in which case the orbital electron is also ejected from the atom due to the recoiling kinetic energy it is imparted. The process is then called

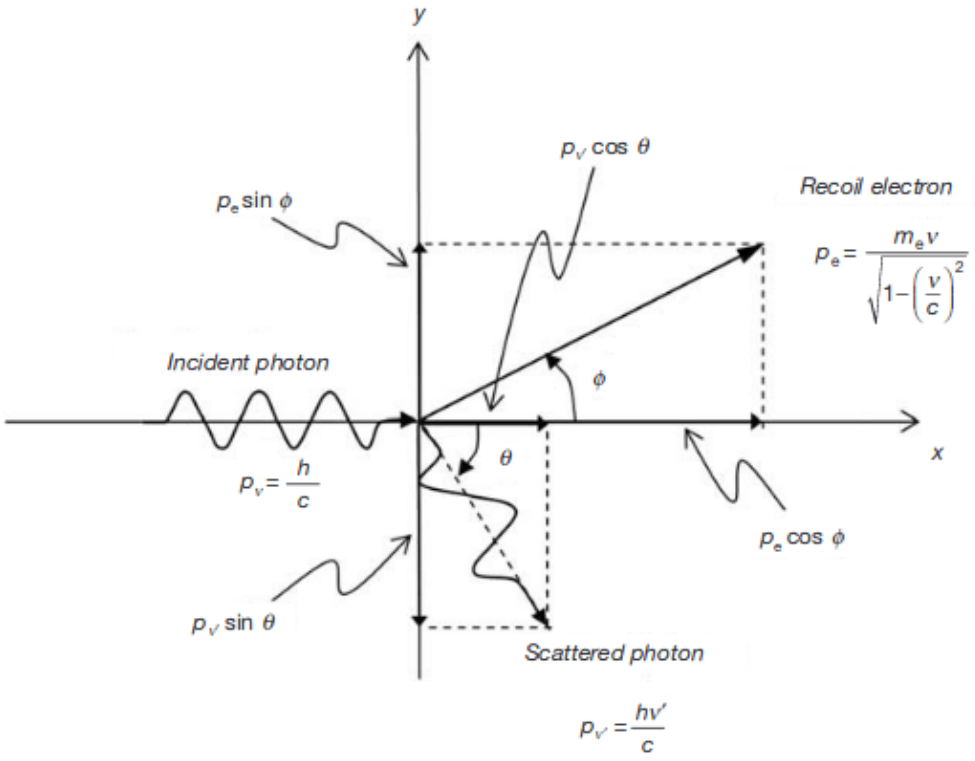

Figure 2–3: Diagram of Compton scattering. Reproduced from [2].

triplet production.

2.2 Monte Carlo dose calculation

The gold standard of dose calculation methods is the Monte Carlo method. In a sense, it can be seen as a naïve and brute force approach. Particle interactions with matter, as described in the preceding section, are stochastic in nature and dictated by their respective cross-sections. The Monte Carlo approach consists of taking a sample of this stochastic process by "rolling the dice" to decide which interaction occurs and how they occur. The complexity in Monte Carlo calculation codes lies in performing both efficient and accurate sampling or "dice rolls". To simulate an interaction, random numbers must be sampled from a probability distribution function that is representative of the cross-section for that interaction. Starting from a single primary particle, its behavior in matter is simulated by sampling for its possible interactions. The dose deposition in the geometry of interest by the

particle is recorded while it is being transported along its trajectory. The secondary and any subsequent particles created from these interactions are similarly transported. This process is then repeated for a large number of primary particles, each called a "history", and their dose deposition distribution in space is averaged over all primary particles simulated. As any probabilistic event, when given a sufficiently large sample size, the averaged value converges to the true value.

In practice, the geometry of interest is modelled by a phantom with accurate description of its constituent material, mass density and their spatial distribution. For patient dose calculations, the patient geometry is spatially discretized into "voxels" of size ranging from 3x3x3 mm^3 to 1x1x1 mm^3, depending on the resolution needed. The dose deposition can thus be scored to each voxel as a whole, allowing for a lower number of histories being simulated to reach acceptably low statistical uncertainties. The material and mass density is assumed to be uniform within a voxel. For patient dose calculations, these are commonly obtained from CT images of the patient and assigned through a CT value-to-density conversion curve. In theory, particles would be transported until they are either entirely absorbed or exit the geometry of interest. However, in practice, to reduce the calculation time, particles below a threshold energy are assumed to locally deposit their remaining energy in the voxel they are found in. This threshold energy is often chosen such that the range of a particle at that energy would be on the order of the dimension of a voxel.

Let $\bar{D}$ be the average dose scored in a voxel v in a Monte Carlo simulation due to a radiation beam. As $\bar{D}$ is averaged over the dose D_n sampled for each simulated history $n \in N$, the type-A uncertainty $\sigma_{\bar{D}}$ can be described by using the Central Limit Theorem such that:

$$\sigma_{\bar{D}} = \sigma_D / \sqrt{N}, \tag{2.10}$$

where σ_D is the standard deviation of the distribution of D_n. So long as all particle interactions are modelled accurately within the dose calculation algorithm, the calculations obtained by Monte Carlo method would theoretically converge to the truth, only being limited by the finite number of simulated histories N. As calculation time grows linearly with N but only reducing uncertainties by $\sqrt{N}$, Monte Carlo calculations are notorious for being computationally expensive, although methods have been developed to improve their efficiency through the use of variance reduction methods.

2.2.1 EGSnrc

EGSnrc is one of the most prominent general-purpose Monte Carlo code used in radiotherapy research settings today. The EGSnrc code [3] was developed at the National Research Council as an improved version of the EGS4 code [4]. EGSnrc handles the transport of photons, electrons and positrons in energy ranges of 1 keV to 10 GeV. One major difficulty with Monte Carlo simulations is the transport of electrons in matter. Due to the sheer number of interactions that an electron would encounter before losing all its energy ($> 10^5$ at megavoltage energies [5]), individually simulating each interaction and the secondary particles they create would make Monte Carlo calculations prohibitively time-consuming. Berger *et al.* [6] proposed a solution to this problem through the condensed history technique. It is based on the premise that most individual electron collisions do not result in significant change in an electron's trajectory. As such, using multiple scattering theory, the combined result of multiple electron interaction can be sampled once over a "step" length. EGS4 employed one type of this condensed history technique (which was further improved in EGSnrc [5]) by defining a threshold energy for the creation of secondary bremsstrahlung photons and knock-on delta electrons. Any interactions that would create such secondary particles above their threshold energy would be explicitly handled. Otherwise, interactions would be combined and the electron energy loss would be dictated by its total stopping power as modelled in

the continuous-slowing-down-approximation.

In combination with the open-source contribution of diverse research groups, user codes of EGSnrc have been developed to facilitate Monte Carlo calculations in specific use cases.

BEAMnrc

BEAMnrc is one such user code that focuses on the transport of radiation within the linac head. Although dose depositions within the linac head itself are not of interest, the accurate depiction of the particle fluence exiting from the linac head is paramount to accurate dose calculations within the phantom geometry. As such, the BEAMnrc user code allows for precise modelling of "component modules" to represent each element in a linac head, from the bremsstrahlung target down to each MLC leaf. For each component, the material, density and dimensions must be rigorously assigned as their impact on the radiation beam's shape and energy spectrum can be profound. A BEAMnrc simulation of an EBRT linac would start as a source of electron immediately prior to impinging on the target. After transporting particles through the linac head, the particles that have made it out are recorded as they cross a chosen plane. The compilation of particle type, energy, position and direction at the plane is the output of BEAMnrc and is called a phase space. Some linac vendors also provide phase spaces of their radiation beams downstream from the target. These can be used as initial particle sources to avoid modelling upstream components, the exact specification of which are often confidential.

DOSXYZnrc

Using the phase spaces obtained from BEAMnrc or directly using particles output by BEAMnrc, the particles can be then be transported in voxelized phantom geometries using DOSXYZnrc. By synchronizing the position of the BEAMnrc collimator modules with the particle source positions in DOSXYZnrc, an accurate simulation of a rotating gantry delivery can be performed, while accounting for the exact collimator aperture shapes. Phantom geometry, density and material information are specified in `.egsphant` files and used as

input by DOSXYZnrc to score doses in each voxel. The dose to each voxel averaged over particles is then output by DOSXYZnrc as `.3ddose`.

SPRRZnrc

As the local dose deposition is often the quantity of interest, it is useful to use the concept of a restricted collision stopping power defined to be the part of the total collision stopping power that excludes energy lost through liberation of a secondary electron of energy larger than Δ. This is relevant in the context of ionization chambers where knock-on electrons released with energy $> \Delta$ will have sufficiently high energy to exit the chamber cavity and not deposit their dose locally.

SPRRZnrc is a user code that allows the user to calculate the Spencer-Attix restricted stopping power ratios, one evaluated in the medium m of a cylindrical RZ geometry to the one of a medium g of a specific cavity (such as the air in an ionization chamber). The Spencer-Attix mass restricted collision stopping power ratio is defined as:

$$\left(\frac{\bar{L}}{\rho}\right)_g^m = \frac{\int_\Delta^{E_{\max}} \Phi (L(\Delta)/\rho)_m dE + TE_m}{\int_\Delta^{E_{\max}} \Phi (L(\Delta)/\rho)_g dE + TE_g}, \tag{2.11}$$

where Φ is the electron fluence at an energy E, $(L(\Delta)/\rho)_m$ is the restricted mass collision stopping power evaluated in medium m at energy E and TE is the track-end term accounting for electrons with energy below Δ that are assumed to fully deposit their energy locally. SPRRZnrc uses an on-the-fly calculation technique [7] described in PIRS-702 of the EGSnrc manual [3]. The total energy deposited by a given input beam of interest is only scored in the medium m of the RZ region. The energy deposition in the medium g relevant for the denominator is instead estimated by multiplying the energy deposited in m by a ratio of stopping power ratios at specific energies. For both the numerator and denominator, the electron fluence Φ_m is only evaluated in the medium m.

REFERENCES

[1] P. Andreo, D. T. Burns, A. E. Nahum, J. Seuntjens, and F. H. Attix, *Fundamentals of ionizing radiation dosimetry*. John Wiley & Sons, 2017.

[2] E. Podgorsak, *Radiation Oncology Physics: A Handbook for Teachers and Students*. Vienna: International Atomic Energy Agency, 2005, p. 696. DOI: 10.1038/sj.bjc.6604224.

[3] I. Kawrakow, D. Rogers, E. Mainegra-Hing, *et al.*, *Egsnrc toolkit for monte carlo simulation of ionizing radiation transport*, doi:10.4224/40001303 [release v2021], 2000.

[4] W. R. Nelson, H. Hirayama, and D. W. Rogers, "Egs4 code system," Dec. 1985.

[5] I. Kawrakow and M. Fippel, "Investigation of variance reduction techniques for monte carlo photon dose calculation using xvmc," *Physics in Medicine & Biology*, vol. 45, no. 8, p. 2163, Aug. 2000. DOI: 10.1088/0031-9155/45/8/308.

[6] M. Berger, *Monte Carlo calculation of the penetration and diffusion of fast charged particles*, 1st ed., B. Alder, S. Fernbach, and M. Rotenberg, Eds. New york: Academic, 1963, vol. 1, pp. 135–215.

[7] A. Kosunen and D. W. Rogers, "Beam quality specification for photon beam dosimetry," en, *Med. Phys.*, vol. 20, no. 4, pp. 1181–1188, Jul. 1993.

CHAPTER 3
Dosimetry and quality assurance

3.1 Dosimetric quantities

In this section, we define the common quantities of interest when performing dose measurements of radiation fields in radiotherapy.

3.1.1 Distance from the source

On C-arm linacs, the gantry head can only perform rotation about a fixed axis within a fixed plane. The treatment couch can perform a rotation about a perpendicular axis. The intersection of these two rotation axes is thus a fixed point in space and corresponds to the machine's isocenter (see Fig. 3–1). As the position of the radiation source is also fixed within the gantry head, the distance from the source to the isocenter is constant in C-arm linacs and defined as the Source-to-Axis Distance (SAD). On most linacs, including the Varian TrueBeam, this distance is SAD = 100 cm.

In vacuum, the fluence of megavoltage photon beams decreases with the square of the distance from the source due to geometrical divergence of the beam. This phenomenon is known as the Inverse Square Law in radiotherapy. Although the SAD is fixed, the distance from the source to a patient body depends on the positioning the patient on the treatment couch and of the position of the treatment couch itself. The distance from the patient's surface to the source is therefore variable and defined as the Source-to-Surface Distance (SSD) (see Fig. 3–2). The SSD is an important quantity as it dictates the beam's fluence, through the inverse square law, immediately prior to entering the patient.

3.1.2 Depth dose

As a megavoltage photon or electron beam travels through matter, its many possible interactions lead to further attenuation of the beam's fluence. The dose deposition of such beam in matter will therefore change with depth and is characterized by the Percent Depth

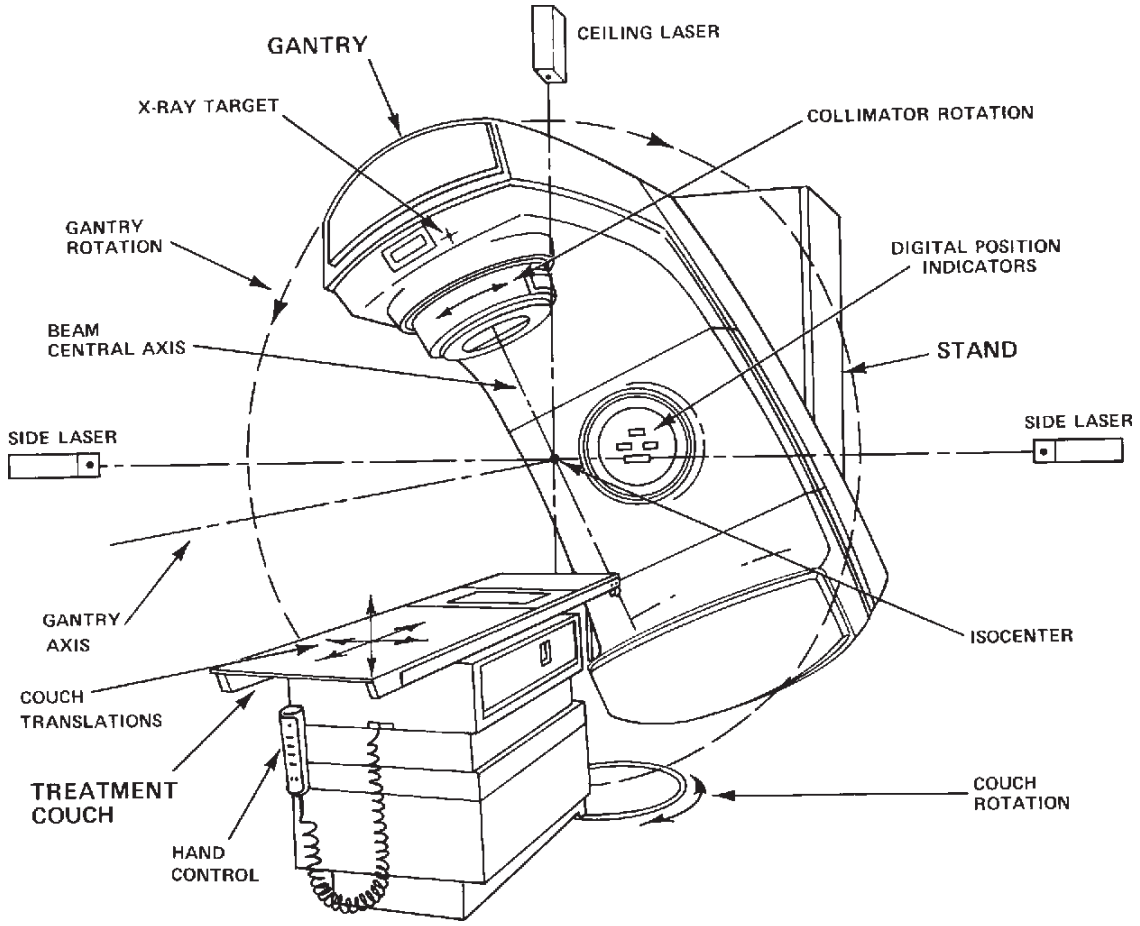

Figure 3–1: Drawing of a linac, indicating the axes of rotation and the position of the isocenter. Reproduced from [1].

Dose (PDD) curve. The PDD is a relative dose metric defined as:

$$\mathrm{PDD}(d) = \frac{D(d)}{D(d_{\max})}, \tag{3.1}$$

where d is the depth at which the PDD is evaluated and $d_{\max}$ is the depth at which a maximum dose $D(d)$ is found. Doses $D(d)$ are nominally evaluated along the beam's central axis. PDD curves of beams of different particle type and energy differ substantially and dictate their use cases. The PDD of a 9 MeV electron and 6 MV photon beam are shown in the Fig. 3–3.

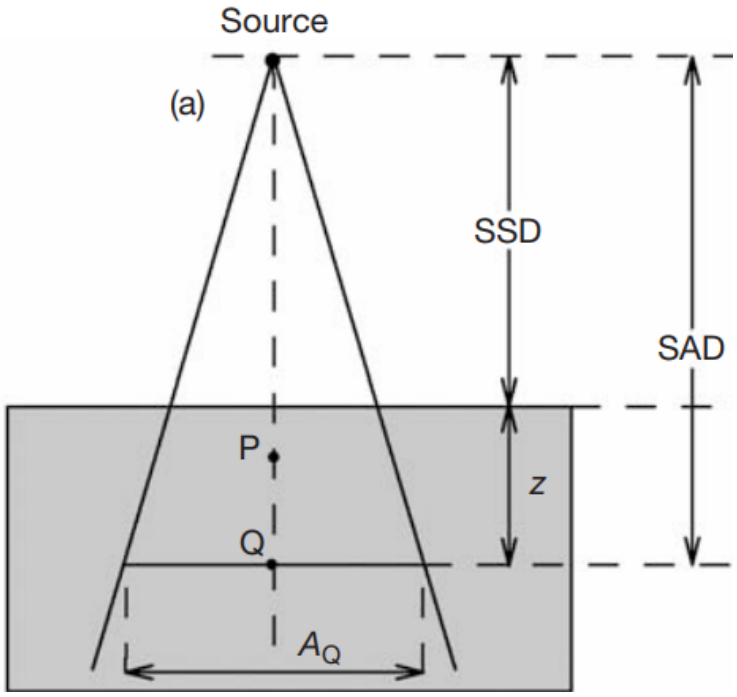

Figure 3–2: Diagram showing the difference between SSD and SAD. Reproduced from [2].

3.1.3 Off-axis dose profile

As the PDD characterizes the evolution of the dose deposition of a beam along its central axis, the transverse and longitudinal dose profiles of a beam define the off-axis dose. The off-axis ratio is defined as:

$$\text{OAR} = \frac{D(x)}{D(0)}, \tag{3.2}$$

where $D(x)$ is the dose evaluated at an off-axis distance x from the central-axis.

3.1.4 Output Factors

Depending on the size of the target, the jaw collimators will have to be closed accordingly to limit the radiation field to only the region of interest. The nominal field size of a beam is defined as the projection of the x and y jaws onto the isocenter plane. This can be alternatively understood as the extent of the radiation field at the isocenter plane. As the radiation field shrinks, there are fewer particles that contribute, through scattering, to the dose on the central axis. This leads to a dependence of the central axis dose on field size.

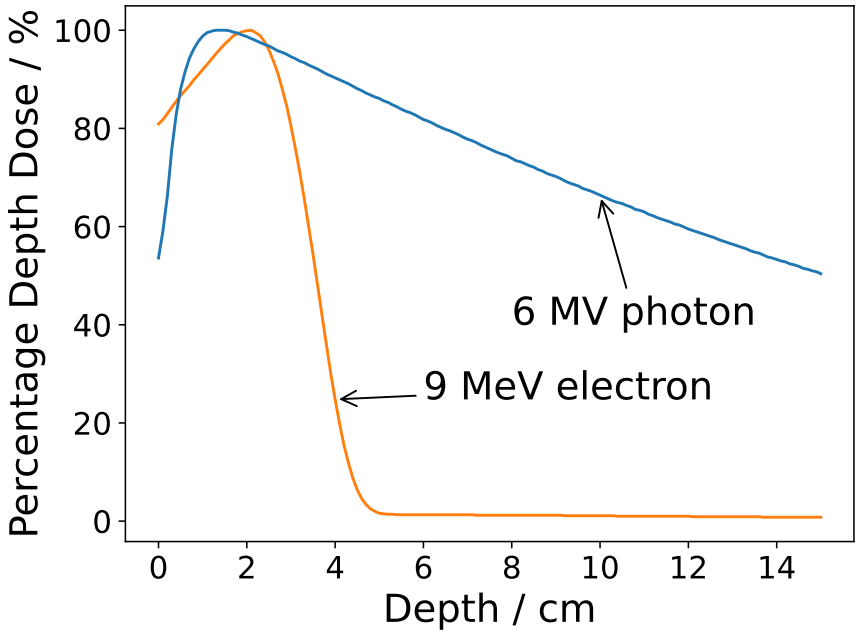

Figure 3–3: PDD curves for a 9 MeV electron and 6 MV photon beam of a Varian TrueBeam linac.

This dependence is characterized by the output factors OF:

$$\mathrm{OF}(X,Y) = \frac{D_d(X,Y)}{D_d(10,10)}, \tag{3.3}$$

where $D_d(X,Y)$ is the dose evaluated at a reference depth d of a radiation beam of field size $X \times Y$. The depth d is commonly taken to be the depth $d_{\max}$ of maximum dose.

3.1.5 Beam Quality

Clinical electron beams produced by the linac for EBRT can range from 4 MeV to 25 MeV. Similarly, photon beams are produced in a continuous spectrum with peak energies in the same range. The characteristics of the dose distribution in patients due to each beam, in both their PDD and profiles, are strongly dictated by the energy spectrum of the beam. Fundamentally, the mass stopping power S/ρ and mass attenuation coefficient μ/ρ are energy dependent. It is therefore important to have a measure of the beam's energy spectrum, or more commonly called the beam "quality". These are quantified by metrics

called beam quality specifiers. For megavoltage electron beams, the beam quality specifier used for clinical beam calibration purposes today in North America is the half-value depth R_{50} [3]. It is defined as the depth in water of the electron PDD for which it reaches 50%:

$$\mathrm{PDD}(R_{50}) = 50\%. \tag{3.4}$$

For megavoltage photons, the PDD at 10 cm depth in water $\mathrm{PDD}(10)_x$ is used with the caveat that it excludes contamination electrons that would be produced in the linac head. The effect of electron contamination is generally assumed to be negligible for flattened photon beams of peak energy below 10 MV but must be corrected for at higher energies. Flattening filter free beams have a significantly larger proportion of contamination electrons and must always be corrected for through a measurement process using a 1 mm lead foil [4]. Both of these beam quality specifiers are quantities that can be measured for each machine at each beam energy that it can provide.

3.2 Detectors

A key role of medical physics in radiation therapy is in ensuring the accurate and safe delivery of radiation. In large part, this involves verifying, through measurements, that the dose delivered by linacs is agreeing with calculations. Many types of detectors exist and their distinct advantages and disadvantages dictate their use cases. In this section, we will go over a few examples of the commonly used detectors.

3.2.1 Ionization chamber

In radiotherapy settings, ionization (or ion) chambers are the most ubiquitous and important detectors. They are composed of 2 electrodes that are set at a fixed voltage potential from each other. A gas, usually air, fills the gap between the 2 electrodes. A drawing of a Farmer-type ion chamber is shown in Fig. 3–4. Ionizing radiation travelling through the gas, will transfer their energy to the gas through ionization events. These events create the release of ion pairs that are then pulled to either electrode due to the electric field between them. The average energy required to create an ion pair is W, which for low LET

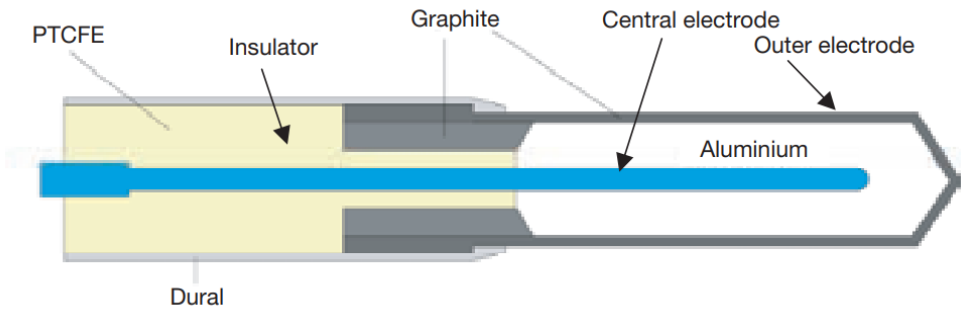

Figure 3–4: Drawing of a Farmer-type ionization chamber. Reproduced from [2]

radiation (photon and electron radiation used in radiation therapy) in air is $W_{\text{air}} = 33.97$ eV [5]. Collection of ion pairs at the electrode lead to a charge Q or current I that can be measured by an electrometer. The dose absorbed in a mass of gas m_{gas} between the 2 electrodes can be derived as:

$$D_{\text{gas}} = \frac{Q}{m_{\text{gas}}} \frac{W}{e}. \tag{3.5}$$

Reference dosimetry

As the readings provided by an ion chamber measurement can be directly related to a value of dose, ion chambers are the detector of choice for absolute dosimetry. Absolute dosimetry is crucial for the calibration of a linac output to set the MU measured by the linac's monitor chamber to correspond to a specific dose in a well-defined reference condition. In North America, the practice of performing reference dosimetry is dictated by the American Association of Physicists in Medicine's TG-51 report [3]. Although, Eq. 3.5 provides a manner to obtain the dose in air from a chamber reading, the mass of air in the chamber is not a well-known quantity for chambers used in the clinic. Furthermore, as we are interested in the absorbed dose to water, which is more closely representative of dose to human tissue, rather than the dose to air, we must convert D_{air} to D_{water} using a ratio of the restricted stopping powers of water to air. These steps are undertaken at primary standards dosimetry laboratories, providing individual clinics with a calibration coefficient $N_{\text{D,w}}^{^{60}\text{Co}}$ for their clinical

ion chambers. The $N_{\mathrm{D,w}}^{^{60}\mathrm{Co}}$ coefficient relates the ion chamber's reading to dose to water as:

$$D_w^{^{60}\mathrm{Co}} = M_{\mathrm{corr}} N_{\mathrm{D,w}}^{^{60}\mathrm{Co}}, \tag{3.6}$$

where $D_w^{^{60}\mathrm{Co}}$ is the dose to water due to a radiation beam produced by a Cobalt-60 source and M_{corr} is the corrected chamber reading in the ^{60}Co beam. The correction factors embedded into M_{corr} typically account for differences in temperature and pressure in the measurement condition, ion recombination and polarity effects. The calibration coefficient is specific to a Cobalt-60 beam as the conversion from dose-to-air to dose-to-water is beam quality dependent. As such, to measure absolute dose-to-water in a beam quality Q delivered by the linac, the calibration coefficient must be corrected by a correction factor k_Q accounting for the difference in beam quality.

3.2.2 Diode

P-n junction silicon diodes can also be used for dose measurements. Ionizing radiation creates electron-hole pairs in the diode. The minority charge carriers (electrons on p side and holes on n side) can diffuse towards the $p-n$ junction and be swept across the junction by the built-in potential [5]. This generates a current that is proportional to the dose absorbed by the diode. As the electron density of silicon is many orders of magnitude higher than air, a silicon diode can be made to be much smaller than ion chambers while providing better sensitivity. This makes diode ideal to be used for precise measurements in small fields or in the penumbra region of a beam profile, where volume averaging effects would plague ion chamber measurements. They are however limited to relative dosimetry usage as they must be cross-calibrated with absolute dosimeters. In addition, over repeated exposure to ionizing radiation, their sensitivity changes and must therefore be re-calibrated.

3.2.3 Film

While ion chamber and diode provide methods to measure the dose at a point, radiochromic films provide a measure of dose over a 2D surface. Radiochromic films work by

having a dye that changes color as it undergoes polymerization under exposure to ionizing radiation [6]. The change of color is detectable by measuring the transmission of light through the film. This can be done with a regular document scanner and does not require developing the film. The absorbance of light by the film can be described by the Optical Density (OD):

$$\mathrm{OD} = \log_{10}(I_0/I), \tag{3.7}$$

where I_0 and I are the initial and transmitted intensity of light, respectively. Although non-linear, the relation between the film's optical density and the dose deposited to it is reproducible and monotonic. A calibration curve of OD to dose can therefore be made by exposing film to well-known amount of dose over multiple dose points. It must however be noted that the polymerization process after radiation exposure continues over several hours, leading to increasing OD over time. The calibration curve is therefore only valid for films being scanned at an equal time interval after radiation exposure. For this reason, a delay of ∼24 hours prior to scanning of the film is usually allowed for the polymerization process to stabilize. A diagram depicting the calibration and the usage of the OD to dose curve is shown in Fig.3–5.

Films therefore provide a method for relative dose measurements over a surface with excellent spatial resolution. In large part due to the uncertainty in the fit of the calibration curve, the dose uncertainty associated with film measurements is around 3% [7]. When comparing film doses against calculations, we must also account for positioning uncertainties of the film setup with respect to the calculation. This is done using the gamma analysis method. Let us define a generalized function $\Gamma(\vec{r_r}, \vec{r_e})$ [8] that relates a point $\vec{r_r}$ in the reference dose space (the calculated dose) to a point $\vec{r_e}$ on the evaluated dose space (e.g. the measured film dose):

$$\Gamma(\vec{r_r}, \vec{r_e}) = \sqrt{\frac{|\vec{r_r} - \vec{r_e}|^2}{\Delta d^2} + \frac{|D_r(\vec{r_r}) - D_e(\vec{r_e})|^2}{\Delta D^2}}, \tag{3.8}$$

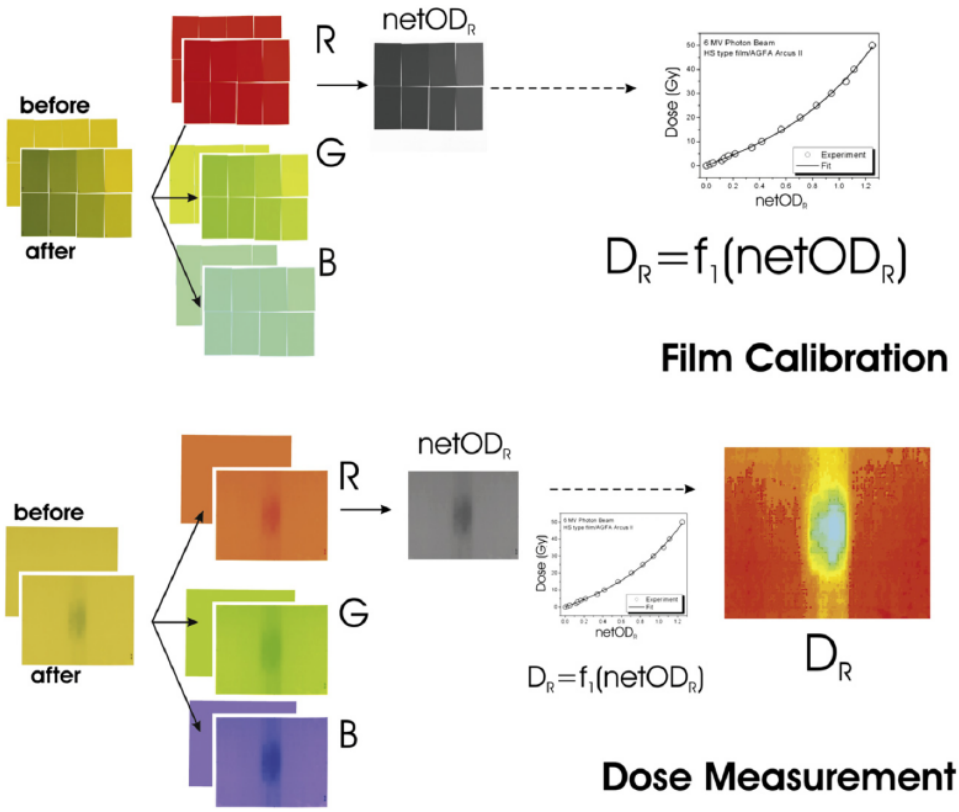

Figure 3–5: Films can be irradiated at known dose points to calibrate an OD to dose curve. Depending on the absolute dose level, the red, green or blue channels can be used. Reproduced from [5].

where $D_r(\vec{r_r})$ and $D_e(\vec{r_e})$ are the reference and evaluated dose at the reference and evaluated points, respectively. Δd and ΔD are the "distance to agreement" and dose difference criteria, respectively. These criteria are chosen by the user to reflect the expected uncertainties in positioning and dose measurement. If the reference and evaluated points coincide ($\vec{r_r} = \vec{r_e}$), then Γ is simply the difference in dose between the two distributions at that point, normalized by the dose difference criterion ΔD. In that case, if we choose ΔD to be 3%, then a difference in $D_r(\vec{r_r})$ and $D_e(\vec{r_e})$ of less than 3% would give $\Gamma < 1$. Similarly, if for a point $\vec{r_r}$, we find the closest point $\vec{r_e}$ such that $D_r(\vec{r_r}) = D_e(\vec{r_e})$, then Γ is simply the distance between the 2 points normalized by the distance to agreement criterion Δd. This is relevant in regions of high dose gradient where small shifts between the 2 dose distributions can lead to large dose differences when evaluated at a fixed point but can be reconciled by a small position shift.

For each point $\vec{r_r}$ in the reference dose space, we can evaluate $\Gamma(\vec{r_r}, \vec{r_e})$ over all evaluated points $\vec{r_e}$. We define the gamma index γ to be:

$$\gamma = \min\{\Gamma(\vec{r_r}, \vec{r_e})\} \forall \vec{r_e}. \tag{3.9}$$

For a set criteria Δd and ΔD, we can count the proportion of points with $\gamma \leq 1$. These points are assumed to "pass" the gamma evaluation and the percentage of passing points is called the "gamma passing rate". Intuitively, we can think of any point $\vec{r_r}$ with a passing gamma index to have a corresponding point $\vec{r_e}$ that is "close enough" in both the position and dose space with respect to Δd and ΔD. For EBRT, gamma criteria of $\Delta D = 3\%$ and $\Delta d = 2$ mm are recommended to evaluate film measurements of IMRT plans [9], with a gamma passing rate above 95% to represent an acceptable agreement between measurement and calculations.

3.3 Patient-specific quality assurance

As EBRT treatment plans have become increasingly complex, involving significant MLC modulations such as in IMRT and VMAT plans, so has the potential for discrepancies arising between the linac delivered dose and the one calculated by the TPS. Indeed, commercial TPSs use many approximations, in particular pertaining to the scatter in the MLCs (if at all modeled), to simplify and expedite the transport of particles in the linac head. Although the dose calculated by the TPS can be verified in simple fields and over a sample of cases at the time of commissioning, substantial discrepancy in the dose due to a custom MLC-shaped aperture could still be possible. Furthermore, complex VMAT deliveries can involve the simultaneous movement of distinct linac axes (MLCs, gantry angle, collimator angle and couch angle) all the while keeping the radiation beam on. Although linac manufacturers include automatic verification system to ensure that the linac components are positioned as commanded, an independent verification is beneficial to the patient's safety. As such, it has become common practice to perform quality assurance of each individual plans prior to their delivery onto patients [9]. This process is called patient-specific quality assurance (PSQA)

and encapsulates any verification method used to ensure that each individual patient treatment plans can be accurately delivered by the linac.

This has typically consisted of transposing the patient treatment plan onto a phantom geometry and performing dose measurements of the delivered dose. The dose measured by the detector can then be compared to a calculation of the dose to the detector's sensitive volume. During PSQA, the treatment plan delivery can either be replicated exactly or simplified such as by collapsing all gantry angle rotation to a fixed angle. This is done to accommodate the dose measurement by dosimeters that may require dose deliveries from a specific angle. For example, in a water tank setups, the gantry angle is typically fixed as the attenuation and scatter of the beam through the tank's sides may not be modeled.

3.3.1 Log file-based dose reconstruction

On state-of-the-art linacs, when treatment plans are being delivered, the positions of each moving component can be recorded at every fractional MU that has been delivered. This includes the position of the jaws, of individual MLC leaves, the gantry angle, the collimator angle, the couch position and angle. As this data can be recorded while the plan is delivered to the patient, it offers one of very few possible methods of estimating the real delivered dose. The recorded machine parameters can then be used by the TPS to reconstruct the dose to the patient. This dose recalculation can be also done using an independent dose calculation algorithm with a different beam model from the TPS, providing a secondary verification of the in-patient radiation transport calculation. As it does not involve a dose measurement, log file-based approaches have the benefit being exceptionally simple and efficient. For this reason, some centers have started employing log file-based dose reconstruction to perform routine PSQA of IMRT and VMAT plans instead of measurements [10].

REFERENCES

[1] C. J. Karzmark and R. J. Morton, "Primer on theory and operation of linear accelerators in radiation therapy. final report," Dec. 1981.

[2] E. Podgorsak, *Radiation Oncology Physics: A Handbook for Teachers and Students*. Vienna: International Atomic Energy Agency, 2005, p. 696. DOI: 10.1038/sj.bjc.6604224.

[3] P. R. Almond, P. J. Biggs, B. M. Coursey, *et al.*, "Aapm's tg-51 protocol for clinical reference dosimetry of high-energy photon and electron beams," *Medical Physics*, vol. 26, no. 9, pp. 1847–1870, 1999. DOI: https://doi.org/10.1118/1.598691.

[4] M. McEwen, L. Dewerd, G. Ibbott, *et al.*, "Addendum to the AAPM's TG-51 protocol for clinical reference dosimetry of high-energy photon beams," *Medical Physics*, vol. 41, no. 4, 2014. DOI: 10.1118/1.4866223.

[5] P. Andreo, D. T. Burns, A. E. Nahum, J. Seuntjens, and F. H. Attix, *Fundamentals of ionizing radiation dosimetry*. John Wiley & Sons, 2017.

[6] M. Williams, P. Metcalfe, A. Rosenfeld, *et al.*, "Radiochromic film dosimetry and its applications in radiotherapy," Wollongong, Australia: AIP, 2011.

[7] E. Y. L. Marroquin, J. A. Herrera González, M. A. Camacho López, J. E. V. Barajas, and O. A. García-Garduño, "Evaluation of the uncertainty in an EBT3 film dosimetry system utilizing net optical density," *J. Appl. Clin. Med. Phys.*, vol. 17, no. 5, pp. 466–481, Sep. 2016.

[8] D. A. Low, "Gamma dose distribution evaluation tool," *Journal of Physics: Conference Series*, vol. 250, no. 1, p. 012 071, Nov. 2010. DOI: 10.1088/1742-6596/250/1/012071.

[9] M. Miften, A. Olch, D. Mihailidis, *et al.*, "Tolerance limits and methodologies for imrt measurement-based verification qa: Recommendations of aapm task group no. 218,"

Medical Physics, vol. 45, no. 4, e53–e83, 2018. DOI: https://doi.org/10.1002/mp.12810.

[10] G. H. Chan, L. C. L. Chin, A. Abdellatif, *et al.*, "Survey of patient-specific quality assurance practice for IMRT and VMAT," en, *J. Appl. Clin. Med. Phys.*, vol. 22, no. 7, pp. 155–164, Jul. 2021.

CHAPTER 4
Review of mixed electron-photon radiation therapy

Today, state-of-the-art photon-based EBRT treatments rely on MLC to deliver radiation fields in highly complex shapes. Starting its development over 3 decades ago [1], [2], IMRT consists of the superposition of numerous radiation fields delivered through MLC-shaped apertures. These fields would be typically delivered from several fixed gantry angles. It was subsequently found that treatment times could be significantly decreased without impacting plan quality by performing dose deliveries through a continuous gantry rotation along an arc, leading to the development of VMAT [3], [4]. With the large degrees of freedom implied from being able to independently position each MLC leaf, these treatment plans must be inversely optimized. IMRT and VMAT have allowed for photon EBRT treatment plans to provide highly conformal dose distributions, offering significantly superior sparing to OARs. In contrast, despite research endeavours by multiple groups over the last 2 decades, Modulated Electron Radiation Therapy (MERT) has not been adopted into clinical practice. The high susceptibility of electrons to scattering presents two significant challenges to performing intensity modulation of electron fields. Firstly, for any collimation system of electron fields to be effective, it must be located at close proximity to the patient's surface. Secondly, it makes the calculation of electron dose difficult to rapidly estimate, thereby impeding inverse optimization of MERT.

4.1 Modulated Electron Radiation Therapy

Development of MERT has historically progressed along two main axes. The first approach consists of designing new electron-MLC (eMLC) specifically used to collimate electron fields while the second approach investigates methods to adequately use photon-MLC (pMLC) to collimate electron fields.

Electron MLC

Lee *et al.* are credited for the first design of eMLC [5]. They proposed that the eMLC be positioned at the cutout position of electron applicators so as to provide collimation of the beam as close to the patient's surface as possible. By limiting the air gap between the final collimator and the patient, in-air scattering is reduced and allows for sharp field edges. A narrow penumbra allows dose distributions to be more conformal to the target and therefore offer better sparing to immediately adjacent healthy tissue. In their first prototype, they designed an eMLC consisting of 30 opposed leaf pairs made of steel (see Fig. 4–1). Each leaf had a width of 0.5 cm and had the particularity of having unfocused leaf ends. The leaves had to be manually positioned. They showed through Monte Carlo simulation that the beam profiles achieved with their eMLC for a 2x2 cm^2 field had identical penumbra shapes as those measured with a similarly-shaped Cerrobend cutout. Ma *et al.* [6] performed inverse planning of a MERT plan using this prototype and electron beams of 6, 12 and 20 MeV on a hypothetical breast case and compared it to a tangential 6 MV photon plan. The optimization relied on Monte Carlo calculation of electron beamlets with EGS4. They found that the MERT plan provided better target dose homogeneity and resulted in better sparing of lung to higher doses.

Hogstrom *et al.* [7] proposed a deployable-retractable eMLC design where the collimator's distance from the source could be changed from 63 cm to 90 cm depending on the treatment type. Shorter source to collimator distance would allow for sufficient clearance for rotational deliveries of electron arc therapy. Their prototype featured 21 brass leaf pairs that could be fully retracted to form a 20x21 cm^2 field when projected to the isocenter. Like previous designs, the leaves also had to be manually positioned. They extensively characterized their eMLC's output factor, depth dose and 2D dose distribution at 5, 10 and 15 MeV and determined it to be suitable to replace electron applicators. They however expressed concerns that the weight of the eMLC could induce sagging of its leaves or the gantry for

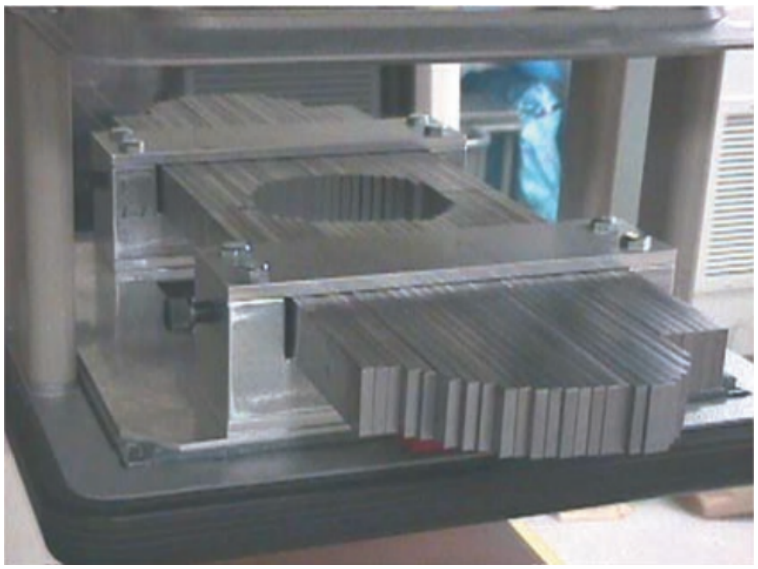

Figure 4–1: Prototype of the eMLC proposed by Lee *et al.* [5] and further studied by Ma *et al.* [6], from which this figure was reproduced.

non-normally incident beam angles.

Al-Yahya *et al.* proposed a much simpler eMLC design using only 2 pairs of copper trimmer bars that could be controlled by 4 motors [8], [9]. This eMLC, called the Few-Leaf Electron Collimator (FLEC), would be placed at the bottom of the electron applicator and be used in conjunction with the linac's jaws to deliver rectangular fields of up to 8x8 cm^2 (see Fig. 4–2). The superposition of multiple such rectangular fields could then be used to deliver complex shaped dose distribution. The FLEC would serve as a secondary collimation of an already-collimated electron field by the jaws. As such, its trimmer bars could be made to be relatively thin (1.2 cm) allowing it to be lighter than previous eMLC designs. They also investigated the dosimetric benefit of combining MERT plans with conventional photon beams [10]. They noted significant reduction in mean dose to the parotid and brain stem in 2 head and neck with the combined MERT-IMRT approach as compared to photon-IMRT alone. Connell *et al.* [11] delivered a FLEC-collimated MERT plan on a Solid Water (GAMMEX, Middleton, WI) phantom and performed 2D dose measurements using radiochromic film and a diode array MapCHECK® device (Sun Nuclear, Melbourne, FL). They noted

a gamma passing rate of 98.7% with film when combining contributions from all electron energies with a gamma criteria of 3%/3mm.

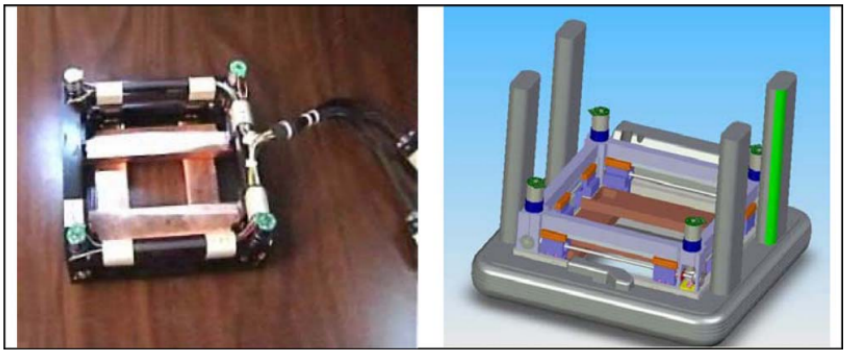

Figure 4–2: A prototype of the FLEC, reproduced from [9].

Multiple further iterations of eMLC designs have been proposed by various authors. Gauer *et al.* [12], [13] presented a prototype consisting of 24 brass leaves pair, fully motorized by the leaf controller system of a micro multileaf collimator. Eldib *et al.* [14] also had a design for a manually-positioned eMLC made of 25 pairs of tungsten leaves. More recently, [15] *et al.* proposed a novel eMLC design consisting of thick acrylic leaves that protrude in the direction parallel to the beam axis. The reverse L-shaped leaf design would allow for collimation of the electron beam over a thickness of over 28 cm, significantly decreasing out-of-field dose. In their prototype, the pair of 16 acrylic leaves were manually positioned.

4.1.1 Photon MLC

On Varian TrueBeam linacs (Varian Medical Systems, Palo Alto, CA), the pMLC is located at around 50 cm from the source. Assuming that the machine isocenter is located at the center of a tumor target, this leaves around 40 cm of air gap between the bottom of the MLC to the patient's surface. In that air gap, the electron scatter leads to a widening of its beam profile, in particular in the penumbra region. This makes using pMLC for MERT difficult due to the poor conformity of the resulting electron fields. Nevertheless, it remains an attractive option as it avoids the design, manufacturing, commissioning and domain-wide

adoption an entirely new eMLC. Furthermore, as pMLC could be used for photons and electrons alike, it would render the delivery of mixed modalities plans seamless.

Klein *et al.* [16] noted that, when collimated with pMLC on the Varian Clinac 2100C, electron fields would have much wider penumbra and worse uniformity than applicator-collimated ones. This effect was exacerbated at lower energies (6 MeV) but could be mitigated by reducing SSD. A shorter SSD implies a smaller air gap between the MLC and the patient surface. They estimated that an SSD of 70 cm would have to be required for pMLC-collimated MERT plans, as corroborated by other studies [17], [18]. Another way of reducing in-air scatter is to replace the air by a less dense gas in which electron scattering is less prominent. Karlsson *et al.* [19] investigated the impact of replacing air in the linac head by helium on the penumbra of pMLC electron fields. They also proposed the placement of a helium bag between the pMLC and the patient's surface. This was also evaluated by Lee *et al.* [5], who noted narrower penumbra width compared to air. At reduced SSD of 80 cm, the helium setup provided comparable electron penumbra width as their eMLC device at 12 and 20 MeV. However, the reduced scattering in helium was not sufficient at 6 MeV.

Salguero *et al.* [20] performed the treatment planning of 4 clinical chest wall cases with MERT. Electron fields were planned using the pMLC at reduced SSD between 60 and 70 cm. The MERT plans were then compared to corresponding cutout-collimated plans. Overall, MERT plans had better target dose homogeneity while providing better dose sparing to lung and heart, specifically in the higher dose region. Similarly, they also evaluated the benefit of MERT on 4 head and neck cases [21]. Compared to photon plans, they noted similar or better PTV coverage with significantly lower doses to certain OAR. Henzen *et al.* [22] presented a beamlet-based direct aperture optimizer using simulated annealing to perform inverse optimization of MERT. Applied to clinical cases of breast, chest wall and parotid, they found that MERT offered significant sparing of OARs compared to standard

of care photon plans. However, their MERT plans showed significant dose heterogeneity in the target. Mueller *et al.* [23] investigated the possibility of replacing applicator and cutout-based electron fields with reduced SSD pMLC-collimated electron fields. For 5 clinical cases, the cutout electron dose distribution is compared to a pMLC electron dose at SSDs varying between 70 and 100 cm. Although pMLC electron fields lead to wider electron beam profiles, even at reduced SSD, compared to the cutout fields, a clinically equivalent plan quality could still be achieved as shown in Fig. 4–3. Ma *et al.* [24] performed a Monte Carlo characterization of the dose from pMLC-collimated electron fields in continuous arc deliveries.

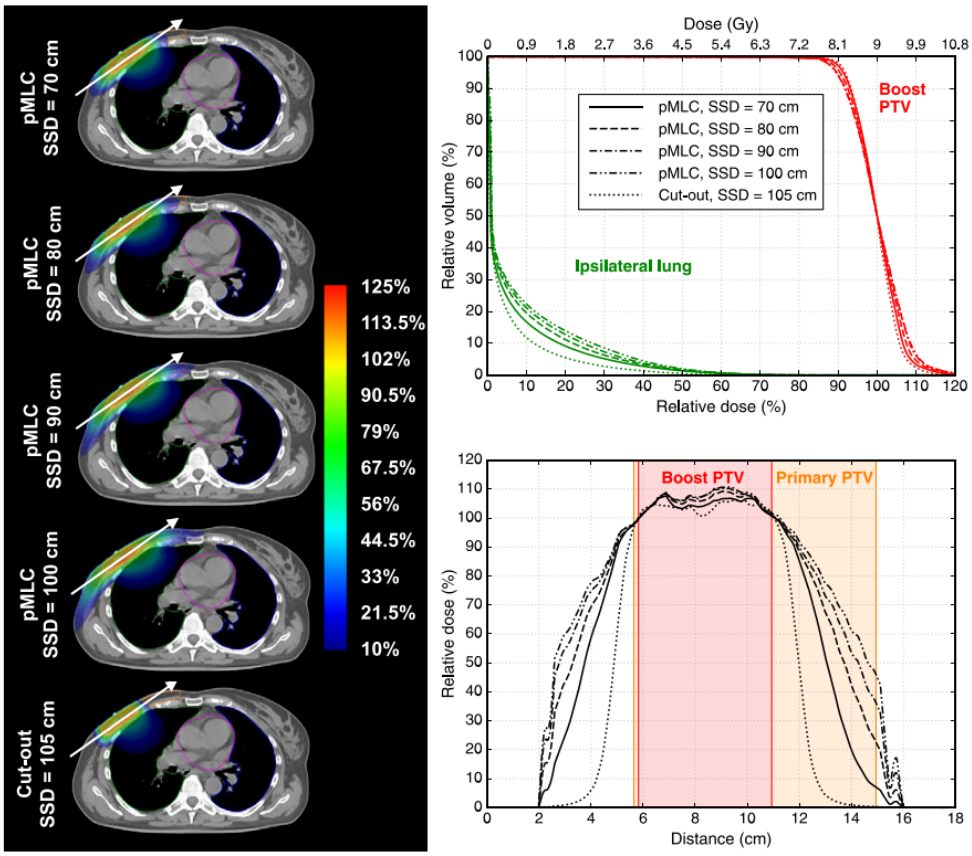

Figure 4–3: Reproduced from the study by Mueller *et al.* [23], where pMLC-collimated MERT plans at differing SSDs are compared to a conventional electron plan for a clinical breast case.

4.2 Mixed electron-photon radiation therapy (MBRT)

The feasibility of pMLC-collimated electron deliveries opens the door for an MBRT approach. Indeed, as both modality can be delivered from the same collimator, this allows for a logistically seamless delivery without repositioning of the patient. Karlsson *et al.* [25] combined fixed pMLC-collimated electron fields (17 MeV and 22 MeV) with parallel opposed photons for planning of 2 breast cases. These beams were produced on the MM50 racetrack microtron (Scanditronix, Uppsala) linac which had a design that was favorable for pMLC collimation of electron fields. The treatment head was filled with helium and the MLC is located at a distance of only 31 cm from the patient. Compared to conventional treatment plans using only parallel opposed photons, the mixed electron-photon plan was found to provide significantly better sparing to lung and heart.

Jansson *et al.* [26] performed a retrospective planning study on 30 breast cases comparing an MBRT plan to conventional parallel-opposed photon plan. The mixed plan consisted of 1 fixed pMLC-collimated electron field and 3 photon fields delivered on the Microtron MM22 (Scanditronix, Uppsala). They used a reduced SSD setup of 85 cm for electron fields. Out of the 30 cases, the MBRT plan was chosen in 12 cases to be of superior quality due to better sparing of lung and heart. The heart dose had particularly better sparing with MBRT in left-sided breast cases.

Similarly, Li *et al.* [27] described an MBRT method using 1 conventional electron field (either 9 or 12 MeV) and 4 IMRT fields for early stage breast cancer. Compared to a 9-field IMRT photon plan, the MBRT plans were observed to have lower doses to the previously-mentioned OARs.

To this day, Míguez *et al.* [28], [29] are the first and only group to have performed pMLC-collimated MBRT treatment in patients. Using a Siemens Primus linac, they treated 7 patients with an accelerated partial-breast irradiation using a combination of MERT and IMRT. Electron fields were delivered from either 1 or 2 fixed angles using 1 or 2 energy

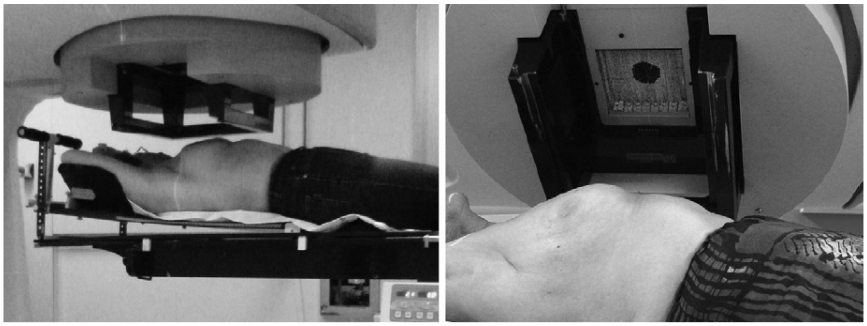

Figure 4–4: Míguez *et al.* [29], from which this figure is reproduced, used a reduced SSD setup for its pMLC-collimated electron beams to perform partial-breast irradiation with MBRT.

among 9, 12, and 15 MeV, while tangential IMRT photons were delivered from 1 or 2 angles. The pMLC-collimated electron fields had a reduced SSD of 60 to 70 cm as shown in Fig. 4–4. A conventional IMRT plan was also prepared for comparison. On average, better sparing to OARs were observed with the MBRT plans while dose homogeneity in the PTV was slightly better in the conventional IMRT plan. Follow-ups were made for a period of 4 years with no severe toxicities being reported. No disruption in the clinical workflow was noted from the implementation of the MBRT approach.

Mueller *et al.* [30] and Renaud *et al.* [31] each proposed methods for beamlet-based simultaneous optimization of pMLC-collimated MBRT plans. In the former, a simulated annealing-based direct aperture optimization approach is used, whereby at each iteration, the shape or the weight of a random aperture is varied. In the latter, the column generation method [32] is applied to MBRT. A more detailed explanation of this implementation will be given in Section 5. Applied to clinical cases of chest wall, squamous cell carcinoma, and sarcomas, both studies found MBRT plans provided superior sparing of OARs without sacrificing PTV dose homogeneity compared to conventional photon plans [30], [31]. In particular, the low dose bath volume was significantly reduced as depicted in Fig. 4–5. Subsequently, Mueller *et al.* proposed a hybrid direct aperture optimization method combining both the

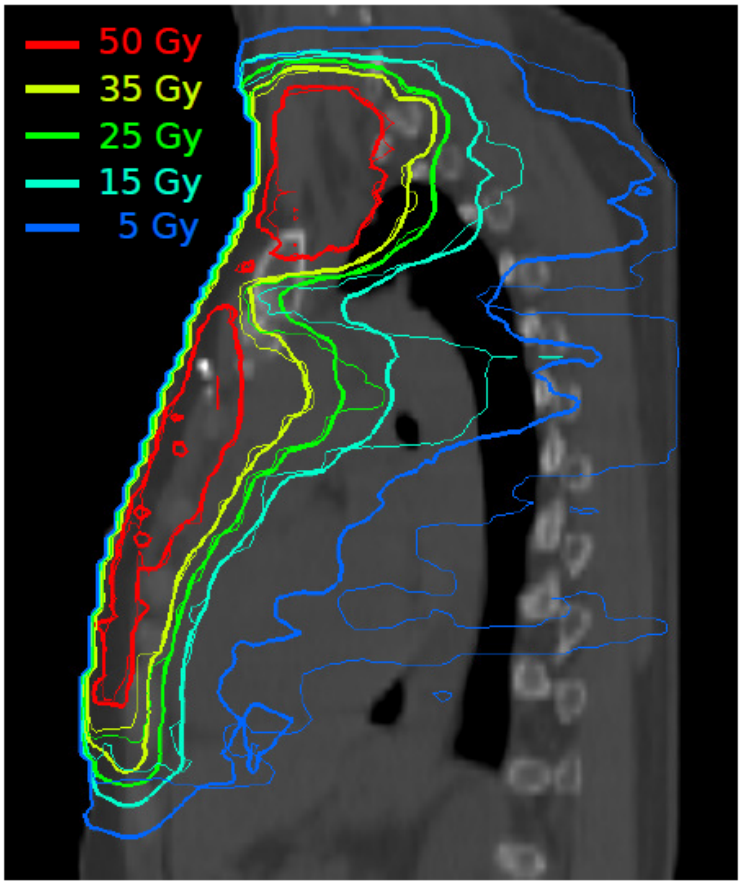

Figure 4–5: Isodose lines of an MBRT plan (thick) vs. photon-only IMRT plan (thin). Reproduced from [31].

column generation and simulated annealing approach [33].

Mueller *et al.* further expanded their optimizer to handle optimization of MERT combined with photon dynamic trajectories, where photon fields are delivered along arc segments that include dynamic rotation of gantry, collimator, and couch angles [34]. Kueng *et al.* [35] used a fluence map optimization approach to simultaneously optimize a mixed beam treatment plan including electrons, photons and protons. Analogously to VMAT, Guyer *et al.* [36] investigated the possibility of delivering pMLC-collimated electron fields along arc segments to reduce MBRT delivery times.

All MBRT techniques so far described consist of sequential deliveries of each modality. Standard linacs can only deliver one beam energy and particle type at a time. Khaledi *et al.* [37], [38] propose the use of a perforated lead sheet to create a truly simultaneous mixed electron-photon beam. The sheet is to be placed in the linac's electron beam path to act as both a bremsstrahlung target for photon production while allowing for electrons to pass through a hole.

4.2.1 Robust optimization

All of the work so far presented featured a PTV-based optimization. The concept of the PTV is defined in the International Commission on Radiation Units and Measurements' report 83 [39] as a geometrical expansion of the CTV to account for spatial mismatch between planning and delivery. It is is based on the assumption of the static dose cloud approximation, whereby the dose distribution in the treatment room's reference frame remains unperturbed by patient setup shifts or by patient motion and/or deformation. As such, in the patient's reference frame, the dose $D(\vec{r}|\Delta\vec{s})$ to a point $\vec{r}$ in the patient coordinate system, subject to a setup error $\Delta\vec{s}$ in the treatment room's frame, can be related to the unshifted patient dose distribution $D(\vec{x}|0)$ as [40]:

$$D(\vec{r}|\Delta\vec{s}) = D(\vec{r} + \Delta\vec{s}|0). \tag{4.1}$$

Although this approximation mostly holds for photon beams, where the fluence attenuation in matter is relatively slow with depth, it is not true for charged particles. In particular, for proton radiation therapy, many studies have looked for alternative methods of accounting for setup uncertainties. Today, the accepted approach consists of performing a robust optimization [41], [42]. Dose distributions are explicitly calculated under multiple "scenarios". Each of these scenarios incorporate an artificial positioning shift of the patient, representing

potential setup errors. The cost function[1] is then evaluated on either the worst-case scenario (minimax approach) or on a weighted-average of all scenarios (stochastic programming approach). As setup errors are theoretically accounted for by these scenarios, the target volume whose coverage must be optimized is therefore the CTV.

As electrons are also charged particles with a sharp dose fall-off with depth, the validity of PTV-based optimization should also be put in question in the case of MERT and MBRT. Renaud *et al.* [43] implemented a setup-robust optimization method to their MBRT column generation optimizer. Beamlets were calculated in 6 setup scenarios and either the minimax or stochastic programming approach could be used to define the cost function. They showed near-identical plan quality for robust optimized MBRT plans with either approaches. They compared robustly optimized vs. PTV-optimized MBRT plans for clinical cases of soft tissue sarcoma and chest wall. In both plans, the PTV-optimized dose distribution was more susceptible to undercover the CTV when evaluated under a setup error as can be seen in Fig. 4–6. In particular, robustly optimized MBRT plans were found to provide more conformal dose distributions in beam-parallel directions, for which electron doses are naturally robust. Heath *et al.* [44] applied the robust optimization method to their hybrid simulated annealing + column generation optimizer. They compared robustly optimized vs. PTV-based MBRT plans for 2 head & neck cases and a brain case. In head & neck plans, they noted that the PTV-based plan lead to larger target dose inhomogeneity and variations when evaluated in the robust scenarios. They also validated the accurate delivery of a robust MBRT plan on an anthropomorphic head phantom with good agreement between film measurement and Monte Carlo calculation, both with and without setup errors.

[1] A definition of the cost function will be given in Chapter 5.

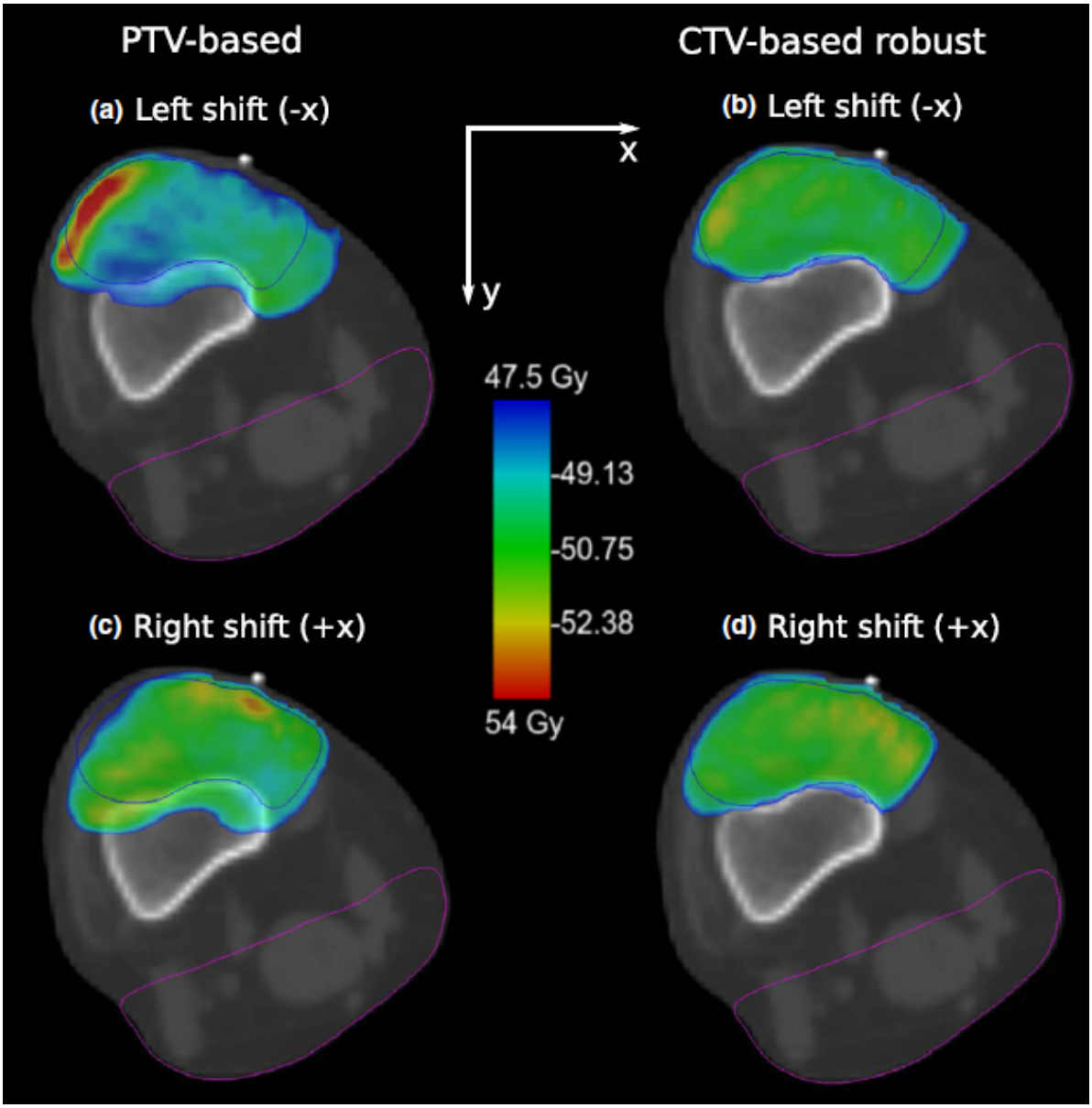

Figure 4–6: Dose distributions of PTV-based (left) vs. robust optimized (right) MBRT plans under setup errors. The blue contour is the CTV, for which loss of target coverage can be observed in the PTV plans. Reproduced from [43].

REFERENCES

[1] A. Brahme, J.-E. Roos, and I. Lax, "Solution of an integral equation encountered in rotation therapy," *Physics in medicine and biology*, vol. 27, no. 10, p. 1221, 1982.

[2] A. Brahme, *Multi leaf collimator*, US Patent 4,672,212, Jun. 1987.

[3] C. X. Yu, "Intensity-modulated arc therapy with dynamic multileaf collimation: An alternative to tomotherapy," *Physics in medicine and biology*, vol. 40, no. 9, p. 1435, 1995.

[4] K. Otto, "Volumetric modulated arc therapy: IMRT in a single gantry arc," *Medical physics*, vol. 35, no. 1, pp. 310–317, 2008.

[5] M. C. Lee, S. B. Jiang, and C. M. Ma, "Monte Carlo and experimental investigations of multileaf collimated electron beams for modulated electron radiation therapy," *Medical Physics*, vol. 27, no. 12, pp. 2708–2718, 2000. DOI: 10.1118/1.1328082.

[6] C. M. Ma, T. Pawlicki, M. C. Lee, *et al.*, "Energy- and intensity-modulated electron beams for radiotherapy," *Physics in Medicine and Biology*, vol. 45, no. 8, pp. 2293–2311, 2000. DOI: 10.1088/0031-9155/45/8/316.

[7] K. R. Hogstrom, R. A. Boyd, J. A. Antolak, *et al.*, "Dosimetry of a prototype retractable eMLC for fixed-beam electron therapy," *Medical Physics*, vol. 31, no. 3, pp. 443–462, 2004. DOI: 10.1118/1.1644516.

[8] K. Al-Yahya, D. Hristov, F. Verhaegen, and J. Seuntjens, "Monte Carlo based modulated electron beam treatment planning using a few-leaf electron collimator - Feasibility study," in *Physics in Medicine and Biology*, vol. 50, 2005, pp. 847–857. DOI: 10.1088/0031-9155/50/5/009.

[9] K. Al-Yahya, F. Verhaegen, and J. Seuntjens, "Design and dosimetry of a few leaf electron collimator for energy modulated electron therapy," *Medical Physics*, vol. 34, no. 12, pp. 4782–4791, 2007. DOI: 10.1118/1.2795827.

[10] K. Al-Yahya, M. Schwartz, G. Shenouda, *et al.*, "Energy modulated electron therapy using a few leaf electron collimator in combination with IMRT and 3D-CRT: Monte carlo-based planning and dosimetric evaluation," en, *Med. Phys.*, vol. 32, no. 9, pp. 2976–2986, Sep. 2005.

[11] T. Connell, A. Alexander, P. Papaconstadopoulos, *et al.*, "Delivery validation of an automated modulated electron radiotherapy plan," *Medical Physics*, vol. 41, no. 6, 2014. DOI: 10.1118/1.4876297.

[12] T. Gauer, D. Albers, F. Cremers, *et al.*, "Design of a computer-controlled multileaf collimator for advanced electron radiotherapy," *Physics in Medicine and Biology*, vol. 51, no. 23, pp. 5987–6003, 2006. DOI: 10.1088/0031-9155/51/23/003.

[13] T. Gauer, J. Sokoll, F. Cremers, *et al.*, "Characterization of an add-on multileaf collimator for electron beam therapy," *Physics in Medicine and Biology*, vol. 53, no. 4, pp. 1071–1085, 2008. DOI: 10.1088/0031-9155/53/4/017.

[14] A. A. Eldib, M. I. ElGohary, J. Fan, *et al.*, "Dosimetric characteristics of an electron multileaf collimator for modulated electron radiation therapy," *J. Appl. Clin. Med. Phys.*, vol. 11, no. 2, pp. 5–22, Mar. 2010.

[15] H. M. P. Paschal, C. N. Kabat, T. Martin, *et al.*, "Dosimetric characterization of a new surface-conforming electron MLC prototype," en, *J. Appl. Clin. Med. Phys.*, e14173, Oct. 2023.

[16] E. E. Klein, Z. Li, and D. A. Low, "Feasibility study of multileaf collimated electrons with a scattering foil based accelerator," *Radiotherapy and Oncology*, vol. 41, no. 2, pp. 189–196, 1996. DOI: 10.1016/S0167-8140(96)01822-1.

[17] F. C. Du Plessis, A. Leal, S. Stathakis, W. Xiong, and C. M. Ma, "Characterization of megavoltage electron beams delivered through a photon multi-leaf collimator (pMLC),"

Physics in Medicine and Biology, vol. 51, no. 8, pp. 2113–2129, 2006. DOI: 10.1088/0031-9155/51/8/011.

[18] E. E. Klein, M. Vicic, C. M. Ma, D. A. Low, and R. E. Drzymala, "Validation of calculations for electrons modulated with conventional photon multileaf collimators," *Physics in Medicine and Biology*, vol. 53, no. 5, pp. 1183–1208, 2008. DOI: 10.1088/0031-9155/53/5/003.

[19] M. G. Karlsson, M. Karlsson, and C.-M. Ma, "Treatment head design for multileaf collimated high-energy electrons," *Medical Physics*, vol. 26, no. 10, pp. 2161–2167, 1999. DOI: https://doi.org/10.1118/1.598732.

[20] F. J. Salguero, B. Palma, R. Arrans, J. Rosello, and A. Leal, "Modulated electron radiotherapy treatment planning using a photon multileaf collimator for post-mastectomized chest walls," *Radiotherapy and Oncology*, vol. 93, no. 3, pp. 625–632, 2009. DOI: 10.1016/j.radonc.2009.08.021.

[21] F. J. Salguero, R. Arrns, B. A. Palma, and A. Leal, "Intensity- and energy-modulated electron radiotherapy by means of an xMLC for head and neck shallow tumors," *Physics in Medicine and Biology*, vol. 55, no. 5, pp. 1413–1427, 2010. DOI: 10.1088/0031-9155/55/5/010.

[22] D. Henzen, P. Manser, D. Frei, *et al.*, "Beamlet based direct aperture optimization for MERT using a photon MLC.," *Medical physics*, vol. 41, no. 12, p. 121 711, Dec. 2014. DOI: 10.1118/1.4901638.

[23] S. Mueller, M. K. Fix, D. Henzen, *et al.*, "Electron beam collimation with a photon MLC for standard electron treatments," *Physics in Medicine & Biology*, vol. 63, no. 2, p. 025 017, 2018. DOI: 10.1088/1361-6560/aa9fb6.

[24] C. Ma, D. Parsons, M. Chen, *et al.*, "Electron modulated arc therapy (EMAT) using photon MLC for postmastectomy chest wall treatment i: Monte carlo-based dosimetric characterizations," en, *Phys. Med.*, vol. 67, pp. 1–8, Nov. 2019.

[25] M. Karlsson and B. Zackrisson, "Matching of electron and photon beams with a multileaf collimator," *Radiotherapy and Oncology*, vol. 29, no. 3, pp. 317–326, 1993. DOI: 10.1016/0167-8140(93)90150-7.

[26] T. Jansson, H. Lindman, K. Nygård, *et al.*, "Radiotherapy of breast cancer after breast-conserving surgery: An improved technique using mixed electron-photon beams with a multileaf collimator," *Radiotherapy and Oncology*, vol. 46, no. 1, pp. 83–89, 1998. DOI: 10.1016/S0167-8140(97)00176-X.

[27] J. G. Li, S. S. Williams, D. R. Goffinet, A. L. Boyer, and L. Xing, "Breast-conserving radiation therapy using combined electron and intensity-modulated radiotherapy technique," *Radiotherapy and Oncology*, vol. 56, no. 1, pp. 65–71, 2000. DOI: 10.1016/S0167-8140(00)00189-4.

[28] B. A. Palma, A. U. Sánchez, F. J. Salguero, *et al.*, "Combined modulated electron and photon beams planned by a Monte-Carlo-based optimization procedure for accelerated partial breast irradiation," *Physics in Medicine and Biology*, vol. 57, no. 5, pp. 1191–1202, 2012. DOI: 10.1088/0031-9155/57/5/1191.

[29] C. Míguez, E. Jiménez-Ortega, B. A. Palma, *et al.*, "Clinical implementation of combined modulated electron and photon beams with conventional MLC for accelerated partial breast irradiation," *Radiotherapy and Oncology*, vol. 124, no. 1, pp. 124–129, 2017. DOI: 10.1016/j.radonc.2017.06.011.

[30] S. Mueller, M. K. Fix, A. Joosten, *et al.*, "Simultaneous optimization of photons and electrons for mixed beam radiotherapy," *Physics in Medicine and Biology*, vol. 62, no. 14, pp. 5840–5860, 2017. DOI: 10.1088/1361-6560/aa70c5.

[31] M.-A. Renaud, M. Serban, and J. Seuntjens, "On mixed electron-photon radiation therapy optimization using the column generation approach," *Medical Physics*, vol. 44, no. 8, pp. 4287–4298, 2017. DOI: 10.1002/mp.12338.

[32] H. E. Romeijn, R. K. Ahuja, J. F. Dempsey, and A. Kumar, "A column generation approach to radiation therapy treatment planning using aperture modulation," *SIAM Journal on Optimization*, vol. 15, no. 3, pp. 838–862, 2005. DOI: 10.1137/040606612.

[33] S. Mueller, G. Guyer, T. Risse, *et al.*, "A hybrid column generation and simulated annealing algorithm for direct aperture optimization," en, *Phys. Med. Biol.*, vol. 67, no. 7, p. 075 003, Mar. 2022.

[34] S. Mueller, P. Manser, W. Volken, *et al.*, "Part 2: Dynamic mixed beam radiotherapy (dymber): Photon dynamic trajectories combined with modulated electron beams," *Medical Physics*, vol. 45, no. 9, pp. 4213–4226, 2018. DOI: https://doi.org/10.1002/mp.13085.

[35] R. Kueng, S. Mueller, H. A. Loebner, *et al.*, "TriB-RT: Simultaneous optimization of photon, electron and proton beams," en, *Phys. Med. Biol.*, vol. 66, no. 4, p. 045 006, Feb. 2021.

[36] G. Guyer, S. Mueller, P.-H. Mackeprang, *et al.*, "Delivery time reduction for mixed photon-electron radiotherapy by using photon MLC collimated electron arcs," en, *Phys. Med. Biol.*, vol. 68, no. 21, p. 215 009, Oct. 2023.

[37] N. Khaledi, A. Arbabi, D. Sardari, M. Mohammadi, and A. Ameri, "Simultaneous production of mixed electron–photon beam in a medical LINAC: A feasibility study," en, *Phys. Med.*, vol. 31, no. 4, pp. 391–397, Jun. 2015.

[38] N. Khaledi, D. Sardari, M. Mohammadi, A. Ameri, and N. Reynaert, "Dosimetric evaluation of a novel electron–photon mixed beam, produced by a medical linear accelerator," en, *J. Radiother. Pract.*, vol. 17, no. 3, pp. 319–331, Sep. 2018.

[39] ICRU, "Report 83: Prescribing, Recording, and Reporting Photon-Beam Intensity-Modulated Radiation Therapy (IMRT)," *Journal of the ICRU*, vol. 19, no. 1, 2010. DOI: 10.1093/jicru/ndq025.

[40] J. Unkelbach, T. Bortfeld, B. C. Martin, and M. Soukup, "Reducing the sensitivity of impt treatment plans to setup errors and range uncertainties via probabilistic treatment

planning," *Medical Physics*, vol. 36, no. 1, pp. 149–163, 2009. DOI: https://doi.org/10.1118/1.3021139.

[41] A. Fredriksson, A. Forsgren, and B. Hårdemark, "Minimax optimization for handling range and setup uncertainties in proton therapy," *Medical Physics*, vol. 38, no. 3, pp. 1672–1684, 2011. DOI: 10.1118/1.3556559.

[42] W. Liu, X. Zhang, Y. Li, and R. Mohan, "Robust optimization of intensity modulated proton therapy," *Medical Physics*, vol. 39, no. 2, pp. 1079–1091, 2012. DOI: 10.1118/1.3679340.

[43] M.-A. Renaud, M. Serban, and J. Seuntjens, "Robust mixed electron-photon radiation therapy optimisation," *Medical Physics*, vol. 0, no. ja, 2019. DOI: 10.1002/mp.13381.

[44] E. Heath, S. Mueller, G. Guyer, *et al.*, "Implementation and experimental validation of a robust hybrid direct aperture optimization approach for mixed-beam radiotherapy," *Medical Physics*, vol. 48, no. 11, pp. 7299–7312, 2021. DOI: https://doi.org/10.1002/mp.15258.

CHAPTER 5
`brems`: a treatment planning system for MBRT

As the clinical TPS cannot perform optimization of MBRT treatment plans, an in-house TPS had to be developed for this purpose [1]. "`brems`" is the most recent version of this webapp TPS.

5.1 External beam treatment planning workflow on brems

In this section, we present a brief description of each step involved in the creation of an MBRT plan on the `brems` TPS. The reader can refer to the workflow flowchart in Fig. 5–1.

5.1.1 Importing patient data

For any treatment plan to be patient specific, it must use patient geometry information. Therefore, a preliminary step to treatment planning is to upload CT images of the patient in treatment condition. These CT images are scanned at an earlier "CT simulation" stage, where the patient is imaged in the same position as they would be when receiving the treatment. This provides an accurate representation of the patient geometry to allow for the treatment planner to accurately calculate patient doses. On state-of-the-art TPS, contouring of target structures (PTV, CTV, GTV) and OARs would then be performed at this stage. However, contouring features are not currently available on `brems`. The structure set file which contains the contouring data must therefore also be uploaded to `brems`. Within a structure set file, each contoured structure is stored as arrays of 2D coordinate points delineating the shape of the structure on each CT image slice. The CT images and their overlaid contours are displayed in the top-left quadrant of the `brems` user interface in Fig. 5–2. Although CT images (and contours) are only obtained along axial slices, their projection onto the sagittal and coronal planes can be computed and are displayed in the bottom 2 quadrants.

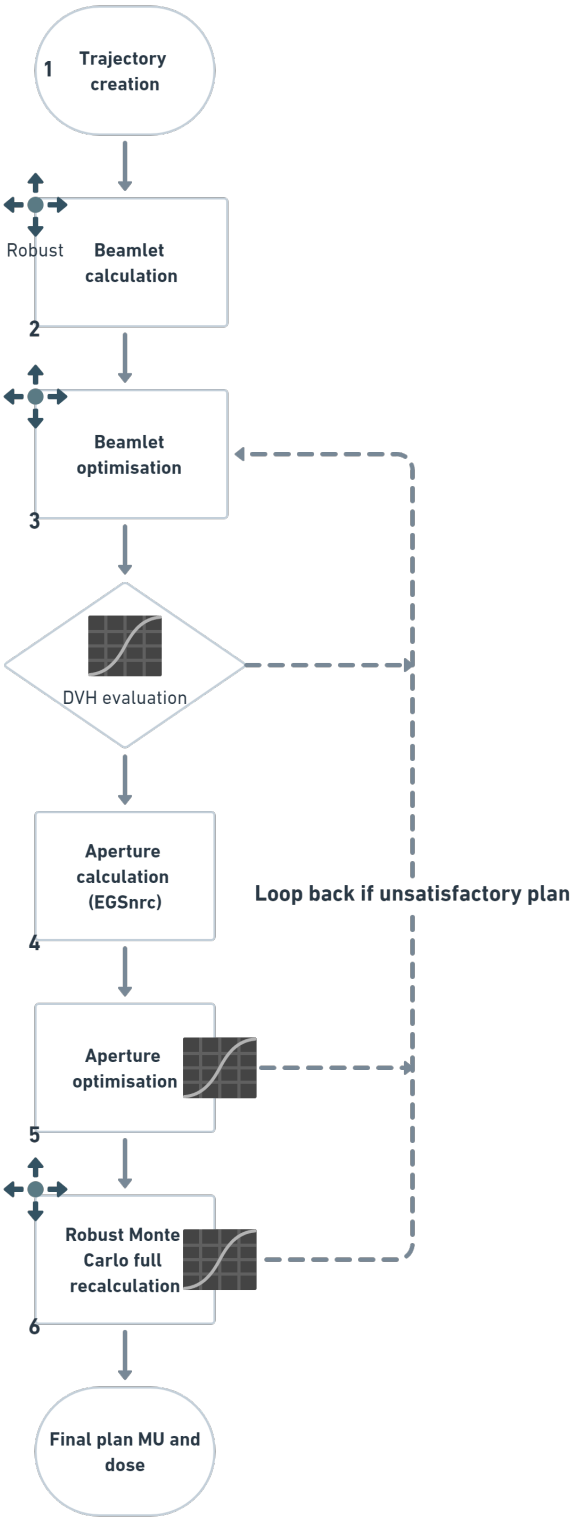

Figure 5–1: Flowchart describing the treatment planning workflow on brems.

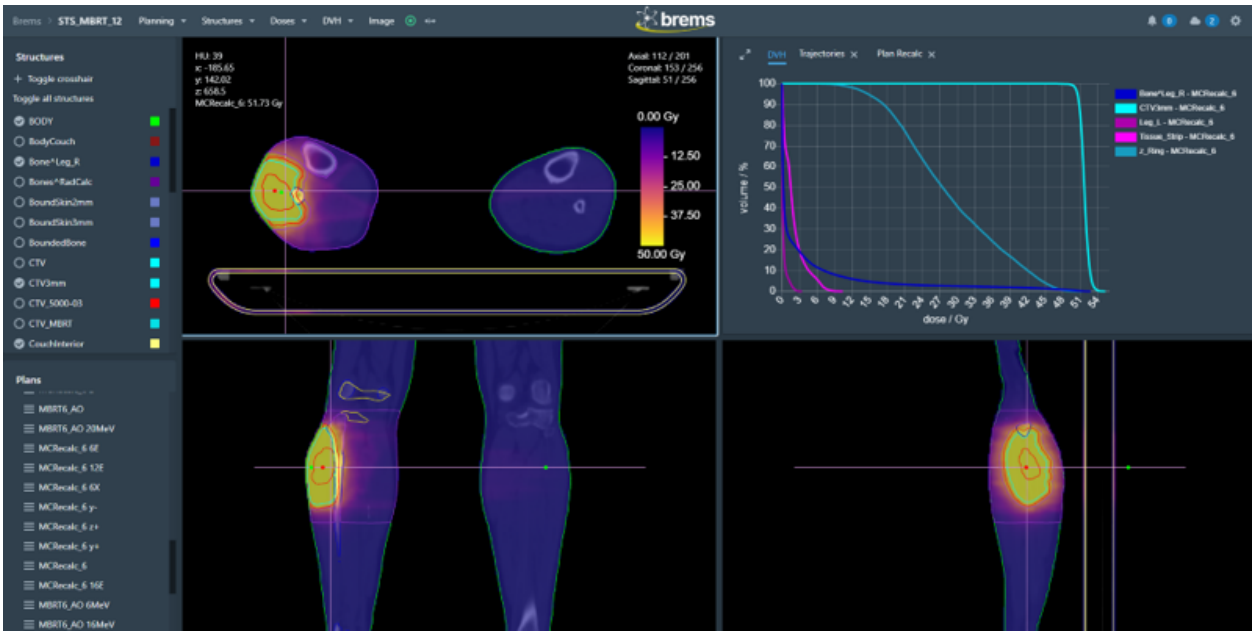

Figure 5–2: Screenshot of the `brems` user interface.

5.1.2 Trajectory creation

The first step to a treatment plan creation is to define the beam geometries of the plan. The treatment planner adds beams to their plan by specifying the particle used, the beam energy, gantry angle, couch angle and distance from the beam's source to the isocenter. For continuous arc deliveries, where radiation is delivered simultaneous to rotating gantry angles, the planner can provide the initial and final gantry angles of the arc segment desired.

For each beam, the planner must select the target structure of the plan. For robust optimization, this would correspond to the CTV. `brems` will then calculate the coordinates of the centroid of target structure and assign it as the isocenter of the beam. For typical single-isocenter treatment plans, this structure would be identical for all beams.

5.1.3 Beamlet dose calculation

When optimizing treatment plans, the optimizer must choose the optimal location of each individual MLC leaf. To do so, it must be provided with the information of the dosimetric effect resulting from having the leaves at any given position. Let us consider a single beam's Beams Eye View (BEV) in Fig. 5–3 and divide the BEV plane into a regular square grid. Particles crossing any given grid element will eventually deposit dose in the patient. The dose distribution resulting from particles crossing 1 such grid element is defined as a beamlet. This can be understood as the dose due to keeping that grid element open while closing off all other grid elements with MLCs. These beamlets must be calculated for each beam and the relevant subspace of the BEV. This subspace is confined to the projection of the target structure onto the BEV plan (+ some margins). Indeed, only grid elements that can geometrically deliver dose to the target should be considered.

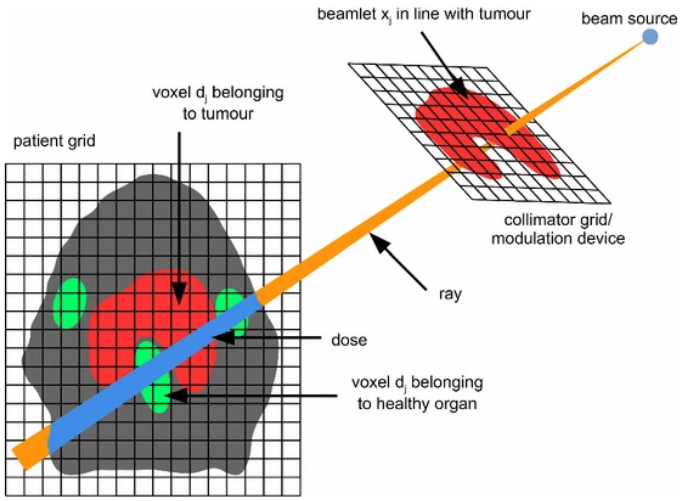

Figure 5–3: Diagram illustrating the decomposition of a beam's eye view into beamlets. Reproduced from Breedveld *et al.* (2017) [2]

With robust optimization, beamlets must be calculated in additional scenarios. For positioning error scenarios, the isocenter of the beamlet is artificially shifted to mimic setup errors. On `brems`, 6 positioning scenarios are calculated by introducing a user-specified shift

distance in each Cartesian direction (-x, +x, -y, +y, -z, +z). Therefore, for each robust beamlet, there are 7 dose distributions calculated.

As beamlets must be calculated for every beam angle, beam energy and particle type, this results in a computationally very expensive dose calculation task. On `brems`, photon beamlets are calculated using an in-house collapsed cone convolution-superposition algorithm, named Supify, while electron beamlets are calculated with an in-house Pre-calculated Monte Carlo (PMC) technique. Both algorithms are coded with the CUDA platform, allowing for rapid Graphics Processing Unit (GPU)-based calculations. More details on the PMC code is provided in section 5.2.

5.1.4 Beamlet optimization

Treatment plan optimization is the core step of the treatment planning workflow. Given the beam arrangements set up in the trajectory creation step, the optimizer must now find the set of aperture shapes and weights that provides the best plan quality. This leads to the obvious question: what defines a good plan? Conceptually, we would want a plan that gives the prescribed dose to the target and the least dose anywhere else. To convey this concept mathematically, we use the notion of a cost function.

Optimization constraints

Characteristics of an undesirable plan are formulated as "constraints" that assign a penalty for dose distributions that violates them. For example, let us consider a constraint that would be placed on the target structure. We want every voxel $v \in V_{\text{target}}$ within the target to receive at least the prescription dose D_{presc}. Therefore, we formulate a constraint that increases in value for every voxel that receives a dose $D(v) < D_{\text{presc}}$:

$$C(D) = \frac{1}{N_{V_{\text{target}}}} \sum_{v \in V_{\text{target}}} (D_{\text{presc}} - D(v))^2 H(D_{\text{presc}} - D(v)), \tag{5.1}$$

where H is the heaviside step function such that no penalty is incurred in voxels with doses $D(v) \geq D_{\text{presc}}$, $N_{V_{\text{target}}}$ is the total number of voxels in the target and C is the cost incurred by

the dose distribution with respect to this constraint. Similar constraints can be formulated to penalize high doses in organs-at-risk such that the total cost function is the weighted-sum of all constraints:

$$F(D) = \sum_i w_i C_i(D), \tag{5.2}$$

where w_i is the arbitrary weight assigned to each constraint i. The goal of the optimizer is then to find the set of aperture shapes and relative aperture weights that minimize the cost function.

Different types of constraint exist to accommodate the specific dose distribution characteristics desired in different region of a patient.

The simplest constraint is the one of a soft constraint. An upper (or lower) threshold dose $D_{\text{threshold}}$ is set to be a maximum (or minimum) dose allowed in a structure of interest. Every voxel within the structure that violates this threshold dose is then penalized by a price equal to the square of the difference between the voxel's dose and $D_{\text{threshold}}$. The constraint in Eq. 5.1 is one such example with the prescription dose D_{presc} being the lower threshold dose.

Although each OAR can have different maximum allowable doses, it is the goal of the planner to minimize the dose delivered anywhere within the patient's body in general. This can be done through a Normal Tissue Objective (NTO) function. Megavoltage external beam dose distribution will tend to fall-off exponentially with distance from the target. This is consistent with the fact that a photon beam travelling a distance x in matter will have its fluence attenuated by $e^{-\mu x}$. Let us consider an exponentially decaying function $D_{\text{NTO}}(x)$ of dose as a function of distance x from the target. For any voxel v outside of the target receiving a dose $D(v)$, we can estimate its distance x from the target as the shortest euclidean distance from the voxel's center to any point on the target's contour. We can then calculate

$D_{\mathrm{NTO}}(x)$ for v and assign a price as:

$$\mathrm{NTO}_v = (D_{\mathrm{NTO}}(x) - D(v))^2 H(D(v) - D_{\mathrm{NTO}}(x)), \tag{5.3}$$

where the heaviside step function ensures that only doses $D(v) \geq D_{NTO}(x)$ incur a non-zero price. The total NTO price is then calculated by summing NTO_v over all voxels v outside of the target, normalized by the total number of summed voxels. This allows the planner to punish dose distributions with dose fall-offs from the target at rates that are slower than the one dictated by $D_{\mathrm{NTO}}(x)$. On `brems`, $D_{\mathrm{NTO}}(x)$ is defined as:

$$D_{\mathrm{NTO}}(x) = \begin{cases} \infty & x < x_{\mathrm{start}} \\ D_0 e^{-k(x-x_{\mathrm{start}})} + D_\infty (1 - e^{-k(x-x_{\mathrm{start}})}) & x_{\mathrm{start}} \leq x \leq x_{\mathrm{max}} \\ \infty & x > x_{\mathrm{max}}, \end{cases} \tag{5.4}$$

where x_{start}, x_{max} D_0, D_∞ and k are input parameters chosen by the treatment planner and represent the minimum and maximum distance from the target where the NTO is imposed, the value of $D_{\mathrm{NTO}}(x)$ at x_{start}, the asymptotic limit of $D_{\mathrm{NTO}}(x)$ as $x \to \infty$ and the rate of dose decay, respectively. An example of $D_{\mathrm{NTO}}(x)$ is plotted in Fig. 5–4.

Column generation

With the cost function defined, we can now proceed with the actual treatment plan optimization. `brems` uses the column generation approach to do this, following the methodology described by Romeijn *et al.* [3] as applied in the context of MBRT [1].

The optimal solution to the treatment plan optimization problem consists of the set of deliverable aperture shapes at each beam angle considered and their relative weights with respect to each other that lead to a patient dose distribution that best minimizes the cost function. However, as each aperture is made of the collection of hundreds of MLC leaf positions, the large theoretical number of possible apertures ($> 10^{17}$) one can include in a treatment plan makes the problem intractable. Romeijn *et al.* [3] propose that, in

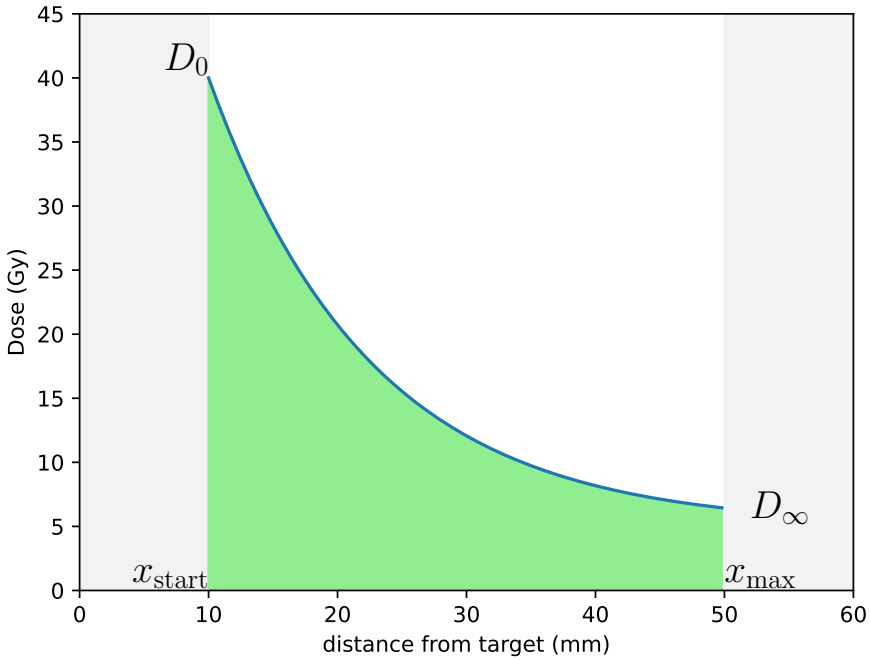

Figure 5–4: Example of $D_{\text{NTO}}(x)$ with user parameters $x_{\text{start}} = 10$ mm, $x_{\text{max}} = 50$ mm, $D_0 = 40$ Gy, $D_\infty = 5$ Gy and $k = 0.08$ mm^{-1}. Voxels located in the gray region or with doses in the green region would not be imposed an NTO price.

practice, only a small fraction of apertures would actually be relevant to the optimal solution. Following this idea, the column generation approach consists of dividing the problem into 2 steps that are repeated iteratively:

1. solving a restricted version of the global problem, called the Restricted Master Problem (RMP), where only a set of accepted "good" apertures are evaluated,
2. solving a pricing problem (PP) where we search for the next best aperture to add to our current set of accepted apertures.

To illustrate this method, let us consider an iteration of the optimization of an MBRT plan in Fig. 5–5. In part 1, we start with a set K of "good" apertures that we are evaluating in our RMP. In this example, we have 6 apertures, one for each energy that we are considering with MBRT, that can be used to minimize the cost function $F(D)$. For each aperture k, each open grid element can be understood to allow for radiation to cross and eventually reach

the patient. The dose distribution due to each such open grid element is what constitutes a beamlet as previously defined. By summing up the beamlets over all open grid elements of k, we thus obtain the dose distribution D_k in the patient due to aperture k. The total dose D of the MBRT plan would then be composed of the weighted sum of the dose of each aperture $k \in K$:

$$D = \sum_{k}^{|K|} D_k y_k, \tag{5.5}$$

where y_k represents the weight of aperture k. Solving the RMP consists of optimizing y_k such that the total MBRT dose D minimizes the price function $F(D)$. On `brems`, this step is performed by using the Interior-Point Optimizer (Ipopt) library. For the example of Fig. 5–5, the optimal y_k at this iteration consisted of assigning 100% of the weight to the 6 MV aperture, leading to a price $F(D)$ of 5467.85 for the current iteration.

In part 2 of Fig. 5–5, we must now solve the PP to find the next "best" aperture to add to our bank of accepted apertures K. Romeijn *et al.* [3] show that the likelihood of an aperture $k \notin K$ to improve our price is dictated by the value of:

$$\rho_k = \sum_{v}^{|V|} D_{k,v} \frac{\partial F}{\partial D_v}, \tag{5.6}$$

where $D_{k,v}$ and D_v are the doses to a voxel v due to aperture k and due to the weighted sum of apertures in K, respectively. ρ_k can be understood as a measure of the change to the price function incurred from adding $k \notin K$ to K. By evaluating ρ_k for all apertures $k \notin K$, the next "best" aperture can be identified as the one with the lowest ρ_k. Only apertures satisfying:

$$\rho_k < 0, \tag{5.7}$$

can be possible candidates. If no aperture $k \notin K$ meets this constraint, then no other apertures can be added to K to further reduce the price function and we have reached the optimal solution.

Multiple possible candidates can exist at each iteration of the PP and multiple such candidate apertures can be added at once to K. In the context of MBRT optimization, Renaud *et al.* [1] describe four aperture addition schemes, where the next "best" apertures to be added to K were chosen according to differing criteria. In their "best per modality" scheme, the aperture with the lowest ρ_k for each modality is added, if viable. This is the addition scheme that was used in the example of Fig. 5–5. For this iteration, only 4 apertures were added as no viable aperture candidates satisfying Eq. 5.7 were found for the 6 MeV and 9 MeV electron modalities. In part 3, these 4 apertures are then added to the K accepted apertures and the RMP is re-solved to obtain new aperture weights y_k and therefore a new price $F(D)$. This iterative process is repeated until no viable candidate can be found during the PP or until the price function $F(D)$ has been deemed to have converged.

In practice, many apertures that get added early on during the optimization are no longer deemed useful in later iterations: they are repeatedly assigned $y_k \approx 0$ weight during the RMP. These apertures are pruned from K after each RMP iteration. A larger overall number of apertures will also increase the delivery time of a treatment plan. A treatment planner may therefore want to assign a maximum number of apertures allowed in a plan. On `brems`, when the maximum of number of apertures is reached, we prune the n apertures with the lowest weight, where n is the maximum number of candidate apertures that can be added to K per iteration according to the addition scheme.

In the case of robust optimization, with the stochastic programming approach, a cost function F_s can be evaluated for each positioning scenario s using only the beamlets specifically calculated for that scenario. F_s would therefore be the value of the cost function if a given setup error represented by the scenario s were to occur. The total cost function to be minimized is then the weighted-average of the scenario cost:

$$F = \sum_s \omega_s F_s, \tag{5.8}$$

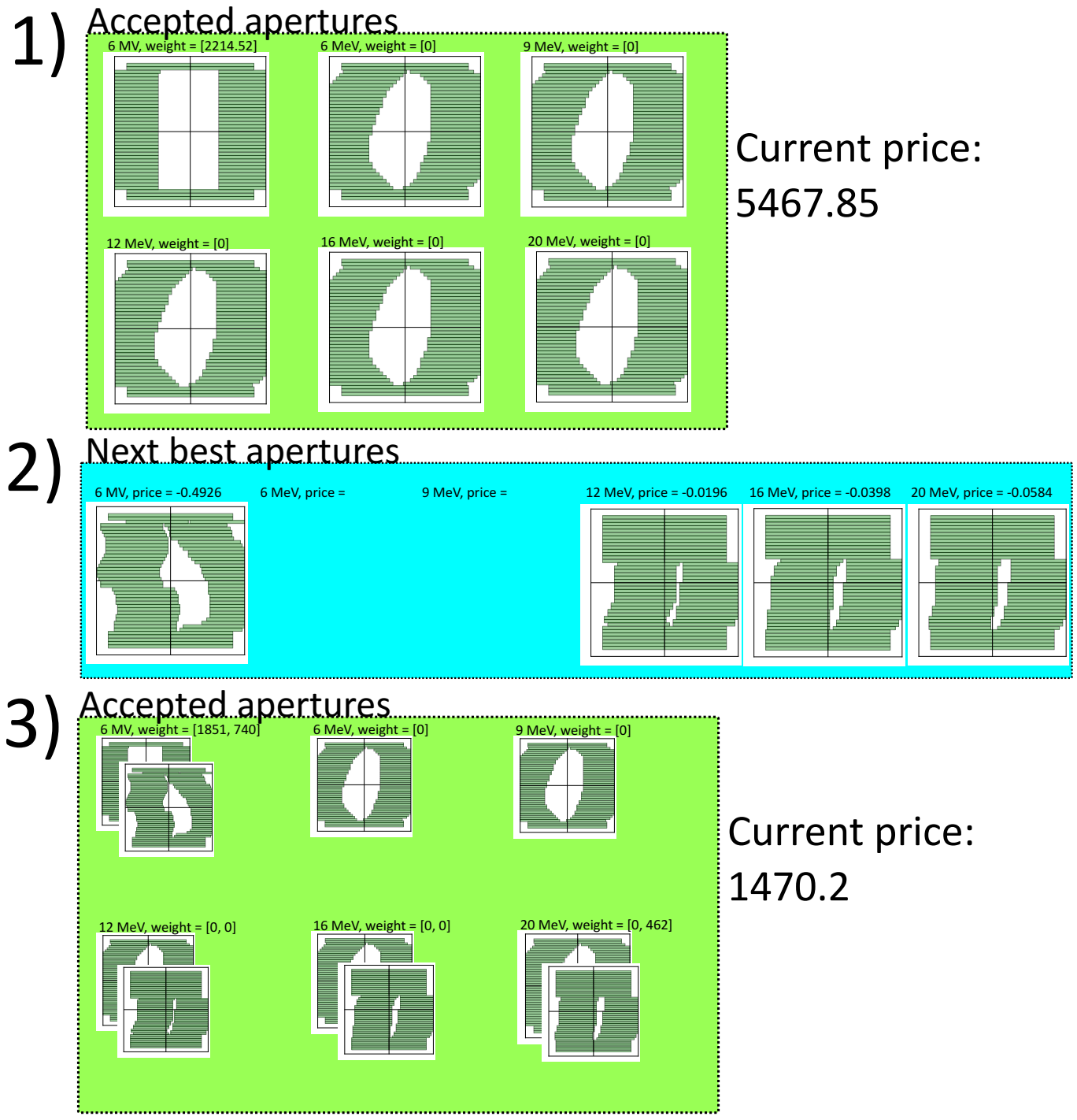

Figure 5–5: Example of an iteration of the column generation optimization as applied for an MBRT plan.

where ω_s are scenario weights pre-assigned by the treatment planner. For all setup-robust optimization presented in this thesis, ω_s was chosen to be constant, such that all scenarios were equally weighted.

Plan normalization

Once an optimal treatment plan is found, it is defined by its set of optimal apertures k at their corresponding control points and their associated weights y_k. The total patient dose distribution due to this plan is given by Eq. 5.5. In clinical practice, doses to be delivered to the tumor are commonly prescribed to a dose metric associated with the target volume. One common prescription scheme is to require that 95% of the PTV is covered by the prescription dose:

$$D95\%_{\mathrm{PTV}} = D_{\mathrm{PD}}. \tag{5.9}$$

Although the optimizer will provide a plan that best meets the cost function, there is no guarantee that the resulting dose distribution will exactly agree with the target's prescription scheme. We must therefore perform a normalization step by applying a uniform multiplicative factor α to all y_k. In the case of a prescription to 95% of the PTV, we would multiply all aperture weights by:

$$\alpha = D_{\mathrm{PD}}/D95\%_{\mathrm{PTV}}. \tag{5.10}$$

Doing so would result in Eq. 5.9 to be exactly met by the plan.

5.1.5 Plan evaluation

The plan is then ready for evaluation. The planner must decide if the quality of the optimized plan is suitable or if further improvements could be achieved by changing the optimization constraints. To do so, they must analyze the dose distribution and the relevant dose metrics to target structures and OAR. Dose-Volume Histogram (DVH) plots are a particularly effective tool as they provide the planner with an overall outlook on the dose to each structures. The cumulative DVH plot is a reverse cumulative histogram of dose absorbed by a structure of interest, where the frequency of a dose bin is normalized by the total volume

of the structure. As such, a point on a DVH plot describes the percentage of volume of a structure (y-coordinate) receiving at least a dose (x-axis). An example of a DVH graph is plotted in the top-right quadrant of Fig. 5–2.

Nevertheless, evaluating the quality of a plan is a complex process that heavily relies on the experience of the planner. Although there are clear guidelines on tolerance doses to OARs or on the homogeneity of doses within the target, it is not always clear how one values improvements in doses to one OAR at the expense of another. Furthermore, the achievable doses to each OAR is heavily dependent on the position of the tumor and the patient's geometry, and is therefore substantially different from case to case. These are aspects that must be considered by the planner at this stage and then translated in mathematical terms to the optimizer via changes in the optimization constraints. In practice, this is often an iterative process of trial-and-error. The planner's experience is essential in being able to gauge how much more improvements in plan quality can be potentially achieved from further tweaking the constraints.

5.1.6 Aperture recalculation

Once the final plan has been decided by the planner, `brems` requires an aperture recalculation step. At the beamlet optimization stage, the patient dose distribution due to each aperture is approximated by summing up their beamlet contributions. However, these beamlets were calculated without properly modelling for the presence of the MLC. This induces potential errors in the estimation of the dose in the penumbra region and in the leakage of particles through closed leaves. To correct these inaccuracies, the patient dose distribution due to each optimal apertures are independently recalculated with Monte Carlo methods using the DOSXYZnrc user-code of EGSnrc, including a full model of the exact geometry and positions of each MLC leaves. A dose distribution is thus obtained for each aperture of the plan.

5.1.7 Aperture weight re-optimization

As the Monte Carlo-recalculated aperture doses can differ from their summed beamlet dose estimation, the weights y_k previously optimized are no longer applicable. We must therefore re-optimize these weights with respect to the cost function. This is essentially performing the RMP step of the column generation algorithm one last time, but using the newly Monte Carlo-calculated aperture doses rather than the beamlets.

5.1.8 Full Monte Carlo recalculation

Finally, a full Monte Carlo dose of the plan as a whole can be recalculated in a single DOSXYZnrc calculation. In most cases, this dose distribution will exactly match the doses obtained from performing the weighted-sum of aperture doses in the previous section. However, this is not the case for continuously rotating gantry deliveries such as VMAT. For these techniques, at the optimization stage, the apertures are approximated to be delivered statically at fixed gantry angles. As such, a continuous 360° arc delivery could be approximated, purely at the optimization stage, as step-and-shoot deliveries from discrete beam angles at every 2° intervals. This introduces some discrepancies in the patient dose distribution between the statically optimized plan and the continuously delivered plan. To reconcile this difference, a full Monte Carlo recalculation of the plan with proper simulation of continuous arc deliveries is possible with DOSXYZnrc. This is the final step of the treatment planning process on `brems`. As no re-optimization of the aperture weights occurs at this point, for plans with continuous arc deliveries, the final Monte Carlo recalculation can result in a worsened plan quality. This is dictated by the extent to which apertures vary from one adjacent gantry angle to another. The planner must judge whether this degradation in plan quality remains acceptable. Otherwise, the plan must be re-optimized with a finer discretization of gantry angles (e.g. 1°) or stricter restriction on MLC leaf motion. If the final Monte Carlo-recalculated dose is accepted by the planner, the plan can be then be exported in `.dcm` or `.xml` format to be delivered by the linac.

5.2 Precalculated Monte Carlo for electron beamlet calculation

5.2.1 Electron transport based on pre-calculated tracks

Beamlet calculations for treatment plan optimizations are extremely computationally expensive. To calculate robust electron beamlets for MBRT treatment planning, Renaud *et al.* [4] used the Monte Carlo EGSnrc code, which required calculation times on the order of a week for all beamlets required in a typical plan, using a cluster of ∼160 CPUs. Although many analytical techniques have been developed for fast dose calculation of photon doses, this has not been the case for electron doses due to their erratic scattering. State-of-the-art TPSs rely on fast implementations of the Monte Carlo method through usage of pre-calculated data [5], [6] or simplification of electron interactions [7]. One such implementation of a fast Monte Carlo dose calculation algorithm was the Pre-calculated Monte Carlo (PMC) code first published by Jabbari *et al.* in 2009 [8]. The core idea of this technique was that the stochastic trajectory of an electron and of its secondary particles could be pre-sampled ahead of time and then used as look-ups at run time. Using the established EGSnrc Monte Carlo code, electrons were generated in an identical initial direction and energy and transported through a homogeneous medium of interest. For each electron, in pre-determined step sizes, the position, direction and energy would be recorded until the electron reached a minimum threshold energy, called the cut-off energy. Any events along its path that set in motion a new particle such as secondary electrons or bremsstrahlung photons were also recorded. The compilation of these step information and events constitute an electron track. A sufficiently high number of these tracks were generated and stored in a so-called track bank for each medium and at differing energy intervals such as to cover the whole energy range of clinical electron beams. At run time, to transport an electron, a track is randomly selected at a suitable initial energy and used to transport the electron step by step through raytracing. Any secondary particles created along the track is added to a stack to be transported subsequently. The dose deposited is assumed to be uniform along an electron step. If an electron travels a pathlength r_v within a voxel v, then the dose deposited to the

voxel e_{dep}, v can be calculated as:

$$e_{\text{dep}}, v = e_{\text{dep}} \frac{r_v}{r}, \tag{5.11}$$

where r is the total length of the step of the electron track along which the electron travelled through v and e_{dep} is the total energy deposition along that step. A linear scaling is acceptable since the mass stopping power varies only modestly as a function of electron energy, except near the track-end. As the electron is assumed to be going in a straight time along each step, a larger step size induces a larger error in the location of the dose deposition. However, smaller step sizes result in larger track bank sizes which must fit within the Random-access memory (RAM) at run time.

Although the generation of a track bank is carried out with EGSnrc, this time-consuming step is only performed once, ahead of time, and is independent of the treatment machine or the patient geometry. The time spent during this step can therefore be ignored for practical timing comparison. This method provides a significant speed-up compared to conventional Monte Carlo methods as no costly interaction sampling needs to be performed during run time. The only significant computation time stems from raytracing the electron voxel-by-voxel along the pre-calculated steps. Jabbari *et al.* observed speedups by a factor of 40 with PMC compared to EGSnrc calculations with dose discrepancies on the order of 2%. In 2015, Renaud *et al.* [9] published a GPU-implementation of the PMC technique which handled both electron and proton transport. They also quantified the uncertainty induced from the finite-size of the track bank as a latent uncertainty on PMC dose calculations. A second component of the PMC dose uncertainty is due to the statistical uncertainty arising from the finite number particles simulated at run time. While the latter can be reduced by increasing running more histories, the former is constant for a pre-generated track bank. If a PMC calculation is performed at high sufficiently histories N such that the statistical uncertainty can be ignored, then the latent uncertainty σ_L can be estimated as the root mean square

deviation of local residuals between PMC doses D^{PMC} and benchmark doses D^b, calculated using a conventional Monte Carlo code such as EGSnrc:

$$\sigma_L = \lim_{N\to\infty} \sqrt{\frac{1}{V}\sum_{v}^{V}\left(\frac{D_v^{\text{PMC}} - D_v^b}{D_v^b}\right)^2}, \quad [1] \tag{5.12}$$

where the summation is performed over all voxels $v \in V$. Voxels with doses lower than 20% of the maximum recorded dose are ignored.

With the rapid performance improvements of GPU cards in recent years, the speedups achievable by running PMC on GPU compared to conventional Monte Carlo code running on Central Processing Unit (CPU) at similar price points has dramatically increased. This made PMC an appealing technique for a faster electron beamlet dose calculation.

5.2.2 Photon transport

Although the PMC code has been validated to provide accurate electron dose calculations when compared with EGSnrc by Renaud *et al.* [9], it was done without accounting for photon transport. However, in megavoltage external electron beam, bremsstrahlung photons and contamination photons generated in the gantry head account for a significant portion of the patient dose and must be corrected for. Therefore, to be adequate for beamlet calculations, a photon transport method was added to the PMC code. Bremsstrahlung photon creation events in electron tracks were recorded at pre-generation time in EGSnrc. During live calculations, each GPU thread loads up a particle from a phase space source file. If the particle is an electron, it is transported according to its track data until they either reach E<`ecut` or cross to a different medium. For all calculations presented in this paper, an electron total energy cutoff of `ecut`=0.7 MeV was used. If secondary electrons or bremsstrahlung photons are generated along the track, they are added to a stack of particles for the thread to transport subsequently. For photon transport, a method similar to the one used in the EGS4

[1] The $\frac{1}{V}$ factor was incorrectly written as $\frac{1}{N}$ in [9].

report [10] and by Fippel [11] is applied. The mass attenuation coefficient for photoeletric, Compton and pair production interactions in water are obtained from NIST [12] and are initialized on the GPU as texture objects. For each photon of energy E, its corresponding total mass attenuation coefficient $\mu(E)/\rho$ is fetched from the texture objects based on its energy E. Let $z(E)$ be the distance to be travelled by a photon. The probability that a photon interaction occurs within this distance $z(E)$ can be written as:

$$P(z(E)) = 1 - e^{-\mu(E)z(E)}. \tag{5.13}$$

Using the direct sampling method, we let $P(z(E))$ be represented by a random number ξ uniformly distributed between 0 and 1 (but cannot be zero). By inverting Eq. 5.13, we obtain:

$$z(E) = -\frac{1}{\mu(E)} \ln(1 - \xi). \tag{5.14}$$

As $1 - \xi$ is also uniform between 0 and 1 for $\xi \in (0, 1)$, the distance $z(E)$ to be travelled by the photon before an interaction occurs can then be sampled as:

$$z(E) = -\frac{1}{\frac{\mu(E)}{\rho}\rho} \ln(\xi'), \tag{5.15}$$

where ξ' is a random number uniformly distributed between 0 and 1. The photon is then ray-traced from voxel to voxel by accounting for each voxel's density ρ until the distance $z(E)$ has been fully travelled. Photons are transported as long as their energy is higher than `pcut`=0.01 MeV and while they remain within the phantom geometry. Photons below the cutoff energy `pcut` are forced to deposit all their energy in the voxel they are found in. Once the photon has travelled the full distance $z(E)$, one of the three interaction types is sampled from the interaction-specific mass attenuation coefficients.

For photoelectric effect, a secondary electron is generated with the same kinetic energy and direction as the initial photon, thereby ignoring binding effects.

If a Compton interaction occurs, the inital photon of energy k_0 interacts with an atomically bound electron to result in a secondary scattered photon of energy k at a scattering angle θ and a scattered electron of energy E_e. Rewriting Eq. 2.7, we have:

$$k = \frac{k_0}{1 + (1 - \cos\theta)k/m}, \tag{5.16}$$

where m is the electron rest mass energy. The ratio of the energy of the scattered photon to the initial photon $\epsilon \equiv k/k_0$ is sampled according to the method described in the EGSnrc manual [13]. The maximum and minimum values for ϵ can be calculated to be $\epsilon_{\max} = 1$ and $\epsilon_{\min} = \frac{1}{1+2k/m}$. Starting from a probability density function for ϵ similar to one written in the EGSnrc manual, we have:

$$P_1(\epsilon) = N\left(\alpha_1(\frac{1}{\epsilon\alpha_1}) + \alpha_2(\frac{\epsilon}{\alpha_2})\right)\left[1 - \frac{\epsilon\sin^2\theta}{1+\epsilon^2}\right], \tag{5.17}$$

where $\alpha_1 \equiv \ln(1/\epsilon_{\min})$, $\alpha_2 \equiv \frac{1-\epsilon_{\min}^2}{2}$ and N is a normalization constant. This is in the form $f(\epsilon) = \sum_{i=1}^{2}\alpha_i f_i(\epsilon)g(\epsilon)$, where $f_1(\epsilon) = \frac{1}{\epsilon\alpha_1}$, $f_2(\epsilon) = \frac{\epsilon}{\alpha_2}$ and $g(\epsilon) = 1 - \frac{\epsilon\sin^2\theta}{1+\epsilon^2}$. This is the correct form to apply mixed sampling method described in the EGS4 manual [10], :

1. we sample 3 random numbers $R1$, $R2$ and $R3$ uniformly distributed between 0 and 1
2. if $R1 < \frac{\alpha_1}{\alpha_1+\alpha_2}$:

   we sample ϵ using f_1

$$R2 = \int_{\epsilon_{\min}}^{\epsilon} f_1(\epsilon)d\epsilon \tag{5.18}$$

$$\epsilon = \epsilon_{\min}e^{\alpha_1 R2} \tag{5.19}$$

   else:

   we sample ϵ using f_2

$$R2 = \int_{\epsilon_{\min}}^{\epsilon} f_2(\epsilon)d\epsilon \tag{5.20}$$

$$\epsilon = \sqrt{\epsilon_{\min}^2 + 2R_2\alpha_2} \tag{5.21}$$

3. we calculate the rejection function $g(\epsilon)$ using the ϵ we just sampled. $\sin^2\theta$ is calculated by solving Eq. 5.16 for $\cos\theta$ and using $\sin^2\theta = (1-\cos\theta)(1+\cos\theta)$
4. if $R3 > g(\epsilon)$:

   loop back to step 1

   else:

   use ϵ and $\cos\theta$

Using ϵ and $\cos\theta$, the energy and in-plane scattering angles of the scattered photon and electron can be derived by enforcing energy and momentum conservation. The electron azimuthal angle is sampled uniformly over 2π and the opposite angle is assigned to the scattered photon.

For pair production, the energies of the resulting positron and electron are sampled using the rejection sampling algorithm described in EGSnrc [13]. The derivation and details of the sampling and rejection functions will not be reproduced here for brevity[2] . The secondary particles angles are assigned using the EGS4 approach with $\theta_\pm = m/k$ where m is the mass of an electron and k is the photon energy. The electron azimuthal angle ϕ_+ is sampled uniformly over 2π, while the positron azimuthal angle is chosen to be the opposite of the former. For simplicity, positrons are assigned the same particle type as electrons and are handled as such.

Each thread is responsible for transporting one particle sampled from the initial source. Any ensuing secondary particle is appended to the thread's stack of particles and transported subsequently. For radiotherapy applications, all body tissue is treated as density scaled water. However, as the initial particle source must be transported from outside the patient body, the PMC code must also handle transporting particles in air. For electrons,

[2] We note that the rejection functions $A(\delta)$ and $B(\delta)$ had a typo in their definition (Eq. 2.1.11 of the EGSnrc manual): Z_V should be replaced by Z_V/Z_{eff}^2 as correctly implemented in the EGSnrc source code.

the tracks are pre-generated in air with a larger maximum step size of 1 cm and lower history of 4000 tracks per energy. This is in contrast to tracks in water being generated with a maximum step size of 0.5 mm and with 40,000 tracks per energy [9]. This reduces the memory size of the air track bank such that it can be loaded onto the GPU simultaneously. If an electron is found to be outside the patient geometry (i.e. in air), the track segment is first verified to intersect the patient's bounding box [14] before performing more costly voxel-to-voxel raytracing. Any particle found to exit the phantom geometry is immediately discarded.

For beamlet generation, at each energy, a Varian-provided phase space file is transported through a TrueBeam model in BeamNRC to generate an intermediate phase space file at the MLC plane. The intermediate phase space is then further divided into 1080 sub-phase space files by binning particles into a regular square grid. Each sub-phase space file thus consists of particles found in a square area at the MLC plane that projects to 1×1 cm^2 at isocenter. Each beamlet is thus calculated by using its corresponding sub-phase space file as its particle source.

Validation and benchmarking

To validate the accuracy of PMC dose calculations, percentage depth dose (PDD) curves were calculated for 5 electron energies (6, 9, 12, 16, and 20 MeV) in a homogeneous water slab of dimension $25.6 \times 25.6 \times 25.6$ cm^3. A profile curve is also traced at a depth of 1.5 cm. For each energy, one such aforementioned sub-phase space file was used as the particle source. The calculations are compared to Monte Carlo calculations using the same sub-phase space files as particle sources on EGSnrc. The latent uncertainty is estimated by using the formalism presented by Renaud *et al.* [9]. All simulations are configured such that the water phantom is located at 100 cm source-to-surface distance (SSD). The same phantom file (`.egsphant`) is used for both calculation methods. For reference, a PMC calculation without photon transport is also included.

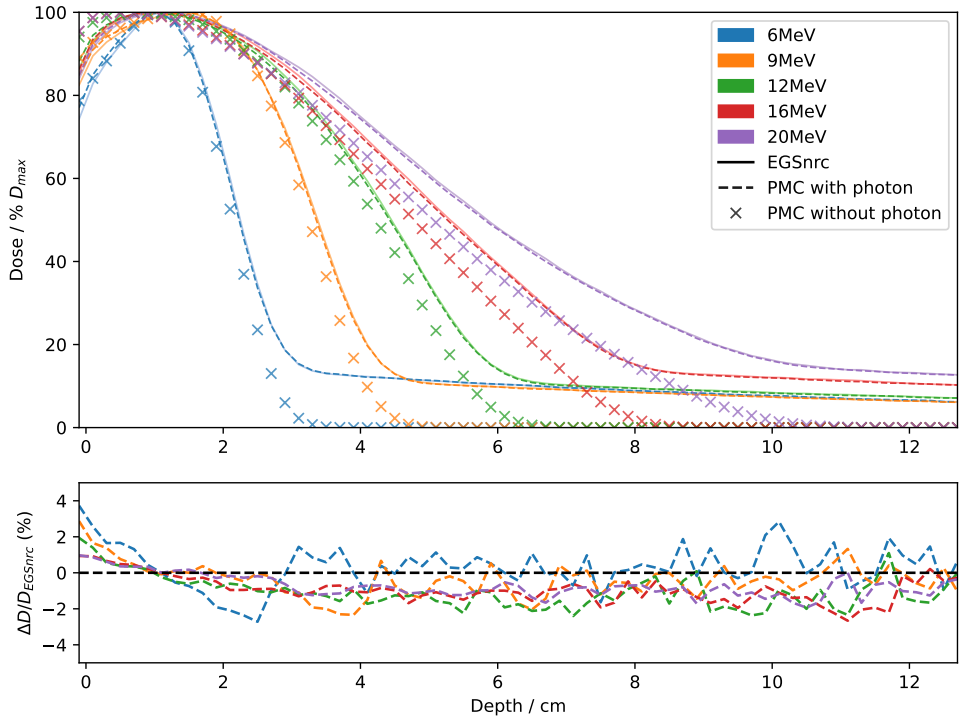

Figure 5–6: Validation of PMC calculation of beamlets' PDD against EGSnrc in a homogeneous water slab. Both EGSnrc and PMC type-A uncertainties are below 0.2% in voxels receiving at least 50% of the maximum dose. The PMC dose as calculated without photon transport is included for comparison. Local residuals are plotted for the PMC dose with photon transport. Error bars were omitted for clarity as the type-A uncertainties are too small to be visually rendered.

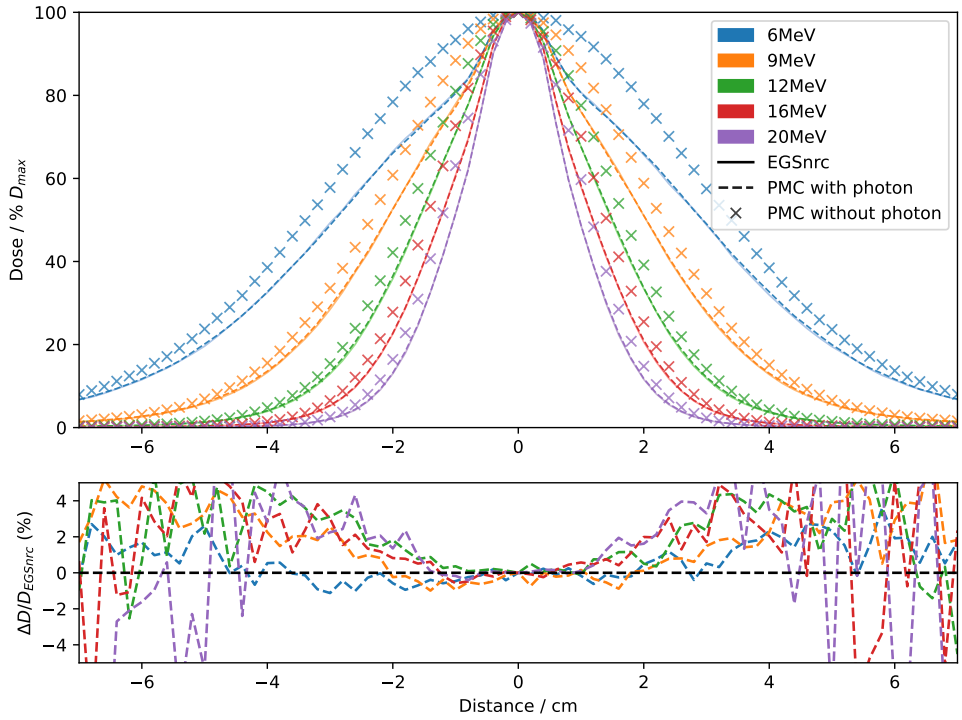

Figure 5–7: Validation of PMC calculation beamlets' profile against EGSnrc in a homogeneous water slab at 1.5 cm depth. Both EGSnrc and PMC type-A uncertainties are below 0.2% in voxels receiving at least 50% of the maximum dose. The PMC dose as calculated without photon transport is included for comparison. Local residuals are plotted for the PMC dose with photon transport. Error bars were omitted for clarity as the type-A uncertainties are too small to be visually rendered.

Both the PDD (Fig. 5–6) and off-axis profile (Fig. 5–7) plots showed excellent agreement between PMC and EGSnrc. Sufficient histories were used with both calculation methods to reach a type-A uncertainty of less than 0.2% on voxels receiving at least 50% of the maximum dose. The latent uncertainty as averaged over the 5 electron beamlet energies was 1.3% as evaluated in voxels receiving at least 20% of the maximum dose [9]. The handling of photon transport in PMC was critical in the rapid dose falloff region and in the bremsstrahlung tail of electron beamlet PDDs. [3] The total GPU memory usage was around 10 GB, mainly due to the track bank size.

The computation time for a beamlet calculation to a type-A uncertainty of 1% was recorded with PMC on 1 NVIDIA TitanRTX GPU and compared to the same calculation with EGSnrc on both 1 CPU core and 160 CPU core[4] in Fig. 5–8. To reach the same type-A uncertainty for a 12 MeV beamlet calculation, PMC is more than 1800 times faster than EGSnrc on a single CPU. Even when compared to our small computer cluster, PMC calculations on a single commercially available GPU outperforms EGSnrc by over a factor of 10. This speed-up in the electron beamlet computation time is crucial for the clinical translation of MBRT. Indeed, for robust optimization, beamlets must be calculated in each robust scenario, at each control points, and at each electron energy. For a typical MBRT

[3] The bremsstrahlung tail in Fig. 5–6 is significantly more pronounced than in conventional uncollimated electron PDDs. This is because a beamlet only accounts for particles at the MLC plane that would be projected to its 1×1 cm^2 grid square. For a beamlet on central axis, this includes the large majority of all contamination photons that will contribute towards the central axis bremsstrahlung tail dose. This is different from the maximum dose region, where, due to their lateral scattering in air and water, a significant contribution from off-axis electrons is not accounted for. This results in a larger bremsstrahlung tail relative to the maximum beamlet dose.

[4] This is the total amount of CPU cores available on the Medical Physics Unit's computer cluster. This consists of: 2x Intel Xeon CPU E5-2697, 2x Intel Xeon CPU E5-2687, 1 Intel Xeon Gold 6140 and 1 Intel Xeon Gold 5220.

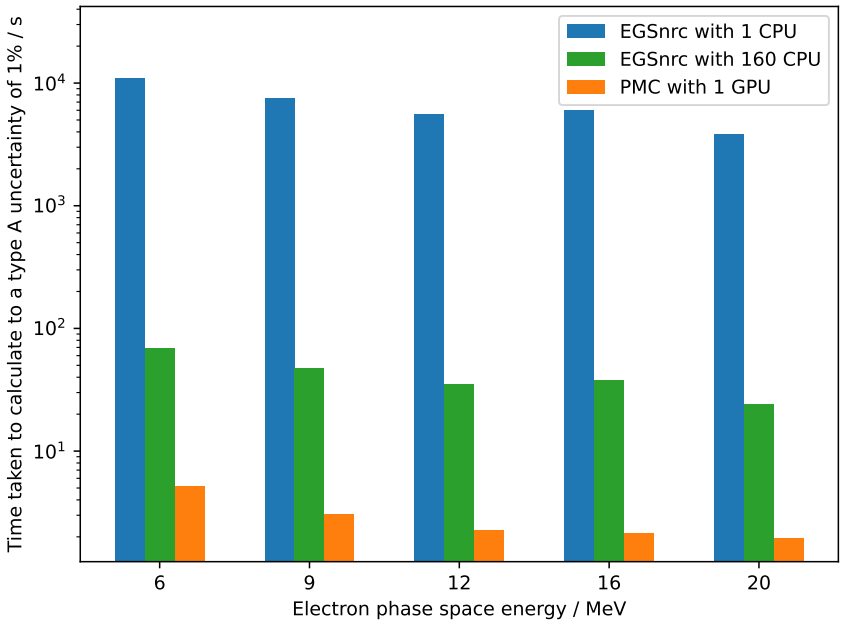

Figure 5–8: Comparison of time taken to calculate to 1% type-A uncertainty by EGSnrc and PMC. For a more practical comparison, the calculation time when using our entire CPU cluster is also included.

plan, this can total to over 30 000 beamlets. With EGSnrc, this beamlet calculation step took on the order of 1 week to compute while PMC does it on the order of 1 day. Furthermore, as consumer GPUs are much more affordable than computer clusters with hundreds of CPU cores, PMC allows for a wider and more accessible implementation of MBRT in the clinic.

REFERENCES

[1] M.-A. Renaud, M. Serban, and J. Seuntjens, "On mixed electron-photon radiation therapy optimization using the column generation approach," *Medical Physics*, vol. 44, no. 8, pp. 4287–4298, 2017. DOI: 10.1002/mp.12338.

[2] S. Breedveld, B. van den Berg, and B. Heijmen, "An interior-point implementation developed and tuned for radiation therapy treatment planning," *Computational Optimization and Applications*, vol. 68, no. 2, pp. 209–242, 2017. DOI: 10.1007/s10589-017-9919-4.

[3] H. E. Romeijn, R. K. Ahuja, J. F. Dempsey, and A. Kumar, "A column generation approach to radiation therapy treatment planning using aperture modulation," *SIAM Journal on Optimization*, vol. 15, no. 3, pp. 838–862, 2005. DOI: 10.1137/040606612.

[4] M.-A. Renaud, M. Serban, and J. Seuntjens, "Robust mixed electron-photon radiation therapy optimisation," *Medical Physics*, vol. 0, no. ja, 2019. DOI: 10.1002/mp.13381.

[5] H. Neuenschwander, T. R. Mackie, and P. J. Reckwerdt, "Mmc-a high-performance monte carlo code for electron beam treatment planning," *Physics in Medicine & Biology*, vol. 40, no. 4, p. 543, Apr. 1995. DOI: 10.1088/0031-9155/40/4/005.

[6] P. J. Keall and P. W. Hoban, "Super-monte carlo: A 3-d electron beam dose calculation algorithm," *Medical Physics*, vol. 23, no. 12, pp. 2023–2034, 1996. DOI: https://doi.org/10.1118/1.597842.

[7] I. Kawrakow, "Vmc++, electron and photon monte carlo calculations optimized for radiation treatment planning," in *Advanced Monte Carlo for Radiation Physics, Particle Transport Simulation and Applications*, A. Kling, F. J. C. Barão, M. Nakagawa, L. Távora, and P. Vaz, Eds., Berlin, Heidelberg: Springer Berlin Heidelberg, 2001, pp. 229–236.

[8] K. Jabbari, P. Keall, and J. Seuntjens, "Considerations and limitations of fast Monte Carlo electron transport in radiation therapy based on precalculated data," *Medical Physics*, vol. 36, no. 2, p. 530, 2009. DOI: 10.1118/1.3058480.

[9] M. A. Renaud, D. Roberge, and J. Seuntjens, "Latent uncertainties of the precalculated track Monte Carlo method," *Medical Physics*, vol. 42, no. 1, pp. 479–490, 2015. DOI: 10.1118/1.4903502.

[10] W. R. Nelson, H. Hirayama, and D. W. Rogers, "Egs4 code system," Dec. 1985.

[11] M. Fippel, "Fast monte carlo dose calculation for photon beams based on the vmc electron algorithm," *Medical Physics*, vol. 26, no. 8, pp. 1466–1475, 1999. DOI: https://doi.org/10.1118/1.598676.

[12] J. Hubbell and S. Seltzer, *Tables of x-ray mass attenuation coefficients and mass energy-absorption coefficients 1 kev to 20 mev for elements z = 1 to 92 and 48 additional substances of dosimetric interest*, en, 1995-01-01 1995.

[13] I. Kawrakow, D. Rogers, E. Mainegra-Hing, *et al.*, *Egsnrc toolkit for monte carlo simulation of ionizing radiation transport*, doi:10.4224/40001303 [release v2021], 2000.

[14] A. Williams, S. Barrus, R. K. Morley, and P. Shirley, "An efficient and robust ray-box intersection algorithm," *Journal of Graphics Tools*, vol. 10, no. 1, pp. 49–54, 2005. DOI: 10.1080/2151237X.2005.10129188.

CHAPTER 6
Ion chamber and film-based quality assurance of mixed electron-photon radiation therapy

Veng Jean Heng, Monica Serban, Jan Seuntjens, Marc-André Renaud

Article published in: *Medical Physics, 2021.* (https://doi.org/10.1002/mp.15081)

6.1 Preface

As a framework has been established for efficient treatment planning of robust MBRT plans, we now focus on verifying that the dose calculated by our TPS is representative of the dose being delivered by the linac. Quality assurance of EBRT deliveries is crucial in ensuring the safety and accuracy of patient treatments. To do so, we validate that the calculated dose of MBRT plans to a detector matches the dose measured by the detector. Ion chambers provide a method for absolute point dose measurement while radiochromic film can be used to measure doses on a plane. However, ion chamber dose measurements in electron field are challenging due to the dependence of their response to the beam quality. In this chapter, we propose a method to correct for the differing beam quality in the measurement condition of MBRT fields while validating the delivery of MBRT plans on 2 different phantoms.

6.2 Abstract

Purpose: In previous work, we demonstrated that mixed electron-photon radiation therapy (MBRT) produces treatment plans with improved normal tissue sparing and similar target coverage, when compared to photon-only plans. The purpose of this work was to validate the MBRT delivery process on a Varian TrueBeam accelerator and laying the groundwork for a patient-specific quality assurance (QA) protocol based on ion chamber point measurements and 2D film measurements.

Methods: MC beam models used to calculate the MBRT dose distributions of each modality (photons/electrons) were validated with a single-angle beam MBRT treatment plan

delivered on a slab of Solid Water phantom with a film positioned at a depth of 2 cm. The measured film absorbed dose was compared to the calculated dose.

To validate clinical deliveries, a polymethyl methacrylate (PMMA) cylinder was machined and holes were made to fit an ionisation chamber. A complex MBRT plan involving a photon arc and three electron delivery angles was created with the aim of reproducing a clinically realistic dose distribution in typical soft tissue sarcoma tumours of the extremities. The treatment plan was delivered on the PMMA cylinder. Point measurements were taken with an Exradin A1SL chamber at 2 nominal depths: 1.4 cm and 2.1 cm. The plan was also delivered on a second identical phantom with an insert at 2 cm depth, where a film was placed.

An existing EGSnrc user-code, SPRRZnrc, was modified to calculate stopping power ratios between any materials in the same voxelised geometry used for dose calculation purposes. This modified code, called SPRXYZnrc, was used to calculate a correction factor, k_{MBRT}, accounting for the differences in electron fluence spectrum at the measurement point compared to that at reference conditions. The uncertainty associated with neglecting potential ionisation chamber fluence perturbation correction factors using this approach was estimated.

Results: The film measurement from the Solid Water phantom treatment plan was in good agreement with the simulated dose distribution, with a gamma pass rate of 96.1% for a 3%/2 mm criteria. For the PMMA phantom delivery, for the same gamma criteria, the pass rate was 97.3%. The ion chamber measurements of the total delivered dose agreed with the MC-simulated dose within 2.1%. The beam quality correction factors amounted to, at most, a 4% correction on the ion chamber measurement. However, individual contribution of low electron energies proved difficult to precisely measure due to their steep dose gradients, with disagreements of up to 28% $\pm$ 15% at 2.1 cm depth (6 MeV). Ion chamber measurement procedure of electron beams was achieved in less than 5 minutes, and the entire validation process including phantom setup was performed in less than 30 minutes.

Conclusion: The agreement between measured and simulated MBRT doses indicates that the dose distributions obtained from the MBRT treatment planning algorithm are realistically achievable. The SPRXYZnrc MC code allowed for convenient calculations of k_{MBRT} simultaneously with the dose distributions, laying the groundwork for patient-specific QA protocol practical for clinical use. Further investigation is needed to establish the accuracy of our ionisation chamber correction factors k_{MBRT} calculations at low electron energies.

Running title: Ion chamber and film-based QA of MBRT

6.3 Introduction

The majority of patients undergoing external beam radiation therapy (EBRT) are treated with photons beams, while electron beams, despite being available in the medical linear accelerators, are only used in the treatment of a limited number of disease sites. All available photon and electron energies constitute modalities that could potentially be combined into a mixed beam (MBRT) plan to produce a superior treatment plan compared to single-energy, single-particle plans, provided that MBRT delivery is logistically feasible within the clinical workflow.

The modulated electron radiation therapy (MERT) literature has historically focused between studying MERT delivery using tertiary electron-specific collimators such as the eMLC [1]–[5] or the few-leaf electron collimator (FLEC) [6]–[8], and the approach of utilising the photon MLC (pMLC) already present in modern linacs [1], [9]–[12]. Early studies showed that a shortened source-to-surface distance (SSD), typically 70 cm, was necessary to produce clinically acceptable electron dose distributions due to the degradation of electron field penumbras in air [13]. Traditional electron RT remains cumbersome to deliver in comparison to photon RT, requiring custom patient-specific cut-outs and more time consuming setup. Despite the fact that MERT delivered using tertiary collimators has been shown to be accurate [8], MERT has seen limited adoption in the clinic due to time consuming tasks related to set-up and commissioning compared to conventional photon RT, and also due to

the high plan quality of modern intensity modulated (IMRT) and volumetric modulated arc therapy (VMAT) dose distributions.

However, there remains an important subset of patients with tumours with a superficial component that would benefit substantially from the limited range of electron radiation to spare organs at risk (OAR) downstream from the tumour. In recent years, there has been a renewed interest in pMLC-based MERT delivery in the context of mixed electron-photon beam treatments. Previous planning studies have shown that, while electron-only MERT treatment plans typically deliver lower doses to normal tissue compared to photon plans, they are unable to provide the same level of dose homogeneity within the target [12], [14]. On the other hand, pMLC-based MBRT plans have recently been shown to provide superior OAR sparing compared to IMRT or VMAT plans without sacrificing target coverage [15]–[18].

MBRT plans delivered using a pMLC as the sole collimation device would be the simplest to integrate into the clinical workflow as they do not, in principle, require staff intervention when switching modalities. Miguez et al. have demonstrated that pMLC-based MBRT for accelerated partial breast irradiation (APBI) can be implemented safely in the clinic. They also performed pre-treatment QA through ion chamber and film measurements on a hemispherical phantom. However, the treatment deliveries typically involved only three gantry angles and fewer than 10 fields. Furthermore, the method used to convert ion chamber readings to dose to water or dose to medium was not described [19]. Recently, Mueller et al. have delivered one brain and two head & neck MBRT plans with a non-coplanar photon component onto an anthropomorphic Alderson head phantom with films and shown 2%/2 mm gamma pass rates above 99.2% for all cases when compared to the expected simulated dose distribution [18], supporting the notion that MBRT using the pMLC can be delivered accurately. However, while the photon delivery was more complex than in the work of Miguez et al., the electron component remained simple, with one or two apertures per energy per beam angle. In addition, the delivered treatment plans did not contain low energy (6 or 9

MeV) components, which are likely to be the most challenging to model accurately. Due to their steep dose gradients, these low energies are also the most problematic for point measurements.

In this work, we present comparisons between simulated and measured MBRT dose distributions for a simple, inherently robust delivery and a complex delivery. The aim was to 1) validate that the MC beam model used to produce MBRT treatment plans could accurately determine the number of MUs necessary to produce a desired dose distribution from each modality, 2) present a methodology for calculating beam quality correction factors for ionisation chamber measurements in MERT and MBRT fields and 3) validate the accuracy of clinical MBRT deliveries using point measurements with an ionisation chamber and film dosimetry.

6.4 Methods

6.4.1 Reference dose measurements for MLC-defined electron fields

Reference dose calibration for the applicator-less electron beams was performed on a Varian TrueBeam linear accelerator using an IBA Blue Phantom 2 water tank and an Exradin A1SL ionisation chamber. The reference conditions were defined to be 80 cm source-to-surface distance (SSD), with the MLC leaves positioned to define a 10 x 10 cm^2 field when projected at the machine isocenter. This choice of non-standard reference conditions was made to closely align the reference conditions with the delivery conditions for the electron component of MBRT plans. Although shorter SSDs lead to better electron penumbras, typical MBRT plans have SSDs closer to 80 cm in order to provide safer gantry clearance. The jaws were set to 35 x 35 cm^2, which is slightly larger than the largest allowable MLC field for our MBRT planning algorithm. MLC leaves were restricted to a 30 cm field in their direction of motion due to their maximum leaf span of 15 cm. Reference dose measurements were performed at d_{ref} following the AAPM Task Group 51 (TG-51) protocol [20].

The charge measured in the ionisation chamber was converted to absorbed dose to water using equation 6.1,

$$D_{ref}(d_{ref}) = M_c \; k_{Q,ecal} \; k'_Q \; N^{Co}_{D,w} \tag{6.1}$$

where M_c is the ionisation chamber reading, corrected for environmental conditions, ion recombination and polarity, $k_{Q,ecal}$ and k'_Q are the beam quality conversion factors described in Muir et al., (2014) [21]. The A1SL $N^{Co}_{D,w}$ coefficient used in this work was traceable to national primary absorbed dose standards.

The conversion factors are similar to $k_{R_{50}}$ and k_{ecal} described in the TG-51 report [20] but explicitly take into account P_{gr}, the gradient correction for the ionisation chamber used in this work. The values for the beam quality conversion factors were obtained from the Monte Carlo work by Muir et al., (2014) [21]. While these conversion factors were calculated in standard reference conditions at 100 cm SSD rather than the reference conditions used in this work, they are specified in terms of R_{50} which we assume remains a faithful specification of the beam quality and, hence, electron fluence spectrum at the reference point for an 80 cm SSD setup.

6.4.2 Absorbed dose measurements in MBRT fields

Ionisation chambers are calibrated in terms of dose to water at the reference depth for a specific beam quality. The k'_Q beam quality correction factors used in eq. 6.1 are therefore only valid for the reference conditions described in section 6.4.1. When attempting to perform measurements in MBRT fields, we must correct the ionisation chamber response for the exact electron fluence spectrum at the point of measurement in the MBRT field, which can vary greatly from the electron fluence spectrum in reference conditions.

Differences in electron fluence spectrum can be caused by differences in measurement depth as well as by intensity modulation and delivery from multiple angles. The electron apertures for a given energy may not deliver radiation directly aimed at the measurement point, as shown in figure 6–1, leading to a potentially different electron fluence spectrum compared to reference conditions.

The beam quality conversion factor is defined as the ratio of the ratio of absorbed dose to water, D_w, to the absorbed dose in the air cavity of the ionisation chamber, D_{ch}, between a beam quality Q and cobalt-60,

$$k_Q = \left(\frac{D_w}{D_{ch}}\right)^{Q}_{Co}. \tag{6.2}$$

This ratio can be calculated with Monte Carlo methods assuming a fully characterised model of the ionisation chamber is included in the calculation [21]–[23]. In the methodology underlying AAPM's TG-51 protocol, however, this ratio was approximated as a ratio of Spencer-Attix stopping power ratios corrected for fluence perturbations,

$$k_Q \approx \frac{\left[\left(\frac{\bar{L}}{\rho}\right)^{water}_{air} P_{cel}P_{fl}P_{wall}P_{gr}\right]^{Q}}{\left[\left(\frac{\bar{L}}{\rho}\right)^{water}_{air} P_{cel}P_{fl}P_{wall}P_{gr}\right]^{Co}}, \tag{6.3}$$

where $\left(\frac{\bar{L}}{\rho}\right)^{w}_{air}$ is the Spencer-Attix stopping power ratio (SPR) between water and air [24]. In this work we followed the latter methodology to apply a conversion factor between the beam quality in reference condition and the MBRT fields,

$$k_{MBRT} = \left(\frac{D_w}{D_{ch}}\right)^{MBRT}_{Q}. \tag{6.4}$$

While an evaluation of eq. 6.4 requires a MC simulation of the local electron fluence with inclusion of the full chamber geometry, we assume that the first order contribution to k_{MBRT} is due to stopping power-ratio differences between water and air for the MBRT beam quality and the reference beam quality and sufficiently accurately corrects for the difference in chamber response between these two situations. This approximation ignores electron fluence *perturbation* by the presence of the ionisation chamber, but does capture the differences in energy response of the detector between reference conditions and MBRT conditions. A similar approach was used in the work by Al-Yahya et al. to successfully calibrate nonstandard electron fields created by the FLEC. [6]

$$k_{MBRT} \approx \frac{\left[\left(\frac{\bar{L}}{\rho}\right)^{w}_{air}\right]^{MBRT}}{\left[\left(\frac{\bar{L}}{\rho}\right)^{w}_{air}\right]^{Q}}. \tag{6.5}$$

With this correction factor, the dose measured by an ionisation chamber in MBRT fields at depth d is given by:

$$D(d) = M_c \; k_{Q,ecal} \; k'_Q \; k_{MBRT} \; N^{Co}_{D,w}. \tag{6.6}$$

To obtain the SPRs for each electron component, we imported the stopping power ratio scoring routines and reporting routines from the SPRRZnrc EGSnrc user-code [25] into the DOSXYZnrc code, so that stopping power ratio distributions can be scored in parallel with patient dose distributions in the same voxelised geometry as DOSXYZnrc. This modified code, SPRXYZnrc, thus allows a SPR distribution to be obtained in the same geometry with the same input file as the one used for DOSXYZnrc. For each electron beam energy, the SPR values between water and air for voxels inside the chamber volume of the phantom were averaged based on the weight of each field and used to determine k_{MBRT}. Within this paper, any mention of "field" refers to the radiation region resulting from a single MLC aperture.

6.4.3 Phantom simulation and planning

A cylindrical polymethyl methacrylate (PMMA) phantom, shown in figure 6–2, was machined for the purpose of this work. The aim was to produce a phantom with a geometry similar to a patient extremity to perform QA measurements on MBRT plans created for soft tissue sarcomas of the leg. Typical superficial extremity soft tissue sarcoma cases suitable for the MBRT technique have targets depths ≤ 6 cm. For ionisation chamber measurements, two holes were drilled with centres at depths of 1.4 cm and 2.1 cm from the surface of the cylinder, respectively. These two lateral depths were chosen as they represent the depth d_{max} of maximum dose at 6 and 9 MeV respectively. Due to the steep dose falloff at these energies, these relatively shallow depths are required to measure a substantial dose. The longitudinal depth of the holes was chosen such that the active volume of an ionisation chamber would

align with the centre of the phantom, along its axis. A second identical PMMA phantom was machined and sliced along its length to create an insert for the placement of a Gafchromic EBT3 film (see Fig. 6–3). The horizontal slice is positioned at a depth of 2 cm from its top lateral face.

A Solid Water (Sun Nuclear Corporation, Melbourne, Florida) slab phantom, used for standard clinical QA was also involved in these experiments. CT simulation scans of the PMMA cylinders and the Solid Water slabs were obtained. During scanning of the PMMA phantom for the ionisation chamber measurements, an Exradin A1SL (Standard Imaging, Madison, Wisconsin) chamber was present in the 1.4 cm insert in order to contour the active volume of the chamber for SPR calculation purposes. CT markers were placed using the in-room lasers for reproducible positioning. The MBRT treatment planning algorithm described in Renaud et al. [16] was used to create treatment plans for the Solid Water slab and the PMMA cylinder. For the PMMA phantoms, the plan was optimised on the chamber phantom and then identically replicated on the film phantom for calculation and delivery purposes.

For the Solid Water slab phantom, a simple MBRT plan was created with a single electron beam angle (0°) while the photon component was composed of an arc from -110° to 110°. A total of 50 apertures spread across 6, 9, 12 MeV electrons and 6 MV photons were included in the treatment plan. The aim was to ensure that many modalities participated in the plan while maintaining a simple plan delivery rather than producing a clinically realistic plan.

The plan created for the PMMA cylinder aimed to reproduce a clinically realistic plan for a superficial target on the top half of the cylinder. The electron beam angles were (-30, 0, 30)° and the photon component was an arc from -110° to 110°. The electron component included a total of 40 electron apertures and was delivered as a step-and-shoot delivery. The beam delivery parameters for each plan are summarised in table 6–1.

Figure 6–4 shows dose colourwashes for a representative axial slice for both plans. For both phantoms, the target is contoured in red. In both cases, the dose distribution is normalised so that 95% of the PTV volume receives 50 Gy.

6.4.4 Calculated dose distributions

In previous work, we have demonstrated PTV-based and CTV-based robust treatment planning algorithms to produce MBRT plans from beamlet-based apertures [16], [26]. However, beamlet-based apertures require a final MC recalculation to account for the effects of MLC leaves and jaw position on the dose distribution and the relative output of each aperture. In this work, each aperture of the treatment plans created for measurement purposes was recalculated using a validated MC beam model, and the MC dose distributions were renormalised from dose per primary particle to dose per monitor unit. At the time of MC recalculation, for photon arcs, MLC leaf movements at any gantry angle are interpolated between its two adjacent apertures.

MC simulations were performed using the phase space files distributed by Varian for the TrueBeam linear accelerator as the particle source (Virtual Linac) [27]. Particles sampled from the phase space files were transported through a BEAMnrc model consisting of the jaws, the base plate, the Millenium 120 MLC and the exit window [28]. Particles were further transported in a voxelised geometry by using DOSXYZnrc [29], [30]. The electron transport cutoff (ECUT) was 0.7 MeV, and the photon cutoff (PCUT) was 0.01 MeV. The EXACT boundary crossing algorithm was used, with a skin depth of 3 mean free paths. The electron stepping algorithm was PRESTA-II. The voxel sizes used in the MC simulations were 2 x 2 x 1 mm^3, where 1 mm was used along the depth axis. For SPR calculations, an ECUT of 0.521 MeV was used instead of 0.7 MeV.

The beam model and the phase space files were validated through measurements of output factors, depth doses and profiles of MLC-defined electron fields. The average energy of particles in some phase space files were tuned to better match measurement data. As

such the average energy of electrons in the 6 MeV, 9 MeV and 12 MeV phase spaces were uniformly increased by 3%, 2% and 1% respectively.

To convert MC dose values into absorbed dose per Monitor Unit (Gy/MU), the MC reference dose calibration factors were obtained by reproducing the conditions described in section 6.4.1 in a Monte Carlo simulation, and noting the MC dose per primary particle value at d_{ref} for each energy. The MC aperture dose distributions were then renormalised as

$$D_{MU}^{MC} = D^{MC} \frac{D_{ref}^{meas}}{D_{ref}^{MC}} \tag{6.7}$$

where D_{ref}^{meas} was the measured dose per MU in reference conditions, and D_{ref}^{MC} was the MC dose per primary particle calculated in the same reference conditions [31]. A monitor chamber backscatter correction was not applied as it has been shown that the correction is negligible when the jaw opening is kept sufficiently large and especially when MLC leaves are used to collimate the field [32]. The same procedure was performed to renormalise photon MC aperture dose distributions, however the reference conditions were taken as standard TG-51 conditions rather than the 80 cm SSD setup done for electrons.

The same treatment planning optimisation criteria were then used to re-optimise the relative weight of each aperture using the MC-calculated aperture dose distributions and obtain the monitor units for each aperture. The number of monitor units delivered from each modality for both plans is given in table 6–2.

6.4.5 Phantom setup and delivery

The phantoms were positioned such that the distance between the geometric centre of the PTV and the source was 80 cm for the electron component (i.e. a virtual 80 cm SAD) and 100 cm for the photon component. The plans were delivered on a Varian TrueBeam linear accelerator, which has a nominal SAD of 100 cm, hence shortened SAD deliveries require a different couch position for each beam delivery angle.

The treatment plans were delivered using the TrueBeam developer mode which allows the couch to be moved dynamically during treatment. The setup and delivery process was as follows:

1. The phantom was positioned on the treatment couch and the CT markers were aligned with the in-room lasers.
2. The couch positions (lat, lng, vrt) displayed on the treatment console were recorded.
3. Using our in-house treatment planning system (TPS), the position of the machine isocenter in the CT coordinate system was identified, as shown in Fig. 6–5 (a), to establish a transformation between the couch coordinate system and the CT coordinate system.
4. The treatment plan was exported as an XML file using our TPS by supplying the information shown in Fig. 6–5 (b). The TPS automatically creates the XML files necessary for delivery using the TrueBeam developer mode and determines the couch position of each control point based on the transformation between the couch and CT coordinate systems shown in eq. 6.8.
5. The treatment plan was delivered on a per-modality basis, as the TrueBeam developer mode does not yet support changing between photon or electron energies within a single XML file.

The couch positions for each control point were determined using a simple translation of the couch based on the difference between the machine isocenter position at each control point and the machine isocenter in the setup position:

$$\boldsymbol{p}_{cpt}^{couch} = \boldsymbol{p}_{setup}^{couch} + (\boldsymbol{p}_{cpt}^{CT} - \boldsymbol{p}_{setup}^{CT}). \tag{6.8}$$

6.4.6 Measurement setup

For the Solid Water phantom, a Gafchromic EBT3 film was placed at a depth of 2 cm and irradiated with all components of the treatment plan. The film was scanned 22 hours after irradiation using an Epson Expression 11000XL flatbed scanner (Epson America, Inc., Long

Beach, CA). The film was then read into FilmQA Pro 2015 (Ashland Advanced Materials, Bridgewater, New Jersey) and the red colour channel was converted to dose using calibration films obtained on the same day. A single electron energy (12 MeV) was used to create the calibration curve. Gafchromic EBT3 films have been found to be suitable for measurements of mixed photon-electron dose distributions due to their low energy dependence in this energy range [33]. This film measurement procedure was repeated on the PMMA film phantom at a depth of 2 cm. In this case, in addition to an overall plan delivery, film measurements were also taken for each individual component of the treatment plan.

For the film measurement on Solid Water slabs, the total plan delivery was divided into 31 fractions and a single fraction was delivered on the film. The number of fractions was chosen such that the maximum dose on the film was approximately 70% of the maximum film calibration dose. This fractionation selection process was applied to each energy component individually delivered on the PMMA film phantom.

The ionisation chamber measurements were performed using an Exradin A1SL chamber inside a Solid Water plug inserted into the 1.4 cm hole of the PMMA cylinder. To ensure the reproducibility of the setup, the chamber measurement was repeated 3 times. For each measurement, the phantom was fully repositioned as described in section 6.4.5. The measurement process was repeated with the chamber and the Solid Water plug inserted in the 2.1 cm hole. The phantom was rotated such that the chamber was always positioned on the top half of the phantom. For the full delivery, a chamber measurement was also taken in the Solid Water slab phantom at 3.4 cm depth. The MBRT plan MC doses for all modalities were recalculated to account for the differences in materials between the planning and measurement conditions. The active volume of the ionisation chamber was converted from air to water in the MC simulation as the chamber is calibrated in terms of absorbed dose to water and thus nominally reports absorbed dose to water. Figure 6–6 shows the materials and densities used for the MC dose calculation. The same phantom was used to calculate SPRs inside the chamber volume.

6.4.7 Uncertainty estimation

In determining the uncertainty associated with the measured dose, D_{meas}, we combined the standard uncertainty on the reference dose determination (1.1%) with the uncertainties associated with the determination of k_{MBRT}, most notably by estimating the uncertainty associated with omitting the cavity fluence perturbation correction (p_{cav}) in the determination of k_{MBRT}, and a dose non-uniformity uncertainty based on the heterogeneity of the dose inside the chamber volume calculated using the MC doses.

The uncertainty associated with neglecting the fluence perturbation correction in the MBRT field was estimated by first assigning a hypothetical beam quality to each energy of the MBRT delivery ($R_{50,MBRT}$). This specifier was determined by inverting the $\left(\frac{\bar{L}}{\rho}\right)^{w}_{air}$ to R_{50} relationship given in the IAEA TRS-398 report, Appendix B, based on the $\left[\left(\frac{\bar{L}}{\rho}\right)^{w}_{air}\right]^{MBRT}$ values calculated using SPRXYZnrc. This hypothetical $R_{50,MBRT}$ was then used to obtain a value for $p_{cav,MBRT}$ using the equation for p_{cav} for cylindrical chambers as a function of R_{50} provided by TRS-398 Appendix B [34], which is based on a broad set of experimental data. $p_{cav,ref}$ was determined from the same formula but using the reference beam R_{50} instead. The relative difference between $p_{cav,MBRT}$ and $p_{cav,ref}$ (i.e., $1.0 - p_{cav,MBRT}/p_{cav,ref}$) does not exceed 1% and was treated as an uncertainty factor.

The uncertainty due to the non-uniformity of the dose inside the chamber volume was determined based on the minimum and maximum dose values inside the volume, and assuming a triangular distribution (i.e., $(D_{max} - D_{min})/D_{avg}/\sqrt{6}$).

6.5 Results

6.5.1 Reference dose measurements

Table 6–3 shows the calibration depths and values measured in the applicator-less electron radiation therapy reference conditions described in section 6.4.1. The R_{50} beam quality specifiers were obtained from percent depth dose curves measured using an IBA RFD 3G diode detector (Ion Beam Applications, Louvain-la-neuve, Belgium) in the same reference conditions. For comparison, the R_{50} in table 6–3 are at most 5.6% larger (6 MeV) than if

they were to be measured in standard reference conditions (100 cm SSD). The Type-A uncertainty on the MC-calculated SPRs was less than 0.2% for all modalities. All uncertainties stated are k = 1.

6.5.2 Film measurements

Fig. 6–7 & 6–8 present the results of the comparison between the film measurement and the planned dose distribution for the overall delivery on the Solid Water slabs and the PMMA cylinder respectively. Both a 3%/2mm and 2%/2mm global gamma analysis were performed with a global 10% dose threshold. The pass rates for either criterion are shown in table 6–4. The average type-A MC uncertainty on voxels with more than 50% of the maximum dose was less than 1%. It should be noted that MC uncertainty can artificially inflate the gamma pass rate. The gamma pass rates at 3%/2mm for the deliveries on both the cylindrical (97.3%) and Solid Water slab phantoms (96.1%) were found to be superior to the 95% pass rate tolerance limit recommended in TG218 [35] for IMRT QA. Only the 6 MeV component was found to have large discrepancies. However, at this low energy, it was found that the 2D dose distribution was highly sensitive to depth. Indeed, by varying the depth of the film slice by 1 mm in the MC calculation, the gamma pass rate at 2%/2mm increased from 62.1% to 99.5%.

6.5.3 Ionisation chamber measurements

To replicate clinical deliveries, the total dose from the PMMA treatment plan was divided into 20 fractions ($N_{frac} = 20$) and a single fraction was delivered in the measurement setup described in section 6.4.6. The plan MU shown in table 6–2 are therefore divided by ($N_{frac} = 20$) for a single measurement delivery.

Table 6–5 shows the measured dose values in the ionisation chamber compared to Monte Carlo-calculated doses for each modality. For each modality, $\left[\left(\frac{\bar{L}}{\rho}\right)^{w}_{air}\right]^{MBRT}$ was Monte Carlo-calculated using the SPRXYZnrc code with the same geometry and particle source as for the dose calculation performed in DOSXYZnrc. The MBRT beam quality correction

factor, k_{MBRT}, was then determined using eq. 6.4 using the reference SPRs in table 6–3. The absorbed dose to water was then calculated using eq. 6.6.

The largest difference between measurement and calculation were observed at 6 MeV with a discrepancy of 8.3% ± 7.5% and 28% ± 15% at 1.4 cm and 2.1 cm depth respectively. However, for the sum of all electrons at 1.4 cm depth, the measured dose and calculated dose agreed to within 0.5% and the total dose at the measurement point agreed to within -0.03%. At 2.1 cm depth, the total measured dose was found to agree with calculations within 2.1%. Overall, the dose delivered by each modalities, with the exception of the 6 MeV electrons, were within uncertainty of their respective calculated doses. The overall chamber dose measured on the Solid Water phantom was also found to agree within 0.73% ± 3.8% with calculations.

Figure 6–9 b) shows the SPR between the phantom material and air as a function of depth along the line shown in Fig. 6–9 a). The effect of the different material compositions on the SPR is clearly visible.

6.6 Discussion

The purpose of the film delivery on slabs of Solid Water phantom was to identify large errors in the planning, simulation and delivery process. The setup was inherently robust to positioning errors as the entire plan was delivered at a normal incidence to the flat phantom, therefore good agreement was expected between the film measurement and the simulated dose.

The cylindrical phantom delivery was set up to closely resemble the types of dose distributions obtainable for MBRT applications to soft tissue sarcomas of the leg. Electron dose distributions are known to be considerably more perturbed than photon dose distributions when delivered at oblique incidences; therefore, this delivery can be seen as a particularly challenging case for the electron MC beam models.

In both phantoms, the film measurements showed good overall agreement with gamma pass rates of 92% for a 2%/2 mm criteria. Although the 6 MeV component had poor

agreement, this discrepancy can be attributed to the difficulty of precisely assigning an accurate film depth. At 2 cm depth, the film lies in the high gradient section of the depth dose curve of 6 MeV electrons. Small variations in depth ($\sim$1 mm) can thus cause large absolute dose shifts in the slice dose.

The difference between the total measured and simulated MBRT dose was -0.03% and 2.1% at a depth of 1.4 cm and 2.1 cm respectively. This discrepancy lies well within an expanded uncertainty ($k = 2$). As expected, the difference between measured and simulated absorbed doses was largest for the lowest energy electrons with discrepancies up to 26% at 6 MeV and depth of 2.1 cm. In addition to the accuracy of the MC models, the accuracy of the setup was expected to have a considerable impact on the delivered dose distribution. Although a mini ionisation chamber (A1SL, 0.053 cc) was used to perform all measurements, there remained large dose gradients inside the chamber volume, contributing to measurement uncertainty as the effective point of measurement is not well defined.

For MBRT plans, the dose distribution of each modality is often highly non-uniform within the PTV. This is because different modalities are usually covering different spatial regions of the PTV. For example, low energy electron components are usually responsible for the dose in superficial regions while photon doses are usually concentrated at edges of the PTV. As such, when performing ionisation chamber measurements, it is difficult to find a single point where the dose gradient is low for all modalities. In this study, although the point of measurement at 1.4 cm depth in the PMMA cylinder was located in a relatively high dose and low gradient region for the 12 MeV component, it was the opposite for the 6 MeV component. This larger dose gradient translates into a larger uncertainty on the measured dose of the 6 MeV component, as can be seen in Table 6–5. Furthermore, the fidelity of the MC models is considerably worse at depths beyond the electron practical range (local discrepancies over 10% for doses below 1% of the maximum dose). As the 6 MeV apertures in the PMMA cylinder plan were predominantly delivered at gantry angles of $\pm 30^{\circ}$ (see Fig. 6–1), the effective depth of the point of measurement was larger than 3 cm, i.e. beyond the

practical range. Comparing MC calculated doses at such depths to measurements would introduce systematic errors due to the inaccuracy of the MC model.

By calculating k_{MBRT} as a simple ratio of stopping power-ratios between measurement and reference conditions, we have implicitly assumed that P_{gr} was constant, which may explain part of the differences between measured and calculated doses. In addition, effects of electron fluence perturbation are ignored in our approach, which would affect the results predominantly at low electron energies (6 MeV and 9 MeV). The overall agreement between planned and delivered dose, however, confirms that for this situation the effects are limited.

The k_{MBRT} correction factor resulted in a 4% correction in measured dose for the highest electron energies. Despite k_{MBRT} being necessary for accurate measurements in MBRT conditions, we conclude that the measurement procedure followed in this work consists of a viable procedure for MBRT plan verification using an ionisation chamber.

Both MBRT plans were deliverable with a single setup procedure as the TrueBeam developer mode allows dynamic couch positioning. Changing between modalities was the longest overhead associated with MBRT compared to conventional photon radiation therapy. In both cases, the electron component of the plan was deliverable in less than 5 minutes, including modality changes, but not including setup time. In terms of beam-on time, all electron components can be delivered at a rate of 1000 MU/min, which speeds up delivery over the 600 MU/min maximum of photon beams with a flattening filter on the TrueBeam accelerator. The complete measurement process was performed in under 30 minutes. Using the methodology described in this paper, a more clinically practical patient-specific QA protocol will be developed based on point dose measurements.

As can be seen from table 6–2, the number of monitor units per component greatly increases for the lower electron energies due to the fact that output factors degrade quickly for the combination of low energies and small fields. For example, we measured the 3×3 cm^2 MLC-defined field output factor to be 0.251 for 6 MeV, compared to 0.855 for 20 MeV. While the deliveries of these components is still accomplished rapidly due to the high

dose rates achievable for electrons, Connell et al. found that electron output factors of FLEC-defined fields were highly sensitive to minute ($\approx$ 0.5 mm) changes in jaws position when the field sizes were on the order of 3×3 cm^2 [8]. With pMLC-defined fields, this could also lead to large discrepancies between simulated and delivered doses if the linac jaws were miscalibrated. We therefore recommend that the MC-simulated output factors be compared to measured output factors regularly if MBRT plans are delivered with a substantial low energy electron component. By default, some manufacturers allow tolerances on MLC leaf positioning during treatment which could allow the beam to be enabled if the leaf is within, e.g., 2 mm of its intended position. For low electron beam energies and smaller MLC apertures, such tolerances could also lead to large differences in output factors. If possible, lower tolerances on MLC leaf positions should be used during MBRT delivery. Our preliminary investigation indicated that lower electron energies to be more sensitive to small deviations in leaf positioning. In our Monte Carlo simulations, for nominal 3x3 cm^2 fields, the output factor of 6 MeV electrons increased by more than 6% when the field size was enlarged by 2 mm. For the same change in field size, higher electron energies had consistently lower output factor variation, such as less than 1% at 20 MeV.

The virtual SAD delivery of the electron components required a different couch position for each beam angle, which is not currently part of routine clinical practice. In an effort to produce plans which required fewer changes to current practice, we attempted to deliver the MBRT plans with a single couch position, hence a varying shortened SSD. However, with such a setup, the target volume is typically not on the beam central axis, leading to off-axis irradiation. The transition between beam angles therefore required large movements of the collimators, during which the beam had to be in the *beam hold* state. Beam holds on Varian accelerators are created by adjusting the grid voltage in the electron gun; during the beam hold state the accelerator is active with RF in the wave guide but the electron source is in a hold state. However, during the course of delivering these plans, we have discovered the

presence of a persistent, low level of leakage radiation during the beam hold states which is high enough to trigger a machine interlock and interrupt the delivery.

A discussion with a representative from Varian Medical Systems confirmed that the leakage is due to the absence of attenuating material in the path of the beam compared to photon beams. This means that low electron currents in the waveguide can deliver appreciable doses to the patient even with the beam in the beam hold state. Virtual SAD deliveries result in less collimator movement which reduces the need for beam holds. However, long beam holds could still occur in virtual SAD deliveries if large collimator movements were needed, for example, if multiple physically separated small lesions were treated within the same session. A bigger engineering limitations of mixed beam deliveries is the time delay required when changing beam energy or particle. As a mixed beam plan can involve five electron energies and a photon component, adding a delay for each modality can considerably increase treatment times.

Although MBRT plans in this study were not robustly optimised, Renaud et al. (2019) [26] have shown that robust MBRT plans are necessary for deliveries of mixed electron-photon modalities in realistic clinical conditions. This however raises the question of how to perform QA on the robustness of a plan. Indeed, MBRT plans created using robust optimisation will no longer be robust to positioning errors when transposed onto measurement phantoms. Therefore, a study is necessary to determine the variation in agreement between simulated and measured doses from clinical robust plans delivered on QA phantoms and define realistic tolerances for QA setups of robust plans for the clinical site of interest.

6.7 Conclusion

The aim of this work was to confirm that the treatment plans produced by our MBRT treatment planning algorithm [16], [26] could be delivered and measured accurately on a Varian TrueBeam accelerator. In addition, we sought to develop the framework required for a potential patient-specific QA protocol.

These goals were first achieved by delivering a simple plan on slabs of Solid Water with a film placed at a depth of 2 cm, and comparing the results to the simulated delivery. The resulting gamma pass rate of 96.1% for a 3%/2 mm criteria confirmed that the MC beam models used in this work performed accurately.

A complex MBRT plan was delivered on a PMMA cylinder specifically constructed for ionisation chamber measurements and performing point dose measurements. A film measurement was also taken on an identically shaped phantom. The chamber measurement from each modality was corrected by a beam quality correction factor calculated using a MC code specifically created to obtain both dose distributions and correction factors with the same input in order to facilitate the QA process. The complete measurement procedure was realised in under 30 minutes, and the agreement between measured and simulated total dose agreed to within 2.1%, leading us to conclude that the procedure can be applied for clinical patient-specific QA.

6.8 Acknowledgements

The authors would like to acknowledge Dr. Tanner Connell for helpful discussions on film measurements, Dr. James Renaud for assistance with reference dosimetry, and Joe Larkin for machining the phantom used in this work. The authors acknowledge support from the Fonds de recherche du Québec Nature et Technologie (FRQNT), the CREATE Medical Physics Research Training Network grant (number 432290) of the Natural Sciences and Engineering Research Council (NSERC) and the Canadian Institute of Health Research Foundation Grant (FDN-143257).

6.9 Conflict of Interest Statement

The authors have no relevant conflicts of interest to disclose.

6.10 Data Availability Statement

The data that support the findings of this study are available from the corresponding author upon reasonable request.

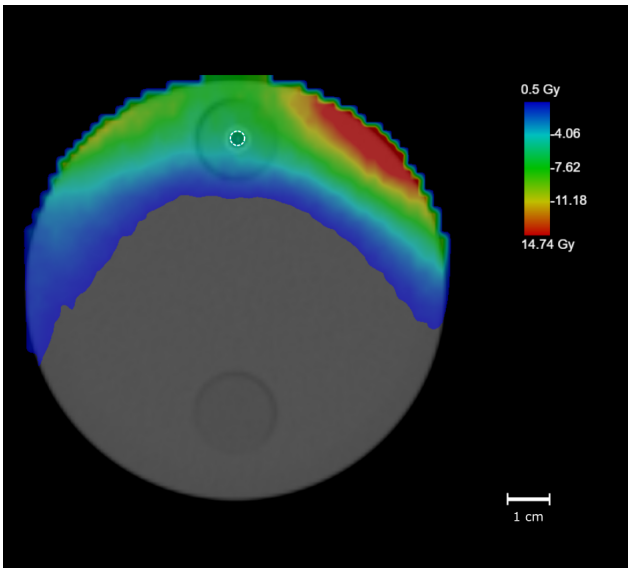

Figure 6–1: Dose colourwash for the 6 MeV component of a MBRT plan delivered on a PMMA phantom. The beam quality of particles inside the chamber air cavity (shown as in dotted white lines) will differ substantially from the beam quality at reference conditions.

Table 6–1: Summary of the planned beam delivery angles and phantom positions. Gantry angles are given in the range of -180° to 180°, with 0° corresponding to the gantry being in its exactly vertical position. A rotation from $-110° \rightarrow 110°$ corresponds to $250° \rightarrow 110°$ in the Varian IEC 601-2-1 convention. * The shortened electron SAD is realised in practice as a virtual SAD, meaning that the couch is moved such that the centre of the target is 80 cm from the source for each beam angle.

	Solid water plan	PMMA cylinder plan
Photon angles (°)	arc from −110 to 110	arc from −110 to 110
Electron angles (°)	0	$(-30, 0, 30)$
Photon SAD (cm)	100	100
Electron SAD (cm)*	80	80

Table 6–2: Distribution of monitor units per modality for the two plans delivered in this work, normalised to deliver 50 Gy to 95% of the contoured target volume.

	Monitor units per modality					
Plan	6 MeV	9 MeV	12 MeV	16 MeV	20 MeV	6 MV
Solid Water	4410	12035	5290	0	0	9264
PMMA	8118	1033	1707	1126	1898	2598

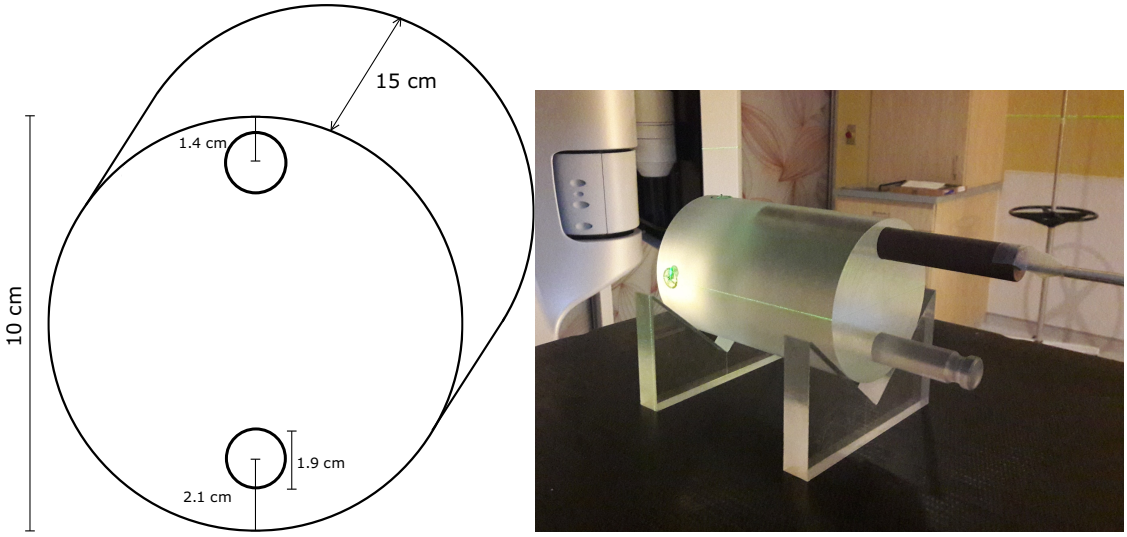

Figure 6–2: (a) Schematic diagram of the PMMA cylinder machined for ionisation chamber measurements. (b) Setup of the PMMA cylinder for chamber measurement.

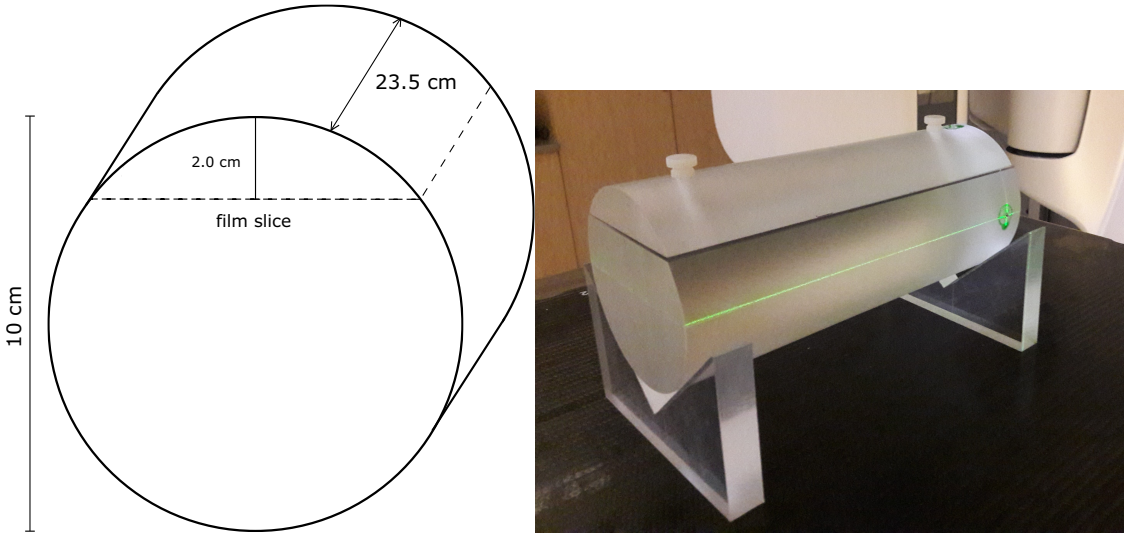

Figure 6–3: (a) Schematic diagram of the PMMA cylinder machined for film measurements. (b) Setup of the PMMA cylinder sliced for film measurement at 2 cm depth.

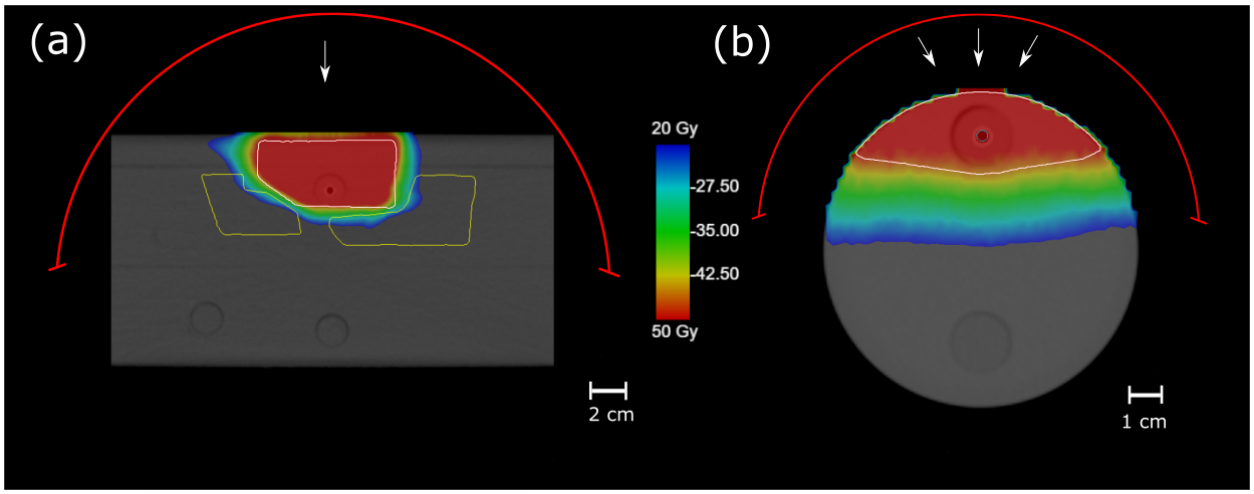

Figure 6–4: Dose colourwash for a representative axial slice of the (a) simplified MBRT plan delivered on Solid Water slabs and (b) complex MBRT plan delivered on the PMMA cylinder. In both cases, the target is shown as a white contour. The yellow contours in (a) represents hypothetical OARs. The red arcs correspond to the range of gantry angle at which photon beams are delivered. Similarly, white arrows are the gantry angles of electron beams.

Table 6–3: Beam quality specifiers and conversion factors for each electron beam energy for the Exradin A1SL ion chamber [21], measured in a water tank using a 10x10 cm^2 MLC-defined field at 80 cm SSD. $k_{Q,ecal}$ for the A1SL was taken to be 0.914. The SPRs were calculated using SPRXYZnrc with a Type A uncertainty of less than 0.2%. An uncertainty of 1.1% on the reference absorbed dose per monitor unit was assessed using the same uncertainty budget approach as detailed in McEwen et al. [23].

Energy (MeV)	R_{50} (cm)	d_{ref} (cm)	k'_Q	$(SPR^w_{air})_Q$	D_{ref} (cGy / MU)
6	2.46	1.38	1.0318	1.079	1.498 ± 0.016
9	3.70	2.12	1.0197	1.062	1.508 ± 0.016
12	5.10	2.96	1.0104	1.045	1.518 ± 0.016
16	6.73	3.94	1.0024	1.034	1.487 ± 0.016
20	8.31	4.89	0.9963	1.023	1.426 ± 0.015

Table 6–4: Film global gamma passing rates for delivery on cylindrical PMMA and flat Solid Water phantom.

	Pass rate criterion	20 MeV	16 MeV	12 MeV	9 MeV	6 MeV	6 MV	Overall
PMMA phantom	3%/2mm (%)	98	99.8	98.8	98.7	84.6	99.2	97.3
	2%/2mm (%)	95.8	98.4	96.4	96.9	62.1	96.8	92.5
		Overall (6 MV, 6 MeV, 9 MeV, 12 MeV)						
Solid Water phantom	3%/2mm (%)	96.1						
	2%/2mm (%)	92.2						

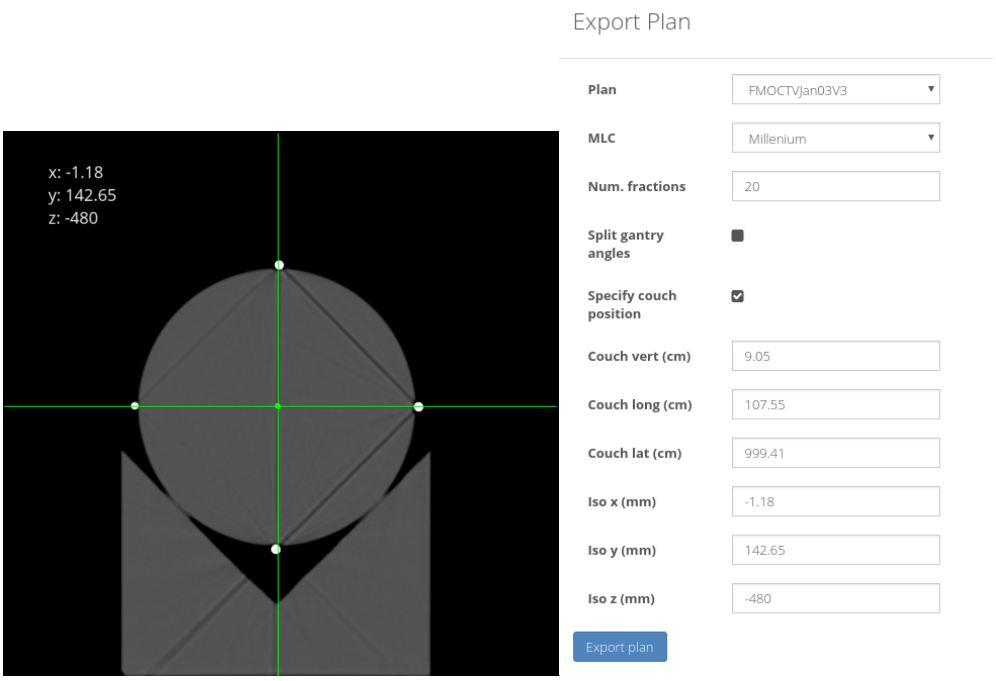

(a) (b)

Figure 6–5: (a) Identification of the machine isocenter position in the CT coordinate system when the phantom BBs are aligned with the in-room lasers. (b) Example of the information supplied by the user when exporting a plan as developer mode XML files from our in-house TPS.

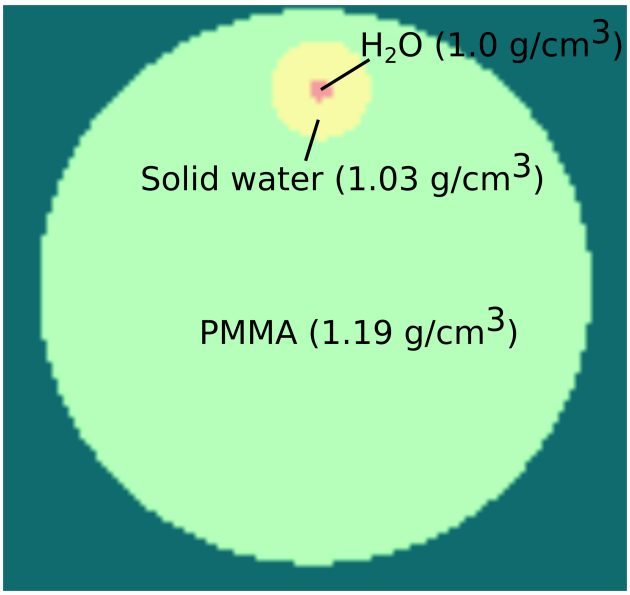

Figure 6–6: MC phantom materials and densities used to calculate the dose inside the ionisation chamber placed at 1.4 cm depth.

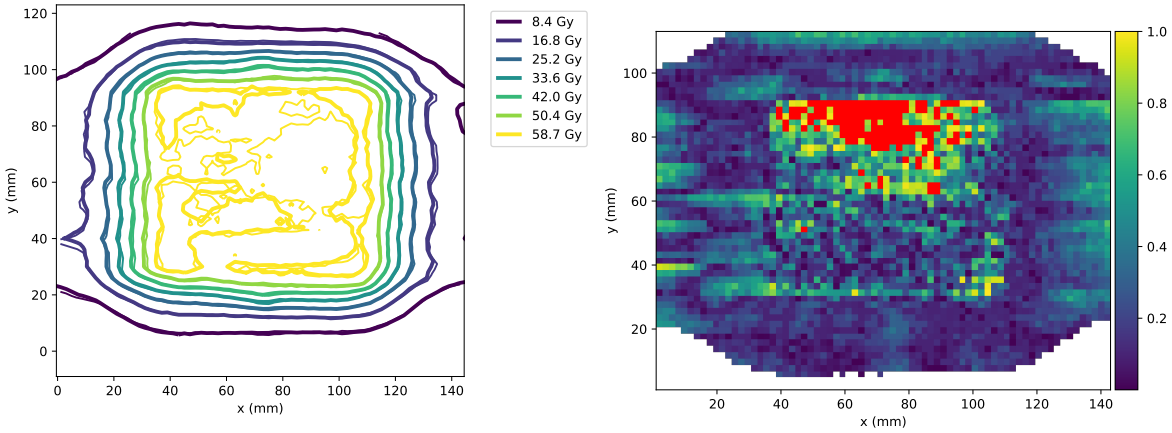

Figure 6–7: (a) Isodose comparison between measured film dose (thin lines) and simulated dose (thick lines) for the overall delivery on the Solid Water slabs. (b) Gamma map for a 3% / 2 mm passing criteria. Pixels in red have $\gamma \geq 1$.

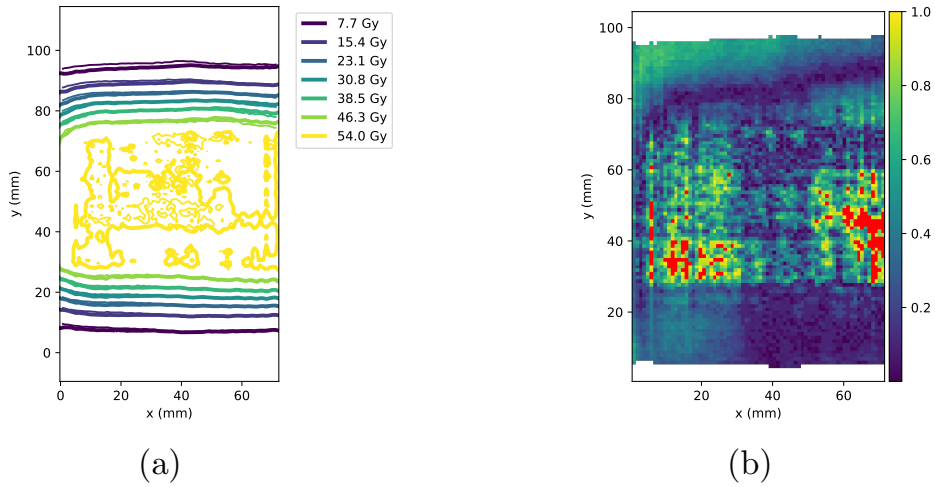

Figure 6–8: (a) Isodose comparison between measured film dose (thin lines) and simulated dose (thick lines) for the overall delivery on the cylindrical PMMA phantom. (b) Gamma map for a 3% / 2 mm passing criteria. Pixels in red have $\gamma \geq 1$.

Table 6–5: Measurement data from an Exradin A1SL ionisation chamber placed in the 1.4 cm insert of the PMMA phantom compared to simulated MC doses. The measurement doses were corrected for the beam quality at the measurement point using k_{MBRT}. The uncertainty on k_{MBRT} is estimated at 1%, dominated by the type B uncertainty associated with neglecting the cavity fluence perturbation. Uncertainties are presented with a coverage factor $k = 1$.

Depth: 1.4 cm	20 MeV	16 MeV	12 MeV	9 MeV	6 MeV	6 MV	Electrons	Total
$\left(\frac{\bar{L}}{\rho}\right)^{w}_{air}$	0.984	0.996	1.015	1.043	1.088	1.120		
k_{MBRT}	0.962	0.966	0.971	0.982	1.008	0.999		
D_{meas} (Gy)	9.59 ± 0.33	9.48 ± 0.39	14.14 ± 0.29	7.81 ± 0.4	5.88 ± 0.47	6.20 ± 0.12	46.90 ± 0.85	53.09 ± 0.86
D_{MC} (Gy)	9.53 ± 0.14	9.52 ± 0.14	14.31 ± 0.21	7.93 ± 0.12	5.39 ± 0.08	6.43 ± 0.06	46.68 ± 0.33	53.11 ± 0.33
ΔD (%)	-0.5 ± 3.8	-0.4 ± 4.4	-1.2 ± 2.6	-1.5 ± 5.4	8.3 ± 7.5	-3.8 ± 2.2	0.5 ± 1.9	-0.0 ± 1.7
Depth: 2.1 cm	**20 MeV**	**16 MeV**	**12 MeV**	**9 MeV**	**6 MeV**	**6 MV**	**Electrons**	**Total**
$\left(\frac{\bar{L}}{\rho}\right)^{w}_{air}$	0.991	1.008	1.03	1.066	1.11	1.119		
k_{MBRT}	0.969	0.978	0.986	1.004	1.029	0.998		
D_{meas} (Gy)	9.93 ± 0.37	9.09 ± 0.29	14.74 ± 0.34	7.73 ± 0.31	3.53 ± 0.75	6.68 ± 0.31	45.01 ± 0.75	51.69 ± 0.76
D_{MC} (Gy)	10.03 ± 0.15	8.86 ± 0.13	14.43 ± 0.22	8.06 ± 0.12	2.54 ± 0.04	6.72 ± 0.07	43.91 ± 0.32	50.63 ± 0.33
ΔD (%)	-1.0 ± 4.1	2.6 ± 3.5	2.1 ± 2.7	-4.2 ± 4.4	28 ± 15	-0.6 ± 4.8	2.4 ± 1.8	2.1 ± 1.6

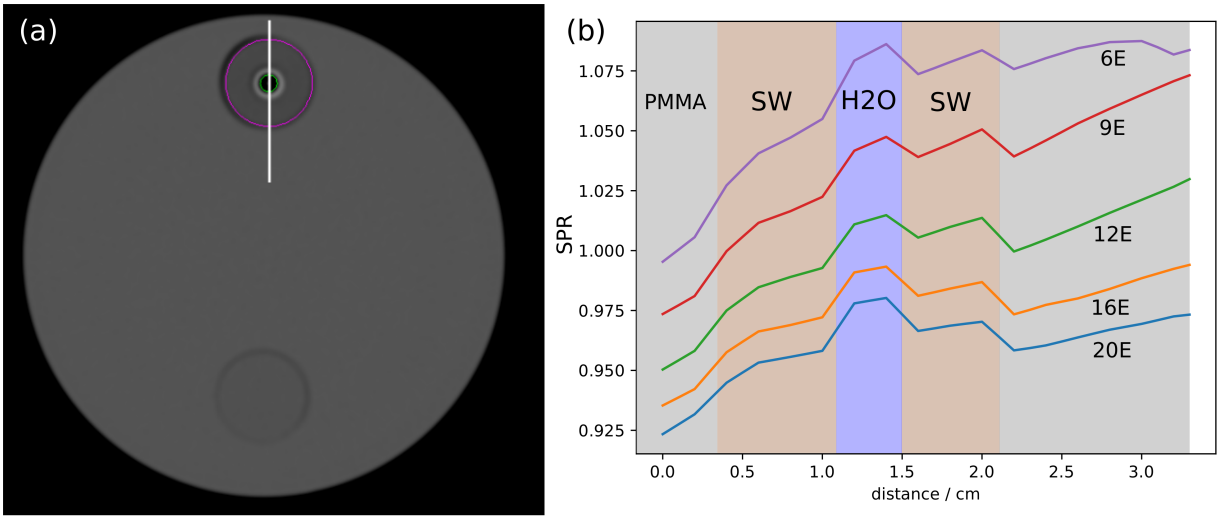

Figure 6–9: (a) Axial CT slice of the PMMA phantom showing the line along which the SPRs are plotted for each modality. (b) SPR between the phantom medium and air. The active volume of the ionisation chamber was modelled as water.

REFERENCES

[1] M. C. Lee, S. B. Jiang, and C. M. Ma, "Monte Carlo and experimental investigations of multileaf collimated electron beams for modulated electron radiation therapy," *Medical Physics*, vol. 27, no. 12, pp. 2708–2718, 2000. DOI: 10.1118/1.1328082.

[2] C. M. Ma, T. Pawlicki, M. C. Lee, *et al.*, "Energy- and intensity-modulated electron beams for radiotherapy," *Physics in Medicine and Biology*, vol. 45, no. 8, pp. 2293–2311, 2000. DOI: 10.1088/0031-9155/45/8/316.

[3] K. R. Hogstrom, R. A. Boyd, J. A. Antolak, *et al.*, "Dosimetry of a prototype retractable eMLC for fixed-beam electron therapy," *Medical Physics*, vol. 31, no. 3, pp. 443–462, 2004. DOI: 10.1118/1.1644516.

[4] T. Gauer, D. Albers, F. Cremers, *et al.*, "Design of a computer-controlled multileaf collimator for advanced electron radiotherapy," *Physics in Medicine and Biology*, vol. 51, no. 23, pp. 5987–6003, 2006. DOI: 10.1088/0031-9155/51/23/003.

[5] T. Gauer, J. Sokoll, F. Cremers, *et al.*, "Characterization of an add-on multileaf collimator for electron beam therapy," *Physics in Medicine and Biology*, vol. 53, no. 4, pp. 1071–1085, 2008. DOI: 10.1088/0031-9155/53/4/017.

[6] K. Al-Yahya, F. Verhaegen, and J. Seuntjens, "Design and dosimetry of a few leaf electron collimator for energy modulated electron therapy," *Medical Physics*, vol. 34, no. 12, pp. 4782–4791, 2007. DOI: 10.1118/1.2795827.

[7] A. Alexander, F. Deblois, and J. Seuntjens, "Toward automatic field selection and planning using Monte Carlo-based direct aperture optimization in modulated electron radiotherapy," *Physics in Medicine and Biology*, vol. 55, no. 16, pp. 4563–4576, 2010. DOI: 10.1088/0031-9155/55/16/S10.

[8] T. Connell, A. Alexander, P. Papaconstadopoulos, *et al.*, "Delivery validation of an automated modulated electron radiotherapy plan," *Medical Physics*, vol. 41, no. 6, 2014. DOI: 10.1118/1.4876297.

[9] F. C. Du Plessis, A. Leal, S. Stathakis, W. Xiong, and C. M. Ma, "Characterization of megavoltage electron beams delivered through a photon multi-leaf collimator (pMLC)," *Physics in Medicine and Biology*, vol. 51, no. 8, pp. 2113–2129, 2006. DOI: 10.1088/0031-9155/51/8/011.

[10] E. E. Klein, M. Vicic, C. M. Ma, D. A. Low, and R. E. Drzymala, "Validation of calculations for electrons modulated with conventional photon multileaf collimators," *Physics in Medicine and Biology*, vol. 53, no. 5, pp. 1183–1208, 2008. DOI: 10.1088/0031-9155/53/5/003.

[11] F. J. Salguero, B. Palma, R. Arrans, J. Rosello, and A. Leal, "Modulated electron radiotherapy treatment planning using a photon multileaf collimator for post-mastectomized chest walls," *Radiotherapy and Oncology*, vol. 93, no. 3, pp. 625–632, 2009. DOI: 10.1016/j.radonc.2009.08.021.

[12] D. Henzen, P. Manser, D. Frei, *et al.*, "Beamlet based direct aperture optimization for MERT using a photon MLC.," *Medical physics*, vol. 41, no. 12, p. 121 711, Dec. 2014. DOI: 10.1118/1.4901638.

[13] E. E. Klein, Z. Li, and D. A. Low, "Feasibility study of multileaf collimated electrons with a scattering foil based accelerator," *Radiotherapy and Oncology*, vol. 41, no. 2, pp. 189–196, 1996. DOI: 10.1016/S0167-8140(96)01822-1.

[14] A. Alexander, E. Soisson, M.-A. Renaud, and J. Seuntjens, "Direct aperture optimization for FLEC-based MERT and its application in mixed beam radiotherapy.," *Medical physics*, vol. 39, no. 8, pp. 4820–31, Aug. 2012. DOI: 10.1118/1.4736423.

[15] B. A. Palma, A. U. Sánchez, F. J. Salguero, *et al.*, "Combined modulated electron and photon beams planned by a Monte-Carlo-based optimization procedure for accelerated

partial breast irradiation," *Physics in Medicine and Biology*, vol. 57, no. 5, pp. 1191–1202, 2012. DOI: 10.1088/0031-9155/57/5/1191.

[16] M.-A. Renaud, M. Serban, and J. Seuntjens, "On mixed electron-photon radiation therapy optimization using the column generation approach," *Medical Physics*, vol. 44, no. 8, pp. 4287–4298, 2017. DOI: 10.1002/mp.12338.

[17] S. Mueller, M. K. Fix, A. Joosten, *et al.*, "Simultaneous optimization of photons and electrons for mixed beam radiotherapy," *Physics in Medicine and Biology*, vol. 62, no. 14, pp. 5840–5860, 2017. DOI: 10.1088/1361-6560/aa70c5.

[18] S. Mueller, P. Manser, W. Volken, *et al.*, "Part 2: Dynamic mixed beam radiotherapy (dymber): Photon dynamic trajectories combined with modulated electron beams," *Medical Physics*, vol. 45, no. 9, pp. 4213–4226, 2018. DOI: https://doi.org/10.1002/mp.13085.

[19] C. Míguez, E. Jiménez-Ortega, B. A. Palma, *et al.*, "Clinical implementation of combined modulated electron and photon beams with conventional MLC for accelerated partial breast irradiation," *Radiotherapy and Oncology*, vol. 124, no. 1, pp. 124–129, 2017. DOI: 10.1016/j.radonc.2017.06.011.

[20] P. R. Almond, P. J. Biggs, B. M. Coursey, *et al.*, "AAPM's TG-51 protocol for clinical reference dosimetry of high-energy photon and electron beams," *Medical Physics*, vol. 26, no. 9, pp. 1847–1870, 1999. DOI: 10.1118/1.598691.

[21] B. R. Muir and D. W. Rogers, "Monte Carlo calculations of electron beam quality conversion factors for several ion chamber types," *Medical Physics*, vol. 41, no. 11, p. 111 701, 2014. DOI: 10.1118/1.4893915.

[22] B. R. Muir and D. W. Rogers, "Monte Carlo calculations of kQ, the beam quality conversion factor," *Medical Physics*, vol. 37, no. 11, pp. 5939–5950, 2010. DOI: 10.1118/1.3495537.

[23] M. McEwen, L. Dewerd, G. Ibbott, *et al.*, "Addendum to the AAPM's TG-51 protocol for clinical reference dosimetry of high-energy photon beams," *Medical Physics*, vol. 41, no. 4, 2014. DOI: 10.1118/1.4866223.

[24] P. Andreo, D. T. Burns, A. E. Nahum, J. Seuntjens, and F. H. Attix, *Fundamentals of ionizing radiation dosimetry*. John Wiley & Sons, 2017.

[25] D. W. O. Rogers, I. Kawrakow, J. P. Seuntjens, B. R. B. Walters, and E. Mainegra-Hing, "NRC User Codes for EGSnrc," National Research Council of Canada, Tech. Rep., 2003. DOI: 10.1080/17425255.2017.1234605.

[26] M.-A. Renaud, M. Serban, and J. Seuntjens, "Robust mixed electron–photon radiation therapy optimization," *Medical Physics*, vol. 46, no. 3, pp. 1384–1396, 2019. DOI: https://doi.org/10.1002/mp.13381.

[27] A. Rodrigues, D. Sawkey, F. F. Yin, and Q. Wu, "A Monte Carlo simulation framework for electron beam dose calculations using Varian phase space files for TrueBeam Linacs," *Medical Physics*, vol. 42, no. 5, pp. 2389–2403, 2015. DOI: 10.1118/1.4916896.

[28] D. W. O. Rogers, B. Walters, and I. Kawrakow, "BEAMnrc Users Manual," National Research Council of Canada, Tech. Rep., 2011.

[29] B. Walters, I. Kawrakow, and D. W. O. Rogers, "DOSXYZnrc Users Manual," National Research Council of Canada, Tech. Rep., 2016. DOI: 10.1118/1.4773883.

[30] J. Lobo and I. A. Popescu, "Two new DOSXYZnrc sources for 4D Monte Carlo simulations of continuously variable beam configurations, with applications to RapidArc, VMAT, TomoTherapy and CyberKnife," *Physics in Medicine and Biology*, vol. 55, no. 16, pp. 4431–4443, 2010. DOI: 10.1088/0031-9155/55/16/S01.

[31] C. M. Ma, R. A. Price, J. S. Li, *et al.*, "Monitor unit calculation for Monte Carlo treatment planning," *Physics in Medicine and Biology*, vol. 49, no. 9, pp. 1671–1687, 2004. DOI: 10.1088/0031-9155/49/9/006.

[32] S. A. Lloyd, I. M. Gagne, M. Bazalova-Carter, and S. Zavgorodni, "Measured and Monte Carlo simulated electron backscatter to the monitor chamber for the Varian

TrueBeam Linac," *Physics in Medicine and Biology*, vol. 61, no. 24, pp. 8779–8793, 2016. DOI: 10.1088/1361-6560/61/24/8779.

[33] P. Sipilä, J. Ojala, S. Kaijaluoto, I. Jokelainen, and A. Kosunen, "Gafchromic ebt3 film dosimetry in electron beams — energy dependence and improved film read-out," *Journal of Applied Clinical Medical Physics*, vol. 17, no. 1, pp. 360–373, 2016. DOI: https://doi.org/10.1120/jacmp.v17i1.5970.

[34] INTERNATIONAL ATOMIC ENERGY AGENCY, *Absorbed Dose Determination in External Beam Radiotherapy* (Technical Reports Series 398). Vienna: INTERNATIONAL ATOMIC ENERGY AGENCY, 2000.

[35] M. Miften, A. Olch, D. Mihailidis, *et al.*, "Tolerance limits and methodologies for imrt measurement-based verification qa: Recommendations of aapm task group no. 218," *Medical Physics*, vol. 45, no. 4, e53–e83, 2018. DOI: https://doi.org/10.1002/mp.12810.

CHAPTER 7
Quality Assurance for Mixed Electron-photon Beam Radiation Therapy using Treatment Log files and MapCHECK

Yee Man Tai[†], **Veng Jean Heng**[†], Marc-André Renaud, Monica Serban, Jan Seuntjens

[†]*: joint first author.*

Article published in: *Medical Physics, 2023.* (https://doi.org/10.1002/mp.16759)

7.1 Preface

In the preceding chapter, we proposed a quality assurance method for MBRT fields using ion chamber and film measurements. For complex and relatively new techniques, it is common clinical practice to perform a PSQA on every EBRT plan to be delivered on patients. However, an ion chamber measurement requires extensive setup and precise phantom positioning, while radiochromic film can only be processed after a delay of several hours. Although feasible, they would represent a significant logistical burden to the clinical workflow were they to be performed prior to every patient treatment. As this problem is applicable to state-of-the-art treatment modalities such as VMAT, vendors have proposed more streamlined PSQA solutions using arrays of detectors such as the MapCHECK®. Similarly, some centers have started using machine log file data to serve as a PSQA tool. Although these methods have been largely applied to photon-based treatments, there are limited studies on their use for QA of electron fields and none in the context of MBRT. In this chapter, we explore the feasibility of using either or a combination of these 2 methods for a more streamlined PSQA of MBRT fields.

7.2 Abstract

Background: Mixed photon-electron beam radiotherapy (MBRT) is a technique that combines the use of both photons and electrons in one single treatment plan to exploit their advantageous and complimentary characteristics. Compared to other photon treatment

modalities, it has been shown that the MBRT technique contributes to better target coverage and organ-at-risk (OARs) sparing. However, the use of combined photons and electrons in one delivery makes the technique more complex and a well established quality assurance (QA) protocol for MBRT is essential.

Purpose: To investigate the feasibility of using MapCHECK and log file-dose reconstruction for MBRT plan verification and to recommend a patient-specific quality assurance (PSQA) protocol for MBRT.

Methods: MBRT plans were robustly optimized for 5 soft tissue sarcoma (STS) patients. Each plan comprised step-and-shoot deliveries of a 6 MV photon beam and a combination of 5 electron beam energies at an SAD of 100 cm. The plans were delivered to the MapCHECK device with collapsed gantry angle and the 2D dose distributions at the detector depth were measured. To simulate the expected dose distribution delivered to the MapCHECK, a MapCHECK computational phantom was modelled in EGSnrc based on vendor-supplied blueprint information. The dose to the detectors in the model was scored using the DOSXYZnrc user code. The agreement between the measured and the simulated dose distribution was evaluated using 2D gamma analysis with a gamma criterion of 3%/2mm and a low dose threshold of 10%.

One of the plans was selected and delivered with a rotating gantry angle for trajectory log file collection. To evaluate the potential inter-linac and intra-linac differences, the plan was delivered repeatedly on three linacs. From the collected log files, delivery parameters were retrieved to recalculate the 3D dose distributions in the patient's anatomy with DOSXYZnrc. The recalculated mean dose to the clinical target volume (CTV) and OARs from all deliveries were computed and compared with the planned dose in terms of percentage difference. To validate the accuracy of log file-based QA, the log file-recalculated dose was also compared with film measurement.

Results: The agreement of the total dose distribution between the MapCHECK measurement and simulation showed gamma passing rates of above 97% for all 5 MBRT plans. In

the log file-dose recalculation, the difference between the recalculated and the planned dose to the CTV and OARs were below 1% for all deliveries. No significant inter- or intra-linac differences were observed. The log file-dose had a gamma passing rate of 98.6% compared to film measurement.

Conclusion: Both the MapCHECK measurements and log file-dose recalculations showed excellent agreement with the expected dose distribution. This study demonstrates the potential of using MapCHECK and log files as MBRT QA tools.

7.3 Introduction

Megavoltage photons remain the most commonly used particle type in external beam radiation therapy (EBRT). Modern radiotherapy techniques like IMRT [1] and VMAT [2] enable the delivery of a highly conformal dose to the target with photon beams. The high penetration power of photons is a desirable feature for treating deep-seated tumours, however, it often contributes to unnecessary dose to surrounding normal tissues. In contrast, electron beams have a short range and a steep dose fall-off, making them suitable for treating superficial targets. Nevertheless, the use of patient-specific cutouts and bolus in conventional electron radiotherapy makes the treatment more complicated and less efficient [3].

Various studies have been conducted to explore the possibility of modulated electron radiotherapy (MERT), in which a tertiary, often multi-leaf collimator (MLC) is used to modulate the energy and intensity of electron beams [3]–[7]. Electron beams can be modulated by either the photon MLC (pMLC) or an electron-specific tertiary collimator [8]. Using pMLC for electron beam collimation enables the delivery of both photon and electrons with the same set-up. However, as pMLC-based MBRT do not use electron applicators, it results in penumbra widening. To restore the electron beam penumbra, Klein *et al.* [4] suggested that the source-to-surface distance (SSD) should be shortened to 70 cm to reduce electron

dispersion. Karlsson *et al.* [6] experimented replacing the air in the treatment head with helium to minimize the effect of electron scattering. The results demonstrated a 40% reduction in the penumbra width at an SSD of 100 cm.

To overcome the difficulties of using pMLC, efforts have been made to develop electron-specific MLC. Ma *et al.* [3] developed a prototype electron MLC that could be attached to an electron applicator on a Varian Clinac 2100C accelerator. It was shown that the dosimetric characteristic of the electron MLC was comparable to that of the photon MLC without needing to replace the air in the accelerator head with helium. Al-Yahya *et al.* [8] proposed using the few-leaf electron collimator (FLEC) to deliver MERT in an automated manner. They showed that using MERT with FLEC results in better treatment quality compared to conventional treatment techniques. However, despite various accessories being designed for tertiary electron beam modulation, their clinical implementation is limited.

Mixed photon-electron beam radiotherapy (MBRT) allows one to exploit the advantageous characteristic of both particles in a single plan. Due to their hybrid energy deposition pattern, MBRT could be well-suited to treat superficial cancer with some deep-seated components [9]. Early studies have demonstrated that the use of pMLC-based mixed-beam plan provided a target coverage comparable to the IMRT technique but contributed a lower healthy tissue dose in loco-regional radiotherapy for breast cancer and head and neck cancers [10], [11]. Alexander *et al.* [12] investigated the possibility of combining FLEC-based MERT with photon beams by re-optimization MERT plans with two tangential MLC-collimated photon beams added. Mueller *et al.* [9] developed a Monte Carlo-based treatment planning process for simultaneous optimization of photon and electron apertures to generate MBRT plans. Renaud *et al.* [13] developed an optimization model using the column generation method for MBRT treatment planning, whereas Renaud *et al.* [14] demonstrated the importance of robust optimization in achieving deliverable plans. These studies demonstrated the superiority of MBRT in target coverage and OARs sparing over other treatment modalities, including IMRT, and MERT.

Like IMRT and VMAT, MBRT uses MLC-collimated beams to achieve conformal dose distribution with sharp dose fall-off but comprises multiple beam energies with each having its specific MLC apertures. Using pMLC to collimate electron beam with no applicator also leads to more significant electron scattering. Therefore, a patient-specific quality assurance (PSQA) protocol for MBRT needs to be well-established before implementing the technique clinically. Heng *et al.* [15] demonstrated the use of an ionization chamber and film dosimetry to perform PSQA for MBRT plans on a PMMA phantom and a Solid Water phantom. Heath *et al.* [16] suggested the possibility of using log file-based dose calculation and EPID measurement for evaluating the delivery accuracy of MBRT. However, to our knowledge, no prior studies have examined the use of commercial QA devices for MBRT plan verification. In this study, we attempt to devise a new QA framework for MBRT by combining MapCHECK (Sun Nuclear, Melbourne, FL) and log file analysis. To do this, we performed ab-initio modelling of the MapCHEKC to simulate its complex electron beam deliveries.

The purpose of this study is to investigate the feasibility of using MapCHECK combined with log file analysis as PSQA tools for MBRT plans of soft-tissue sarcoma patients.

7.4 Methods

7.4.1 Robust Treatment Planning and Delivery

MBRT plans for five patients with soft-tissue sarcoma (STS) were robustly optimized using `brems`, an in-house web-based treatment Monte Carlo planning and inverse optimization system. Robustness was established with respect to setup errors by optimizing on the nominal isocentre position combined with -5 mm, +5 mm shifted positions along the three axes. The plans consisted of step-and-shoot deliveries of a 6 MV photon beam and a combination of electron beams of 5 energies (6 MeV, 9 MeV, 12 MeV, 16 MeV, 20 MeV) at an SAD of 100 cm. The plans were delivered on several Varian TrueBeam linacs.

The five robust MBRT plans were delivered onto the MapCHECK with collapsed gantry angle at 0 degree (Varian IEC 601-2-1 convention). This was to avoid complications arising

from attenuation and scattering when beams enter the MapCHECK through the sides or travel through the couch.

Log file-3D dose reconstruction was performed for one patient plan. To this end, the plan was delivered with a rotating gantry angle and log files were collected for 3D dose recalculation in the patient's anatomy. To examine the potential variations across repeated deliveries on one linac or different linacs, the plan was delivered five times on each of the three Varian TrueBeam linacs (Linac 1, Linac 2, Linac 3) to evaluate the inter-linac and intra-linac differences.

7.4.2 MapCHECK-based Quality Assurance

Phantom Modelling

MapCHECK 2 is a two-dimensional planar dosimetry tool that contains a 26 cm x 32 cm detector array consisting of 1527 solid state detectors arranged in a staggered pattern (Fig. 7–1). Above the detector array, there is a 1.2 cm thick buildup layer made of polycarbonate, which is equivalent to 2 cm of water [17]. MapCHECK 2 was accompanied by the Sun Nuclear Corporation® (SNC) patient software, which handles calibration and measurement.

To compare the measurements to simulations, a computational MapCHECK phantom was modelled in EGSnrc [18] to calculate the dose to the detectors in the MapCHECK. The device was precisely modelled according to blueprints provided by the manufacturer. The detectors' position and arrangement of the MapCHECK phantom as modeled in EGSnrc is shown in Fig. 7–1. The computational model also included the treatment couch in order to simulate the effect of back-scattering during the delivery.

MapCHECK Calibration

Before measurement, a MapCHECK array calibration was performed to account for the sensitivity difference between detectors. A 37 cm $\times$ 37 cm jaw-defined 6 MV field was used for the array calibration of photon beams. For the array calibration of electron beams, a 25 cm $\times$ 25 cm 12 MeV field collimated by an electron applicator were delivered to the device. Both energies were delivered at 100 cm SSD. The exposure was repeated over four MapCHECK

orientations as instructed in the SNC patient software. The array was calibrated separately for photons and electrons to minimize differences in energy dependence between detectors. The experimental setup for MapCHECK calibration and measurement is shown in Fig. 7–2.

Dose calibration in absolute terms was performed for the conversion from relative dose to absorbed dose. The device was exposed to a 10 cm × 10 cm radiation field of each energy of interest at an SSD of 100 cm. The corresponding MC-calculated absorbed dose-to-water $D_{\text{water}}^{\text{Calibration}}$ at the detector depth was entered into the SNC patient software. The MapCHECK was positioned such that the centre detector aligned with the central axis of the radiation field. The dose calibration was repeated for 6 MV, 6 MeV, 9 MeV, 12 MeV, 16 MeV, and 20 MeV.

To derive $D_{\text{water}}^{\text{Calibration}}$, the delivery of 10 cm × 10 cm fields was simulated for the MapCHECK phantom in EGSnrc. The Varian-supplied phase space files were used as the beam source and the dose to each voxel in the phantom was scored with the DOSXYZnrc user-code. The Monte Carlo dose $D_{\text{detector}}^{\text{MC}}$ to the voxel of the centre detector in the MapCHECK phantom was obtained and converted to the MC dose-to-water $D_{\text{water}}^{\text{MC}}$ with the mass electronic stopping power ratio $[S_{el}/\rho]_{\text{detector}}^{\text{water}}$ of water-to-detector material (eq. 7.1),

$$D_{\text{water}}^{\text{MC}} = D_{\text{detector}}^{\text{MC}} \times [S_{\text{el}}/\rho]_{\text{detector}}^{\text{water}} \tag{7.1}$$

Then, the MC dose-to-water $D_{\text{water}}^{\text{MC}}$ was converted into physical dose-to-water $D_{\text{water}}^{\text{Reference}}$ with the energy-dependent Monte Carlo reference dose calibration coefficient N_{MC} (MC dose/1 cGy · MU/primary history) and the number of MU delivered (eq. 7.2),

$$D_{\text{water}}^{\text{Reference}}\,(\text{cGy}) = \frac{D_{\text{water}}^{\text{MC}}}{N_{\text{MC}}} \left(\frac{1\ \text{cGy}}{MU}\right) \times MU \tag{7.2}$$

Since the use of N_{MC} assumed the linac was calibrated in terms of absorbed dose to water to 1 cGy/MU under clinical reference conditions, $D_{\text{water}}^{\text{Reference}}$ (cGy) was further scaled by the actual output D_{output} (cGy/MU) of the linac on the day of measurement to derive the

dose-to-water $D_{\text{water}}^{\text{Calibration}}$ under the calibration condition (eq. 7.3),

$$D_{\text{water}}^{\text{Calibration}}\,(\text{cGy}) = D_{\text{water}}^{\text{Reference}} \times \frac{D_{\text{output}}\,(\text{cGy}/MU)}{1\,(\text{cGy}/MU)} \tag{7.3}$$

The output D_{output} of the linac was measured using an ion chamber in a QA solid water phantom at the reference depth d_{ref}.

2D Dose Interpolation

To analyse the agreement of the dose distributions obtained from simulation and measurement, the two dose planes at the detector depth were compared through 2D gamma analysis. In the MapCHECK, the detector array consists of two detector layers at different depths arranged in a staggered grid pattern, with each layer having a detector spacing of 1 cm (Fig. 7–3). To perform a 2D gamma analysis, the dose to a hypothetical intermediate layer is interpolated in both the measured and simulated dose distributions. For each layer, the detector dose at each of the 2 layers were separately input as scattered data into the Python function `scipy.interpolate.griddata` to interpolate the dose in a 26.2 × 32.2 cm^2 plane with a pixel size of 5 × 5 mm^2. Then, the dose to the intermediate plane was derived by averaging the two interpolated dose planes.

MapCHECK Phantom Verification

To verify the accuracy of the MapCHECK phantom model, field output factors were calculated through Monte Carlo simulations on the phantom and were compared to the measurement. The field output factors were defined as the ratio of the dose to the centre detector in a given field to the dose in the 10 cm × 10 cm field. MLC-defined 3 cm × 3 cm, 5 cm × 5 cm, 8 cm × 8 cm and 10 cm × 10 cm fields of 6 MV photon and 12 MeV electron beams were delivered to the MapCHECK at 100 cm SSD, and the dose to the centre detector was measured and simulated.

To validate that the detector spacing and dimensions of the phantom were correctly modelled, 10 cm × 10 cm and 4 cm × 4 cm fields of all electron energies of interest were also simulated on the MapCHECK phantom and delivered to the MapCHECK at an SSD of 100

cm. The measured and simulated dose distribution of the square fields were compared and their agreement was evaluated by gamma analysis with a 2%/1mm criterion.

MBRT Plan Measurements

The five MBRT plans were delivered to the MapCHECK with collapsed gantry angle and the delivered dose distribution was measured for each energy. The expected dose distribution was simulated on the MapCHECK phantom. When travelling through the MLCs and the phantom, electron beams lose energy due to intensity modulation and scattering. Since the scattering conditions change across positions in the MapCHECK phantom, the energy spectrum of the beam to each voxel of the phantom varies. To account for the difference in beam quality between the calibration condition and the MBRT field, a correction factor was applied to each voxel i in the MapCHECK phantom. The correction factor was derived using the stopping power ratio (SPR) $[[S_{el}/\rho]^{water}_{detector}]^{MBRT}$ of water to detector at a voxel i in the MapCHECK phantom under the measurement condition, and the stopping power ratio of water to detector at the centre detector of the MapCHECK phantom under the calibration condition [15]:

$$D^{MBRT}_{water,i}\,(cGy) = D^{Calibration}_{water,i} \times \frac{[[S_{el}/\rho]^{water}_{detector}]^{MBRT}_{i}}{[[S_{el}/\rho]^{water}_{detector}]^{Calibration}_{centre}} \tag{7.4}$$

The stopping power ratio for each voxel in the MapCHECK was calculated with the SPRXYZnrc Monte Carlo code, which was modified from the SPRRZnrc and DOSXYZnrc code [19]. This code allows the calculation of stopping power ratios to a phantom according to the input parameters defined in the DOSXYZnrc input files. With the SPRXYZnrc code, the distribution of stopping power ratio in the MapCHECK phantom can be obtained in the same scoring grid as in the dose calculation using DOSXYZnrc.

The agreement between the measured and the corrected simulated dose distribution was evaluated using gamma analysis with a gamma criterion of 3%/2mm and a low dose threshold of 10%, as recommended in AAPM TG218 [20] for IMRT QA.

7.4.3 Logfile-based Quality Assurance

Log file collection and dose recalculation

To recalculate the dose distribution in the patients' anatomy, the plan for patient 4 was delivered for log file collection. During the delivery, the Varian TrueBeam system records the axis positions and MU delivered at each control point at every 20 ms [21]. The axis data include gantry angle, collimator angle, couch positions, couch angle, MLC leaf positions and jaw positions. Upon each delivery, the recorded information was output in the format of a trajectory log file. The data in the trajectory log files were then read and parsed with the log analyzer module of the Pylinac Library [22].

The axis data obtained were translated into geometry parameters used in the EGSnrc simulations. The MLC leaves and jaw positions obtained were used in the BEAMnrc input files for beam modelling. The gantry angle, collimator angle, couch positions, couch angle were defined in the DOSXYZnrc input files for dose calculation. The dose was scored in the Monte Carlo phantom of the patients' anatomy with a voxel size of $2.5 \times 2.5 \times 2.5$ mm^3 generated from the CT slices of the patients.

Dose comparison

The mean dose to the patient's CTV and three OARs were computed and the deviations among all set of data were evaluated in terms of percentage difference. The dose discrepancies across deliveries on three linacs and repeated deliveries on one linac were analysed. The dose distribution of the planned and the measured dose were also compared by 3D global gamma analysis with a criterion of 1%/0 mm and 10% low dose threshold.

Validation against film measurement

To validate the accuracy of the log file-reconstructed dose, the patient 4 plan was delivered on a cylindrical PMMA phantom following the procedure described in Heng *et al.* [15]. A Gafchromic EBT3 film was placed at 2 cm depth. The trajectory log file for this delivery was recorded and used for dose reconstruction. Both the log file-reconstructed dose and the

planned dose distribution were compared to the film dose through Gamma analysis with a criterion of 3%/2mm and 10% low dose threshold.

7.5 Results

7.5.1 MapCHECK Phantom Verification

Field output factors

The field output factor for 3 cm × 3 cm, 5 cm × 5 cm, 8 cm × 8 cm and 10 cm × 10 cm 6 MV and 12 MeV radiation fields were computed from simulation results and measurements. The Type A uncertainty of the centre detector dose for both energies and all field sizes was less than 0.2%. The dose to the centre detector and the output factors are shown in Table 7–1. The deviations in field output factors between measurement and calculation were within 1% for 6 MV beam of all field sizes. For 12 MeV, the differences varied from 0.09% for the 8 cm × x 8 cm field to 2.41% for the 3 cm × 3 cm field. The higher difference in output factor for 12 MeV 3 cm × 3 cm field could be caused by the non-flat dose distribution. A small deviation of the centre detector position from the central axis will lead to a substantial discrepancy in the measured dose. For photon fields and larger electron fields, the effect is less pronounced due to their flat dose distribution.

Square Fields

The dose distribution of 4 cm × 4 cm and 10 cm × 10 cm square fields of the six energies of interest were measured and calculated. The SPR $[[S_{el}/\rho]^{water}_{detector}]^{MBRT}_{i}$ of water to detector of each voxel in the phantom was calculated and the SPR ratio correction factor was applied for each delivery. The statistical uncertainty of the SPR of the centre voxel was less than 0.1%. The distribution of the correction factor for a 6 MeV 10 cm × 10 cm field is shown in Fig. 7–4. The agreement between the measurement and calculation was evaluated with gamma analysis with a criterion of 2%/1mm and a low dose threshold of 10%. The gamma passing rates (%GP) of each energy are presented in Table 7–2. For all energies except 6 MeV, the passing rates were above 97% for both field sizes. For 4 cm × 4 cm fields above 6 MeV, the agreement slightly deteriorated with increasing energy, possibly due to the

sharper penumbra of higher energies. The measurement accuracy in the penumbra region was limited by the 1 cm MapCHECK detector spacing. The 4 cm × 4 cm 6 MeV field were found to have the worst agreement with a 88.6% passing rate. This could be caused by the inaccuracies in the effective spot size of the beam model. Since the spot size parameter have a significant impact on the calculated output factor and the field penumbra, especially for small field sizes. A slight deviation of the beam model spot size from the actual treatment unit can result in considerable difference between the calculation and measurement.

7.5.2 MBRT plan verification with MapCHECK

The dose distributions of the collapsed delivery of the five MBRT plans were measured and simulated. The SPR ratio correction factor was applied for each energy contribution (Fig. 7–5). The measurement-calculation agreement was evaluated for each energy contribution and for the sum of all energies in the delivery. The gamma passing rate and MU for each energy for the five plans are tabulated in Table. 7–3. The isodose contour and the gamma map of the dose distribution for patient 1 are shown in Fig. 7–6. The gamma passing rate was above 95% for all energies and all plans except for the energy 9 MeV in Patient 1 and 5.

7.5.3 Log file-dose Reconstruction

For 3D dose reconstruction, the selected plan was delivered five times on each of the three TrueBeam linacs and a total of 15 sets of log file data were collected. The statistical uncertainty of each energy was 2% for voxels receiving more than 50% of the maximum dose. The mean dose to the CTV and three OARs of the patient were computed from the planned and recalculated dose distribution. Table 7–4 compares the planned and recalculated dose from the five deliveries on Linac 1. The averaged mean dose to the CTV was 51.98 with a standard error of ± 0.08 Gy, which was only 0.16% different from the planned dose. Table 7–5 summarizes the dose averaged over the repeated deliveries on each of the three linacs. The inter linac differences in the recalculated and the planned dose to the CTV and OARs were all below 1%. The planned and the reconstructed 3D dose distributions demonstrated a gamma passing rate of 99.1% with 1%/ 0 mm.

A film measurement of the selected plan was compared to its planned and log file-reconstructed dose in Fig. 7–7 and 7–8. Using a gamma criterion of 3%/2mm, the planned dose and log file-reconstructed dose were found to have a gamma passing rate of 98.2% and 98.6%, respectively.

7.6 Discussion

7.6.1 MapCHECK-based Quality Assurance

The comparisons for the simulated and measured output factors and the square field dose distribution verified the accuracy of the MapCHECK phantom model. This ensured that the scattering conditions, the detector spacing and materials in the computational phantom are an accurate representation of the physical MapCHECK device. Excellent agreement between simulated and measured square fields were achieved for all energies with the exception of the 6 MeV 4 cm x 4 cm field, which had a gamma passing rate of only 88.6%. The substantially lower passing rate for this particular field could be attributed to a mismatch in the real beam's spot size as compared to the Varian-supplied phase space. Any discrepancy in the spot size will have the largest effect at smaller field sizes and lower energy due to the increased scattering. A tuning of the phase space to individual linacs may be required to reach better accuracy for 6 MeV beams at smaller field sizes. Nevertheless, this error was only noticeable at the stricter gamma criterion of 2%/1mm. In mixed-beam deliveries of plans, the measured and calculated dose distributions in the physical and the modeled MapCHECK phantom showed excellent agreement. With a gamma criterion of 3%/2mm, the 6 MeV component of every plan had a passing rate over 96.9%. The lowest gamma passing rate, 93.6%, was found in energy 9 MeV of the plan for patient 1. Due to the low MU contribution of the 9 MeV component in this plan, it had minimal impact on the agreement of the plan's total dose distribution, which had an excellent pass rate of 99.8%. The gamma passing rate of the combined dose distribution was above 97% for all plans. Connell *et al.* [23] delivered an automated modulated electron radiation therapy (MERT) plan consisting

of 9 MeV, 12 MeV, 16 MeV and 20 MeV electron beams with the Few Leaf Electron Collimator (FLEC) at a fixed gantry angle onto the MapCHECK and compared the measured dose to the simulated 2D dose plane at a depth of 2 cm in the solid water phantom [23]. The gamma passing rates in that study varied from 86.1% for 12 MeV to 94.8% for 20 MeV using a gamma criterion of 3%/3 mm. The difference in plan-measurement agreement compared to our study could possibly be due to a more accurate representation of the MapCHECK model in the present study compared to the MERT study where it was represented as a homogeneous Solid Water phantom. As the detectors are individually modeled, a direct dose comparison between calculated and measured dose to detector is possible. An accurate modeling of the MapCHECK phantom also simplified the dose calibration at each relevant electron energy since the uncertainty on appropriate water-equivalent thickness, when representing the MapCHECK as a homogeneous Solid Water block, was eliminated.

Various studies have demonstrated the practicability of MapCHECK for rotational IMRT QA [24]–[26]. In the study by Gloi *et al.* [25], the dose distribution of 17 partial arc deliveries from 60° to 300° measured by the MapCHECK showed an average of 97.5% gamma passing rate when compared to the planned dose predicted by the treatment planning system. To reduce the angular dependence of MapCHECK to measure plans with intense lateral fluence, Jursinic *et al.* [24] modified the MapCHECK by filling the air gap with Lucite and offsetting the asymmetry of the diode with copper pieces. It was found that modifying the MapCHECK reduced the angular dependence from ±20% to ±2%.

Ideally, the QA for MBRT could be performed with a rotating gantry, where trajectory log files can be collected while the dose distribution is being measured by the MapCHECK. This could provide a calculation-based and measurement-based QA for an MBRT plan in a single QA delivery. However, in non-collapsed delivery, beams delivered at a gantry angles larger than 90° from the central axis experience high attenuation in the MapCHECK and the couch before reaching the detectors. The scattering condition changes as a function of the incident angle of the beam to the MapCHECK. To accurately simulate the dose to the

MapCHECK in non-collapsed delivery, the configuration and structure of each detector in the phantom needs to be modelled in further detail. In our study, we decided to perform the measurement with collapsed gantry angle as a first step to simplify the validation of the model. The disadvantage of collapsed delivery is that any dose variation due to treatment delivery errors, such as gantry sag, are not considered. But this limitation can be complemented by the log file approach. Future work will investigate the viability of non-collapsed gantry MBRT deliveries on the MapCHECK. A possible way to measure non-collapsed delivery would be to attach the MapCHECK to the gantry. This allows us to take into account the potential delivery errors while keeping the beam perpendicular to the detector plane.

7.6.2 Log file-based Dose Reconstruction

The dose distribution reconstructed using log file data showed excellent agreement with the planned dose with no inter- and intra- linac differences observed. Three Varian TrueBeams and one MBRT plan have been tested in this study. Both planned and log file-reconstructed dose distributions were found to have good agreement with film measurement. Studies have been conducted to evaluate the feasibility of reconstructing VMAT dose distribution in patient anatomies with log file data [27]–[29]. Qian *et al.* [27] replaced the DICOM-RT file with log file data after VMAT delivery and reconstructed the delivered dose distribution on a Catphan-600 phantom generated by CBCT using the anisotropic analytical algorithm (AAA) on Eclipse. The mean dose to the target reconstructed on the CBCT differed from the treatment plan by 1%. Defoor *et al.* [28] reconstructed VMAT dose distribution with log files data using Pinnacle TPS. In their study, the reconstructed mean dose to the PTV for all 15 patients was within 1% when compared to the planned dose. Katsuta *et al.* [29] cross-validated the mean dose to the ionization chamber volume of 10 VMAT plans by log file-reconstruction and measurement. For all plans, the difference between the measured and log file-reconstructed dose to the ionization chamber was $0.00\% \pm 0.01\%$. All these studies showed that log file-reconstructed dose exhibited minimal deviation from the planned dose or measured dose for VMAT plans. In our work, we extended the use of log

file-dose to reconstruct electron deliveries and although the results are not generalizable to other machines, the feasibility of accurately reconstructing the dose distribution of a complex mixed-beam treatment plan is demonstrated for the first time.

In log file-based QA, the planned dose and the recalculated dose are obtained using the same Monte Carlo beam model which had been verified in the previous study by Heng *et al.* [15]. The dose is scored on the true patient's anatomy. This enabled a fair comparison of the two dose distributions as it eliminates difference in the calculation algorithms and the geometry of the phantom [28]. Any deviations observed between the planned and the recalculated dose can be attributed to machine performance and the clinical impact of delivery errors can be identified easily. However, the limitation of using log files is that the log file data is dependent on the linac. Dosimetric error due to linac miscalibrations cannot be detected by log files [29]. Therefore, a log file-based QA should be accompanied by measurement-based QA.

7.6.3 Patient-specific QA protocol for MBRT

A QA protocol for MBRT plan verification could comprise (1) an absolute point dose measurement with ion chamber, (2) a 2D dose measurement using MapCHECK and (3) a 3D dose reconstruction with treatment log files. In the study by Heng *et al.* [15], absolute dose measurement in MBRT fields was performed by inserting an ion chamber into a PMMA cylindrical phantom. Although there were energy dependent differences, the overall composite measured dose differed from the Monte Carlo simulated dose by only -0.03% at a measurement depth of 1.4 cm. With the absolute point dose being verified, the 2D dose distribution under collapsed delivery can be validated by MapCHECK with gamma analysis with the recommended gamma criterion of 3%/2mm. Correcting beam quality difference using SPR ratio may be not clinically feasible as it requires Monte Carlo calculation of the SPR corresponding to the measurement condition for each beam. In Fig. 7–5, the SPR correction factor for each point is close to unity and well within the dose tolerance limits. The gamma maps of the plan for patient 1 with and without applying SPR correction using

the gamma criterion of 1%/2 mm were compared (See Appendix 7–9). The gamma passing rate for the dose distribution with and without SPR correction was 91.58% and 91.50% respectively, which means applying SPR correction contributed minimally to the plan quality and can be ignored. Finally, log file-dose reconstruction could confirm that the machine parameters during the delivery agree with the baseline values.

7.7 Conclusion

This study examined the feasibility of using MapCHECK and log files for PSQA in mixed photon-electron beam radiation therapy (MBRT). Five MBRT plans of patients with soft-tissue sarcoma were optimized for the study. A MapCHECK computational phantom was modelled to simulate the expected dose distribution to the MapCHECK under collapsed delivery. The simulated and the measured total dose distributions demonstrated excellent agreement in all five plans. For 3D dose reconstruction with trajectory log files data, the recalculated dose to the CTV and 3 OARs differed from the planned dose by less than 1% with no significant inter- and intra-linac difference. A PSQA protocol for MBRT using ion chamber, MapCHECK and log files was suggested. Future work will focus on investigating the viability of measuring and simulating dose distributions on MapCHECK under non-collapsed gantry delivery.

7.8 Acknowledgements

The authors would like to acknowledge Dr. Tanner Connell and Michael Evans for their guidance and advice on the use of dosimetry instruments and measurement setups. We thank Mr. Bill Simon of Sun Nuclear Corporation for providing us, under NDA, with construction details of the MapCHECK-2 device. The authors acknowledge support from the Canadian Institute of Health Research Foundation Grant (FDN-143257).

7.9 Conflict of Interest Statement

The authors have no relevant conflicts of interest to disclose.

7.10 Data Availability Statement

The data that support the findings of this study are available from the corresponding author upon reasonable request.

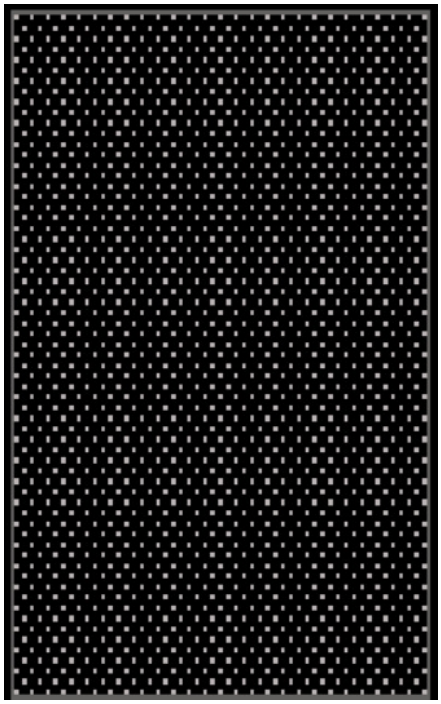

Figure 7–1: Detectors' arrangement of the MapCHECK phantom modelled on EGSnrc. The gray dots represent the positions of detectors.

Table 7–1: Comparison between the simulated and measured output factors for a 3 x 3 cm^2, 5 x 5 cm^2, 8 x 8 cm^2 and 10 x 10 cm^2 for a 6 MV and 12 MeV field.

		Simulation		Measurement		% Difference
	Field size (cm^2)	Detector dose (Gy)	Output factor	Detector dose (Gy)	Output factor	
6 MV	3 x 3	87.70	0.930	87.95	0.938	-0.86
	5 x 5	91.10	0.966	91.06	0.971	-0.53
	8 x 8	93.25	0.989	93.32	0.995	-0.65
	10 x 10	94.29	1	93.75	1	0
12 MeV	3 x 3	34.61	0.457	34.11	0.446	2.41
	5 x 5	58.98	0.778	59.06	0.772	0.79
	8 x 8	73.20	0.966	73.82	0.965	0.09
	10 x 10	75.80	1	76.50	1	0

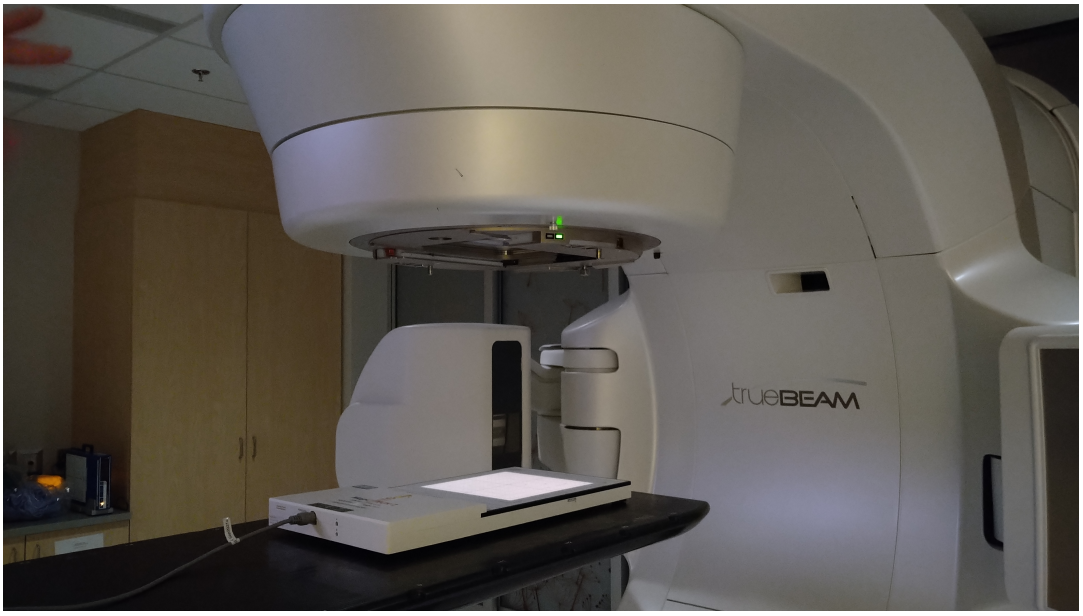

Figure 7–2: Setup for MapCHECK calibration and measurement.

Table 7–2: Gamma passing rate (2%/1mm) of the 10 cm × 10 cm and 4 cm × 4 cm field for each energy.

Beam Energy	6 MeV	9 MeV	12 MeV	16 MeV	20 MeV
4 cm x 4 cm	88.60	100.0	99.29	98.13	97.34
10 cm x 10 cm	99.92	99.90	97.39	98.09	98.92

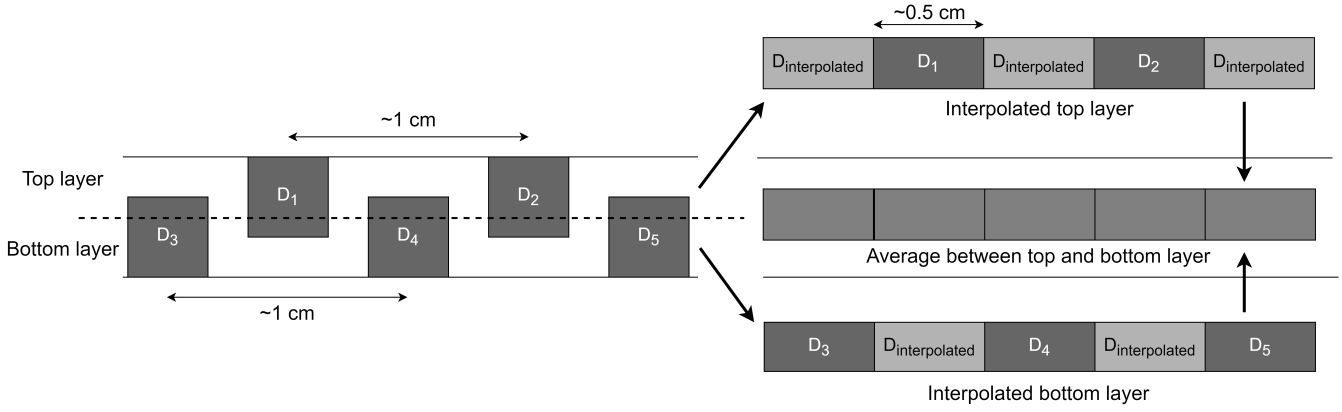

Figure 7–3: Diagram illustrating the two layers of detectors in the MapCHECK detector plane and the method of interpolation.

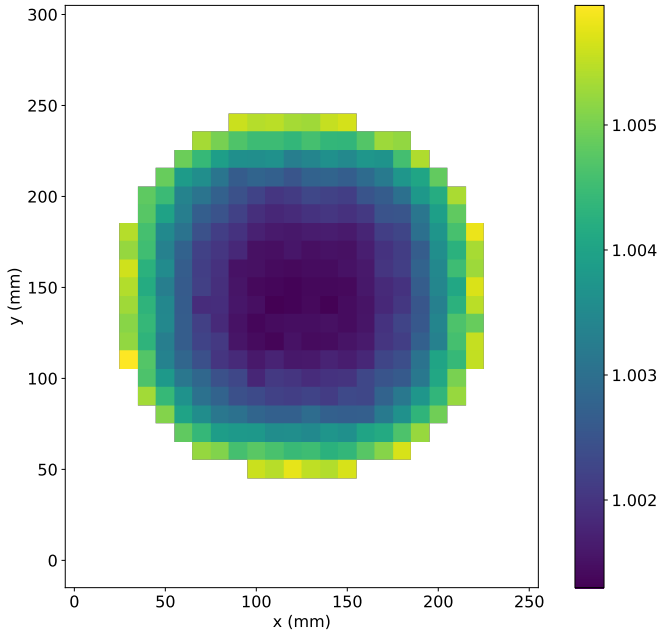

Figure 7–4: Distribution of Stopping Power Ratio (SPR) ratio for a 6 MeV 10 cm × 10 cm field.

Table 7–3: Gamma passing rate (3%/2mm) and MU for each energy components of the five MBRT plans.

Patients	Energy	6 MV	6 MeV	9 MeV	12 MeV	16 MeV	20 MeV	Total
Patient 1	MU	6342	0	445	6878	6370	5525	25565
	% GP	98.4	/	93.6	95.6	99.9	99.9	99.8
Patient 2	MU	8093	0	1444	2045	9072	7995	28649
	% GP	97.4	/	100	98.8	97.1	100	97.2
Patient 3	MU	6975	2414	0	9164	11262	9229	39045
	% GP	96.4	99.3	/	98.2	100	99.6	97.8
Patient 4	MU	5807	2401	5598	3129	13579	12334	42847
	% GP	96.2	96.9	95.1	98.2	98.7	100	98.0
Patient 5	MU	6799	7829	5426	5991	4072	8010	38126
	% GP	97.6	98.2	93.7	98.3	97.8	99.7	98.2

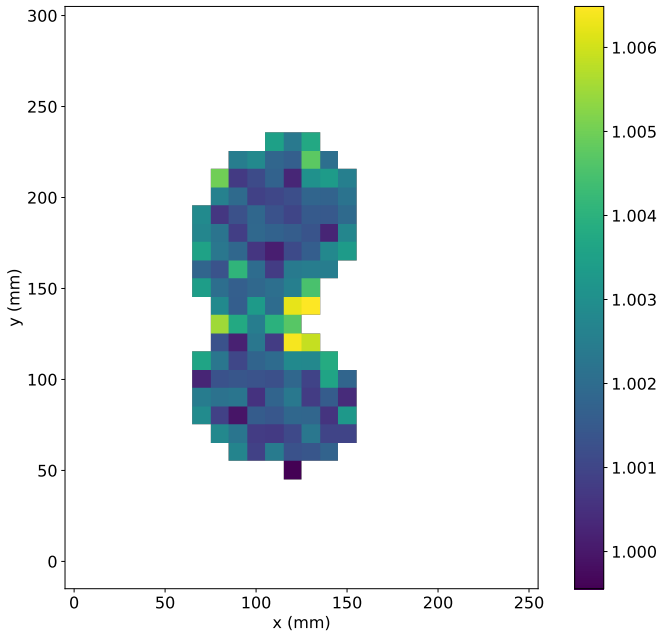

Figure 7–5: Distribution of Stopping Power Ratio (SPR) ratio for the 12 MeV components of patient 3.

Table 7–4: Comparison between planned and log file-recalculated mean dose to the CTV and 3 OARs of the 5 deliveries on Linac 1. "Tissue strip" refers to a structure defined as the normal tissue region outside of the PTV.

	CTV		Bone (Left leg)		Left leg		Tissue Strip	
Planned dose (Gy)	51.89		3.13		4.81		7.19	
	Min	Max	Min	Max	Min	Max	Min	Max
Log file dose (Gy)	51.89	52.28	3.15	3.16	4.80	4.84	7.17	7.22
	51.98 ± 0.08		3.15 ± 0.00		4.83 ± 0.01		7.21 ± 0.01	
	Min	Max	Min	Max	Min	Max	Min	Max
Difference (%)	-0.01	0.74	0.35	0.67	-0.25	0.58	-0.36	0.36
	0.16 ± 0.15		0.56 ± 0.05		0.39 ± 0.16		0.18 ± 0.14	

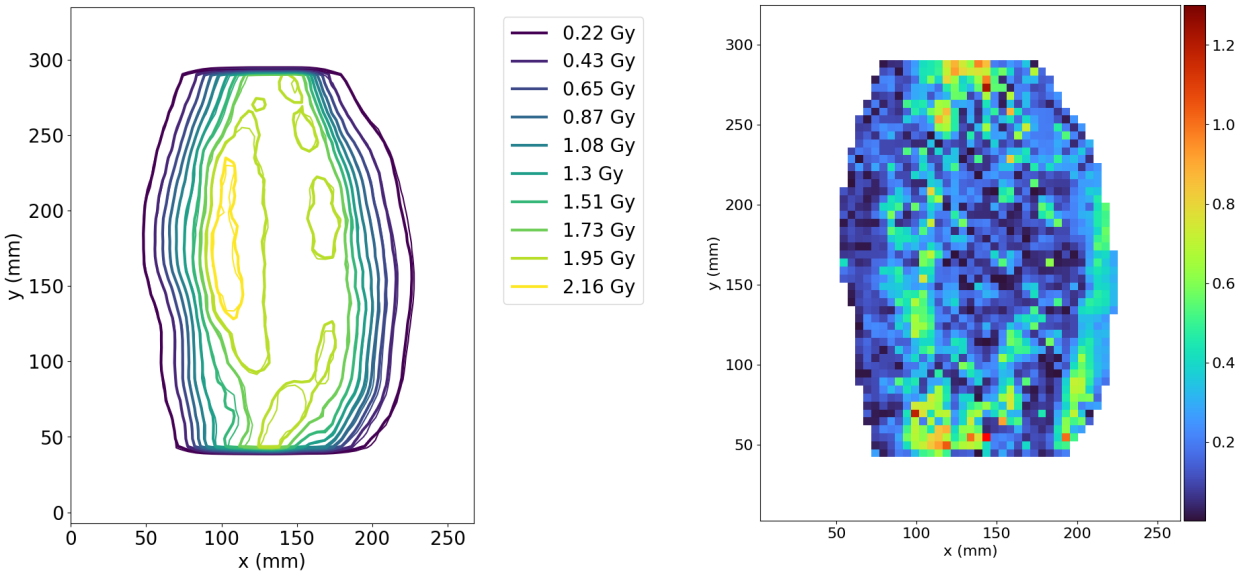

(a) Isodose line contour.

(b) Gamma map.

Figure 7–6: Isodose line contour (a) and the gamma map (b) of the MBRT plan total dose distribution for patient 1. The thin and thick isodose line indicate the measurement and the simulation, respectively.

Table 7–5: Comparison between the planned and log file-recalculated mean dose to the CTV and 3 OARs averaged over 5 deliveries on each of the 3 linacs.

		CTV	Bone (Left leg)	Left Leg	Tissue Strips
Planned	Dose (Gy)	51.89	3.13	4.81	7.19
Log file (Linac 1)	Dose (Gy)	51.98 ± 0.08	3.15 ± 0.00	4.83 ± 0.01	7.21 ± 0.01
	Difference (%)	0.16 ± 0.15	0.56 ± 0.05	0.39 ± 0.16	0.18 ± 0.14
Log file (Linac 2)	Dose (Gy)	51.76 ± 0.01	3.11 ± 0.00	4.81 ± 0.00	7.16 ± 0.00
	Difference (%)	-0.26 ± 0.02	-0.63 ± 0.08	-0.04 ± 0.03	-0.54 ± 0.04
Log file (Linac 3)	Dose (Gy)	51.91 ± 0.01	3.15 ± 0.00	4.84 ± 0.00	7.21 ± 0.00
	Difference (%)	0.03 ± 0.01	0.63 ± 0.02	0.49 ± 0.01	0.23 ± 0.02

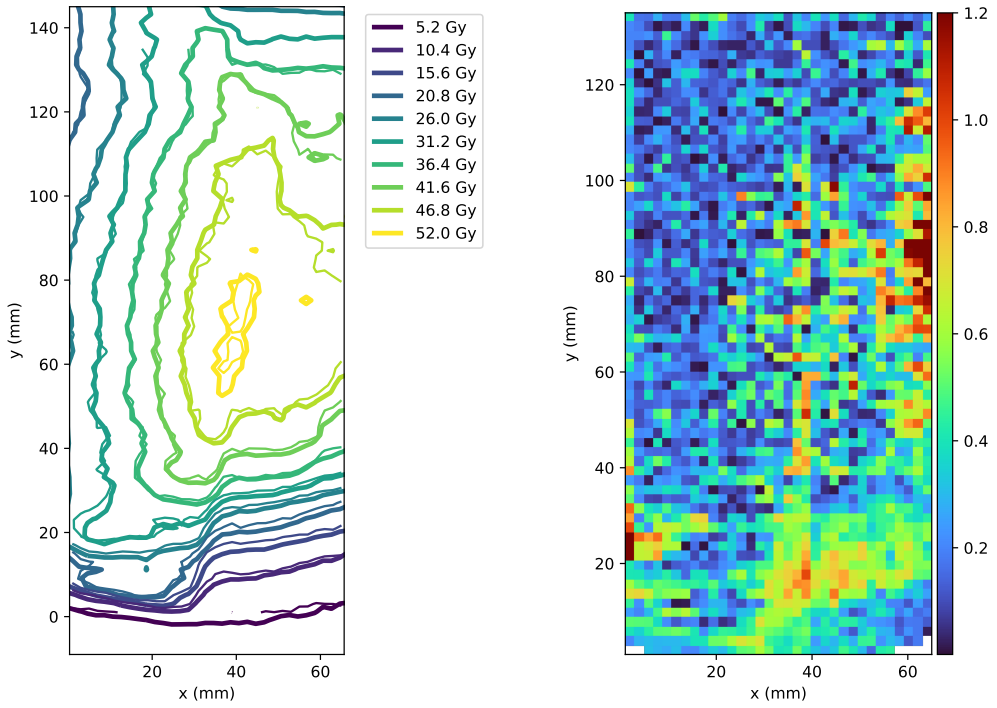

(a) Log file isodose line contour

(b) Log file gamma map

Figure 7–7: Gamma map comparison of the log file dose vs. measured film dose with a gamma pass rate is 98.6% (3%/2mm). The thin and thick isodose line indicate the measurement and the simulation, respectively.

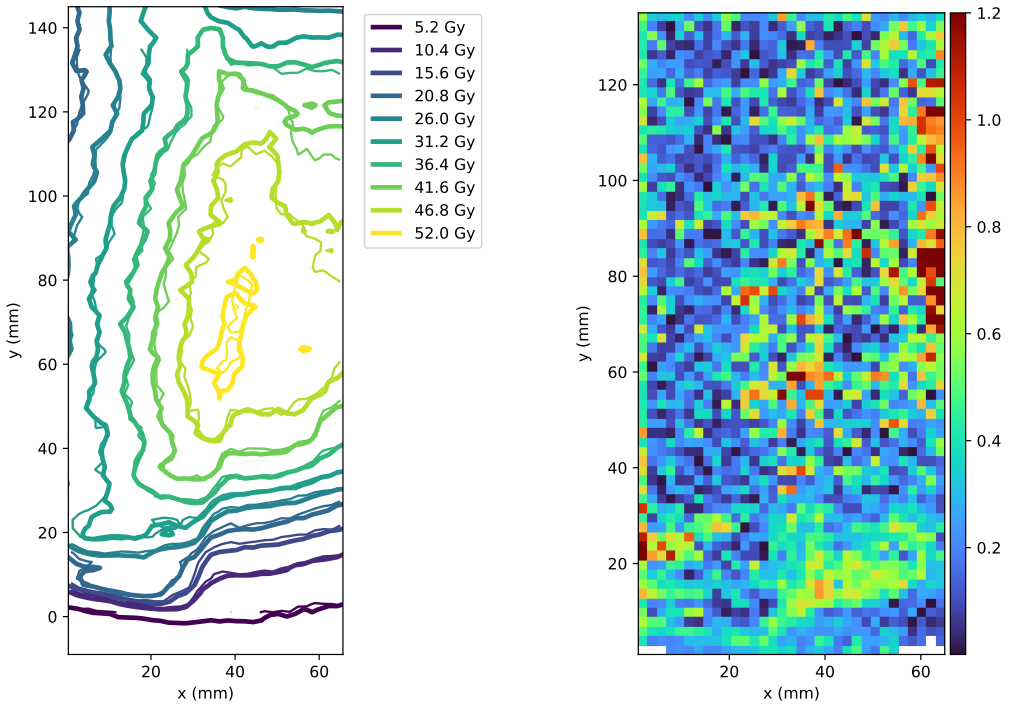

(a) Planned isodose line contour

(b) Planned gamma map

Figure 7–8: Gamma map comparison of the planned vs. measured film dose with a gamma pass rate of 98.2% (3%/2mm). The thin and thick isodose line indicate the measurement and the simulation, respectively.

7.11 Appendix

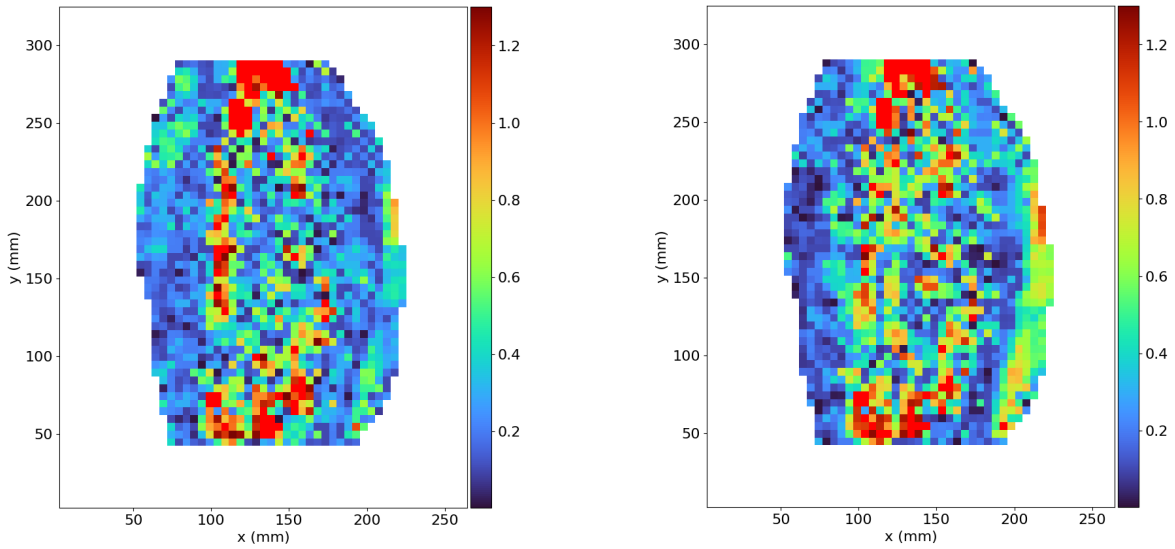

(a) With SPR correction.

(b) Without SPR correction.

Figure 7–9: The gamma map (1%/2mm) of the MBRT plan total dose distribution for patient 1 with (a) and without (b) stopping power ratio (SPR) ratio.

REFERENCES

[1] T. Bortfeld, "IMRT: A review and preview," *Physics in Medicine and Biology*, vol. 51, no. 13, R363–R379, Jun. 2006. DOI: 10.1088/0031-9155/51/13/r21.

[2] K. Otto, "Volumetric modulated arc therapy: Imrt in a single gantry arc," *Medical Physics*, vol. 35, no. 1, pp. 310–317, 2008. DOI: https://doi.org/10.1118/1.2818738.

[3] C.-M. C. Ma, T. Pawlicki, M. Lee, *et al.*, "Energy- and intensity-modulated electron beams for radiotherapy," *Physics in medicine and biology*, vol. 45, pp. 2293–311, Sep. 2000. DOI: 10.1088/0031-9155/45/8/316.

[4] E. E. Klein, Z. Li, and D. A. Low, "Feasibility study of multileaf collimated electrons with a scattering foil based accelerator," *Radiotherapy and Oncology*, vol. 41, no. 2, pp. 189–196, 1996. DOI: https://doi.org/10.1016/S0167-8140(96)01822-1.

[5] J. M. Moran, M. K. Martel, I. A. D. Bruinvis, and B. A. Fraass, "Characteristics of scattered electron beams shaped with a multileaf collimator," *Medical Physics*, vol. 24, no. 9, pp. 1491–1498, 1997. DOI: https://doi.org/10.1118/1.598046.

[6] M. G. Karlsson, M. Karlsson, and C.-M. Ma, "Treatment head design for multileaf collimated high-energy electrons," *Medical Physics*, vol. 26, no. 10, pp. 2161–2167, 1999. DOI: https://doi.org/10.1118/1.598732.

[7] M. Blomquist, M. Karlsson, B. Zackrisson, and M. Karlsson, "Multileaf collimation of electrons - clinical effects on electron energy modulation and mixed beam therapy depending on treatment head design," *Physics in medicine and biology*, vol. 47, pp. 1013–24, May 2002. DOI: 10.1088/0031-9155/47/7/302.

[8] K. Al-Yahya, D. Hristov, F. Verhaegen, and J. Seuntjens, "Monte carlo based modulated electron beam treatment planning using a few-leaf electron collimator - feasibility study," *Physics in medicine and biology*, vol. 50, pp. 847–57, Apr. 2005. DOI: 10.1088/0031-9155/50/5/009.

[9] S. Mueller, M. K. Fix, A. Joosten, *et al.*, "Simultaneous optimization of photons and electrons for mixed beam radiotherapy," *Physics in Medicine & Biology*, vol. 62, pp. 5840–5860, 2017.

[10] T. Jansson, H. Lindman, K. Nygård, *et al.*, "Radiotherapy of breast cancer after breast-conserving surgery: An improved technique using mixed electron–photon beams with a multileaf collimator," *Radiotherapy and Oncology*, vol. 46, no. 1, pp. 83–89, 1998. DOI: 10.1016/s0167-8140(97)00176-x.

[11] X.-k. Mu, L. Olofsson, M. Karlsson, R. Sjögren, and B. Zackrisson, "Can photon imrt be improved by combination with mixed electron and photon techniques?" *Acta Oncologica*, vol. 43, pp. 727–735, 2004.

[12] A. Alexander, E. T. Soisson, M. Renaud, and J. Seuntjens, "Direct aperture optimization for flec-based mert and its application in mixed beam radiotherapy.," *Medical physics*, vol. 39 8, pp. 4820–31, 2012.

[13] M.-A. Renaud, M. Serban, and J. Seuntjens, "On mixed electron–photon radiation therapy optimization using the column generation approach," *Medical Physics*, vol. 44, no. 8, pp. 4287–4298, 2017. DOI: https://doi.org/10.1002/mp.12338.

[14] M.-A. Renaud, M. Serban, and J. Seuntjens, "Robust mixed electron–photon radiation therapy optimization," *Medical Physics*, vol. 46, no. 3, pp. 1384–1396, 2019. DOI: https://doi.org/10.1002/mp.13381.

[15] V. J. Heng, M. Serban, J. Seuntjens, and M.-A. Renaud, "Ion chamber and film-based quality assurance of mixed electron-photon radiation therapy," *Medical Physics*, vol. 48, no. 9, pp. 5382–5395, 2021. DOI: https://doi.org/10.1002/mp.15081.

[16] E. Heath, S. Mueller, G. Guyer, *et al.*, "Implementation and experimental validation of a robust hybrid direct aperture optimization approach for mixed-beam radiotherapy," *Medical Physics*, vol. 48, Sep. 2021. DOI: 10.1002/mp.15258.

[17] *Reference guide, mapcheck 2™*, Sun Nuclear Corporation, Melbourne, Florida, USA, 2010, pp. 229–230.

[18] I. Kawrakow and D. W. O. Rogers, "The egsnrc code system: Monte carlo simulation of electron and photon transport," eng, Tech. Rep., 2003, Collection / Collection : NRC Publications Archive / Archives des publications du CNRC.

[19] D. W. O. Rogers, I. Kawrakow, J. P. Seuntjens, B. R. B. Walters, and E. Mainegra-Hing, "NRC User Codes for EGSnrc," National Research Council of Canada, Tech. Rep., 2003. DOI: 10.1080/17425255.2017.1234605.

[20] M. Miften, A. Olch, D. Mihailidis, *et al.*, "Tolerance limits and methodologies for imrt measurement-based verification qa: Recommendations of aapm task group no. 218," *Medical Physics*, vol. 45, no. 4, e53–e83, 2018. DOI: https://doi.org/10.1002/mp.12810.

[21] *Truebeam™ trajectory log file specification*, Varian Medical System, Palo Alto, California, USA, 2011.

[22] J. Kerns, *Pylinac*, https://github.com/jrkerns/pylinac, 2021.

[23] T. Connell, A. Alexander, P. Papaconstadopoulos, *et al.*, "Delivery validation of an automated modulated electron radiotherapy plan," *Medical Physics*, vol. 41, no. 6Part1, p. 061 715, 2014. DOI: https://doi.org/10.1118/1.4876297.

[24] P. A. Jursinic, R. Sharma, and J. Reuter, "Mapcheck used for rotational imrt measurements: Step-and-shoot, tomotherapy, rapidarc," *Medical Physics*, vol. 37, no. 6Part1, pp. 2837–2846, 2010. DOI: https://doi.org/10.1118/1.3431994.

[25] A. Gloi, R. Buchanan, C. Zuge, and A. Goettler, "Rapidarc quality assurance through mapcheck," *Journal of applied clinical medical physics / American College of Medical Physics*, vol. 12, p. 3251, Jan. 2011. DOI: 10.1120/jacmp.v12i2.3251.

[26] G. Rinaldin, L. Perna, G. Agnello, *et al.*, "Quality assurance of rapid arc treatments: Performances and pre-clinical verifications of a planar detector (mapcheck2)," *Physica Medica*, vol. 30, no. 2, pp. 184–190, 2014. DOI: https://doi.org/10.1016/j.ejmp.2013.05.004.

[27] J. Qian, L. Lee, W. Liu, *et al.*, "Dose reconstruction for volumetric modulated arc therapy (vmat) using cone-beam ct and dynamic log files," *Physics in medicine and biology*, vol. 55, pp. 3597–610, Jul. 2010. DOI: 10.1088/0031-9155/55/13/002.

[28] D. L. Defoor, L. A. Vazquez-Quino, P. Mavroidis, N. Papanikolaou, and S. Stathakis, "Anatomy-based, patient-specific vmat qa using epid or mlc log files," *Journal of Applied Clinical Medical Physics*, vol. 16, no. 3, pp. 206–215, 2015. DOI: https://doi.org/10.1120/jacmp.v16i3.5283.

[29] Y. Katsuta, N. Kadoya, Y. Fujita, *et al.*, "Patient-specific quality assurance using monte carlo dose calculation and elekta log files for prostate volumetric-modulated arc therapy," *Technology in Cancer Research & Treatment*, vol. 16, pp. 1220–1225, 2017.

CHAPTER 8
Robust mixed electron-photon radiation therapy planning for soft tissue sarcoma

Veng Jean Heng, Monica Serban, Marc-André Renaud, Carolyn Freeman, Jan Seuntjens

Article published in: *Medical Physics, 2023.* (https://doi.org/10.1002/mp.16709)

8.1 Preface

In chapter 5, we described the treatment planning workflow for MBRT while in chapter 6 and 7 we proposed multiple methods for MBRT QA as well as evidence of accurate dose deliveries of MBRT plans. However, paramount to the clinical implementation of any new treatment technique is its benefit to patients. Clinicians must be able to clearly identify a subset of patients for which an MBRT treatment offers a clinically significant improvement to the patient's care compared to the current standard of care. Although some studies have demonstrated the dosimetric potential of MBRT on head & neck, chest walls, breast and sarcomas, they were of limited scope as their sample size consisted of 1-2 handpicked cases. In this chapter, we compare the use of MBRT for soft tissue sarcomas of the lower extremity to the photon-only standard of care treatment through a retrospective treatment planning study.

8.2 Abstract

Background: Mixed electron-photon beam radiation therapy (MBRT) is an emerging technique in which external electron and photon beams are simultaneously optimized into a single treatment plan. MBRT exploits the steep dose falloff and high surface dose of electrons while maintaining target conformity by leveraging the sharp penumbra of photons.

Purpose: This study investigates the dosimetric benefits of MBRT for soft tissue sarcoma (STS) patients.

Material and methods: A retrospective cohort of 22 STS of the lower extremity treated

with conventional photon-based VMAT were replanned with MBRT. Both VMAT and MBRT treatments were planned on the Varian TrueBeam linac using the Millenium multi-leaf collimator. No electron applicator, cutout or additional collimating devices were used for electron beams of MBRT plans. MBRT plans were optimized to use a combination of 6 MV photons and 5 electron energies (6, 9, 12, 16, 20 MeV) by a robust column generation algorithm. Electron beams in this study were planned at standard 100 cm SAD. The dose to the CTV, bone, normal tissue strip and other OARs were compared using a Wilcoxon signed-rank test.

Results: As part of the original VMAT treatment, tissue-equivalent bolus was required in 10 of the 22 patients. MBRT plans did not require bolus by virtue of the higher electron entrance dose. CTV coverage by the prescription dose was found to be clinically equivalent between plans of either modality: $V_{50\text{Gy}}(\text{MBRT}) = 97.9 \pm 0.2\%$ vs $V_{50\text{Gy}}(\text{VMAT}) = 98.1 \pm 0.6\%$ (p=0.34). Evaluating the absolute paired difference between doses to organs-at-risk in MBRT and VMAT plans, we observed lower $V_{20\text{Gy}}$ to normal tissue in MBRT plans by $14.9 \pm 3.2\%$ ($p < 10^{-6}$). Similarly, $V_{50\text{Gy}}$ to bone was found to be decreased by $8.2 \pm 4.0\%$ ($p < 10^{-3}$) of the bone volume.

Conclusion: For STS with subcutaneous involvement, MBRT offers statistically significant sparing of organs-at-risk without sacrificing target coverage when compared to VMAT. MBRT plans are deliverable on conventional linacs without the use of electron applicators, shortened SSD or bolus. This study shows that MBRT is a logistically feasible technique with clear dosimetric benefits.

Running title: Robust MBRT for soft tissue sarcoma

8.3 Introduction

Soft tissue sarcoma (STS) is a rare malignant tumor with 13,190 new cases estimated in the United States in 2022[1]. Although STS can affect any site of the body, the majority arise in the extremities with 59% of them localized [2]. Treatment consists of surgical

resection with negative margins. Many will also receive preoperative radiation therapy to reduce the risk of local recurrence after surgery alone [3]. Image-guided radiation therapy has allowed for more conformal treatment, leading to lower doses to normal tissues and lower risk of wound complications [4], [5]. The use of bolus (tissue-equivalent material placed on patient's skin) may be needed for cases where the clinical target volume (CTV) involves skin or subcutaneous tissue that would not receive an adequate dose otherwise [3]. The use of bolus is however associated with greater risk of skin toxicity [6] and the variability in its preparation results in greater uncertainty in planning dose calculations. The American Society for Radiation Oncology (ASTRO) guidelines recommend against the routine use of tissue-equivalent bolus for most sarcomas [3].

The feasibility and potential benefits of modulated electron radiation therapy (MERT), delivered using either additional collimators [7]–[14] or the photon multi-leaf collimators (pMLC) [7], [15]–[18], is addressed in a number of studies. By leveraging the limited penetration depth and high surface dose of electron beams, electron-only MERT treatment plans were shown to deliver lower doses to normal tissue than photon-only plans. This however comes at the cost of worse target dose homogeneity [18], [19]. Mixed electron-photon beam radiation therapy (MBRT) delivered using an existing pMLC is an emerging technique in which both external electron and photon beam are simultaneously optimized into a single treatment plan [20]–[26]. MBRT has been shown to provide superior sparing of normal tissue without sacrificing target coverage [20], [22]–[24]. For tumors with superficial involvement, MBRT offers the possibility of excellent target coverage without the use of bolus. The steep depth dose curve of electron beams allow MBRT plans to better spare healthy tissue and organs-at-risk (OAR) at depths beyond the tumor. Electron apertures in MBRT deliveries are collimated using only the existing pMLC. Due to significant electron scatter in air, the penumbra of electron beams collimated with pMLC is known to be wider at larger source-to-surface distance (SSD) [15], [27]. Deliveries of electron apertures in MERT and MBRT

plans have therefore so far been thought to require shortened SSD of 70-80 cm [28].

Patient setup error is traditionally accounted for in photon-based radiotherapy by using the concept of a planning target volume (PTV) [29]. Assuming an adequate choice of margins, by prescribing the dose to the PTV, the CTV will receive the prescription dose despite setup errors or patient/organ motion. The underlying assumption in this method is that the static dose cloud approximation holds: the spatial dose distribution is not significantly affected by changes in patient positioning. This assumption has been shown to not hold true in the case of charged particles and has lead to the development of robust optimization for intensity modulated proton therapy [30]. Using a similar approach, Renaud et al. implemented robust optimization in the context of MBRT [25]. They showed that MBRT plans must be robustly optimized to properly account for patient setup and motion uncertainties. In this particular implementation, dose distributions are calculated explicitly in additional error scenarios where a positioning error is artificially introduced. The cost function can then be calculated as a weighted average of the cost function of each scenario. Accurate deliveries of robust MBRT plans have been experimentally validated on conventional linacs with excellent agreements between Monte Carlo-calculated doses and ion chamber and film measurements [26], [31].

This study seeks to demonstrate the applicability and benefits of MBRT for STS of the extremity. By performing a retrospective treatment planning study, MBRT is dosimetrically compared to the standard of care: photon-based Volumetric Modulated Arc Therapy (VMAT).

8.4 Methods

8.4.1 Patient selection

A retrospective cohort of 22 STS patients was selected among 38 consecutive patients treated at the McGill University Health Centre between December 2017 and June 2021. All

patients completed a 25-fraction photon-only VMAT preoperative treatment on a Varian TrueBeam linear accelerator (Varian Medical Systems, Palo Alto, CA). Only patients with STS of the lower extremity, without tumor extent above the groin or within the foot or ankle, were chosen. This was done to keep the patient geometry within the cohort to be mostly homogeneous. Exclusion criteria included interrupted treatments, CTVs length >36 cm in the cranial-caudal direction, CTV size >14 cm in the axial plane, or CTV location being unsuitable for electron treatments. Unsuitable CTV location refers to CTVs starting either too deep (>1 cm from the skin) or whose shallow regions are obstructed by OARs such as the contralateral leg. The exclusion of patients with too long or large CTV is such that the memory size of beamlets do not exceed our cluster's maximum memory during MBRT plan optimization. The consort diagram in Fig. 8–1 enumerates the number of patients excluded for each criterion. The median tumor size, as measured by its largest diameter, was 11.7 cm. For comparison, the median tumor size of the Radiation Therapy Oncology Group RTOG 0630 trial's cohort B was 10.5 cm [5]. Written institutional permission for the use of anonymized patient treatment planning data was obtained from the Quality Improvement Committee of the Department of Radiation Oncology at the McGill University Health Centre. The relevant recommendations given in the RATING guidelines [32] were followed in this study.

8.4.2 Clinical treatment planning and dose prescription

Planning was performed on a computed tomography (CT) scan of the patient in the treatment position with 3 mm slice thickness and pixel spacing of around 1 mm. All CT scans were obtained on the Philips Brilliance Big Bore scanner (Philips, Amsterdam, Netherlands) in one of the following patient position: feet first supine (n=19), feet first prone (n=1), or head first supine (n=2). Patients were immobilized with a Vac-Lok device. Magnetic Resonance Imaging studies were co-registered with CT images to aid the contouring of the gross tumour volume (GTV). For GTVs larger than 8 cm, the CTV was contoured with 1.5 cm axial margins and 3 cm cranial-caudal margins from the GTV. For smaller tumours, CTV

axial margins of 1 cm and cranial-caudal margins of 2 cm were used as per RTOG 0630 and our standard practice. CTV contours did not include any intact bony structures. When skin surfaces were not involved by gross tumor, CTVs were cropped 3-5 mm from the skin (n=12). If the gross tumor involved the skin and bolus was used, CTVs were not cropped (n=10). While following the same skin cropping rule as the CTV, the PTV consisted of a 5 mm geometrical expansion from the CTV.

Contoured OARs relevant for plan optimization included the following: normal tissue strip, skin, bone, joints, testes, genitalia, anus. The dose constraints to the OARs used for evaluation of treatment plans are tabulated in Table 8–1. These constraints aim to reduce long-term sequelae such as edema, fibrosis, joint stiffness and bone fracture. For consistency, the normal tissue strip OAR was uniformly contoured as the subtraction of the PTV + 5 mm margin and any bone from the leg contour, on axial slices within 2 cm proximal and distal to the PTV. An example of this contour is shown in Fig. 8–2. The ipsilateral bone contour is limited to PTV axial slices, so as to only include bone within the radiation field as described in the RTOG 0630 protocol [5].

VMAT treatment planning of clinical plans were performed on the Eclipse (versions 11 and 15) treatment planning system (TPS). For VMAT plans, a dose of 50 Gy (2 Gy/fraction) was prescribed to 95% of the PTV. Although planning strategy varied according to the planner, highest priority was given to lower and upper optimization constraints on target structures. Optimisation constraints and priority for each OAR were chosen according to their volume, their distance from the target, and their position with respect to the beam arrangement. The maximum dose to the PTV was generally restrained to below 107% of the prescription dose. Doses to OARs were minimized while ensuring that the constraints in Table 8–1 are met. In exceptional cases, OAR constraints were exceeded to meet PTV coverage. For plan optimization purposes, patient doses were calculated with the Analytical Anisotropic Algorithm (AAA). At the time of planning, the dose distribution was calculated on a $2.5\times2.5\times3.0$ mm^3 grid. The VMAT plans consisted of either 2 or 3 arcs of 6 MV flattened photon beams

delivered at different collimator angles. Control points were set at gantry angle intervals of 2°. Only the Varian Millennium multi-leaf collimator (MLC) was used.

8.4.3 MBRT planning

All patient plans and CT images were exported from Eclipse and imported to our in-house TPS "*Brems*". "*Brems*" is a TPS hosted as a web app that was developed as a rewrite of the old "*Radify*" TPS [22], [33] to better accommodate MBRT treatment planning. It integrates the necessary components of the MBRT treatment planning workflow in one platform: selection of gantry angles, beamlet calculation, beamlet-based optimization, dose recalculation with Monte Carlo, evaluation of plan quality using DVH and other dose statistics, generation of plan files in `.dcm` or `.xml` formats, etc.

MBRT treatments were planned on the same TrueBeam linac originally used for VMAT treatment. For each patient, 3-4 and 5-8 beam angles were selected for the electron and photon components, respectively. Both electron and photon beams were planned as step-and-shoot apertures at standard source-axis distance (SAD) of 100 cm. Both photons and electrons were collimated with the Millennium photon-MLCs. As such, electron fields were planned without the use of standard electron applicators and cutouts.

For each beam angle, the beam's eye view plane is divided into a regular square grid. The dose distribution due to radiation traversing one grid element is referred to as a beamlet. Beamlets were calculated at 5 electron energies (6, 9, 12, 16, and 20 MeV) and at a 6 MV photon beam with flattening filter. A pre-calculated Monte Carlo method was used to efficiently calculate electron beamlets using pre-calculated electron tracks [34], [35]. Photon beamlets were calculated using an in-house collapsed cone convolution superposition algorithm [22]. The particle source for both these methods were generated from Varian-provided phase space files. Electron phase space files had their energy tuned to match measured data [31]. All beamlet calculations were performed on GPUs. Beamlets were robustly calculated to account for positioning uncertainty. This was done by calculating each beamlet in 6

equally weighted additional scenarios, in addition to the nominal (non-shifted) scenario. In each shifted scenario, the isocenter is translated by 5 mm in one of the following directions: cranial-caudal, anterior-posterior and lateral right-left.

A robust column generation optimizer [25] was used to perform simultaneous photon and electron beamlet optimization of MBRT plans. Optimization constraints were applied on the following structures (if applicable): CTV, contralateral leg, ipsilateral bone, testes, and 2 mm skin strip. A normal tissue objective (NTO) function was employed to enforce a rapid dose fall-off in voxels outside the CTV. The NTO penalizes voxels exceeding a pre-assigned threshold dose. The threshold dose is calculated based on the voxel's distance to the CTV. The plan was normalized such that the average $\bar{V}_{50\text{Gy}}$ over all 7 scenarios of CTV volumes receiving 50 Gy is 95%. It must be noted that for MBRT plans, robust optimization is performed on the CTV rather than the traditional PTV-based optimization.

In this study, no MBRT plans made use of bolus. For the purpose of MBRT planning, any bolus present in the CT (n=10) had its density overridden to air. For these 10 patients, the CTV in the MBRT plan was cropped 2 mm from the skin to allow for buildup in the absence of bolus. This cropped CTV was used for the evaluation of both the VMAT and MBRT plan. As such, any dose comparison presented in this study is performed on identical structures.

The planning aim for MBRT consisted of ensuring similar or better dose homogeneity in the CTV as its VMAT counterpart while minimizing dose to bone and the normal tissue strip. In practice, this was achieved by starting with strict NTO parameters to demand sharp dose fall-offs and progressively relaxing them at following optimization iterations until the CTV dose homogeneity was satisfactory. To be deemed acceptable, the near-maximum dose D2% to the CTV in MBRT plans had to remain strictly below 110%. Doses to OAR had to meet the constraints of Table 8–1, except in cases where the VMAT plan was also unable to meet the constraint. In general, planning objective weights for each structure were

set in the following descending priority order: CTV, skin, NTO, testes, bone, contralateral leg. The active planning time spent per patient by the planner and the total time (including time waiting for dose calculation and optimization) was recorded. As this is a retrospective study, the VMAT planning times could not be obtained for comparison.

For plan evaluation, patient doses were recalculated in all 7 robust scenarios with an EGSnrc [36] Monte Carlo model using Varian TrueBeam phase space files. All voxels within the patient body contour were set to water with variable density assigned via a CT-to-mass density curve, exported from Eclipse. As such, dose-to-water is reported in this study. Dose calculations were performed on uniform voxels of dimension 2.5 x 2.5 x 2.5 mm^3. For a fair comparison, the dose of the clinical VMAT plan was also robustly recalculated using the same Monte Carlo model. The same positioning shifts were introduced in the robust calculation of either treatment modalities. No renormalization or re-optimization of the VMAT plan was performed at this step.

To distinguish the dosimetric impact of a mixed modality treatment from the robust optimization process, an additional non-robust MBRT plan was generated for one representative patient. For this plan, target coverage constraints and prescription were applied on the PTV, as is done in the VMAT plan. All other constraints were otherwise kept identical to the robust MBRT plan. This was only done for illustrative purpose, as a realistic implementation of MBRT should always be done robustly.

8.4.4 Plan evaluation & statistical analysis

The Dose-Volume Histogram (DVH) of all patients was computed for the CTV, the ipsilateral bone and the normal tissue strip for each treatment modality. The DVH of the nominal scenario of all 22 plans were aggregated and the mean of each DVH point and its standard error were calculated. The cohort's mean DVH is calculated by evaluating the mean volume receiving at least x Gy over all 22 plans at every dose point x ranging from 0

to the maximum dose received by the structure in any plan.

For each OAR, the dose metrics tabulated in Table 8–1 were evaluated for both modalities and compared to their corresponding constraints. In particular, the dose to skin in VMAT plans were found to be distinctly different between patients that required bolus usage and those that did not. As such, for the purpose of the comparison of skin dose, patients were also separated according to their use or non-use of bolus during their VMAT treatment.

The dose conformity to the CTV was evaluated using the following definition of the conformity index:

$$CI = \frac{\text{isodose volume}}{\text{clinical target volume}}, \tag{8.1}$$

where the isodose volume corresponds to the sum of volume within the body contour that exceeds a given isodose level. A conformity index of 1 would thus correspond to the case where the isodose volume equates the CTV. This conformity index was calculated for multiple isodose levels (40%, 60%, 80% and 95%) to compare the dose fall-off rate of either modality. The near-maximum dose D2% to the CTV was also evaluated in both plans. For both treatment modalities, all DVHs and dose metrics were evaluated on *Brems* using the same methodology. Differences in any metrics between MBRT and VMAT plans were evaluated with a two-tailed Wilcoxon signed-rank test using the *SciPy* library on Python. Statistical significance is assumed for $p < 0.05$. Differences between all uncertainties on mean or median values in this study are reported with a coverage factor of $k = 2$.

To give a depiction of the composition of an MBRT plan, the mean CTV dose due to the photon component and each electron energy was evaluated. The overall distribution was represented in a boxplot to show the variance of electron vs. photon usage across the cohort.

8.5 Results

All 22 patients were successfully planned with MBRT with clinically acceptable plan quality. The mean DVH over the distribution of all 22 patients is plotted in Fig. 8–3a for both the MBRT and VMAT plans. The DVH bands represent the $\pm 2\sigma$ standard error on the

mean. MBRT plans provide equivalent CTV DVH as compared to VMAT. In the nominal scenario, the CTV's coverage by the prescription dose was found to be equivalent in either modality: $V_{50\text{Gy}}(\text{MBRT}) = 97.9 \pm 0.2\%$ vs $V_{50\text{Gy}}(\text{VMAT}) = 98.1 \pm 0.6\%$ ($p = 0.34$, Wilcoxon signed-ranked test). The dose to normal tissue and bone, which are the two common OARs in all sarcoma patients, was found to be significantly lower in MBRT plans. For each patient, the DVH of the MBRT plan was subtracted from that of the VMAT plan to show the decrease in dose to OARs in Fig. 8–3b. For normal tissue, $V_{20\text{Gy}}$ was reduced on average by $14.9 \pm 3.2\%$ in MBRT plans ($p < 10^{-6}$). For bone, $V_{50\text{Gy}}$ decreased on average by $8.2 \pm 4.0\%$ of the bone volume ($p < 10^{-3}$). The dose constraints for the remaining OARs are evaluated for each plan and plotted in Fig. 8–4a as a scatter plot. $V_{50\text{Gy}}$ to the joint and D_{mean} to the femoral head and to the bone were found to be significantly lower in MBRT plans according to a two-tailed Wilcoxon signed-ranked test (mean reduction of 4.0 ± 2.9 % $p = 0.003$, 4.7 ± 4.4 Gy $p = 0.03$, and 8.0 ± 1.4 Gy $p < 10^{-6}$, respectively). No significant difference was found in the evaluated metric of the other OARs of Fig. 8–4a. For VMAT plans, the dose metrics are evaluated on the Monte Carlo-recalculated dose and can significantly differ from the AAA dose used during treatment planning. This lead to 1 plan being shown to violate testes constraints despite originally meeting them at the time of planning.

The near-maximum dose $D_{0.5\text{cc}}$ to a 2 mm thick contour of the skin is plotted in Fig. 8–4b. Patients were separated according to their bolus usage in the clinical VMAT plan, while no MBRT plans used bolus. MBRT plans had significantly lower ($p = 0.002$) median $D_{0.5\text{cc}}$ (50.7 ± 0.5 Gy) than VMAT plans (52.5 ± 0.4 Gy) in patients that had used bolus. However, in patients that did not use bolus, $D_{0.5\text{cc}}$ was found to be significantly higher ($p < 10^{-3}$) in MBRT plans (48.5 ± 0.5 Gy) than in VMAT plans (42.8 ± 2.6 Gy) due to the higher electron surface dose.

The conformity index to the CTV was evaluated for 4 isodose levels to compare the rate of the dose fall-off and plotted in Fig. 8–4c. At 95% of the prescription dose, both the MBRT and VMAT plans for all patients have a CI larger than 1. At the 40% isodose level (20 Gy), the median CI was found to be significantly smaller in MBRT plans: 2.4 ± 0.3 vs. 3.3 ± 0.3 for VMAT ($p < 10^{-6}$). This indicates a more rapid dose fall-off in MBRT plans outside the CTV, such that a smaller volume of the body is subjected to lower dose baths. The near-maximum dose D2% to the CTV is also plotted in Fig. 8–4d. MBRT plans were found to have a statistically significantly higher D2% than VMAT plans: median $D2\%_{\mathrm{MBRT}} = 53.6 \pm 0.2$ Gy vs. $D2\%_{\mathrm{VMAT}} = 53.2 \pm 0.2$ Gy, $p = 0.046$. This difference can also be observed in the slightly wider CTV DVH curve in MBRT plans in Fig. 8–3a. Nevertheless, as the difference in D2% is small in magnitude, the CTV homogeneity would be deemed practically equivalent in clinical practice.

A comparison of the two modalities is depicted in Fig. 8–5 for a representative patient of the cohort. Bolus was used for the VMAT treatment of this patient but was overridden to be air for MBRT planning. For the 4 isodose levels that were evaluated (20%, 40%, 80% and 100% of the prescription dose), the isodose volumes were consistently smaller in the MBRT plan (Fig. 8–5a). This illustrates the steeper dose fall-off that is characteristic to MBRT. Due to this effect, a lower dose to both the normal tissue strip and bone can be observed over almost the entirety of their DVH curves in Fig. 8–5b. The shaded DVH bands represent the robust range of DVH values as evaluated over 7 positioning scenarios. Without resorting to bolus, the CTV DVH of the MBRT plan can be seen to overlap with the VMAT's DVH, indicating equivalent target coverage. The 50 Gy isodose shows higher dose conformity and bone sparing of the MBRT plan, while CTV is adequately covered in all robust scenarios as evidenced by the overlapping CTV bands.

To evaluate the contribution of photons and each electron energy in MBRT plans, the mean CTV dose due to each component is plotted as a boxplot in Fig. 8–6. Although there is considerable variation across plans, the CTV dose is overall somewhat evenly distributed between electrons vs. photons. Among electron energies, the higher energies have a significantly larger contribution to the mean CTV dose. Nevertheless, it must be noted that lower electron energies tend to be responsible for doses in specific spatial regions of the target (e.g. more superficial regions). Therefore, when averaged over the entire CTV, their mean CTV dose will appear smaller due to the smaller volume in which they have a dose contribution.

For one representative patient, an additional non-robust PTV-based MBRT plan was generated and compared to the robust MBRT and non-robust VMAT plans in Fig 8–7. The CTV's $V_{50\text{Gy}}$ was evaluated to be similar in the 3 plans: 97.4%, 98.2% and 99.2% in the PTV-based MBRT, robust MBRT and VMAT plans, respectively. On the other hand, both MBRT plans offered better sparing of the normal tissue strip than VMAT with $V_{20\text{Gy}}$(MBRT-PTV) = 8.8% and $V_{20\text{Gy}}$(MBRT-Robust) = 5.1% vs. $V_{20\text{Gy}}$(VMAT) = 12.2%.

On average, MBRT plans required around 1 hour of active planning time, with less than 3 optimization attempts for most cases. However, the total planning time took on average 3 days due to the time-consuming robust beamlet calculations, robust optimization, and robust Monte Carlo recalculation.

A RATING score of 98% was achieved and the score sheet is provided in the *Supplementary material*.

8.6 Discussion

In STS, higher nominal doses have been associated with increased edema and bone fracture rate [6], [37]. Lower incidence of late toxicities in two phase II clinical trials [4],

[5] is attributed to smaller target volumes. To reduce the risk of long-term sequelae, doses outside the target should therefore be minimized. The average DVH difference plot in Fig. 8–3b shows consistently lower dose volumes at practically all dose points to the normal tissue contour and bone in the MBRT plan. The normal tissue was systematically contoured to be the subtraction of the PTV + 5 mm margin and bone contours from the limb contour. Therefore, this result indicates that on average, MBRT plans deliver significantly less dose outside the target. This effect is even more pronounced when examining volumes subjected to low dose baths. As the dose of electron beams falls off much more rapidly with depth than photon beams, MBRT subjects fewer voxels beyond the target to low dose baths.

The dose to the CTV was found to feature slightly higher hot spots in MBRT plans as indicated by the D2% in Fig. 8–4d. As MLC-collimated electron beams at SSD 100 cm have inherently wider penumbras than photon beams and a distinct depth dose curve, their usage tends to increase the dose heterogeneity within the CTV. MBRT as a technique aims to compensate for this downside by using both electrons and photons. More electron usage tends to decrease doses beyond the target at the cost of target homogeneity. This is an optimization problem that is defined by the constraints and weights chosen by the planner. MBRT plans were observed to have a median D2% to the CTV of 53.6 ± 0.2 Gy (≈107% of the prescription dose), 0.4 Gy higher than their VMAT counterpart. As per the RTOG 0630 protocol, no more than 20% of the PTV must receive more than 110% of the prescription dose (= 55 Gy in this study). This criterion was met by all MBRT and VMAT plans in this study.

In routine clinical practice, for photon planning without bolus, the PTV needs to be cropped 5 mm from the surface to leave enough tissue for buildup to occur. If a higher superficial dose is required, a tissue equivalent bolus is used to raise the dose to the surface. In theory, despite the superficial target, the skin should still be spared from excessive

dose as it is associated with a higher risk of wound healing complications. However, controlling the dose downstream from the bolus is difficult when the prescription dose must be met in the target and the reproducibility of bolus setup is uncertain. This leads to high doses to skin as observed in Fig. 8–4b which exceed the maximum skin dose constraint of 103% of the prescription dose. With MBRT, a thinner buildup region is required due to the electron's higher entrance dose. As such, it provides the option of sparing 2 mm of skin while also adequately covering the rest of the target without using bolus. For this reason, for plans that used bolus with VMAT (n=10), we have opted to crop the CTV 2 mm from the surface. In fact, the dose to the 2 mm of skin is further restricted in MBRT plans such that its near-maximum dose meet the 103% constraint (Fig. 8–4b). At the time of surgery, if there is suspicion of skin involvement, any underdosed skin would also be resected. It is important to note that for these 10 plans, the cropped CTV has been used for dose evaluation of both VMAT and MBRT. Therefore, for every patient in this study, any dose metrics that is compared between VMAT vs. MBRT is reported on identical CTVs.

Of the 22 patients that were planned in this study, 10 patients required the use of bolus for their original VMAT treatment. In contrast, no patients required the use of bolus in MBRT plans. Similarly, Mueller et al. have shown for a superficial chest wall case that the plan quality of MBRT plans was not significantly affected by the absence of bolus [23]. Bolus usage entails significant logistical effort in the clinical workflow. Bolus must be positioned in similar conditions during simulation and at every fraction of the treatment. It is difficult to quantify the difference in bolus thickness and density at each instance. This introduces a substantial uncertainty on the dose to the skin and to the target in the VMAT delivery. Bolus usage has been associated with increased frequency of chronic skin telangiectasias [6]. Although the use of bolus has not been directly correlated with major wound complications [38], [39], it tends to increase the dose to skin as can be seen in Fig. 8–4b. Higher doses to skin can lead to acute skin toxicity such as radiation dermatitis [40]. Moreover, LeBrun et

al. found radiation dermatitis to be a predictor of wound complications in STS [39].

When bolus was not used with VMAT (n=12), a slightly higher dose to skin was observed with MBRT. This is expected as electron beams have higher entrance doses than photon beams. Larger volumes of future surgical skin flaps receiving higher doses have been associated with higher risk of wound complications [4]. In this study, the near-maximum dose to skin in MBRT plans were ensured to be lower than 103% of the prescription dose. This was done by placing an upper optimization constraint on a 2 mm skin contour. It must be noted that despite the higher near-maximum skin dose in these 12 MBRT plans, they do not exceed the skin dose constraint. As higher weighting is placed on achieving lower doses to skin, the optimizer will tend to reduce the proportion of electrons vs. photons in the MBRT plan. Although reducing electron usage does decrease doses to skin, it also has the effect of increasing dose to deeper normal tissue due to the resulting increase in photons. The planner must therefore make a trade-off between skin dose and normal tissue dose. As wound healing complications due to high skin dose can still be managed, a higher concern is generally placed on limiting risks of long-term sequelae associated with elevated dose to normal tissue.

In the RTOG 0630 protocol [5] and the current study, the dose to a longitudinal strip of normal tissue is constrained such that $V_{20\text{Gy}} < 50\%$. However there is no consensus on the definition of the normal tissue strip contour, which is usually left at the discretion of the radiation oncologist. Depending on the proximity of the normal tissue contour to the CTV and its extent, there is significant variance of the $V_{20\text{Gy}}$ metric for a same plan. To avoid this inconsistency from introducing bias in the comparison of MBRT and VMAT plans, all normal tissue strips in this study were contoured according to a consistent rule described in the *Methods* section. As such, normal tissue strips in this study are representative of a proportion of the limb and, conceptually it is precisely the volume of interest given the

long-term sequelae correlate with volume of normal tissue irradiated.

In current clinical practice, dose prescriptions for STS are given as dose-to-water. As such, all doses in this study have been calculated as dose-to-water to provide a fair comparison. One can question whether the conclusions of this study would remain the same if the absorbed dose-to-medium were to be reported. This is a reasonable concern as electrons are used as part of MBRT plans. The impact of scoring dose-to-medium vs. dose-to-water is estimated in the *Supplementary material*. We have found that dose conversions from dose-to-water to dose-to-medium would have a clinically equivalent effect on both MBRT and VMAT doses. The conclusions of this study would therefore remain valid if dose-to-medium had been calculated.

The present study assesses the potential dosimetric benefits of an implementation of MBRT compared to the current clinical practice. To provide a representative comparison to the dose distributions being delivered to patients, no re-optimization of VMAT plans were performed. All VMAT plans were optimized on Eclipse, using AAA for dose calculation. On the other hand, MBRT was optimized with in-house algorithms featured on *Brems*. In particular, MBRT optimization was performed robustly while VMAT optimization was PTV-based. Photon-based treatment plans are not currently using robust optimization in routine clinical practice. Nevertheless, one may question if the dosimetric sparing achieved in MBRT plans can be truly attributed to its mixed modality or if it is a result of the robust optimization. Indeed, by explicitly calculating the perturbed dose distributions, the robust optimizer can achieve a more conformal MBRT plan than required when imposing isotropic PTV margins [25]. For one representative case, the MBRT plan was re-optimized non-robustly using the PTV, but otherwise identical optimization constraints. The DVH in Fig. 8–7 shows that a PTV-optimized MBRT plan still achieves better sparing of normal

tissue than VMAT. The sharp dose fall-off with depth is characteristic of electron dose distributions and cannot be featured in megavoltage photon-based treatments. Although robust optimization can be responsible for some of the healthy tissue sparing seen in MBRT plans, the contribution from the electron beams' limited penetration depth is the primary reason for MBRT's superior healthy tissue sparing.

Due to the retrospective nature of this planning study, no direct conclusions can be made on the impact of MBRT on patient outcomes and toxicities. Due to the limited cohort size obtained from a single institution, the generalizability of the dosimetric benefits found in this study may need to be confirmed on a larger multi-institutional cohort. Although the difference in dose metrics to the relevant structures were quantified, the overall plan quality of each patient was not individually scored by clinicians and the comparison between plans of either modality was not blinded. Furthermore, in this study, MBRT plans were retrospectively re-optimized and compared to clinical VMAT plans. Plans of each modality were therefore optimized by different planners who could have spent a differing length of time. This could be a potential source of bias and constitutes a limitation of the present study. As MBRT requires no modification on current linacs to be deliverable, its clinical applicability could be immediate. However, optimization of MBRT plans remains time-consuming and resource intensive. Future work will focus on alleviating the optimization's bottleneck and on investigating the applicability of MBRT to other treatment sites.

A subset of 5 plans were verified to be deliverable on Varian TrueBeam linacs using *Developer Mode* as part of a separate study [41]. *A priori*, all other plans should also be deliverable. Total delivery time for 1 fraction was under 15 minutes, with photon apertures accounting for around half the time. As all apertures were delivered at standard SAD, no intra-fraction couch translation was required. This is in contrast to previous MBRT studies that have all reported the use of shortened SSD setups for deliveries of electron apertures

[20]–[26], [31].

8.7 Conclusion

The purpose of this study was to investigate the dosimetric benefits of MBRT when applied to cases of STS of the extremity. To this end, a retrospective MBRT treatment planning study was performed and the resulting plans were compared to the clinically delivered VMAT plans. MBRT plans achieved clinically equivalent target coverage and homogeneity as compared to VMAT, without the need for bolus. For all patients, MBRT plans had either significantly lower or equivalent doses to normal tissue and bone. Being deliverable on current state-of-the-art linacs without the use of electron applicators [26], [31] or shortened SSD [41], MBRT offers significant dosimetric benefits at reduced logistical cost.

8.8 Acknowledgement

The authors acknowledge support from the Fonds de recherche du Québec Nature et Technologie (FRQNT) (award number 290039) and the Canadian Institutes of Health Research Foundation Grant (FDN-143257).

8.9 Conflict of Interest Statement

The authors have no relevant conflicts of interest to disclose.

8.10 Data Availability Statement

The data that support the findings of this study are available from the corresponding author upon reasonable request.

8.11 Supplementary material

8.11.1 Dose-to-medium vs. dose-to-water

Reynaert et al. [42] have reported that in equilibrium condition, the conversion from dose-to-water to dose-to-bone for photon beams can be approximated by using the ratio of mass energy absorption coefficients. However, the conversion from dose-to-water to dose-to-medium for electrons is dictated by their mass collision stopping power ratio. Therefore, in media where there is a substantial discrepancy between the mass collision stopping power

ratio and the mass energy absorption coefficient ratio of medium to water, the conversion to dose-to-medium could differently impact the plan quality of MBRT vs. VMAT plans. The mass collision stopping power ratio of cortical bone (ICRP) to water $[S_{\text{col}}]^{\text{bone}}_{\text{water}}$ for a 12 MeV electron and the mass energy absorption coefficient ratio of cortical bone to water $[\mu_{\text{en}}]^{\text{bone}}_{\text{water}}$ for a 2 MeV photon (most common energy of a 6 MV linac spectrum) can be evaluated, using ESTAR [43] and XCOM [44], to be:

$$[S_{\text{col}}]^{\text{bone}}_{\text{water}}(12\text{ MeV}) = \frac{1.819\text{ MeV cm}^2/\text{g}}{1.989\text{ MeV cm}^2/\text{g}} = 0.915, \tag{8.2}$$

$$[\mu_{\text{en}}]^{\text{bone}}_{\text{water}}(2\text{ MeV}) = \frac{2.421 \cdot 10^{-2}\text{ cm}^2/\text{g}}{2.609 \cdot 10^{-2}\text{ cm}^2/\text{g}} = 0.928. \tag{8.3}$$

It must be noted that while electron energy varies with depth, the ratio of stopping power $[S_{\text{col}}]^{\text{bone}}_{\text{water}}$ is mostly constant with electron energy at the relevant energy range and can be arbitrarily evaluated at 12 MeV for the purpose of this argument. Therefore as a very rough approximation, we would expect the conversion of dose-to-water to dose-to-bone to decrease the dose due to 12 MeV electrons by $1 - [S_{\text{col}}]^{\text{bone}}_{\text{water}}(12\text{ MeV})/[\mu_{\text{en}}]^{\text{bone}}_{\text{water}}(2\text{ MeV}) = 1.4\%$ more than that due to 6 MV photons. However, in practice, the observed difference between MBRT and VMAT plans will be even smaller. This is because electrons only account for a fraction of the patient dose in MBRT plans, with 6 MV photons being responsible for the remaining dose. In addition, as most of the contoured bone volume is cancellous bone with CT number closer to soft tissue, only a fraction of the bone structure would have their medium assigned as cortical bone. The corresponding relative difference in mass collision stopping power ratio and mass energy absorption ratio for soft tissue (ICRP) to water can be calculated to be -0.4%.

To better illustrate this exercise, a patient with significant dose to bone in both the MBRT and VMAT plan was recalculated to score dose-to-medium in medium. The dose ratio as scored to bone vs. water $D^{\text{bone}}_{\text{water}}$ was evaluated for all voxels within the bone contour,

receiving at least 10 Gy. The average ratio for each modality was found to be:

$$D^{\text{bone}}_{\text{water}}(\text{VMAT}) = 0.9694, D^{\text{bone}}_{\text{water}}(\text{MBRT}) = 0.9660, \tag{8.4}$$

such that $1 - D^{\text{bone}}_{\text{water}}(\text{MBRT})/D^{\text{bone}}_{\text{water}}(\text{VMAT}) = 0.35\%$. As this difference would be considered insignificant in clinical practice, the conclusions of this study would therefore not change by scoring dose-to-medium in medium rather than dose-to-water.

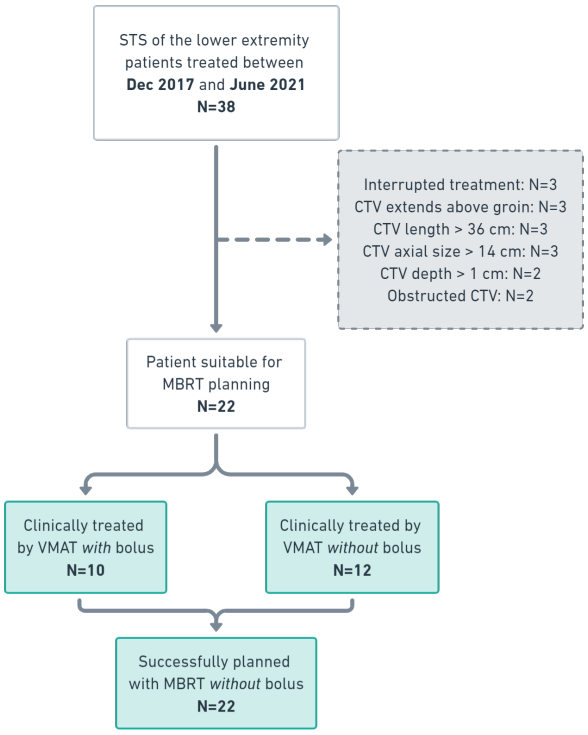

Figure 8–1: Consort diagram describing patient selection criteria. A total of 38 patients with STS of the lower extremity (excluding foot and ankle) were treated between Dec. 2017 and June 2021. Twenty-two patients were eligible for the planning study. Bolus was not used for any patients for MBRT plans. The CTV length, size and depths are illustrated in Fig. 8–2.

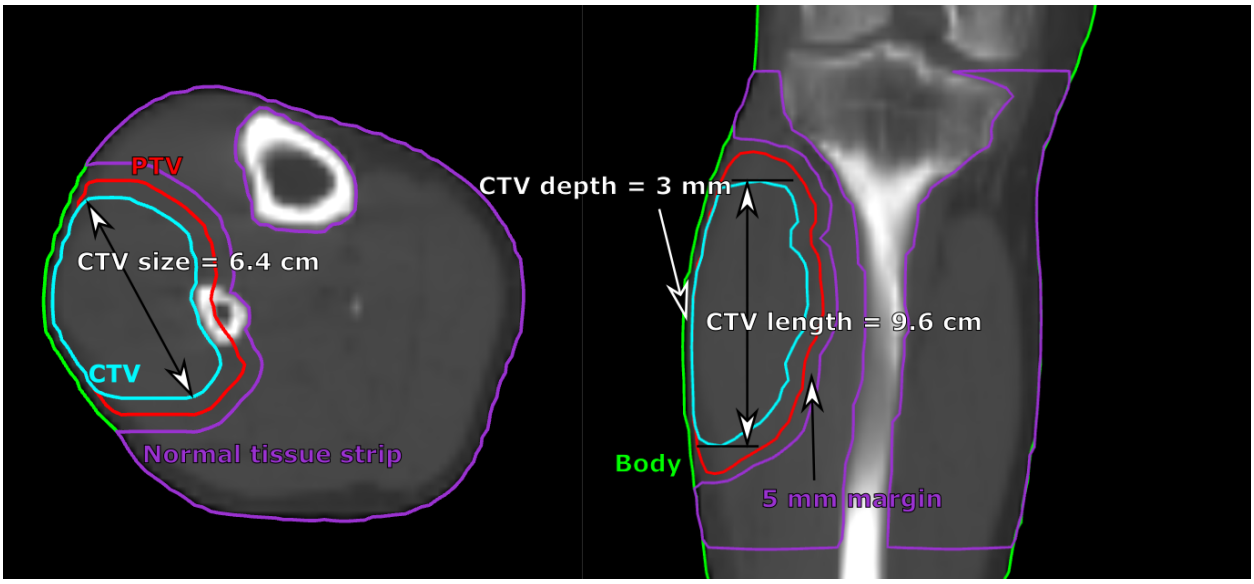

Figure 8–2: Axial (left) and coronal (right) CT slices of a representative patient. The CTV size, depth and length used as exclusion criteria in Fig. 8–1 are illustrated with arrows. The normal tissue strip is uniformly contoured as the rest of the limb excluding any bone and a 5 mm margin around the PTV.

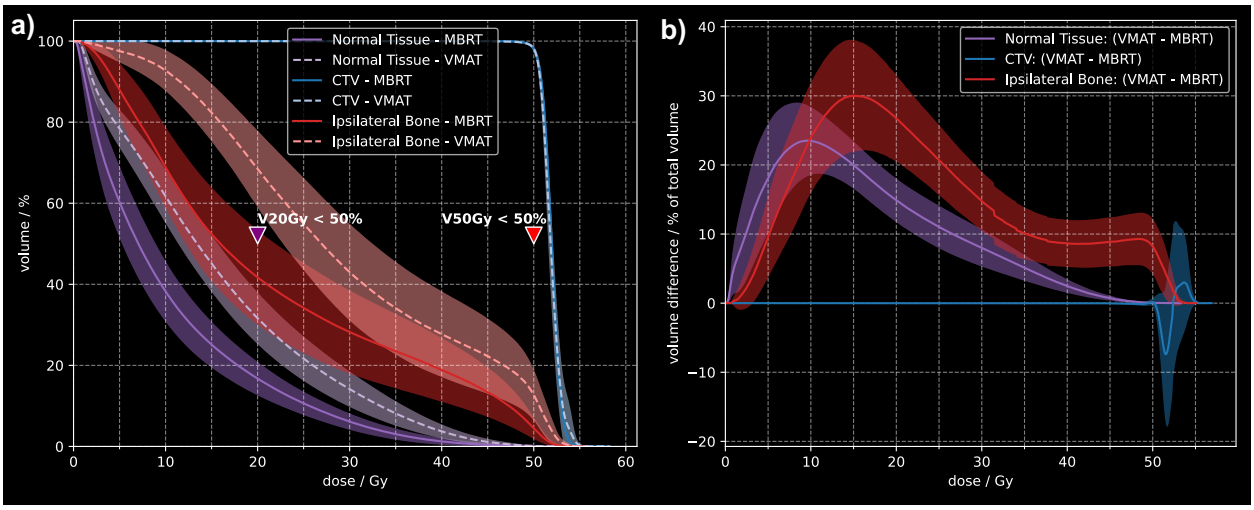

Figure 8–3: a) Average DVH of all 22 patients. Lines represent the mean DVH for each structure and the bands represent the 2 σ confidence interval on the mean. The planning constraints for the 2 OARs are plotted as inverted triangles. MBRT plans show equivalent CTV DVH to VMAT with significant reduction in dose to normal tissue and bone. b) Average difference DVH of all 22 patients. Lines represent the mean difference in DVH between the VMAT and the MBRT plan for each patient, while the bands represent the 2 σ confidence interval on the mean difference.

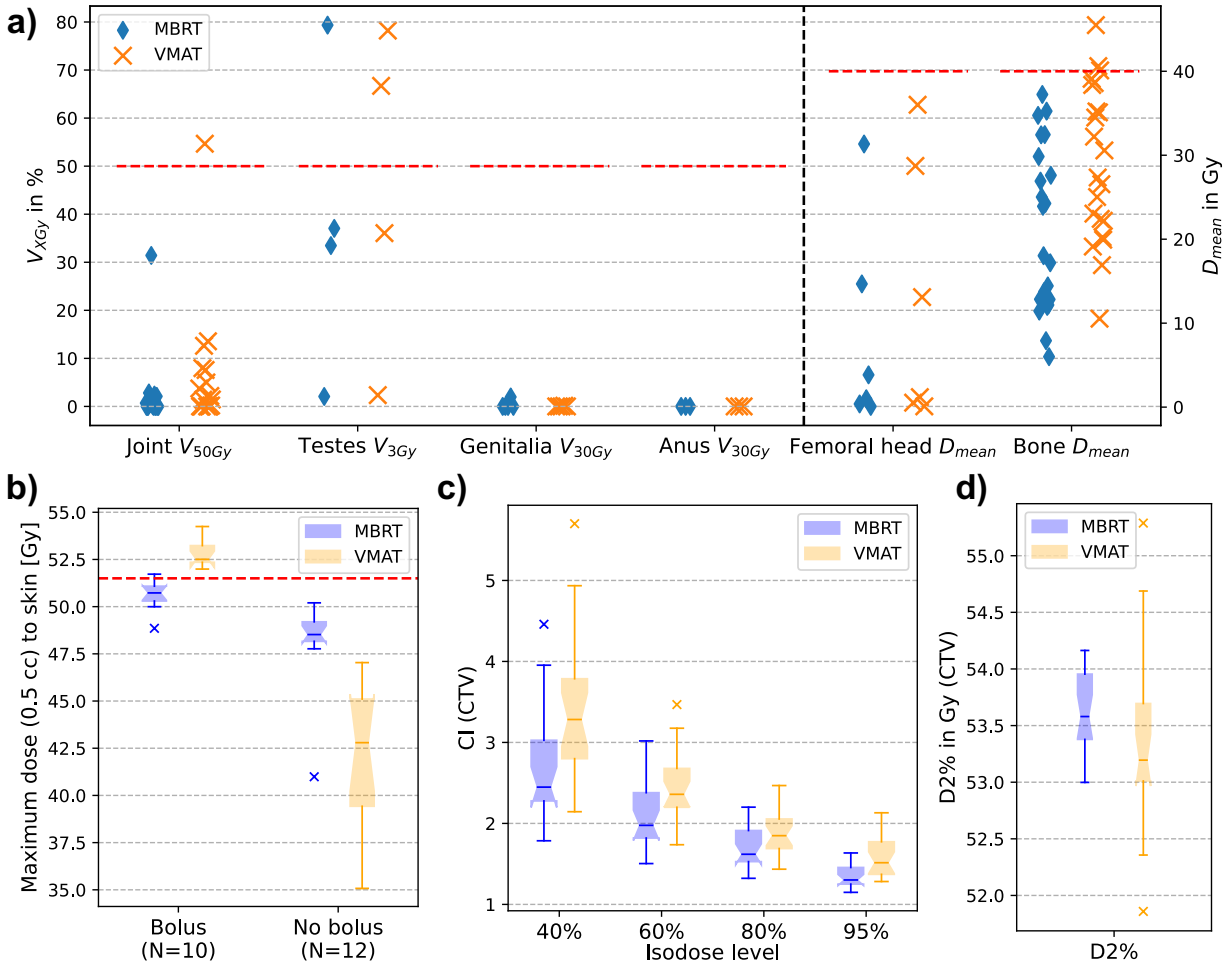

Figure 8–4: a) Comparison of the dose to various OARs. The metric evaluated for each OAR are obtained from Table 8–1. The red dotted lines represent the maximum constraint for each metric. Doses to the joint, the femoral head and to the whole ipsilateral bone were found to be significantly lower in MBRT plans according to a Wilcoxon signed-ranked test. b) Near-maximum (0.5 cc) dose to 2 mm skin. The maximum dose constraint to skin (51.5 Gy, 103% of the prescription dose) is drawn with red dotted lines. Patients are separated according to their bolus usage in their VMAT plans. No bolus was used in any of the MBRT plans. c) Conformity index to the CTV for different isodose levels. d) Near-maximum dose D2% to the CTV. Lines within the boxplots represent the median of each distribution. Notches represent the 95% confidence interval on the median. Outliers, calculated to be lying beyond 1.5× the interquartile range, are illustrated as crosses.

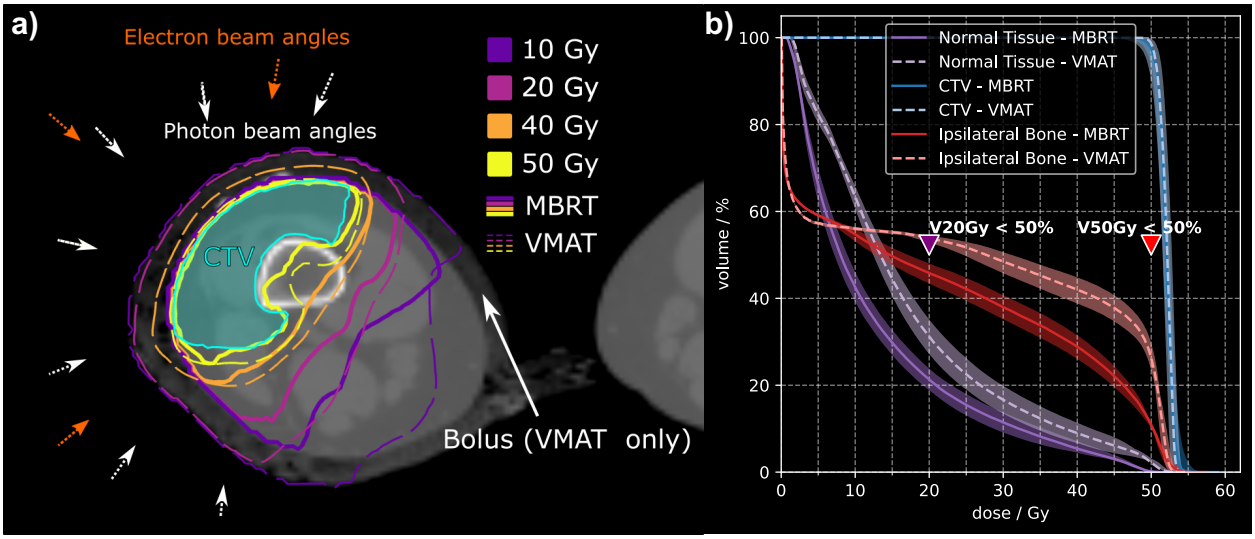

Figure 8–5: a) Comparison of 4 isodose levels between MBRT (full lines) and VMAT (dashed lines) plans for a representative patient. The MBRT plan can be observed to have a more rapid dose fall-off outside the CTV. The angles of electron (orange) and photon (white) beams in the MBRT plan are illustrated as arrows. The bolus visible in the CT image is only taken into account in the calculation of the VMAT plan; it is overridden to be air for MBRT calculations. The CTV being shown was cropped 2 mm from the skin to allow for buildup in the bolus-free MBRT plan. b) Comparison of the DVH of the MBRT (full lines) and VMAT (dashed lines) plans for the same patient. The shaded bands represent the range of DVH values attained over 7 positioning scenarios. The CTV evaluated in both the MBRT and VMAT DVHs corresponds to the aforementioned cropped CTV.

Table 8–1: Dose constraints to OAR used for evaluation of both clinical and MBRT plans.

OAR	Dose constraint
Bone	$D_{\text{mean}} < 37$ Gy
	$V_{50\text{Gy}} < 50\%$
Femoral head	$D_{\text{mean}} < 40$ Gy
Joint	$V_{50\text{Gy}} < 50\%$
Normal tissue strip	$V_{20\text{Gy}} < 50\%$
Skin	$D_{\text{max}} < 51.5$ Gy
Anus	$V_{30\text{Gy}} < 50\%$
Genitalia	$V_{30\text{Gy}} < 50\%$
Testes	$V_{3\text{Gy}} < 50\%$

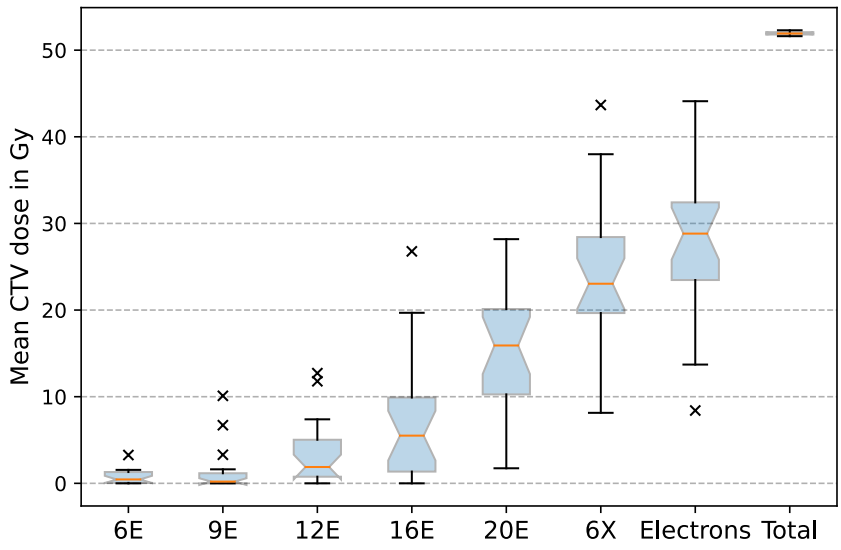

Figure 8–6: Distribution of the dose contribution towards the mean CTV dose due to each energy component of MBRT plans. The sum of electrons contribution and the total contribution of all components are also plotted for reference. Higher electron energies and photons have a higher contribution to the mean CTV dose.

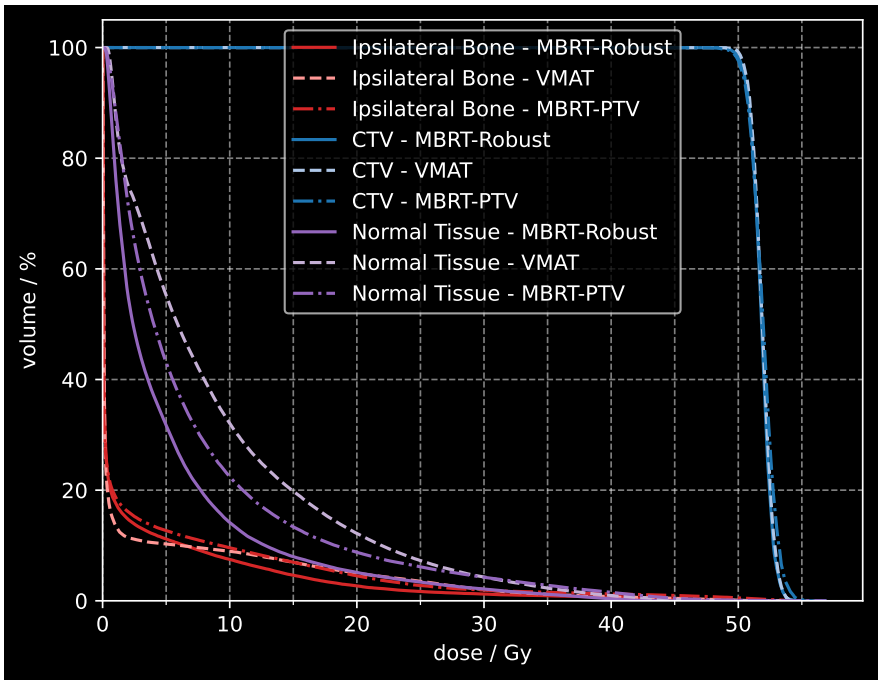

Figure 8–7: DVH of one representative patient featuring 3 plans: the robustly optimized MBRT plan, the clinical VMAT plan and a PTV-optimized MBRT plan. Both the robustly optimized and PTV-optimized MBRT plans used the same optimization constraints. The PTV-optimized MBRT plan shows superior sparing of normal tissue compared to VMAT due to the sharper electron dose fall-off with depth. However, even more sparing is achieved in the robustly-optimized MBRT plan.

REFERENCES

[1] R. L. Siegel, K. D. Miller, H. E. Fuchs, and A. Jemal, "Cancer statistics, 2022," *CA: A Cancer Journal for Clinicians*, vol. 72, no. 1, pp. 7–33, 2022. DOI: https://doi.org/10.3322/caac.21708.

[2] National Cancer Institute. "SEER cancer stat facts: Soft tissue cancer." (2022), [Online]. Available: https://seer.cancer.gov/statfacts/html/soft.html.

[3] K. E. Salerno, K. M. Alektiar, E. H. Baldini, *et al.*, "Radiation therapy for treatment of soft tissue sarcoma in adults: Executive summary of an astro clinical practice guideline," *Practical Radiation Oncology*, vol. 11, no. 5, pp. 339–351, 2021. DOI: https://doi.org/10.1016/j.prro.2021.04.005.

[4] B. O'Sullivan, A. M. Griffin, C. I. Dickie, *et al.*, "Phase 2 study of preoperative image-guided intensity-modulated radiation therapy to reduce wound and combined modality morbidities in lower extremity soft tissue sarcoma," *Cancer*, vol. 119, no. 10, pp. 1878–1884, 2013. DOI: https://doi.org/10.1002/cncr.27951.

[5] D. Wang, Q. Zhang, B. L. Eisenberg, *et al.*, "Significant reduction of late toxicities in patients with extremity sarcoma treated with image-guided radiation therapy to a reduced target volume: Results of radiation therapy oncology group rtog-0630 trial," *Journal of Clinical Oncology*, vol. 33, no. 20, pp. 2231–2238, 2015, PMID: 25667281. DOI: 10.1200/JCO.2014.58.5828.

[6] S. F. Stinson, T. F. Delaney, J. Greenberg, *et al.*, "Acute and long-term effects on limb function of combined modality limb sparing therapy for extremity soft tissue sarcoma," *International Journal of Radiation Oncology*Biology*Physics*, vol. 21, no. 6, pp. 1493–1499, 1991. DOI: https://doi.org/10.1016/0360-3016(91)90324-W.

[7] M. C. Lee, S. B. Jiang, and C. M. Ma, "Monte Carlo and experimental investigations of multileaf collimated electron beams for modulated electron radiation therapy," *Medical Physics*, vol. 27, no. 12, pp. 2708–2718, 2000. DOI: 10.1118/1.1328082.

[8] C. M. Ma, T. Pawlicki, M. C. Lee, *et al.*, "Energy- and intensity-modulated electron beams for radiotherapy," *Physics in Medicine and Biology*, vol. 45, no. 8, pp. 2293–2311, 2000. DOI: 10.1088/0031-9155/45/8/316.

[9] K. R. Hogstrom, R. A. Boyd, J. A. Antolak, *et al.*, "Dosimetry of a prototype retractable eMLC for fixed-beam electron therapy," *Medical Physics*, vol. 31, no. 3, pp. 443–462, 2004. DOI: 10.1118/1.1644516.

[10] T. Gauer, D. Albers, F. Cremers, *et al.*, "Design of a computer-controlled multileaf collimator for advanced electron radiotherapy," *Physics in Medicine and Biology*, vol. 51, no. 23, pp. 5987–6003, 2006. DOI: 10.1088/0031-9155/51/23/003.

[11] T. Gauer, J. Sokoll, F. Cremers, *et al.*, "Characterization of an add-on multileaf collimator for electron beam therapy," *Physics in Medicine and Biology*, vol. 53, no. 4, pp. 1071–1085, 2008. DOI: 10.1088/0031-9155/53/4/017.

[12] K. Al-Yahya, F. Verhaegen, and J. Seuntjens, "Design and dosimetry of a few leaf electron collimator for energy modulated electron therapy," *Medical Physics*, vol. 34, no. 12, pp. 4782–4791, 2007. DOI: 10.1118/1.2795827.

[13] A. Alexander, F. Deblois, and J. Seuntjens, "Toward automatic field selection and planning using Monte Carlo-based direct aperture optimization in modulated electron radiotherapy," *Physics in Medicine and Biology*, vol. 55, no. 16, pp. 4563–4576, 2010. DOI: 10.1088/0031-9155/55/16/S10.

[14] T. Connell, A. Alexander, P. Papaconstadopoulos, *et al.*, "Delivery validation of an automated modulated electron radiotherapy plan," *Medical Physics*, vol. 41, no. 6, 2014. DOI: 10.1118/1.4876297.

[15] F. C. Du Plessis, A. Leal, S. Stathakis, W. Xiong, and C. M. Ma, "Characterization of megavoltage electron beams delivered through a photon multi-leaf collimator (pMLC),"

Physics in Medicine and Biology, vol. 51, no. 8, pp. 2113–2129, 2006. DOI: 10.1088/0031-9155/51/8/011.

[16] E. E. Klein, M. Vicic, C. M. Ma, D. A. Low, and R. E. Drzymala, "Validation of calculations for electrons modulated with conventional photon multileaf collimators," *Physics in Medicine and Biology*, vol. 53, no. 5, pp. 1183–1208, 2008. DOI: 10.1088/0031-9155/53/5/003.

[17] F. J. Salguero, B. Palma, R. Arrans, J. Rosello, and A. Leal, "Modulated electron radiotherapy treatment planning using a photon multileaf collimator for post-mastectomized chest walls," *Radiotherapy and Oncology*, vol. 93, no. 3, pp. 625–632, 2009. DOI: 10.1016/j.radonc.2009.08.021.

[18] D. Henzen, P. Manser, D. Frei, *et al.*, "Beamlet based direct aperture optimization for MERT using a photon MLC.," *Medical physics*, vol. 41, no. 12, p. 121 711, Dec. 2014. DOI: 10.1118/1.4901638.

[19] A. Alexander, E. Soisson, M.-A. Renaud, and J. Seuntjens, "Direct aperture optimization for FLEC-based MERT and its application in mixed beam radiotherapy.," *Medical physics*, vol. 39, no. 8, pp. 4820–31, Aug. 2012. DOI: 10.1118/1.4736423.

[20] B. A. Palma, A. U. Sánchez, F. J. Salguero, *et al.*, "Combined modulated electron and photon beams planned by a Monte-Carlo-based optimization procedure for accelerated partial breast irradiation," *Physics in Medicine and Biology*, vol. 57, no. 5, pp. 1191–1202, 2012. DOI: 10.1088/0031-9155/57/5/1191.

[21] C. Míguez, E. Jiménez-Ortega, B. A. Palma, *et al.*, "Clinical implementation of combined modulated electron and photon beams with conventional MLC for accelerated partial breast irradiation," *Radiotherapy and Oncology*, vol. 124, no. 1, pp. 124–129, 2017. DOI: 10.1016/j.radonc.2017.06.011.

[22] M.-A. Renaud, M. Serban, and J. Seuntjens, "On mixed electron-photon radiation therapy optimization using the column generation approach," *Medical Physics*, vol. 44, no. 8, pp. 4287–4298, 2017. DOI: 10.1002/mp.12338.

[23] S. Mueller, M. K. Fix, A. Joosten, *et al.*, "Simultaneous optimization of photons and electrons for mixed beam radiotherapy," *Physics in Medicine and Biology*, vol. 62, no. 14, pp. 5840–5860, 2017. DOI: 10.1088/1361-6560/aa70c5.

[24] S. Mueller, P. Manser, W. Volken, *et al.*, "Part 2: Dynamic mixed beam radiotherapy (dymber): Photon dynamic trajectories combined with modulated electron beams," *Medical Physics*, vol. 45, no. 9, pp. 4213–4226, 2018. DOI: https://doi.org/10.1002/mp.13085.

[25] M.-A. Renaud, M. Serban, and J. Seuntjens, "Robust mixed electron–photon radiation therapy optimization," *Medical Physics*, vol. 46, no. 3, pp. 1384–1396, 2019. DOI: https://doi.org/10.1002/mp.13381.

[26] E. Heath, S. Mueller, G. Guyer, *et al.*, "Implementation and experimental validation of a robust hybrid direct aperture optimization approach for mixed-beam radiotherapy," *Medical Physics*, vol. 48, no. 11, pp. 7299–7312, 2021. DOI: https://doi.org/10.1002/mp.15258.

[27] E. E. Klein, Z. Li, and D. A. Low, "Feasibility study of multileaf collimated electrons with a scattering foil based accelerator," *Radiotherapy and Oncology*, vol. 41, no. 2, pp. 189–196, 1996. DOI: 10.1016/S0167-8140(96)01822-1.

[28] S. Mueller, M. K. Fix, D. Henzen, *et al.*, "Electron beam collimation with a photon MLC for standard electron treatments," *Physics in Medicine & Biology*, vol. 63, no. 2, p. 025 017, 2018. DOI: 10.1088/1361-6560/aa9fb6.

[29] ICRU, "Report 83: Prescribing, Recording, and Reporting Photon-Beam Intensity-Modulated Radiation Therapy (IMRT)," *Journal of the ICRU*, vol. 10, no. 1, 2010. DOI: 10.1093/jicru/ndq025.

[30] J. Unkelbach and H. Paganetti, "Robust Proton Treatment Planning: Physical and Biological Optimization," *Seminars in Radiation Oncology*, vol. 28, no. 2, pp. 88–96, 2018. DOI: 10.1016/j.semradonc.2017.11.005.

[31] V. J. Heng, M. Serban, J. Seuntjens, and M.-A. Renaud, "Ion chamber and film-based quality assurance of mixed electron-photon radiation therapy," *Medical Physics*, vol. 48, no. 9, pp. 5382–5395, 2021. DOI: https://doi.org/10.1002/mp.15081.

[32] C. R. Hansen, W. Crijns, M. Hussein, *et al.*, "Radiotherapy treatment plannINg study guidelines (RATING): A framework for setting up and reporting on scientific treatment planning studies," *Radiotherapy and Oncology*, vol. 153, pp. 67–78, Dec. 2020.

[33] M. Renaud and F. DeBlois, "Webtps: A complete web application for monte carlo treatment plan recalculation," *International Journal of Radiation Oncology, Biology, Physics*, vol. 87, no. 2, S625, Oct. 2013. DOI: 10.1016/j.ijrobp.2013.06.1651.

[34] K. Jabbari, P. Keall, and J. Seuntjens, "Considerations and limitations of fast Monte Carlo electron transport in radiation therapy based on precalculated data," *Medical Physics*, vol. 36, no. 2, p. 530, 2009. DOI: 10.1118/1.3058480.

[35] M. A. Renaud, D. Roberge, and J. Seuntjens, "Latent uncertainties of the precalculated track Monte Carlo method," *Medical Physics*, vol. 42, no. 1, pp. 479–490, 2015. DOI: 10.1118/1.4903502.

[36] I. Kawrakow, D. Rogers, E. Mainegra-Hing, *et al.*, *Egsnrc toolkit for monte carlo simulation of ionizing radiation transport*, doi:10.4224/40001303 [release v2021], 2000.

[37] G. E. Holt, A. M. Griffin, M. Pintilie, *et al.*, "Fractures following radiotherapy and limb-salvage surgery for lower extremity soft-tissue sarcomas: A comparison of high-dose and low-dose radiotherapy," *The Journal of Bone & Joint Surgery*, vol. 87, no. 2, pp. 315–319, 2005. DOI: 10.2106/JBJS.C.01714.

[38] E. H. Baldini, M. R. Lapidus, Q. Wang, *et al.*, "Predictors for major wound complications following preoperative radiotherapy and surgery for soft-tissue sarcoma of the extremities and trunk: Importance of tumor proximity to skin surface," *Annals of Surgical Oncology*, vol. 20, no. 5, pp. 1494–1499, May 2013. DOI: 10.1245/s10434-012-2797-1.

[39] D. G. LeBrun, D. M. Guttmann, J. E. Shabason, *et al.*, "Predictors of wound complications following radiation and surgical resection of soft tissue sarcomas," *Sarcoma*, vol. 2017, p. 5 465 130, Jun. 2017. DOI: 10.1155/2017/5465130.

[40] S. R. Hymes, E. A. Strom, and C. Fife, "Radiation dermatitis: Clinical presentation, pathophysiology, and treatment 2006," *Journal of the American Academy of Dermatology*, vol. 54, no. 1, pp. 28–46, 2006. DOI: https://doi.org/10.1016/j.jaad.2005.08.054.

[41] Y. M. Tai, V. J. Heng, M.-A. Renaud, M. Serban, and J. Seuntjens, "Quality assurance for mixed electron-photon beam radiation therapy using treatment log files and MapCHECK," Manuscript submitted for publication.

[42] N. Reynaert, F. Crop, E. Sterpin, I. Kawrakow, and H. Palmans, "On the conversion of dose to bone to dose to water in radiotherapy treatment planning systems," *Physics and Imaging in Radiation Oncology*, vol. 5, pp. 26–30, 2018. DOI: https://doi.org/10.1016/j.phro.2018.01.004.

[43] M. Berger, J. Coursey, and M. Zucker, *Estar, pstar, and astar: Computer programs for calculating stopping-power and range tables for electrons, protons, and helium ions (version 1.2.3)*, en, 2005.

[44] M. Berger, J. Hubbell, S. Seltzer, J. Coursey, and D. Zucker, *Xcom: Photon cross section database (version 1.5)*, en, 1999.

CHAPTER 9
Technical Note: Impact of range uncertainties for MBRT

Veng Jean Heng, Marc-André Renaud, Monica Serban, Jan Seuntjens

Manuscript in preparation.

9.1 Preface

Although Renaud *et al.* [1] have established the framework for setup-robust MBRT optimization, they did not consider the effect of range uncertainties on MBRT dose distribution. When clinically employed for planning of intensity modulated proton therapy, robust optimization involve both setup and range scenarios. As setup uncertainties were shown to require a robust optimization approach to be adequately accounted for with MBRT, it is therefore a reasonable precaution to investigate the relevance of range uncertainties. The latter arise due to the uncertainties in assigning the mass density of patient tissue from CT data. As electrons have limited penetration range in matter, an uncertainty in the density of matter could impact their depth dose deposition distribution. In this chapter we assess the extent of this impact and the discuss the necessity of including range scenarios in the optimization process.

9.2 Abstract

Purpose: Robust optimization has been employed to account for both setup and range uncertainties by explicitly calculating patient dose distributions under simulated errors. In the context of mixed electron-photon radiation therapy (MBRT), robust optimization to setup uncertainties has been demonstrated to be necessary. This study seeks to assess the impact of range uncertainties on MBRT plans.

Methods: The percent depth dose of 2 electron beams (6 MeV and 20 MeV) and 1 photon beam (6 MV) are calculated by Monte Carlo using EGSnrc in 3 slab phantoms. Range errors are simulated by generating 2 copies of the phantom with each voxel's mass density

upscaled or downscaled by 3.5%. Furthermore, 2 clinical plans, a leg sarcoma case and a post-mastectomy breast case, were replanned with MBRT with 2 optimization methods: once without robust optimization and once robust to both setup and range errors. The robust optimizer was modified to account for range uncertainties by introducing 2 new range scenarios where the CT numbers were upscaled/downscaled by 3.5% prior to conversion to mass density. Setup scenarios were calculated by introducing 5 mm shifts to the plan's isocenter in six Cartesian directions.

Results: Dose discrepancies between the PDDs of density-scaled phantoms and the nominal phantom were found to be much larger for electron beams than photons with maximum offsets of 6.9% vs. 1.6% of the maximum dose. In both clinical cases, the region of largest dose discrepancy between the range and nominal scenarios was found to be along the electron's beam path, immediately beyond the target's depth. Depending on the plan and organs, DVHs of organs-at-risk were either much less susceptible or equally as susceptible to range errors than setup errors. No significant change in the DVHs of range scenarios were observed between the robust and non-robust plan.

Conclusion: Errors in the assignment of mass densities from the CT numbers can have substantial impact on external electron beam's dose distributions. In MBRT plans, these errors can be expected to manifest in regions immediately beyond the target. Nevertheless, for the 2 cases investigated in this study, the introduction of range scenarios did not significantly improve the plan's robustness to range uncertainties.

9.3 Introduction

As external beam radiotherapy treatments have become increasingly conformal, it is important to ensure that patient motion and setup errors do not compromise coverage of the target. In photon radiotherapy, this issue has been handled by the concept of the planning target volume (PTV) as defined in the ICRU83 report [2]. The establishment of geometrical margins around the target allows for the target to remain covered by the prescription dose

despite being potentially subjected to spatial shifts. However, this approach relies on the assumption of the static dose cloud approximation. Although this assumption is relatively accurate for photons, it fails for charged particles like protons and heavy ions. It is in this context that robust optimization was developed. [3]–[7] With the robust optimization approach, setup errors are accounted for by explicitly calculating the dose distribution under such errors. In this method, multiple samples of the patient's dose distribution are calculated under different so-called "scenarios". For each scenario, a representative shift is either judiciously chosen [5], [6], [8] or randomly sampled from a Gaussian distribution [4]. The shift is artificially introduced to the patient's position to mimic setup errors. The optimizer then prices a plan based on the dose in all considered scenarios.

In addition to accounting for setup errors, robust planning also commonly accounts for range uncertainties. To accurately calculate the dose deposited by a charged particle in the patient body, the mass density or electron density of the latter must be mapped. In clinical practice, this is done by converting Hounsfield units from single energy kV CT images to mass densities using a pre-calibrated conversion curve. However, it is known that the relationship between HU from conventional CT and mass density is non-bijective [9], [10]. As HU derived from single energy kV X-ray can theoretically be associated with multiple mass densities depending on the tissue's exact elemental composition, this introduces uncertainties in the assignment of mass density of the patient phantom. Coupled with uncertainties in the CT acquisition and reconstruction, a non-negligible uncertainty is incurred on the calculation of mass density, and thereby the range of charged particle. Uncertainties of 3.7% in assignment of lung CT number have been reported [11]. Range uncertainties have been often accounted for by introducing additional range scenarios in the robust optimization approach. These scenarios consist of either uniformly upscaling or downscaling the particle's stopping power by an arbitrary factor. Range scenarios would then be handled within the robust optimizer the same way as setup scenarios to produce a both range-robust and setup-robust

plan. [4], [12]

Mixed electron-photon beam radiation therapy (MBRT) is a novel technique that combines the use of both particle type to better leverage each of their dosimetric characteristics [1], [13]–[21]. MBRT treatments exploit electron beams' high surface dose and limited penetration depth, while compensating for their wider penumbra with sharper penumbras of photon beams. With MBRT, external electron beams are modulated using only the existing photon multi-leaf collimators, eliminating the need for applicators and cutouts while allowing for more flexible delivery setups. Renaud et al. [1] have demonstrated that MBRT must be robustly optimized to adequately account for patient setup errors. In their approach, they had only considered setup uncertainties. In this study, we investigate the impact of range uncertainties within the context of robust MBRT optimization and assess whether its addition as a robust scenario is necessary.

9.4 Methods

To assess the dosimetric impact of mass density uncertainties on MBRT beams, the percent depth dose (PDD) of three representative fields were calculated in slab geometry phantoms. Three phantom-types were considered: a homogeneous water phantom, a water/lung/water phantom and a water/bone/water phantom. For the two heterogeneous phantoms, the water and bone slabs have a thickness of 3 cm while it is 10 cm for lung. The lung and bone slabs are modelled as density-scaled water, with default mass densities of 0.26 and 1.85 g/cc, respectively. The PDDs are calculated by Monte Carlo using the EGSnrc user-code DOSXYZnrc for 5×5 cm^2 6 MV photon, 20 MeV and 6 MeV electron fields. Both electron and photon fields were collimated using the Millennium MLC as is done in MBRT plans. Varian-provided phase space files are used as the source of initial particles. To simulate errors in mass density assignment, two copies of each phantom was generated with densities downscaled/upscaled by 3.5%, such that three PDDs were calculated for each phantom-type and each field. Sufficient histories were used so as to reach an average type-A

uncertainty of less than 0.4% in voxels receiving at least 50% of the maximum dose.

To account for range uncertainties in MBRT plans, two additional range scenarios are calculated for all beamlet calculations by generating an upscaled and a downscaled phantom in the nominal setup position. The scaling is performed by either upshifting or downshifting the HU in the CT image by a uniform factor prior to conversion to mass density. For this study, this factor was arbitrarily chosen to be 3.5% as conservatively estimated by the Harvard group [22]. The range scenarios beamlet are then assigned a user-defined weight to be used when priced by the robust optimizer. In this study, a weight of 1/6 was assigned to each range scenarios while positioning scenarios had a weight of 1/14. These weights were chosen so that the sum of the 3 range scenarios (nominal, downscaled and upscaled) weights equated the sum of the 7 positioning scenarios (nominal and ±x,y,z) weights. As the nominal scenario beamlets represents both the nominal range and nominal positioning scenarios, it had a combined weight of $1/14 + 1/6 = 0.2381$. This is done so that the choice of number of scenarios assigned to each uncertainty type does not bias its overall weight assigned by the optimizer. A more accurate method would be to account for an upscaled and downscaled range scenarios for each setup scenario. This would lead to a total of $3 \times 7 = 21$ scenarios that could then be individually equally weighted. However, the required random-access memory to store beamlets during the optimization (as well as the optimization time) increases linearly with the number of scenarios. Due to the large size of electron beamlets, this was not feasible with our current hardware. A more detailed description of the robust optimizer can be found in Renaud et al. 2019 [1]. Photon beamlets were calculated using an in-house collapsed cone algorithm while an in-house precalculated Monte Carlo method was used for electron beamlets.

Range-robust plans were generated on two sites: a leg sarcoma and a post-mastectomy breast cancer. For each patient, a plan was optimized while accounting for both range and setup errors while another plan was optimized non-robustly. All optimization constraints

are kept identical between robust and non-robust plans. Although the robust scenario doses are not used to optimize the non-robust plans, they are nevertheless evaluated to assess the impact of range errors when they are not accounted for.

9.5 Results

The PDD for the 3 fields are plotted in Fig. 9–1 for each phantom-type. The residual subplot shows the degree of dose offset introduced by a 3.5% error in the density of each material. As expected, for all phantom-types, the electron fields are significantly more perturbed by the range uncertainty than the 6 MV photon field. In the homogeneous water phantom, the PDD of the range scenarios reach a global dose offset of up to 6.9% and 5.5% from the nominal PDD for the 6 MeV and 20 MeV electron fields, respectively. In contrast, for the same phantom, the 6 MV photon PDD differed by less than 1.6%. In the heterogeneous phantoms, the lung and bone slabs, had the effect of stretching and compressing the PDD curve, respectively. This is expected as these slabs were modelled as water with scaled mass densities. The amplitude of dose offsets introduced by the range uncertainties remained similar across all phantom types.

Range scenarios were evaluated in MBRT plans on 2 clinical cases. For each case, the DVHs as evaluated for the nominal, setup and range scenarios are plotted in Fig. 9–2, where a setup and range-robust MBRT plan is compared to a non-robust MBRT plan. In the leg sarcoma case (Fig. 9–2a and 9–2b), the extent of DVH deviations caused by range errors (dashed lines) were substantially smaller than setup errors (shaded bands). However, for the breast case (Fig. 9–2c and 9–2d), the DVH of some OARs (ipsilateral lung, heart) had degradations due to range errors that were equivalent, albeit small, in magnitude to the worst setup error scenarios. These observations were true for both the robust and non-robust plans. In fact, the range scenario DVHs were not substantially different between robust and non-robust plans. This in stark contrast to setup scenarios which were found to more significantly degrade the CTV coverage in the non-robust plan than when robustly optimized against. For example in the post-mastectomy breast case, the CTV V50Gy, which

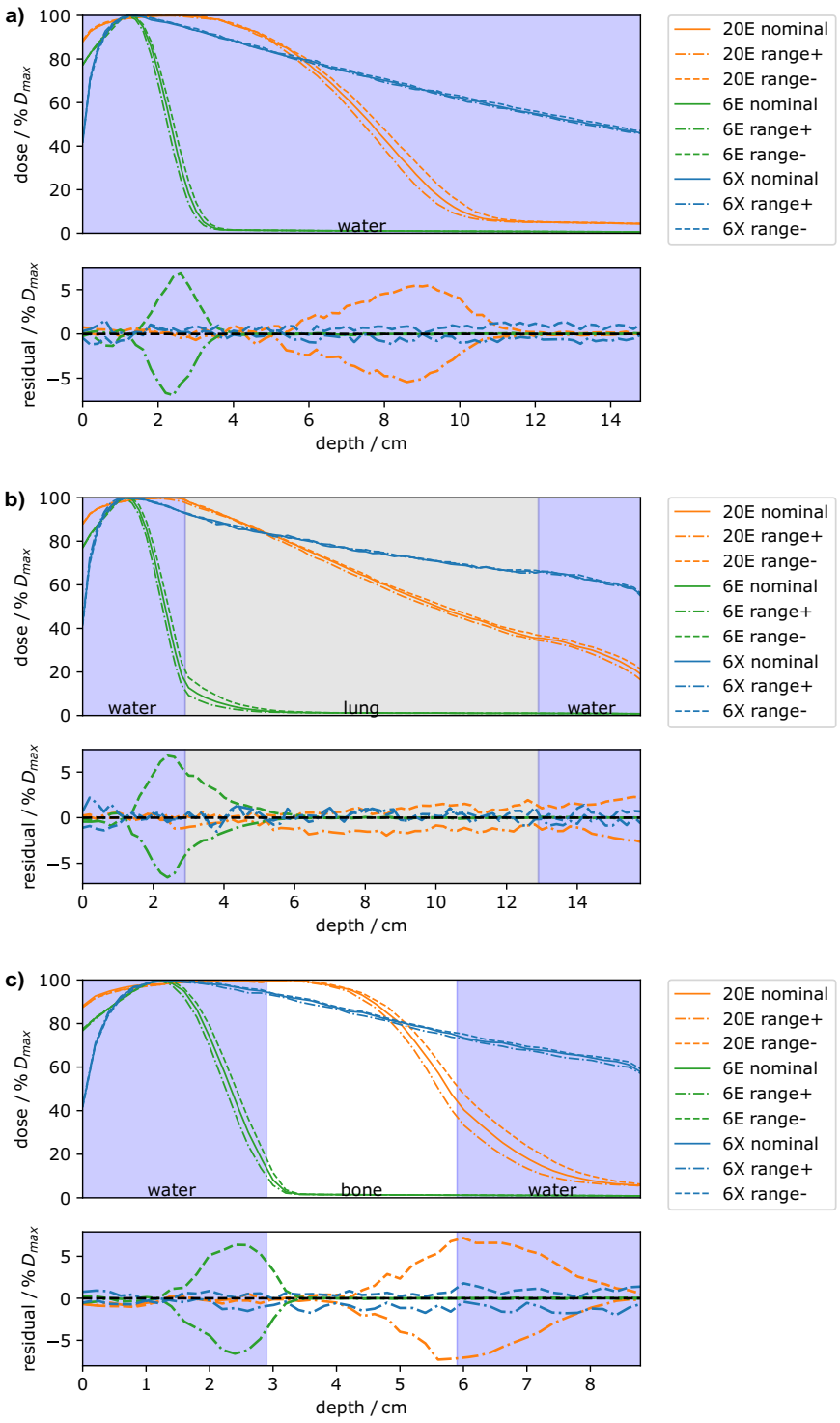

Figure 9–1: PDD for 3 beam qualities in 3 phantoms: (a) Homogeneous water phantom. (b) Water/Lung/Water slabs. (c) Water/Bone/Water slabs. The PDD is calculated in the nominal scenario and in the upscaled (range+) and downscaled (range-) scenarios. The bottom residual curve shows the global dose difference of each range scenarios from nominal for the same beam. The PDD of electrons beams are significantly more offset from the nominal scenario than their photon counterpart.

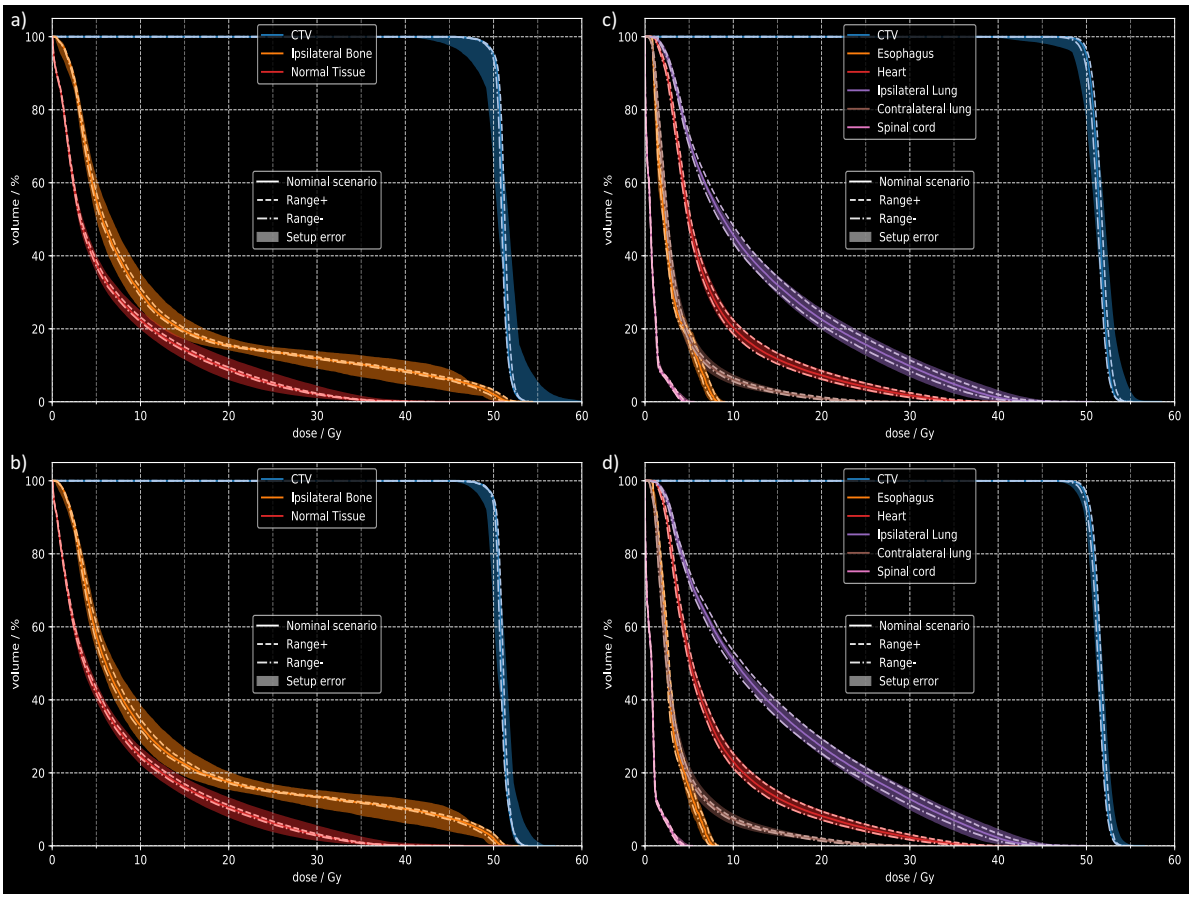

Figure 9–2: DVH of a leg sarcoma case planned with a) non-robust MBRT vs. b) robust MBRT and DVH of a post-mastectomy breast case planned with c) non-robust MBRT vs. d) robust MBRT. The shaded bands represent the extent of the largest deviations of DVH from the nominal scenario by setup scenarios while dashed lines represent the DVH of the range scenarios.

is normalized to 95% in the nominal scenario, was found to be degraded down to 76% in the non-robust plan when the patient phantom was shifted by 5 mm to their right. This same shift in the robust plan maintained a CTV V50Gy of 86%. This effect is exacerbated in the shoulder and tail region of the target DVH.

The difference of the dose distribution as evaluated in the CT-downscaled range scenario and the nominal scenario is shown in Fig. 9–3 for the robust plans. The near-maximum voxel-wise dose differences were calculated as the D2cc of the distribution of dose differences. They were relatively small: D2cc = 1.3 Gy (2.6% of the prescription dose) in the leg sarcoma case and D2cc = 2.5 Gy (5.0%) in the breast case. However, the region of largest dose

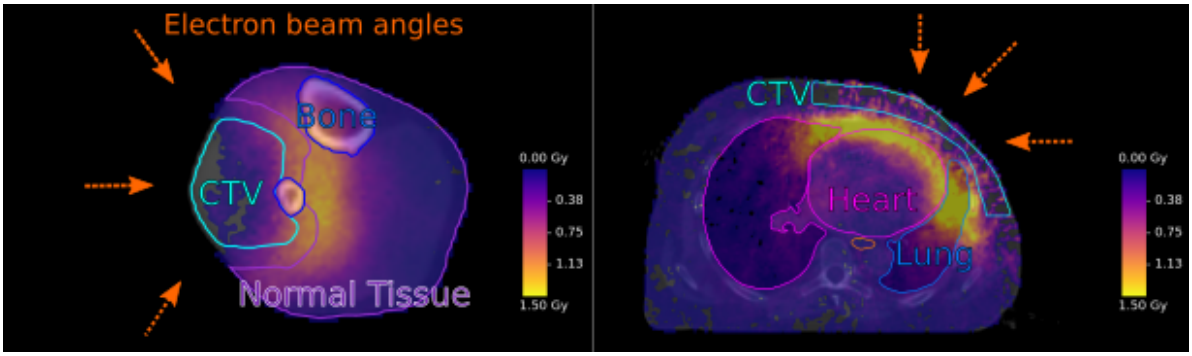

Figure 9–3: Difference of robust MBRT dose as evaluated in the CT-downscaled scenario and the nominal scenario for the leg sarcoma case (left) and the breast case (right). The electron beam angles for each plan are depicted by orange dashed arrows. The largest dose difference was consistently found in the region immediately beyond the target.

discrepancies was consistently found to be located along the electron beams paths, at depths immediately beyond the target.

9.6 Discussion

As observed in the PDD curves on density scaled phantoms, the electron fields are much more substantially affected by range uncertainties than photons. In this study, range uncertainties were simulated by changing the phantom's mass density. This affected the photon PDD curve by changing the linear attenuation coefficient and similarly the electron PDD curve by changing the stopping power. Down-scaling the density of a phantom can be alternatively viewed as stretching the length of the phantom while keeping its overall mass equal. This results in a more stretched-out PDD than the PDD for the nominal density, as can be seen in Fig. 9–1.However, as electron PDDs have a much higher dose gradient, this also leads to a larger pointwise dose discrepancy when varying the phantom's mass density. Indeed, the largest dose residual between the electron PDD as evaluated in range scenarios vs. in the nominal scenario was observed in the rapid dose fall-off region. In contrast, photon PDDs having a relatively smaller and consistent dose gradient were found to have more constant and smaller dose deviation in range vs. nominal scenario.

When not explicitly accounted for, range scenarios have a much smaller and consistent impact on the DVH than positioning scenarios. The impact of range errors are also mitigated with MBRT compared to electron-only plans due to 2 reasons. The presence of photons means that a significant portion of the dose is going to be inherently more range robust. The use of multiple electron beam angle and energies spreads out the impact of range errors over different spatial regions and depths. This leads to smaller dose discrepancy between range scenarios and nominal scenario doses at any one point than compared to single beam angle and energy setups as in Fig. 9–1.

Fang et al. [23] have investigated the impact of the uncertainty on the assignment of mass density on electron dose calculation. Although some large voxel-wise dose differences were observed, they assessed that target dose metrics were not perturbed to a clinically significant level. They suggested that the depths of targets in electron treatments were shallow enough for differences in densities to not have a significant dosimetric impact in this region. Similarly, in the 2 clinical cases presented in this study, the CTV DVH was not significantly perturbed in the range error scenarios when compared to setup error scenarios. We observed in both cases that the largest dose discrepancies between CT-number-perturbed scenarios and the nominal scenario were located immediately beyond the depth of the target. This can be explained from the PDD curves in Fig. 9–1: the largest dose discrepancy region coincides with the rapid dose-fall off regions. As the target dose is generally optimized to receive the maximum dose, this entails that the target is positioned in the maximum plateau dose region of electron beams. At depths immediately beyond the target, optimization constraints are generally set to restrict doses to normal tissue. In practice, this means that at that depth, the electron beams will be in their rapid dose fall-off region, where they are most susceptible to range errors.

The introduction of range scenarios in the robust optimizer did not make either clinical plan more robust to range scenarios. This could be partly because the impact of the range

scenarios were limited on the OARs that were relevant to these cases. Although the lungs and the heart in the breast case had part of their volume in the region most susceptible to range errors, this region remains relatively small compared to the overall OAR volume and its impact on the DVH would therefore not be visible. As such, the range scenarios do not incur a significant price to the averaged cost function of these OARs. A case that would have a smaller critical OAR located in close proximity to the target could potentially be more severely impacted by range errors. More work must be done to identify clinical cases that would benefit from a range-robust optimization and the extent of its benefit.

9.7 Conclusion

This study evaluated the impact of range uncertainties on robust MBRT plans by introducing 2 new range scenarios to the robust optimizer. In clinical plans, the largest dose discrepancies were observed to be located at depths immediately beyond the target. Nevertheless, discrepancies between range scenarios and nominal scenario doses were found to be equivalent between range-robust and non-robust plans. Although explicitly accounting for range scenarios in robust MBRT planning did not provide any additional benefit in this study, a larger and more diverse cohort is required to verify and generalize this finding.

9.8 Conflict of Interest Statement

The authors have no relevant conflicts of interest to disclose.

9.9 Data Availability Statement

The data that support the findings of this study are available from the corresponding author upon reasonable request.

REFERENCES

[1] M.-A. Renaud, M. Serban, and J. Seuntjens, "Robust mixed electron–photon radiation therapy optimization," *Medical Physics*, vol. 46, no. 3, pp. 1384–1396, 2019. DOI: https://doi.org/10.1002/mp.13381.

[2] ICRU, "Report 83: Prescribing, Recording, and Reporting Photon-Beam Intensity-Modulated Radiation Therapy (IMRT)," *Journal of the ICRU*, vol. 19, no. 1, 2010. DOI: 10.1093/jicru/ndq025.

[3] J. Unkelbach and U. Oelfke, "Incorporating organ movements in imrt treatment planning for prostate cancer: Minimizing uncertainties in the inverse planning process," *Medical Physics*, vol. 32, no. 8, pp. 2471–2483, 2005. DOI: https://doi.org/10.1118/1.1929167.

[4] J. Unkelbach, T. Bortfeld, B. C. Martin, and M. Soukup, "Reducing the sensitivity of impt treatment plans to setup errors and range uncertainties via probabilistic treatment planning," *Medical Physics*, vol. 36, no. 1, pp. 149–163, 2009. DOI: https://doi.org/10.1118/1.3021139.

[5] A. Fredriksson, A. Forsgren, and B. Hårdemark, "Minimax optimization for handling range and setup uncertainties in proton therapy," *Medical Physics*, vol. 38, no. 3, pp. 1672–1684, 2011. DOI: 10.1118/1.3556559.

[6] W. Liu, X. Zhang, Y. Li, and R. Mohan, "Robust optimization of intensity modulated proton therapy," *Medical Physics*, vol. 39, no. 2, pp. 1079–1091, 2012. DOI: 10.1118/1.3679340.

[7] J. Unkelbach and H. Paganetti, "Robust Proton Treatment Planning: Physical and Biological Optimization," *Seminars in Radiation Oncology*, vol. 28, no. 2, pp. 88–96, 2018. DOI: 10.1016/j.semradonc.2017.11.005.

[8] D. Pflugfelder, J. J. Wilkens, and U. Oelfke, "Worst case optimization: A method to account for uncertainties in the optimization of intensity modulated proton therapy," *Physics in Medicine and Biology*, vol. 53, no. 6, pp. 1689–1700, 2008. DOI: 10.1088/0031-9155/53/6/013.

[9] C. G. Ainsley and C. M. Yeager, "Practical considerations in the calibration of ct scanners for proton therapy," *Journal of Applied Clinical Medical Physics*, vol. 15, no. 3, pp. 202–220, 2014. DOI: https://doi.org/10.1120/jacmp.v15i3.4721.

[10] A. Sudhyadhom, "On the molecular relationship between hounsfield unit (hu), mass density, and electron density in computed tomography (ct)," *PLOS ONE*, vol. 15, no. 12, pp. 1–15, Dec. 2021. DOI: 10.1371/journal.pone.0244861.

[11] M. Yang, X. R. Zhu, P. C. Park, *et al.*, "Comprehensive analysis of proton range uncertainties related to patient stopping-power-ratio estimation using the stoichiometric calibration," en, *Phys. Med. Biol.*, vol. 57, no. 13, pp. 4095–4115, Jul. 2012.

[12] J. Unkelbach, T. C. Y. Chan, and T. Bortfeld, "Accounting for range uncertainties in the optimization of intensity modulated proton therapy," *Physics in Medicine & Biology*, vol. 52, no. 10, p. 2755, Apr. 2007. DOI: 10.1088/0031-9155/52/10/009.

[13] B. A. Palma, A. U. Sánchez, F. J. Salguero, *et al.*, "Combined modulated electron and photon beams planned by a Monte-Carlo-based optimization procedure for accelerated partial breast irradiation," *Physics in Medicine and Biology*, vol. 57, no. 5, pp. 1191–1202, 2012. DOI: 10.1088/0031-9155/57/5/1191.

[14] C. Míguez, E. Jiménez-Ortega, B. A. Palma, *et al.*, "Clinical implementation of combined modulated electron and photon beams with conventional MLC for accelerated partial breast irradiation," *Radiotherapy and Oncology*, vol. 124, no. 1, pp. 124–129, 2017. DOI: 10.1016/j.radonc.2017.06.011.

[15] M.-A. Renaud, M. Serban, and J. Seuntjens, "On mixed electron-photon radiation therapy optimization using the column generation approach," *Medical Physics*, vol. 44, no. 8, pp. 4287–4298, 2017. DOI: 10.1002/mp.12338.

[16] S. Mueller, M. K. Fix, A. Joosten, *et al.*, "Simultaneous optimization of photons and electrons for mixed beam radiotherapy," *Physics in Medicine and Biology*, vol. 62, no. 14, pp. 5840–5860, 2017. DOI: 10.1088/1361-6560/aa70c5.

[17] S. Mueller, P. Manser, W. Volken, *et al.*, "Part 2: Dynamic mixed beam radiotherapy (dymber): Photon dynamic trajectories combined with modulated electron beams," *Medical Physics*, vol. 45, no. 9, pp. 4213–4226, 2018. DOI: https://doi.org/10.1002/mp.13085.

[18] V. J. Heng, M. Serban, J. Seuntjens, and M.-A. Renaud, "Ion chamber and film-based quality assurance of mixed electron-photon radiation therapy," *Medical Physics*, vol. 48, no. 9, pp. 5382–5395, 2021. DOI: https://doi.org/10.1002/mp.15081.

[19] E. Heath, S. Mueller, G. Guyer, *et al.*, "Implementation and experimental validation of a robust hybrid direct aperture optimization approach for mixed-beam radiotherapy," *Medical Physics*, vol. 48, no. 11, pp. 7299–7312, 2021. DOI: https://doi.org/10.1002/mp.15258.

[20] V. J. Heng, M. Serban, M.-A. Renaud, C. Freeman, and J. Seuntjens, "Robust mixed electron-photon radiation therapy planning for soft tissue sarcoma," *Medical Physics*, vol. 50, no. 10, pp. 6502–6513, 2023. DOI: https://doi.org/10.1002/mp.16709.

[21] Y. M. Tai, V. J. Heng, M.-A. Renaud, M. Serban, and J. Seuntjens, "Quality assurance for mixed electron–photon beam radiation therapy using treatment log files and mapcheck," *Medical Physics*, pp. 1–13, 2023. DOI: https://doi.org/10.1002/mp.16759.

[22] H. Paganetti, "Range uncertainties in proton therapy and the role of monte carlo simulations," *Physics in Medicine & Biology*, vol. 57, no. 11, R99, May 2012. DOI: 10.1088/0031-9155/57/11/R99.

[23] R. Fang, T. Mazur, S. Mutic, and R. Khan, "The impact of mass density variations on an electron monte carlo algorithm for radiotherapy dose calculations," *Physics and*

Imaging in Radiation Oncology, vol. 8, pp. 1–7, 2018. DOI: https://doi.org/10.1016/j.phro.2018.10.002.

CHAPTER 10
Summary and outlook

10.1 Summary

External megavoltage electron beams have well-established dosimetric properties that are clinically beneficial for the treatment of superficial tumors. Their high entrance dose and rapid dose fall-off allows for better sparing of healthy tissue beyond the tumor depth. However, their clinical use remains limited to rudimentary delivery setups. Conventional electron treatments are delivered using an applicator and cutouts molded to the shape of the desired field. These devices provide additional collimation to the electron beam to counteract the relatively high scattering of electrons in air. However, this comes at the cost of a higher logistical burden and limits treatments to mostly using single beam angles and single energies. In contrast, external megavoltage photon treatments are currently delivered using highly precise MLCs which allow for treatments to use hundreds of aperture shapes. MBRT is an emerging technique which aims to combine the use of external electron and photon beams, both delivered using MLC. MBRT treatment plans can leverage the dosimetric benefits of either particle type while benefiting from the flexibility in treatment deliveries found in state-of-the-art photon treatments.

The work described in this thesis aim to bring MBRT closer to a realistic implementation in the clinic. This involved considerations of distinct, yet related, elements

10.2 Faster electron beamlet calculation using the Precalculated Monte Carlo method.

A TPS, `brems`, has been rewritten to provide a more efficient planning of MBRT treatment plans. Notably, a PMC code previously developed for fast GPU-based electron dose calculation [1] has been modified to properly handle bremsstrahlung photon transport. This

allowed PMC to be used on `brems` for faster calculations of robust electron beamlets. PMC achieves faster dose calculation than full Monte Carlo codes by pre-calculating electron tracks at all relevant energies. As a result, planning time of robust MBRT plans has been reduced from ∼1 week to ∼1 day.

10.3 Ion chamber and film-based QA of MBRT

To ensure that the MBRT dose calculated by our TPS is representative of the dose delivered to patients, quality assurance QA of MBRT plans must be performed. In particular, dose delivery of electron beams collimated with the MLCs is not mandated by linac manufacturers and must therefore be rigorously validated. Electron dose measurements with ion chamber are challenging as their beam quality differs depending on the measurement depth and can be impacted by the MLC modulation. To account for differences in beam quality between reference conditions and patient-specific QA of MBRT plans, we introduce a formalism that corrects the measurement reading with a ratio of stopping power ratios of water to air. The correction factor can be calculated in the phantom's voxelized geometry through a modified EGSnrc user-code: SPRXYZnrc. An MBRT plan was delivered on a PMMA cylindrical phantom and dose measurements were taken with an ion chamber and film. Ion chamber measurements agreed with Monte Carlo calculations with 2.1% and a gamma passing rate of 97.3% was obtained for film with a gamma criterion of 3%/2 mm. This work established a formalism for ion chamber measurement in MBRT fields and demonstrated the accurate deliverability of MBRT plans using photon-MLCs.

10.3.1 QA for MBRT using treatment log files and MapCheck

It is common practice to perform patient-specific QA prior to delivery of any new treatment technique. This ensures that each individual plan can be accurately delivered. Although an ion chamber and film-based QA method has been devised, they are time-consuming procedures that would constitute a substantial logistical burden if to be done

prior to each treatment. To remedy this, we commissioned the MapCHECK®, a diode array detector, and a log file-based dose reconstruction approach for MBRT dose verification. An *ab initio* model of the MapCHECK® was created using the manufacturer's blueprint data to precisely model detector's geometry. This step was necessary due to the sharp dose gradient found in electron fields. Five MBRT plans were delivered onto the MapCHECK® and measurements were compared to Monte Carlo calculation through a gamma analysis with a gamma criterion of 3%/2 mm. All five plans had a gamma passing rate of above 97%. For one representative plan, the trajectory log files were collected, and the machine parameters were used to recalculate the patient's Monte Carlo dose. No clinically relevant differences in dose to any relevant structures were found between the log file-recalculated dose and the theoretical planned dose.

10.4 Robust MBRT planning for STS

To demonstrate the dosimetric benefit of MBRT compared to the standard of care, a retrospective treatment planning study was performed on a cohort of 22 soft tissue sarcoma of the lower extremity. Robust MBRT plans were re-optimized for each patient and dosimetrically compared to their standard of care VMAT treatment plans. Although VMAT plans required the use of bolus in 10 of the 22 patients, no MBRT plans required bolus to reach an equivalent coverage of the clinical target volume by the prescription dose. Doses to organs-at-risk were significantly lower in MBRT plans with $V_{20\text{Gy}}$ to normal tissue decreasing by $14.9 \pm 3.2\%$ ($p < 10^{-}6$) and $V_{50\text{Gy}}$ to bone decreasing by $8.2 \pm 4.0\%$ ($p < 10^{-3}$).

10.5 Impact of range uncertainties for MBRT

Past studies have demonstrated the necessity for MBRT plans to be optimized robustly to setup errors [2], [3]. In this study, the impact of range uncertainties on MBRT plans due to errors in the mass density assignment are investigated. Range scenarios are introduced by calculating beamlets in 2 additional scenarios. Patient CT numbers are either upscaled or

downscaled by a constant factor conservatively chosen to be 3.5%. Both setup and range scenarios are then priced by the optimizer and a scenario-weighted price is then evaluated. The most susceptible regions to dose discrepancies due to range errors were found to be located along electron beams' path, immediately downstream from the target. Nevertheless, within the limited scope of this study, no significant improvement in the MBRT plan's robustness was observed with the introduction of range scenarios.

10.6 Future directions

The PMC method was repurposed for fast electron beamlet calculation within `brems`. At this point, `brems` uses 3 different dose calculation algorithm: PMC for electron beamlet, collapsed cone convolution superposition for photon beamlet and EGSnrc for MC recalculations of aperture doses and of the final plan. This process could be streamlined and homogenized by performing both beamlet (including photon) and final dose calculations using the PMC algorithm. This would involve creating a beam model in PMC to adequately account for the scattering effects of the jaws and MLCs. Alternatively, the BEAMnrc user code could be used to supply PMC with particles downstream of the MLCs. PMC would therefore replace DOSXYZnrc, immensely speeding up the calculation of particles in the patient geometry. Beamlet memory size are also of major concern due to the sheer number required by robust optimization. This could be reduced in the future by using a stringent low dose threshold or by employing a variable grid size.

The efficiency of the current implementation of the column generation optimizer could be greatly improved by employing multi-threading strategies. For large targets and robust plans, the current beamlet optimization time is a major bottleneck within the treatment planning pipeline. It is crucial to reduce this optimization time for a realistic clinical implementation as it is common to require many iterations of re-optimization to find the best achievable plan. This could be achieved by multi-threading the aperture pricing problem

step.

Any new treatment technique comes with its unique planning challenges and quirks. A wide-spread adoption of MBRT would be hindered by the necessary training of treatment planners. It is difficult for a new planner to determine the best plan quality that can be achieved for a given patient. More effort can always be expended to try to reach a better plan quality, but how good is good enough? How should optimization constraints be changed from iteration to iteration? One way to facilitate the choice of these complex decisions would be through automated planning approaches using either knowledge-based planning [4] or deep learning [5]. A major challenge with artificial intelligence methods is the requirement of a large training set. For a new technique, it is difficult to come up with a sufficiently large training set of good quality. In this case, a deep reinforcement learning [6] approach could be well-suited as the training data can be generated on-the-fly on a small set of patients. However, this would be dependent on very fast beamlet calculation and optimization.

Currently, some parameters are manually pre-chosen by the planner at the trajectory creation step. Notably, this includes the electron and photon beam angles, their SSD and their allowed energies. However, these parameters have a profound impact on the overall achievable OAR sparing and conformity of the plan. A novice planner may not have the expertise to judiciously pick the correct parameters right from the onset. It would be worthwhile to investigate the benefit of having a machine learning model that can make preliminary recommendations of these parameters based on the position of the target with respect to OARs and the patient body.

While further improvements can be made on the technical front, any clinical implementation requires the endorsement of radiation oncologists. Unequivocal clinical benefits of MBRT must be demonstrated for clearly identified cancer types. Although lower extremity soft tissue sarcomas were shown to benefit from MBRT treatments, other treatment sites

with superficial tumors remain to be investigated at a larger scale. Head & neck and breast are examples of such sites, with much higher incidence rate, for which preliminary studies have shown potential benefits of an MBRT approach. The next step would be to perform a pilot study, similar to the one by Míguez *et al.* [7]. This would aim to demonstrate the feasibility of patient treatment with our MBRT approach and ensure that it does not lead to severe radiation-induced toxicities.

REFERENCES

[1] M. A. Renaud, D. Roberge, and J. Seuntjens, "Latent uncertainties of the precalculated track Monte Carlo method," *Medical Physics*, vol. 42, no. 1, pp. 479–490, 2015. DOI: 10.1118/1.4903502.

[2] M.-A. Renaud, M. Serban, and J. Seuntjens, "Robust mixed electron–photon radiation therapy optimization," *Medical Physics*, vol. 46, no. 3, pp. 1384–1396, 2019. DOI: https://doi.org/10.1002/mp.13381.

[3] E. Heath, S. Mueller, G. Guyer, *et al.*, "Implementation and experimental validation of a robust hybrid direct aperture optimization approach for mixed-beam radiotherapy," *Medical Physics*, vol. 48, no. 11, pp. 7299–7312, 2021. DOI: https://doi.org/10.1002/mp.15258.

[4] S. Shiraishi and K. L. Moore, "Knowledge-based prediction of three-dimensional dose distributions for external beam radiotherapy," *Medical Physics*, vol. 43, no. 1, pp. 378–387, 2016. DOI: https://doi.org/10.1118/1.4938583.

[5] D. Nguyen, X. Jia, D. Sher, *et al.*, "3D radiotherapy dose prediction on head and neck cancer patients with a hierarchically densely connected u-net deep learning architecture," en, *Phys. Med. Biol.*, vol. 64, no. 6, p. 065 020, Mar. 2019.

[6] C. Shen, D. Nguyen, L. Chen, *et al.*, "Operating a treatment planning system using a deep-reinforcement learning-based virtual treatment planner for prostate cancer intensity-modulated radiation therapy treatment planning," *Medical Physics*, vol. 47, no. 6, pp. 2329–2336, 2020. DOI: https://doi.org/10.1002/mp.14114.

[7] C. Míguez, E. Jiménez-Ortega, B. A. Palma, *et al.*, "Clinical implementation of combined modulated electron and photon beams with conventional MLC for accelerated

partial breast irradiation," *Radiotherapy and Oncology*, vol. 124, no. 1, pp. 124–129, 2017. DOI: 10.1016/j.radonc.2017.06.011.